Structural examination of hydrophobic tunnels in proteins

vorgelegt von

Diplom Biochemikerin

Jacqueline Kalms

geb. in Schmölln

von der Fakultät II - Mathematik und Naturwissenschaften

der Technischen Universität Berlin

zur Erlangung des akademischen Grades

Doktor der Naturwissenschaften

- Dr. rer. nat. -

genehmigte Dissertation

Promotionsausschuss

Vorsitzender: Prof. Dr. Nediljko Budisa

Gutachter: Dr. Patrick Scheerer

Gutachter: Prof. Dr. Peter Hildebrandt

Tag der wissenschaftlichen Aussprache: Berlin, 10. Mai 2017

Berlin 2018

Summary

Enzymes are the biological macromolecular catalysts of life, which work with high substrate specificity, under fine-tuned conditions compared to chemical catalysts. The majority of the catalytic centres of enzymes are located deeply within the protein matrix. To provide efficient substrate accessibility to the active site most proteins offer permanent or transient tunnels as transport pathways. In this thesis, the substrate tunnels of the O_2-tolerant membrane-bound [NiFe] hydrogenase (MBH) from the β-proteobacterium *Ralstonia eutropha* (*Re*) and the lipoxygenase (LOX) from the human pathogen *Pseudomonas aeruginosa* (Pa) are studied with protein X-ray crystallography, novel gas-pumping techniques for protein crystal derivatisation, molecular dynamics (MD) simulations, computational tunnel calculations, site-directed mutagenesis as well as basic structure ligand modelling.

Hydrogenases play an important role in the search for clean energy technologies as they are catalysing the reversible oxidation of hydrogen into protons and electrons. Especially, *Re*MBH with its remarkable feature of O_2 tolerance came into research focus as part of enzymatic fuel cells. A significant interest of this research is to understand the structural features leading to O_2 tolerance. A unique [4Fe3S]-cluster found in *Re*MBH plays a major role in maintaining the catalytic activity under ambient oxygen level. A different approach might be the impact of the characteristics of the substrate pathway. The X-ray crystallography structures of krypton and O_2 derivatised *Re*MBH crystals revealed two distinct gas tunnels connecting the protein exterior with the [NiFe] active site. 15 identified krypton atom positions allowed a comprehensive description of the tunnel positions as well as a cavity for possible gas storage. Several molecular oxygen sites have been found within that substrate pathway system, proving that O_2, the inhibitor of O_2-sensitive hydrogenases, travels through the same hydrophobic tunnels. The *Re*MBH tunnels were further inspected by computational characterisation with the program *Caver 3.0*. The tunnel features of *Re*MBH were compared with other O_2-tolerant and O_2-sensitive hydrogenases uncovering a difference in tunnel quantity and size between the two groups. The variations of the tunnel network might influence the gas diffusion rates, thus O_2 tolerance. The crystallography results were accompanied with molecular dynamics (MD) simulations finding the same routes as proposed from the crystal structures. These outcomes show only small differences between static and dynamic protein conditions, further supporting the results from the comparative study between O_2-sensitive and O_2-tolerant hydrogenases showing variations in the quantity of tunnels. Further experiments based on site-directed

mutagenesis and computational studies might shed a detailed light on the role of the hydrophobic substrate tunnels in O_2 tolerance.

LOXs are enzymes catalysing the peroxidation of polyunsaturated fatty acids (PUFAs) into their hydroperoxy products. Eukaryotic LOXs are well studied and play a role in immune response, tumorigenesis and reproduction in animals or seed germination and pest resistance in plants. However, only in a small amount of bacteria (< 0.5 %) LOX genes have been detected, leading to the question of their role in bacterial life. Apparently, bacterial LOXs have no influence in bacterial survival, but seem to improve the ability for bacteria to adapt to a wide range of environments. In this thesis, the structural characteristic of the substrate tunnel of Pa-LOX and an Ala420Gly mutant have been examined with protein X-ray crystallography and computational calculations. The first structure of a bacterial Pa-LOX has been solved in 2013 showing a structural difference in domain composition compared to the eukaryotic LOX. The two additional lid-helices in Pa-LOX expand the sn-1 cavity by a second (sn-2) cavity. A conserved feature with in the LOXs is the U-shaped sn-1 cavity, which orients the functional unit of the substrate close to the catalytic centre. The sn-2 cavity in Pa-LOX enables the enzyme to bind phospholipids as found in Pa host membranes. Spectroscopic studies indicate that Pa-LOX, as most LOXs, follows the Ala-Gly concept and in the wild-type form is classified as arachidonic acid 15*S*-LOX. However, the Pa-LOX Ala420Gly mutant shows dual regio- and stereospecificity with the formation of 15*S*- and 11*R*-hydroperoxide. Alanine at a critical position at the active site is assigned to LOX with *S*-configuration, whereas *R*-LOX carry a glycine. In this study, the structural alteration associated with the Ala-Gly amino acid exchange within the O_2 access tunnel of Pa-LOX is presented. Removal of the blocking alanine side chain leads to a widening of the substrate tunnel and giving O_2 additional access to the fourth position of the 1,4-pentadiene moiety.

Zusammenfassung

Enzyme sind makromolekulare Biokatalysatoren und im Vergleich zu chemischen Katalysatoren arbeiten sie mit hoher Substratspezifizität, unter spezifisch angepassten Bedingungen. Die meisten katalytischen Zentren in Enzymen sind tief in der Proteinmatrix verborgen. Damit die Substrate das aktive Zentrum erreichen können, bilden ein Großteil dieser Proteine permanente oder transiente Tunnel als Transportwege aus. In dieser Dissertation werden für Substrate zugängliche Tunnel der sogenannten sauerstoff-toleranten, membran-gebundenen [NiFe] hydrogenase (MBH) von dem β-Proteobakterium *Ralstonia eutropha* (*Re*) und der Lipoxygenase (LOX) von dem humanen Pathogen *Pseudomonas aeruginosa* (Pa) mit Hilfe der Röntgenkristallographie, Molekulardynamik-Simulationen (MD), computergestützten Tunnel-Berechnungen, molekular-biologischen Untersuchungen (Punktmutationen) und Proteinliganden-Modellierungen untersucht.

Hydrogenasen katalysieren die umkehrbare Reaktion von Wasserstoff in Protonen und Elektronen und spielen eine wichtige Rolle in der Suche nach erneuerbaren Energien. Speziell die sauerstoff-tolerante *Re*MBH gelangte in den Fokus der Forschung von enzymatischen Bio-Brennstoffzellen. Ein bedeutendes Interesse gilt dem Verständnis der strukturellen Eigenschaften der *Re*MBH im Zusammenhang mit ihrer Sauerstofftoleranz. Ein neu entdeckter bisher einzigartiger Eisen-Schwefel-Cluster ([4Fe3S]-Cluster) der *Re*MBH spielt eine entscheidende Rolle in der Aufrechterhaltung der katalytischen Aktivität unter atmosphärischen Sauerstofflevel, das sich sonst oft schädigend auf diese Enzyme auswirkt. Weiterhin können auch Substratwege im Protein die Sauerstofftoleranz in Hydrogenasen beeinflussen. Die Proteinkristallstrukturen von Krypton- und Sauerstoff-derivatisierten Kristallen, die im Rahmen dieser Arbeit gelöst wurden, offenbarten zwei eindeutig zu verfolgende Gastunnel, welche die Proteinoberfläche mit dem aktiven [NiFe] Zentrum verbinden. 15 in der Struktur identifiezierte Krypton-Atompositionen ermöglichten eine umfassende Beschreibung der Tunnelwege und zeigten außerdem einen Proteinhohlraum, der möglicherweise der Speicherung von Substraten und Gasmolekülen dient. Die in den Tunneln gefundenen Sauerstoffpositionen bestätigen, dass Sauerstoff vergleichbare Wege benutzt wie Krypton. Die *Re*MBH Tunnel wurden zusätzlich mit Tunnel-Berechnungen im Programm *Caver 3.0* charakterisiert. Die Größe, Lage and Anzahl der *Re*MBH Tunnelnetzwerke wurden mit weiteren sauerstoff-toleranten und sauerstoff-sensitiven Hydrogenasen verglichen. Die Ergebnisse zeigten Unterschiede in der Tunnelanzahl und -größe zwischen den beiden

Gruppen. Die Abweichungen im Tunnelnetzwerk könnten die Gasdiffusionsraten und somit die Sauerstofftoleranz beeinflussen. Die MD-Simulationen bestätigten die in den Kristallstrukturen der *Re*MBH gefundenen Transportwege. Diese Ergebnisse zeigten nur sehr geringe Unterschiede zwischen statischen und dynamischen Proteineigenschaften und unterstützen die Aussage der Vergleichsuntersuchungen zwischen sauerstoff-sensitiven und sauerstoff-toleranten Hydrogenasen zu den unterschiedlichen Tunnelanzahlen. Zukünftige experimentelle Mutations- und theoretische Computersimulationsexperimente können möglicherweise eine noch detaillierte Beschreibung über die Rolle der hydrophoben Substrattunnel in der Sauerstofftoleranz dieser Enzyme geben.

Lipoxygenasen sind Enzyme, welche die Peroxidation von mehrfach ungesättigten Fettsäuren in Hydroperoxide katalysieren. Eukaryotische LOX sind umfangreich untersuchte Enzyme und spielen eine Rolle in der Immunantwort, der Tumorgenese und der Reproduktion bei Tieren oder in der Keimung und der Schädlingsabwehr bei Pflanzen. Jedoch wurden nur sehr wenige Gene in Bakterien (< 0.5 %) für die Expression von LOX gefunden. Dies führt zu der Frage inwiefern LOX überhaupt eine Rolle für das Leben von Bakterien spielt. Anscheinend haben LOX keinen Einfluss auf das Überleben von Bakterien, verbessern jedoch die Anpassungsfähigkeit von Bakterien an ein weites Spektrum von Lebensräumen. In dieser Dissertation werden die strukturellen Eigenschaften der Substrattunnel von Pa-LOX sowie einer Ala420Gly Mutante mittels Röntgenkristallographie und Computerberechnungen untersucht. Die erste Proteinkristallstruktur der bakteriellen Pa-LOX wurde in 2013 gelöst und zeigte strukturelle Unterschiede in der Zusammensetzung der Proteindomänen im Vergleich zu eukaryotischen LOX. Die zwei zusätzlichen Helices, die wie ein Deckel über der Substrat-Bindungstasche fungieren, erweitern den Substrat-Hohlraum (sn-1) um einen zweiten Hohlraum (sn-2). Der sn-1 Hohlraum ist in den meisten LOX hauptsächlich U-förmig und orientiert das Substrat in die Nähe des katalytischen Zentrums. Der Pa-LOX sn-2 Hohlraum ermöglicht die Bindung von z.B. Phospholipiden wie sie in den Membranen der Pa-Wirte vorkommen. Spektroskopische Untersuchungen deuten darauf hin, dass Pa-LOX wie die meisten LOX, dem sogenannten Ala-Gly Konzept folgt. Pa-LOX wurde außerdem als Arachidonsäure-15*S*-LOX eingestuft. Untersuchungen der Pa-LOX Ala420Gly Mutante zeigen hingegen eine duale Regio- und Stereospezifität. Die Mutante bildet die beiden Produkte 15*S*- und 11*R*-Hydroperoxid aus. Alanin befindet sich an einer entscheidenden Position in der Nähe des aktiven Zentrums und wird der LOX mit *S*-konfiguration zugeschrieben, wohingegen bei *R*-LOX ein Glycin an der gleichen Stelle sitzt. In dieser Arbeit werden die strukturellen

Veränderungen am Sauerstoffzugangstunnel in Pa-LOX, die durch den Ala-Gly Aminosäureaustausch entstehen, gezeigt. Die Entfernung der blockierenden Alanin-Seitenkette öffnet den Tunnel und macht zusätzlich die vierte Position der funktionellen Gruppe für O_2 zugänglich.

Publications

Publications part of this thesis (*contribution as first author)

1. Krypton Derivatization of an O_2-Tolerant Membrane-Bound [NiFe] Hydrogenase Reveals a Hydrophobic Tunnel Network for Gas Transport. Kalms J*, Schmidt A, Frielingsdorf S, van der Linden P, von Stetten D, Lenz O, Carpentier P, Scheerer P. ***Angew Chem Int Ed Engl.*** 2016 Apr 25; 55(18):5586-90. https://doi.org/10.1002/anie.201508976
2. Tracking the route of molecular oxygen in O_2-tolerant membrane-bound [NiFe] hydrogenase. Kalms J*, Schmidt A, Frielingsdorf S, Utesch T, Gotthard G, von Stetten D, van der Linden P, Royant A, Mroginski MA, Carpentier P, Lenz O, and Scheerer P. ***Proc Natl Acad Sci U S A.*** 2018 Mar 6;115(10):E2229-E2237. https://doi.org/10.1073/pnas.1712267115
3. Structural and functional basis of phospholipid oxygenase activity of bacterial lipoxygenase from Pseudomonas aeruginosa. Banthiya S, Kalms J*, Galemou Yoga E, Ivanov I, Carpena X, Hamberg M, Kuhn H, Scheerer P. ***Biochim Biophys Acta.*** 2016 Nov; 1861(11):1681-1692. https://doi.org/10.1016/j.bbalip.2016.08.002
4. The crystal structure of Pseudomonas aeruginosa lipoxygenase Ala420Gly mutant uncovers its altered specificity. Kalms J*, Banthiya S, Galemou Yoga E, Hamberg M, Kuhn H, Scheerer P. ***Biochim Biophys Acta.*** 2017 May; 1862(5):463-473. https://doi.org/10.1016/j.bbalip.2017.01.003

Publications not relevant for this thesis

5. Resonance Raman Spectroscopic Analysis of the [NiFe] Active Site and the Proximal [4Fe-3S] Cluster of an O2-Tolerant Membrane-Bound Hydrogenase in the Crystalline State. Siebert E, Rippers Y, Frielingsdorf S, Fritsch J, Schmidt A, **Kalms J**, Katz S, Lenz O, Scheerer P, Paasche L, Pelmenschikov V, Kuhlmann U, Mroginski MA, Zebger I, Hildebrandt P. ***J Phys Chem B.*** 2015 Oct 29; 119(43):13785-96. https://doi.org/10.1021/acs.jpcb.5b04119
6. The class III cyclobutane pyrimidine dimer photolyase structure reveals a new antenna chromophore binding site and alternative photoreduction pathways. Scheerer P, Zhang F, **Kalms J**, von Stetten D, Krauß N, Oberpichler I, Lamparter T. ***J Biol Chem.*** 2015 May 1; 290(18):11504-14. https://doi.org/10.1074/jbc.M115.637868
7. Reversible [4Fe-3S] cluster morphing in an O(2)-tolerant [NiFe] hydrogenase. Frielingsdorf S, Fritsch J, Schmidt A, Hammer M, Löwenstein J, Siebert E, Pelmenschikov V, Jaenicke T, **Kalms J**, Rippers Y, Lendzian F, Zebger I, Teutloff C, Kaupp M, Bittl R, Hildebrandt P, Friedrich B, Lenz O, Scheerer P. ***Nat Chem Biol.*** 2014 May; 10(5):378-85. https://doi.org/10.1038/nchembio.1500

Table of Contents

Introduction & Motivation

1 Hydrogenases

The conflict between the steady increase in energy demands and the decrease in availability of fossil fuels requires the implementation of renewable energy technologies. For this purpose, hydrogen is considered the most promising zero-emission fuel on earth. The technical production of hydrogen is still coupled to the generation of CO_2 through processes like steam reforming. Therefore, an enzymatic approach is an extremely interesting alternative to existing techniques. Enzymatic hydrogen production can be performed by hydrogenases, e.g. photocatalytic from light and water.[1] A different strategy is the energy production through electrocatalysis in enzymatic biofuel cells.[1] To setup an enzymatic process of hydrogen based energy production several aspects need to be considered e.g. catalytic efficiency, protein stability and O_2 tolerance. The research of structure-function relationships of hydrogenases can promote this goal. In this thesis, I will focus on the important feature of O_2 tolerance in hydrogenase metallo-enzymes.

Hydrogenases are multi-subunit metallo-enzymes that catalyse the reversible oxidation of dihydrogen into protons and electrons.

Equation 1

$$H_2 \rightleftharpoons H^- + H^+ \rightleftharpoons 2H^+ + 2e^-$$

Hydrogenases are present in all three domains of life, mainly bacteria and archaea, but can also occur in some eukaryotes. They can be found as either soluble or membrane-bound form in the cytoplasm or periplasm of the organism. Many microorganisms make use of different hydrogenases to either catalyse H_2 oxidation to gain energy for metabolic processes or H_2 evolution for the removal of reducing agents, depending on the demand of the cell.[2]

1.1 Active site

Hydrogenases can be characterized by the specific metal ions forming the catalytic centre and are class-divided into [Fe], [FeFe] and [NiFe] hydrogenases including the subgroup of [NiFeSe] hydrogenases. The members of the class of [Fe] hydrogenases catalyse a crucial step of methanogenesis in hydrogenotrophic archaea.[3] The iron atom in [Fe] hydrogenases (Hmd) is coordinated by a cysteine, two CO ligands, one iron-guanylylpyridinol cofactor and one

"unknown" ligand, which is not shown in the structure in ***Figure 1A***.[4] The [FeFe] hydrogenases are mostly involved in H_2 evolution under strictly anaerobic conditions. The bimetallic iron-only active site ($2Fe_H$) is coordinated by three CO ligands, two CN^- ligands, a dithiolate-bridge and a cubane cysteine-linked [4Fe4S]-cluster (***Figure 1C***).[5] Both components are termed H-cluster. [NiFe] hydrogenases catalyse the energy-yielding oxidation of H_2. Here, the iron atom is bound to three inorganic ligands, two CN^- and one CO, and is bridged via two cysteines to the nickel atom, which is further coordinated by two terminal cysteine residues (***Figure 1B***).[6] In the [NiFeSe] hydrogenase subgroup one terminal cysteine is exchanged by a seleno-cysteine compared to the [NiFe] hydrogenases and they conduct a high H_2 evolution activity (***Figure 1D***).[7]

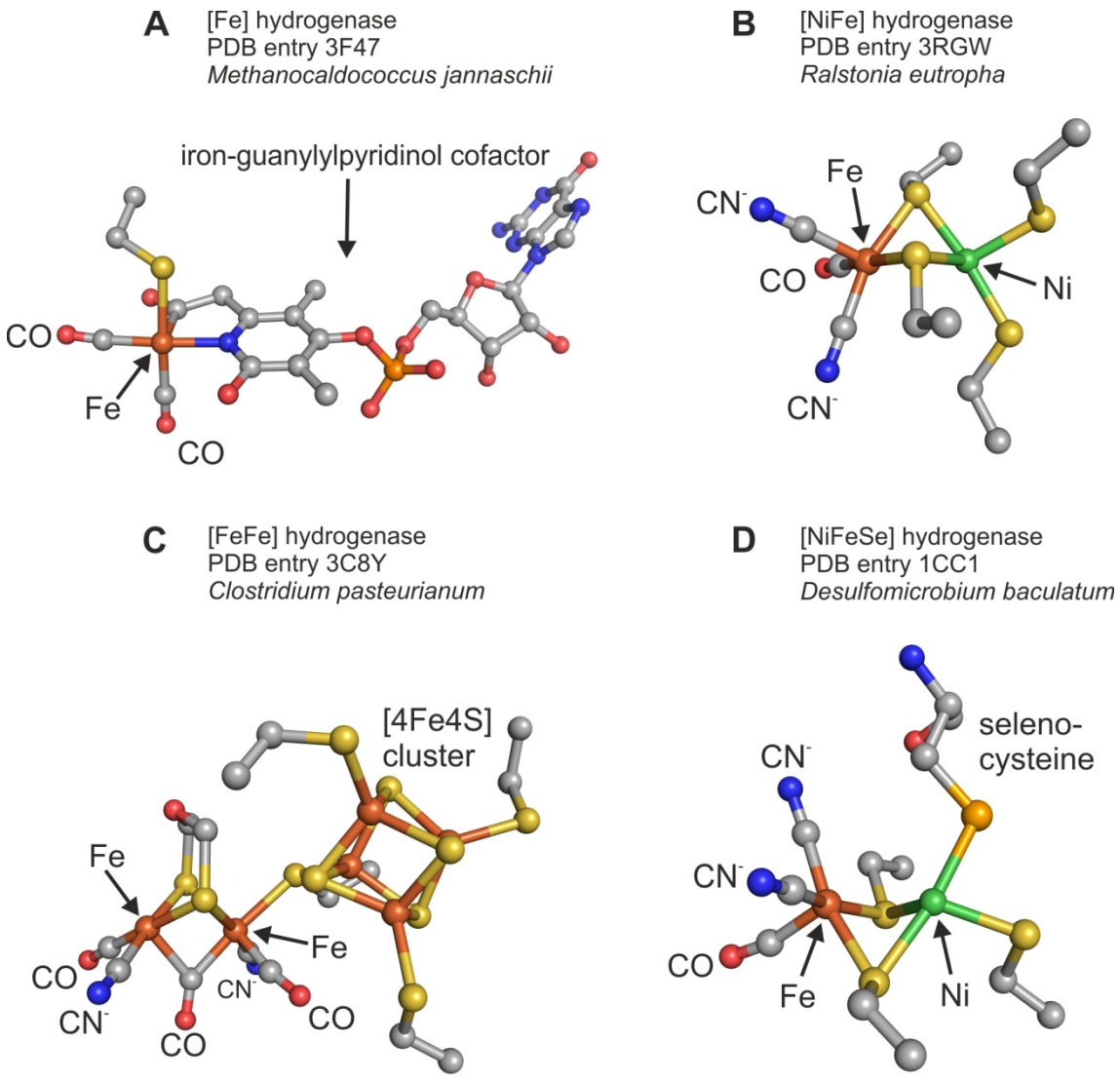

Figure 1: Overview of active sites of the four hydrogenase classes. All active sites are presented in ball/stick representation. Fe ions are coloured in orange. Ni is depicted in green. Oxygen, nitrogen and sulfur atoms are shown in red, blue and yellow, respectively. Carbon atoms are grey spheres. **(A)** The iron ion in [Fe] hydrogenases is coordinated by one cysteine, two CO ligands and one iron-guanylylpyridinol cofactor. **(B)** In [NiFe] hydrogenases the Ni and Fe are bridged by two cysteines. Further, the Ni is coordinates by two terminal cysteines,

whereas the Fe ion is linked to three inorganic ligands (2x CN^-, 1x CO). **(C)** The H-cluster in [FeFe] hydrogenases is composed of a 2FeH-site coordinated by three CO ligands, two CN- ligands, a dithiolate-bridge and a cubane cysteine-linked [4Fe4S]-cluster. **(D)** In [NiFeSe] hydrogenases one terminal cysteine is exchanged by a seleno-cysteine compared to [NiFe] hydrogenases.

For a biotechnological setup, the [FeFe] hydrogenases are very promising due to the higher H_2 turnover rates compared to [NiFe] hydrogenases.[8] However, [FeFe] hydrogenases get irreversibly inactivated even by traces of molecular oxygen, whereas a small subgroup of [NiFe] hydrogenases evolved the remarkable feature of O_2 tolerance.[9,10] Understanding how the structure and function of the different hydrogenases are correlated will help to engineer an enzymatic setup for H_2 production under ambient oxygen level.

1.2 Four hydrogenases of *Re*MBH

Intriguing enzymatic examples are the four O_2-tolerant [NiFe] hydrogenases expressed by *Ralstonia eutropha*, a β-proteobacterium found in soil and fresh water ***(Figure 2***). Each of the four hydrogenases belong to a different phylogenetically group. The membrane-bound [NiFe] hydrogenase (*Re*MBH) belongs to group 1 (membrane-bound uptake hydrogenases) and is an energy-generating hydrogenase.[2] The regulatory hydrogenase (*Re*RH) acts as hydrogen sensor and regulates the gene expression for hydrogenase synthesis.[11–13] It belongs to the phylogenetic group 2b of cytoplasmic H_2-sensing hydrogenases. The soluble NAD^+-reducing hydrogenase (*Re*SH) is assigned to the group 3d, the bidirectional NAD(P)-linked hydrogenases.[2] The *Re*SH reduces NAD^+ to NADH by oxidising H_2.[14,15] Recently, a group 5 (re-classified into group 1h) high-affinity hydrogenase has been found in *Ralstonia eutropha* (*Re*AH).[16,17] The actinobacterial-type hydrogenase catalyses H_2 uptake under H_2 atmospheric level, whereas the majority of [NiFe] hydrogenases can only oxidise H_2 at higher concentrations.[18,19,20] The *Re*MBH and its exceptional feature of O_2 tolerance will be elaborated in more detail in this thesis and compared with other O_2-tolerant (*Escherichia coli* (*EcHyd-1*), *Hydrogenovibrio marinus* (*Hm*), and *Salmonella enterica* (*Se*)) and O_2-sensitive [NiFe] hydrogenases (*Desulfovibrio gigas* (*Dg*), *Desulfovibrio desulfuricans* (*Dd*), *Desulfovibrio vulgaris* (*Dv*), *Desulfovibrio fructosovorans* (*Df*), *Allochromatium vinosum* (*Av*)).

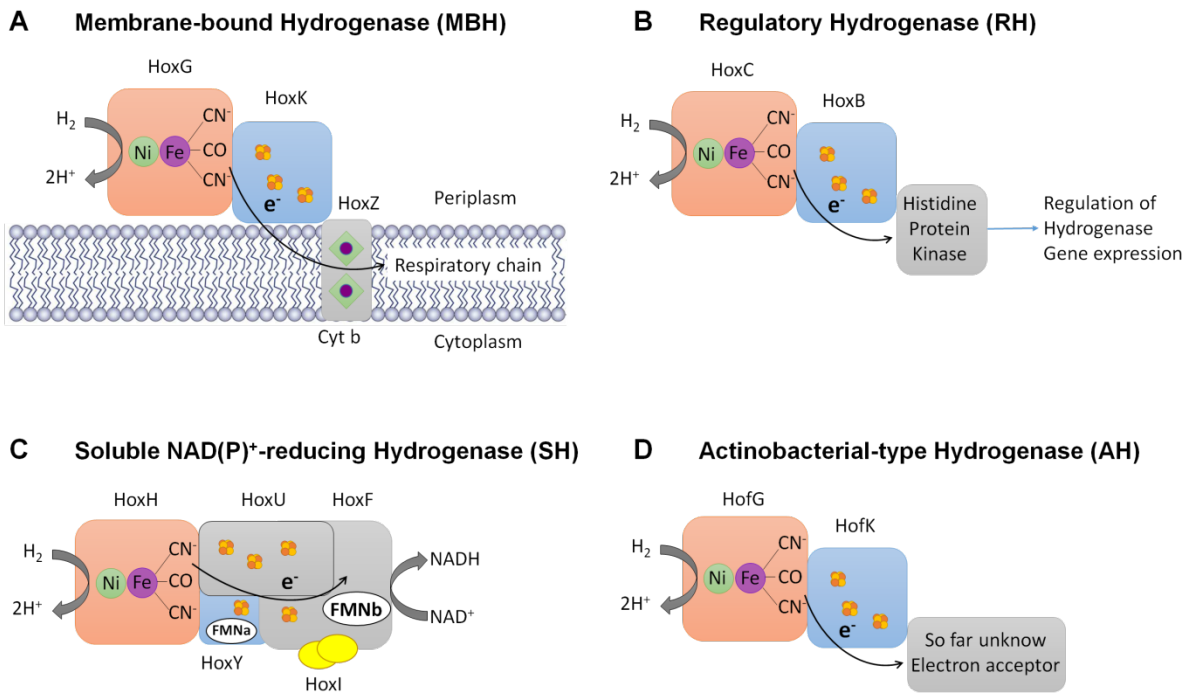

Figure 2: Overview of the different subunits of all four [NiFe] hydrogenases expressed in *Ralstonia eutropha*. (A) The MBH is composed of three subunits. The large subunit (HoxG, orange square) encloses the [NiFe] active site. The small subunit (HoxK, blue square) has three [FeS]-clusters (yellow-orange balls) and is linked to the third subunit (HoxZ, grey square), a membrane integral cytochrome *b*. The membrane is depicted as paired chains of beads. **(B)** The RH consists of three subunits. A large subunit (HoxC, orange square) with the active site and small subunit (HoxB, blue square) with the electron relay as found in MBH and a histidine protein kinase as third subunit (HoxJ, grey square). **(C)** The SH possibly consists of two functional modules: *(i)* a hydrogenase dimer composed HoxH with the [NiFe] active site and HoxY with a flavin mononucleotide (FMN) cofactor, *(ii)* a NADPH-dehydrogenase dimer composed of HoxU with an [FeS]-cluster electron relay and HoxF with another [FeS]-cluster plus a FMN cofactor. Further, a HoxI subunit is bound to the dehydrogenase domain potentially providing a specific binding domain for NADPH. **(D)** The AH is composed of three subunits. A large subunit (HofG, orange square) harbouring the [NiFe] active site, a small subunit (HofK, blue square) with the [FeS] electron relay and a yet unknown electron acceptor (grey square).

*Re*MBH consists of a large subunit (HoxG) containing the deeply buried [NiFe] active site, where hydrogen splitting occurs, a small subunit (HoxK) with three [FeS]-clusters serving as electron relay to connect the catalytic centre with the third subunit, a membrane integral cytochrome b_{562} (HoxZ).[6,21] The small subunit is embedded into the membrane via a helical anchor (***Figure 2***). The [FeS]-clusters in the small subunit are located proximal, medial and distal to the catalytic centre and are composed of [4Fe3S], [3Fe4S] and [4Fe4S], respectively.[22] O_2-sensitive hydrogenases contain a [4Fe4S]-cluster at the proximal position of the electron relay compared to the [4Fe3S]-cluster in *Re*MBH , which will be shown in the results, is an important element for O_2 tolerance.[23] In the structural studies the catalytically active *Re*MBH heterodimer lacking cytochrome b_{562} was applied.

1.3 Mechanism

The enzymatic course of action for the O_2-tolerant *Re*MBH involves two operational steps. H_2 is oxidized to protons and electrons during the catalytic cycle (***Figure 3***). Protons are transported to the protein surface via protonatable amino acids and water molecules.[24] Electrons are guided through a relay composed of several iron–sulfur clusters to the respiratory chain.[6] During this cycle the catalytic centre alternates between the two active redox states, Ni_a-C and Ni_a-S. In the Ni_a-C state the nickel and iron are bridged through a hydride ligand. In the event of O_2 approach a putative hydroxyl ligand is bridging the Ni and Fe ion in the inactive Ni_r-B state and an additional reaction is proposed to occur at the [NiFe] active site. In this reactivation cycle, electrons are redirected from the electron relay to reduce O_2 with the aid of protons to H_2O, which then is released to the protein surface through a nearby water channel (***Figure 3***). This step is coupled to a structural change in the proximal [4Fe3S]-cluster, which is a crucial feature of the O_2 tolerance. Under aerobic conditions the [4Fe3S]-cluster can undergo two redox transitions within a physiological potential range and transfers a second electron to the active site. In this two-electron mode one iron ion (Fe4) changes its binding partners (iron shift).[22] In comparison, the cubane [4Fe4S]-cluster of O_2-sensitive hydrogenases does not allow the structural modification and can only deliver one electron to the active site. The [4Fe3S]-cluster is linked to the protein backbone via six cysteines, whereas the [4Fe4S]-cluster is coordinated by four cysteines. The iron shift is supported by the two additional cysteines during the reactivation cycle.

The crystal structures available so far for *Re*MBH[6,22] revealed plausible pathways for electron transport and water release, while both the proton pathways and gas transport routes remained largely undefined. Efficient gas transport to the deeply buried active site requires a tunnel that connects the protein exterior with the catalytic centre.[25]

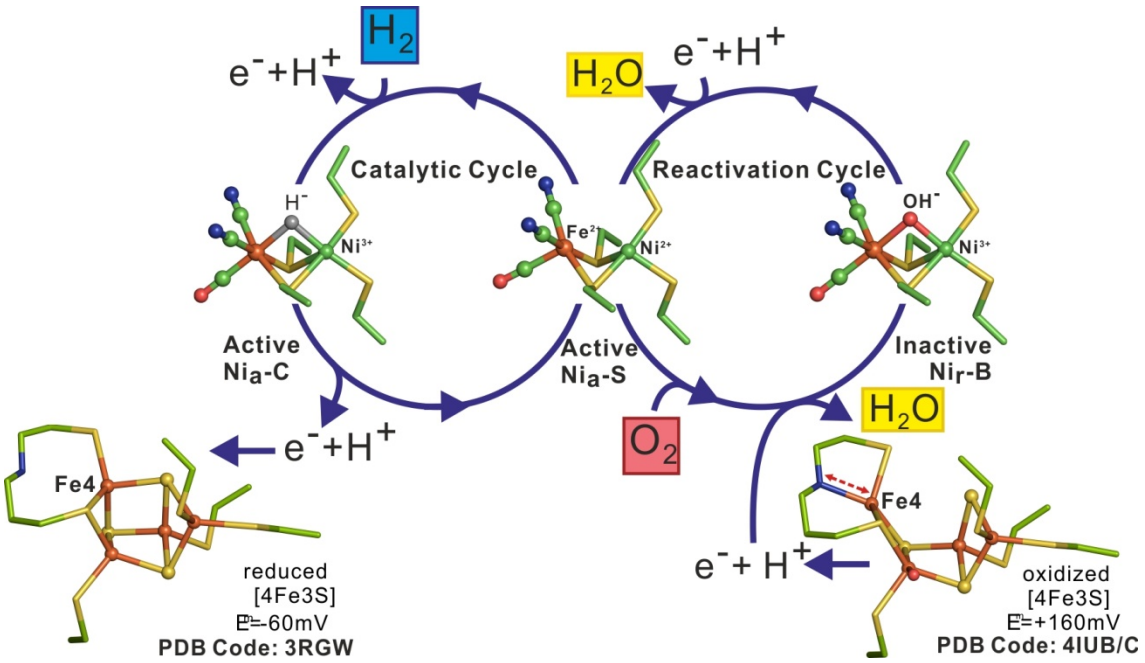

Figure 3: Catalytic and reactivation cycle of *Re*MBH. The active site in the three redox states as well as the proximal [4Fe3S]-cluster are shown as ball/stick. In the catalytic cycle hydrogen gets oxidised to protons and electrons at the active site. The active site redox states change between the active Ni_a-C and Ni_a-S. The electrons are transferred to the [FeS]-clusters. Additionally, under aerobic conditions the reactivation cycle takes place. The inactive Ni_r-B state of the active site includes a bridging hydroxyl ligand. Electrons are redirected from the [FeS]-clusters to the active site, O_2 is reduced to H_2O and the active site regains the catalytically active state Ni_aS.[6]

1.4 Oxygen tolerance

All four hydrogenases of *Ralstonia eutropha* have evolved the remarkable feature of O_2 tolerance, however, they seem to use different strategies to prevent O_2 related inhibition. Mutation experiments of *Re*RH and RH from *Rhodobacter capsulatus* (*Rc*RH) revealed that the bulky residues isoleucine and phenylalanine, gating the [NiFe] active site, limit the accessibility of molecular oxygen to the catalytic centre. Mutations of the gate amino acids to valine and leucine, found in O_2-sensitive hydrogenases, led to O_2 sensitivity in *Re*RH and *Rc*RH.[11,26] It has also been proposed that the standard [NiFe] active site of RH itself is sensitive to O_2 inactivation.[11] Horch and co-workers proposed, based on the unique IR spectrum, a NADH-dependent reduction of active site oxygen species via sulfoxygenated active site cysteine intermediates.[15] The recently published structure of *Re*AH provides two further possible mechanisms for O_2 tolerance. First, it has been proposed that the dimerization of the heterodimer plays a role in reducing O_2 through electrons provided by the other functional unit. Second, a [4Fe4S]-cluster found proximal to the active site is coordinated by three cysteines and one aspartate, compared to a standard cubane cluster, which is linked to the protein

backbone via four cysteines. The aspartate enables the cluster to a moderate increase in its redox potential and therefore might play a role in O_2 tolerance.[27] A similar structural feature has been found earlier in *Re*MBH, a novel [4Fe3S]-cluster. The six cysteine coordinated proximal [4Fe3S] cluster of *Re*MBH can undergo two redox transitions and deliver a second electron for oxygen reduction at the active site.[22] The catalytic centre of *Re*MBH is equivalent to a standard [NiFe] active site and therefore might also be sensitive to O_2 attack as hypothesized for *Re*RH. Therefore, the question arises, if O_2 tolerance of *Re*MBH is additionally supported by the characteristics of the substrate tunnel similar to *Re*RH.

In 1997, Montet and colleagues studied the hydrophobic tunnels of the O_2-sensitive [NiFe] hydrogenases from *Desulfovibrio gigas* and *Desulfovibrio fructosovorans* with molecular dynamics (MD) simulations and Xenon derivatisation, respectively (***Figure 4***). The results point out the importance of the hydrophobic tunnels in substrate transport and storage and show several putative entrance sites.[28] This was supported by the research findings of Teixeira and colleagues also performing MD simulations on O_2-sensitive [NiFe] hydrogenases from *Desulfovibrio gigas* (PDB entry 2FRV) and a V67A mutant of the same enzyme.[29] Three channels were found in the enzyme, which are merging on the site of the Ni ion and in some regions, serve as gas reservoirs. Valine 67 is close to the active site and is supposed to serve as gate amino acid regulating substrate access to the catalytic site. The mutant shows an increase in H_2 molecules in the hydrophobic tunnels as well as the gas is getting closer to the active site compared to the wild-type (< 4Å).[29] A O_2-sensitive [NiFe] hydrogenase was examined by Wang *et al.* due to H_2 and O_2 access of the hydrophobic tunnels using MD simulations. In this case, it could be shown that there is a 3-fold higher selectivity for H_2 than O_2, H_2 has a higher diffusion rate and O_2 uses the same pathways as H_2.[30] All these results are limited to O_2-sensitive [NiFe] hydrogenases. In this study, I will present research results of the hydrophobic tunnel network of the O_2-tolerant *Re*MBH using X-ray crystallography and computational studies.

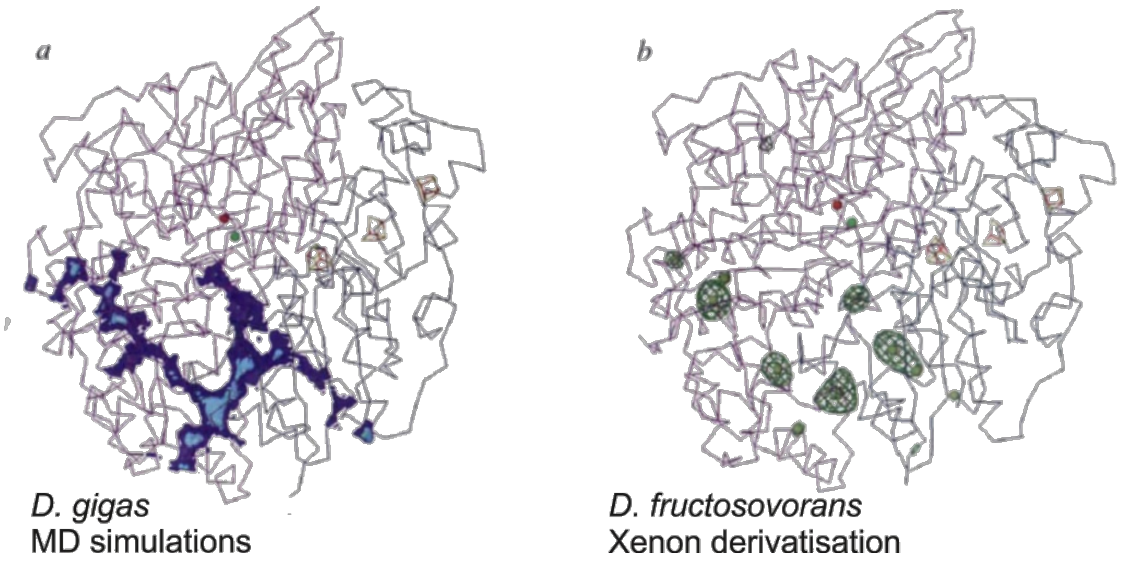

Figure 4: Hydrophobic tunnel studies on O_2-sensitive [NiFe]-hydrogenases from *D. gigas* and *D. fructosovorans*. Figure 4 was inherited from Montet *et al*.[28] Both enzymes are depicted in cα-backbone ribbon representation with the large subunit in magenta and the small subunit in blue. Ni and Fe ions of the active site are spheres in green and red, respectively. The [FeS]-clusters of the small subunit are shown in red and yellow sticks, respectively. **(a)** *D. gigas* hydrogenase: MD simulation cavity maps with a probe radius of 1.0 Å and 1.6 Å in white and blue, respectively. **(b)** *D. fructosovorans* hydrogenase: Xenon (Xe) atoms from crystal derivatisiation experiment illustrated in green spheres. F_{Xe}-F_{nat} difference map of the Xe sites contoured at 4 σ and shown as green mesh.

2 Lipoxygenases

Lipoxygenases (LOXs) are non-heme, iron (FeLOX) or manganese (MnLOX) containing dioxygenases catalysing the formation of hydroperoxide derivatives from polyunsaturated fatty acids (PUFAs), which represents the first step in the oxylipin pathway.[31,32] LOXs have been extensively studied in animals and plants. The first LOX was discovered in plants in 1932 by Andre and Hou.[33] Plant LOX was found to be located in chloroplast membranes, vacuoles or oleosomes of leaves, in fruit or cotyledons.[34] In plants the most common fatty acids are linoleic acid (18:2 ω-6) and linolenic acid (18:3 ω-3).[35–37] The oxylipin products, e.g. phytohormones and jasmonates, are involved in seed germination, plant growth and development, homeostasis, signalling or pest resistance.[38–40] Whereas in animals, the main fatty acid is arachidonic acid (20:4 ω-6) as component of phospholipids in membranes.[41] Animal LOX is present e.g. in epidermis, thrombocytes or immune cells.[42,43] The animal oxylipins cover a variety of physiological functions including reproduction, maintenance of the epithelium, inflammation processes, immune response, tumorigenesis or as secondary messengers.[36,43–45] Furthermore, lipoxygenases were also found in fungi, moss, coral and more recently in bacteria.[46,47] However, the lower number of bacteria (< 0.5 %) holding LOX-like sequences in their genome[48] raises the question of the biological role of the enzyme in bacterial life.

2.1 Fatty acids

Fatty acids are the basic modules of lipids and are composed of an aliphatic chain with a carboxyl group (alpha (α)-end) as head group and a methyl group (omega (ω)-end) as tail. They exist as saturated or unsaturated molecules with no or ≥ 1 carbon-carbon double bonds, respectively.[41] In nature, the double bonds are mainly in *cis* configuration, whereas *trans* double bonds are the result of industrial modifications. Fatty acids are either “free” single chains or in their esterified form complexed with glycerol. These glycerolipids are composed of the glycerol backbone with 1-3 fatty acids (mono-, di-, triacylglyceride).[41] Contains one of the fatty acids a phosphate group it is termed phospholipid, which play a key role in biological membranes. The nomenclature is described as followed, for e.g. arachidonic acid (20:4 ω-6) consists of a chain of 20 carbon atoms with 4 double bonds and the first double bond is located 6 carbon atoms away from the ω-end (methyl group) (***Figure 5***).

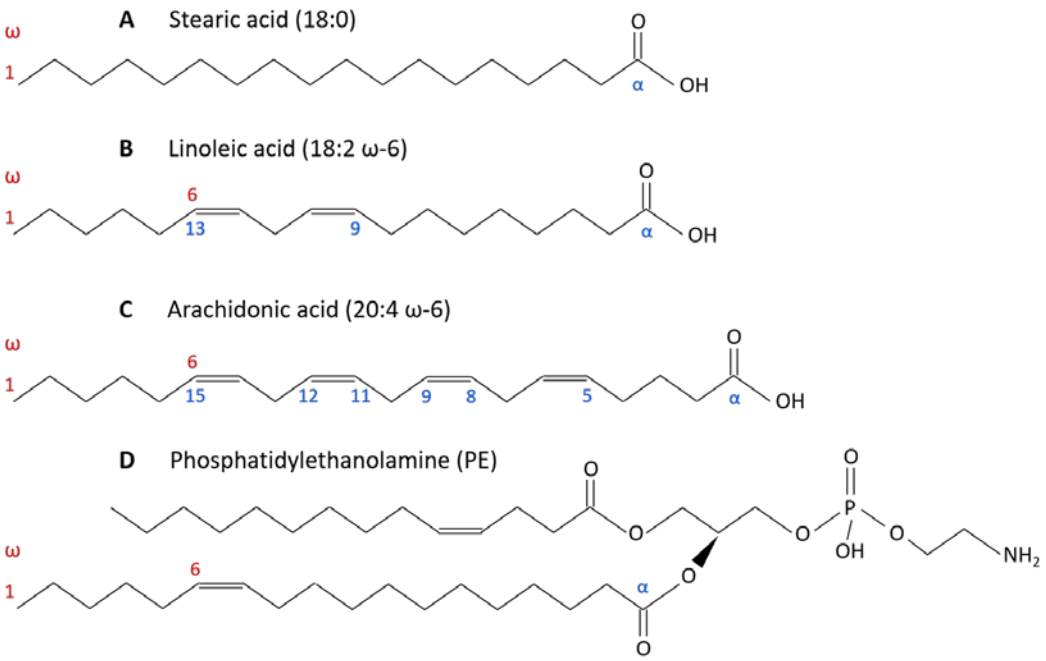

Figure 5: Fatty acids. Saturated fatty acid without carbon-carbon double bonds. **(A)** Stearic acid. Unsaturated fatty acids with ≥ 1 carbon-carbon double bonds. **(B)** Linoleic acid. **(C)** Arachidonic acid. **(D)** Phospholipid: Phosphatidylethanolamine.

2.2 Mechanism

The enzymatic lipid peroxidation is initiated by the active form of LOX in its ferric (Fe^{3+}) state through the stereoselective hydrogen abstraction at a bisallylic methylene on one site of the substrate, creating an organic radical. [31,37] The hydrogen is abstracted as a proton, whereas the electron is transferred to the iron atom forming the inactive ferrous (Fe^{2+}) state. Within the 1,4-pentadiene moiety of the substrate the delocated electron can rearrange in [+2] or [-2] direction from the bisallylic methylene towards the methyl end or carboxyl end, respectively. The radical rearrangement involves a *Z,E*-double bond conjugation.[49] Molecular oxygen is inserted antarafacial (at the opposite site of the hydrogen abstraction) at either carbon 1 or carbon 5 of the pentadiene moiety creating a hydroperoxide radical. In the final step, the reduction of the radical to an anion is linked with the oxidation of the iron ion back to its active ferric state (***Figure 6***).

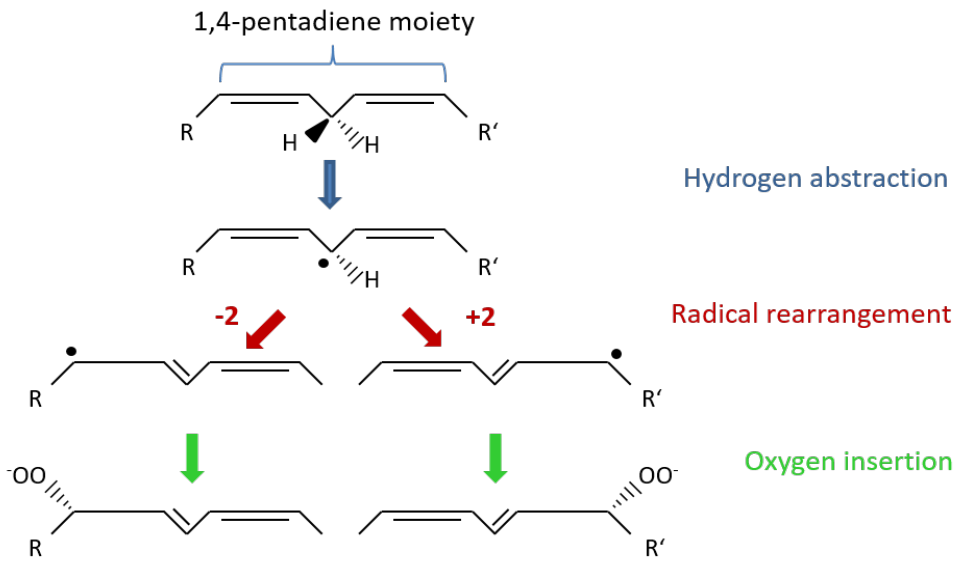

Figure 6: LOX mechanism. In the first step one hydrogen is abstracted from position 3 of the 1,4-pentadiene moiety of the polyunsaturated fatty acid. Followed by a radical rearrangement within the moiety to position 1 or 5. The molecular oxygen is inserted creating a hydroperoxide radial, which is finally reduced to a hydroperoxide anion.

A common way of classifying LOXs is based on the reaction specificity of the enzyme. In mammals six LOXs have been found due to four *cis* double bonds in arachidonic acid (5-LOX, 8-LOX, 9-LOX, 11-LOX, 12-LOX, 15-LOX) and possible O_2 insertion at C5, C8, C9, C11, C12 or C15 (***Figure* 5**).[37] In plants, linoleic acid consists of one pentadiene moiety, where the hydrogen abstraction takes place at carbon 11 and depending on the position of the O_2 insertion we can find 9-LOX and 13-LOX (***Figure 5***). Also dual regiospecificity can be used in LOX nomenclature due to the ratio of e.g. 9- and 13-hydroperoxides produced, leading to 9/13-LOX or 13/9-LOX.[50] Further, LOXs nomenclature can include stereospecificity. Plant LOX forming different stereoisomeric products in *S*- or *R*-configuration are termed 9*S*-LOX or 13*R*-LOX, respectively.

The regiospecificity of the O_2 insertion, however, might be the result of a possible difference in orientation of the fatty acid chain as well as the depth of the substrate positioning in the cavity. In plant LOX different amino acids, lining the bottom of the substrate cavity, have been found determining the depth of the lipid insertion. 13-LOX shows a phenylalanine or histidine amino acid at the same position of valine in 9-LOX (***Figure* 7*A***). A conversion of plant 13-LOX to 9-LOX was achieved through point mutations of the larger 13-LOX histidine into 9-LOX valine supporting the hypothesis of inverse substrate binding (***Figure* 7*A***), where linoleic acid is bound in head-to-tail orientation with the carboxyl group at the bottom of the cavity.[51] A similar space-determined model could be detected in animal 12/15-LOX for arachidonic acid. An

exchange of the larger (Ile, Ile, Phe) amino acids at the cavity bottom of 15-LOX to smaller (Ala, Ala, Ile) residues leads to a smaller volume of the substrate cavity resulting in a positional shift of arachidonic acid and a 12-LOX activity (***Figure 7B***).[52,53]

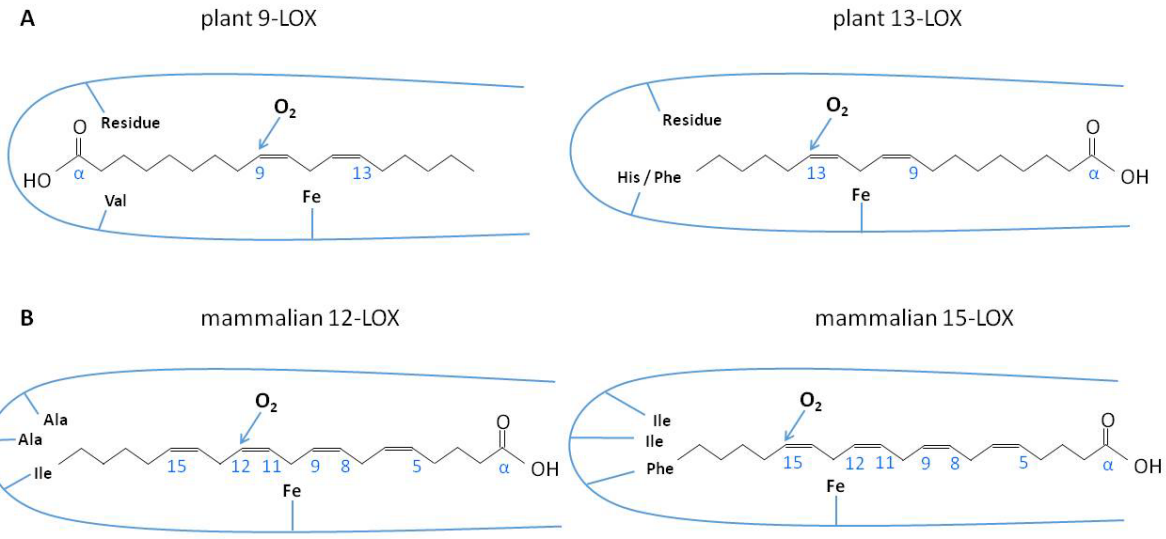

Figure 7: Regiospecificity of eukaryotic LOXs. (A) Regiospecificity and head-to-tail orientation of plant 9-LOX and 13-LOX. **(B)** Mutation of the larger amino acids Ile, Ile and Phe in mammalian 15-LOX into Ala, Ala and Ile resulted in a 12-LOX activity due to a positional shift of arachidonic acid in the larger cavity.

The stereospecificity of the O_2 insertion, however, seems to be determined by an amino acid opposite the catalytic centre. The relationship of the *S*- or *R*-stereospecificity is determined by oxygenation at either one end or the other of the substrate pentadiene moiety (***Figure* 8**). In 2004, Coffa and Brash revealed two highly conserved amino acids, alanine or glycine, defining *S*- or *R*-configuration of the peroxidation product, respectively.[54] A switch of alanine to glycine or *vice versa* leads to a switch in stereochemistry. The bulkier alanine compared to glycine blocks the O_2 insertion at the pentadiene radical position closer to the opening of the lipid substrate cavity (α-end).[37,54] The enzyme with an alanine residue is referred to as *S*-LOX and with a glycine as *R*-LOX (***Figure* 9**). The bacterial LOX from the human pathogen *Pseudomonas aeruginosa* (Pa-LOX) an alanine (Ala420) occupies the position close to the active site leading to the oxygenation in *S*-configuration. Ala-Gly exchange experiments in this thesis provide information about the stereochemical influence of this specific amino acid in bacteria. The very reverse has been shown by Jansen and colleagues in 2011. The LOX-1 of zebrafish with a glycine catalysed arachidonic acid into a hydroperoxide with *S*-configuration.[55] Also different from the convention of a conserved alanine in *S*-LOX is the serine found in mouse 12*S*-LOX at this critical position.[54] Ser to Ala mutation experiments did not change the stereospecificity

of mouse 12*S*-LOX showing that either Ala or Ser confer to the same specificity and assuming a similar blocking of the O_2 tunnel by Ser.[54]

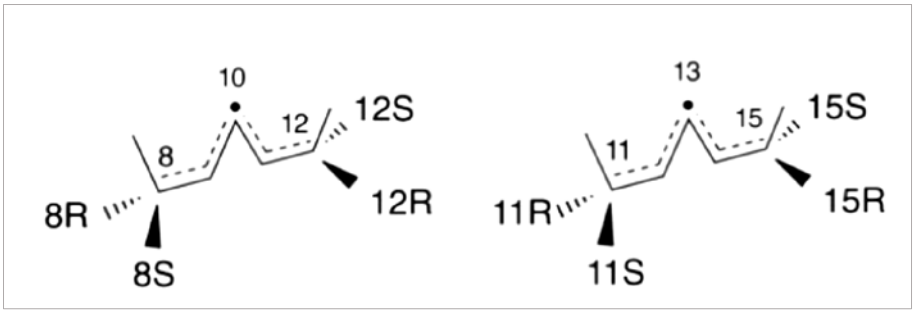

Figure 8: *S*- and *R*-Configuration in LOX. Figure 8 was inherited from Coffa and Brash.[54] Depicted is the 1,4-pentadine moiety of a PUFA showing the 8,11-double bonds (left) and 11,14-double bonds (right). After the hydrogen abstraction, the radial rearranges in [+2] or [-2] direction from the bisallylic methylene. The molecular oxygen can react on the opposite face of the hydrogen abstraction (antarafacial) at either end of the pentadiene moiety. There is a stereospecific relationship between 8*S*/12*R* and 8*R*/12*S* on the left as well as 11*S*/15*R* and 11*R*/15*S* on the right.

A

	Sequence	Name	GenBank Accession
407	I N T K **A** R E Q L I	Human 5(S)-LOX	J03600
399	I N T R **A** R T Q L I	Human 12(S)-LOX	M58704
399	I N V R **A** R T G L V	Human 15(S)-LOX-1	BC029032
412	I N T L **A** R E L L I	Human 15(S)-LOX-2	U78294
407	I N T K **A** R E Q L I	Mouse 5(S)-LOX	L42198
399	I N T L **A** R N N L V	Mouse ep 12(S)-LOX	X99252
400	I N V R **A** R S D L I	Mouse leu 12(S)-LOX	L34570
399	I N T R **S** R T Q L I	Mouse pl 12(S)-LOX	AK087724
413	I N T L **A** R E L L V	Mouse 8(S)-LOX	AK028724
400	I N V R **A** R N G L V	Rabbit 15(S)-LOX-1	P12530
558	I N A L **A** R Q I L I	Arabidopsis LOX-1	JQ2267
538	I N A L **A** R Q S L I	Soybean LOX-1	S25064
595	I N A L **A** R E A L I	Barley LOX-2	AJ507213
437	I N S I **G** R A V L L	Human 12(R)-LOX	AF038461
437	I N S I **G** R A L L L	Mouse 12(R)-LOX	Y14334
423	I D T I **G** R K E L I	Coral 8(R)-LOX domain	AF003692
447	V N S V **G** I K A L L	Coral 8(R)-LOX	U59223

B

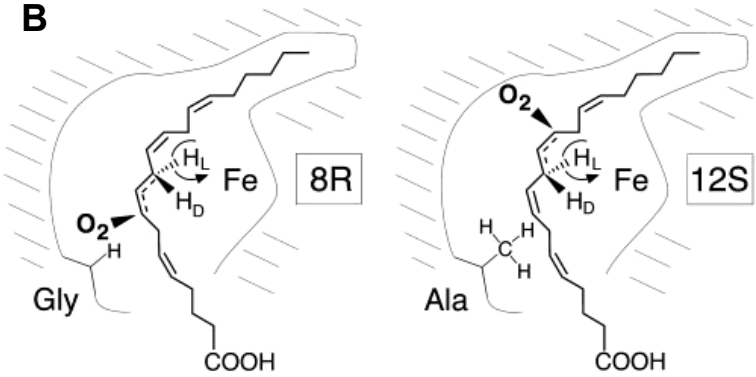

Figure 9: (A) Sequence alignment of *S*-LOX and *R*-LOX. The overview of a selection of *S*-LOX and *R*-LOX shows a conserved alanine (Ala) or glycine (Gly), respectively. An exception is mouse platelet *S*-LOX with a serine (Ser) at this position. **(B) Basis for *R*- and *S*-stereospecificity in product formation.** The picture shows arachidonic acid with the tail-first orientation and with the hydrogen abstraction on one face of the substrate. Left: A Gly residue in the critical position of the active site allows antarafacial oxygenation towards the carboxyl end of the reactive pentadiene moiety in 8*R*-configuration. Right: The larger Ala residue blocks the insertion of molecular oxygen at C8. Antarafacial oxygenation occurs towards the methyl end in the 12*S*- configuration. Figure 9 was inherited from Coffa and Brash.[54]

2.3 Lipoxygenase structure

LOXs have been found in the eukaryotic and prokaryotic kingdom and the first eukaryotic crystal structure was solved in 1993 of an arachidonic acid 15-LOX from *Glycine max* (soybean LOX-1).[56] The overall primary structure of all LOX enzymes is a single amino acid chain. In eukaryotic LOXs the single chain mainly folds into an N-terminal β-barrel domain and catalytic domain, which harbours the deeply buried active site (***Figure 10B***, human LOX). The N-terminal domain also termed PLAT (Polycyctin-1, Lipoxygenase, Alpha-Toxin) domain consists of two β-sheets of four β-strands (β-sandwich) and has been assigned as potential membrane binding domain. Several identified Ca^{2+} ions bound within the β-barrel domain might be involved in conformational changes and stabilisation of alleged membrane-insertion loops.[37,57,58] Interestingly, the PLAT domain seems to be absent in fungal Manganese-LOXs as illustrated for LOX from rice blast fungus *Magnaporthe oryzae* in ***Figure 10D***.[59,60] The same applies for prokaryotic Pa-LOX (***Figure 10A***). The first structure of bacterial LOX was solved in 2013 by Garreta *et al*. (PDB entry 4G32 and 4G33), showing a single catalytic domain mainly composed of α-helices.[61] However, the structure revealed two α-helices of ~ 100 amino acids (***Figure 10A***, *Pseudomonas aeruginosa*, black helix) functioning as a lid over the substrate cavity entrance.[61] Surprisingly, cyanobacterial LOX from *Cyanothece sp*. PCC8801 shows structural features of eukaryotic and bacterial LOXs. It is composed of an N-terminal β-barrel domain, a catalytic domain and an α-helical N-terminal extension of 40 amino acids (***Figure 10C***, *Cyanothece sp.* PCC8801, black helix).[62] The α-helical N-terminal extension has been proposed to promote binding of liposomes. The same function could be assumed for the lid-helices of Pa-LOX.[62] However, the β-barrel domain is over 90° rotated in *Cyanothece sp*. PCC8801 compared to the eukaryotic counterparts due to a α-helix to β-sheet conversion.[62]

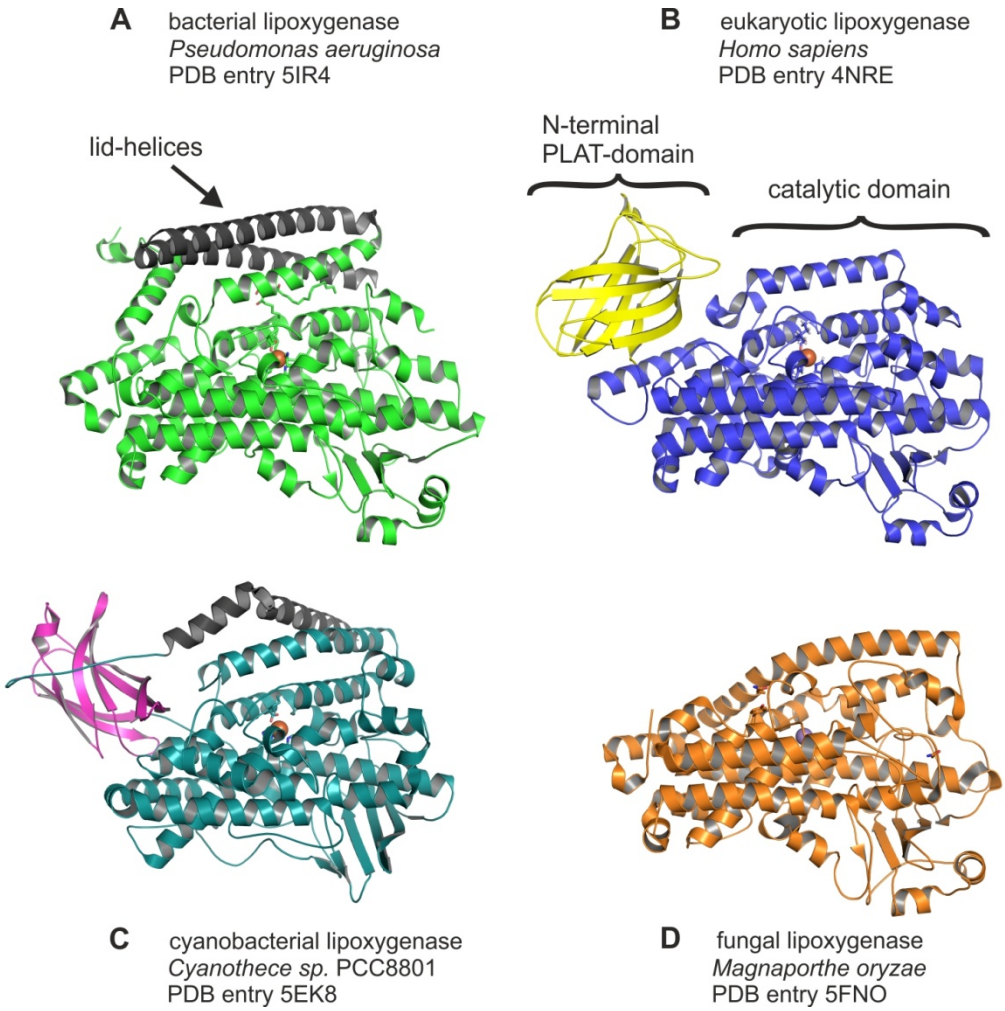

Figure 10: Overview of domain composition of bacterial and eukaryotic LOX structures. A) Bacterial LOX of *Pseudomonas aeruginosa* with the catalytic domain shown as green cartoon and the N-terminal lid-helices in black. The iron ion of the active site is illustrated as orange sphere. **B)** Human LOX with the N-terminal PLAT domain depicted in yellow and the catalytic domain as blue cartoon. The iron ion of the active site is illustrated as orange sphere. **C)** Cyanobacterial LOX from *Cyanothece sp*. PCC8801 with the N-terminal PLAT domain in magenta and the catalytic domain shown as teal cartoon. An additional helix structure is shown in black. The iron ion of the active site is illustrated as orange sphere. **D)** Fungal LOX from *Magnaporthe oryzae* with a single catalytic domain depicted as orange cartoon. The manganese ion of the active site is illustrated as purple sphere.

The catalytic domain, however, shows higher degrees in similarity compared to the PLAT domain. All LOXs have a highly conserved catalytic core composed of four α-helices (superposition of the core helices, ***Figure 11***). The catalytic metal ion, Fe or Mn, is coordinated by amino acids of the α-helices α7 and α14 as well as the oxygen of the C-terminal carboxyl group (eukaryotic helix nomenclature). Intriguing, the C-terminal amino acid enters the protein between the helices as part of the metal ion coordination sphere. Noticeable is the bending of helix α8, which is capping the bottom of the substrate cavity. The penultimate helix is located close to the substrate entrance (***Figure 11***).[37]

The metal ion is placed in the centre of the helical core and is in general coordinated in a pseudo octahedral geometry by three conserved histidines, an asparagine or histidine and a terminal isoleucine. In Pa-LOX the iron is coordinated through His377, His382, His555, Asn559, the C-terminal Ile685 and a water molecule (hydroxyl) (***Figure 12***).[61,63]

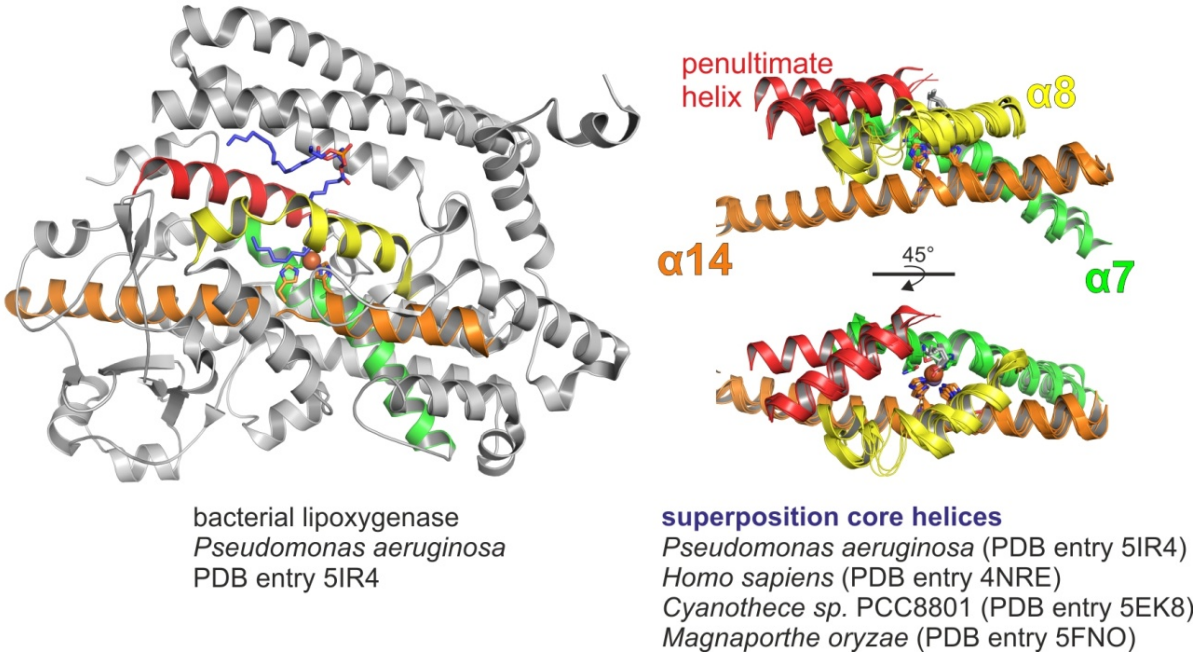

Figure 11: Core helices of LOXs. All LOX enzymes have a core of four α-helices embedding the active site. Helix α14 and α7 provide four amino acids (histidine and arginine) as part of the iron coordination sphere. Helix α8 has an "arched" conformation in all LOXs and defines the bottom of the substrate cavity. Finally, the penultimate helix is close to the substrate cavity entrance and might play a role in substrate coordination.

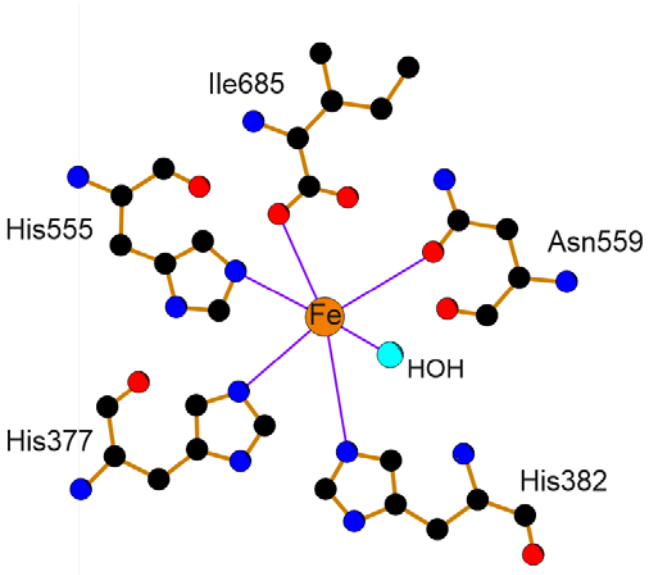

Figure 12: Pa-LOX active site. The iron ion in the Pa-LOX active site is coordinated by three histidines, one asparagine, the C-terminal isoleucine and a water molecule (hydroxyl) occupying the sixth position in the pseudo octahedral geometry.

2.4 Lipoxygenase substrate tunnels

In the first LOX crystal structure from soybean LOX-1 two cavities for substrate and O_2 interaction with the active site have been found. The hydrophobic cavity 1 (nomenclature from LOX-1 reference) adjoins the protein exterior with the catalytic cavity opposite the coordinating His504 and therefore has been proposed to represent a pathway for O_2 access. Cavity 2 contains mainly hydrophobic residues and was large enough to incorporate a fatty acid substrate.[56] In eukaryotic LOXs this substrate-binding pocket has been described as U-shaped form (***Figure 13***).[37,60,64] The same U-shape can be found in prokaryotic Pa-LOX. Here, though, the substrate tunnel extents due to the additional lid-helices and a complete phospholipid can be incorporated in the two cavities (***Figure 13***). The structure of Pa-LOX revealed the binding of a phosphatidylethanolamine suggesting a high affinity for phospholipids as found in eukaryotic membranes. The ability of Pa-LOX in catalysing eukaryotic membrane phospholipids enables the bacteria to interact with the host cell and interfere with hosts defence and inflammation response system.[61,65] In cyanobacteria *Cyanothece sp.* PCC8801 a substrate tunnel connects the protein exterior with the catalytic iron, however, is shorter than reported in other LOXs (***Figure 13***). The cavity lining amino acids Tyr360, Glu355 and Phe413 might enlarge the tunnel during substrate binding through side chain rearrangements.[62]

A potential O_2 access tunnel has been proposed in eukaryotic and prokaryotic LOXs. Molecular dynamics simulations, structural modelling, mutational and kinetic studies proofed the presence of a possible pathway in rabbit 12/15-LOX. The side-directed mutagenesis of L326F within a critical position of the gas pathway obstructed the O_2 access to the active site indicated by a reduced O_2 diffusion.[66] The same tunnel could also be reported for Pa-LOX and human LOX (***Figure 13***). [64,67] The O_2 tunnel is mainly lined by hydrophobic residues and enters the catalytic cavity on the opposite site of the iron atom. According the newly described suprafacial (on the same face) hydrogen abstraction in the recently published structure of fungal MnLOX, an O_2 access tunnel at the same site of the catalytic Mn^{3+}-moiety has been assumed. However, no gas tunnel equivalent to FeLOX was reported for this structure.[60]

The structure of the substrate tunnels and the amino acid composition interlock tightly with the regio- and stereospecificity of each LOX. The biological role of bacterial LOX still remains unclear. Especially, understanding the structure and function of Pa-LOX might shed light on to its role for the pathogen *Pseudomonas aeruginosa*. *Pseudomonas aeruginosa* is a multi-drug

resistant, gram-negative bacteria causing serious infections in humans such as pneumonia, general inflammation or sepsis. In this thesis, the structure related stereospecificity of Pa-LOX will be studied according to the Ala-Gly exchange in association with changes in the O_2 access tunnel.

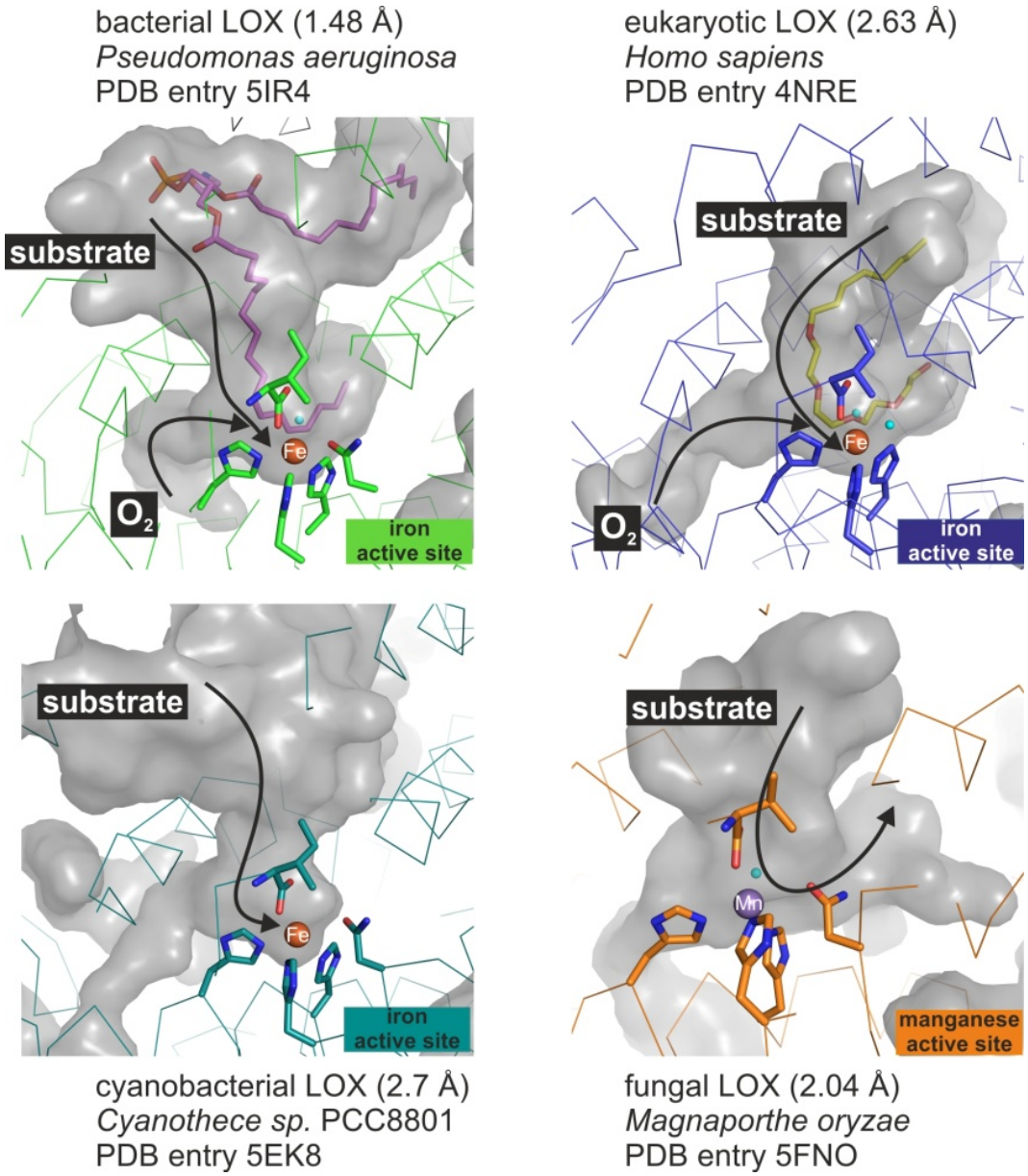

Figure 13: Substrate tunnels in eukaryotic and prokaryotic LOXs. Substrate tunnels are depicted as grey surface using the program *Py*MOL. The active site metal ion, Fe or Mn, are illustrated as spheres in orange or purple, respectively and are coordinated by the active site amino acids shown as sticks. Possible tunnel access paths are indicated by black arrows **A)** The sn-1 and sn-2 cavity of the substrate tunnel from bacterial Pa-LOX shows a bound phospholipide in purple sticks. The possible O_2 access tunnel is shown on the left. **B)** Human Lox has a substrate mimic bound to the substrate cavity shown in yellow sticks. The putative O_2 access tunnel is indicated on the left. **C)** Cyanobacterial LOX from *Cyanothece sp.* PC8801 shows an empty substrate tunnel in the structure with the PDB entry 5EK8 without the universally present U-shape. **D)** The fungal LOX from *Magnaporthe oryzae* shows the typical U-shaped substrate tunnel, however, no O_2 access tunnel has been found so far.

3 Tunnels

Proteins undertake a large variety of functions within organisms, including transport of molecules, signalling, immune response, acting as structural components, DNA replication and catalysing enzymatic reactions. These complex molecules consist of an alterable composition of only 20 amino acids. One or more chains of these amino acid residues fold into the unique three-dimensional structure of the protein, which in turn stands in relation to its function. Through protein folding amino acids which are far distant in the sequence are now able to interact and constitute functional units. These functional units contain different specific characteristics like pockets, grooves or protrusions, cavities, channels or pores and tunnels, which play an important role in biological processes through the interaction with substrates (***Figure 14***).[68] Channels across biological membranes govern the selective transport of ions and molecules. In most enzymes, the active site(s) are usually located in a cavity deeply buried inside the protein. The active site consists of a substrate specific binding site and a catalytic site primarily formed of amino acids, ions and/or cofactors. For substrate access to the catalytic centre and product release molecular tunnels connecting the protein exterior with the active site. However, solving the X-ray structures of the first poly-functional enzymes also revealed tunnels between multiple active sites for the tunnelling of intermediates.

Harbouring the catalytic centre(s) inside the protein and the presence of molecular tunnels provide several advantages for the enzyme: *(i)* higher substrate selectivity, *(ii)* protection of the catalytic site from reactive products and inhibitors, *(iii)* protection of chemically unstable intermediates from the external environment, *(iv)* reduction of transport time between multiple active sites, *(v)* preventing diffusion of the substrate into the bulk solvent, which increases the catalytic efficiency as well as *(vi)* regio- and stereospecific control.[69,70] Molecular tunnels are present in all six enzyme classes and appear as permanent transport pathways in an permanent state or as transient tunnels.[69,71] The special selectivity of the tunnels is influenced by its properties such as hydrophobicity or hydrophilicity as well as dimensions like shape, length and radius. They also differ in quantity and with or without openings to the protein surface. A unifying terminology for channels and tunnels has been introduced by Chovancova *et al*.[72] Channels are referred to as pathways with no interruption by an internal cavity and both channel openings are to the bulk solvent. Tunnels are pathways connecting the protein exterior with an

internal cavity or bridge multiple internal cavities. In my thesis, I will use this terminology for the channels and tunnels.

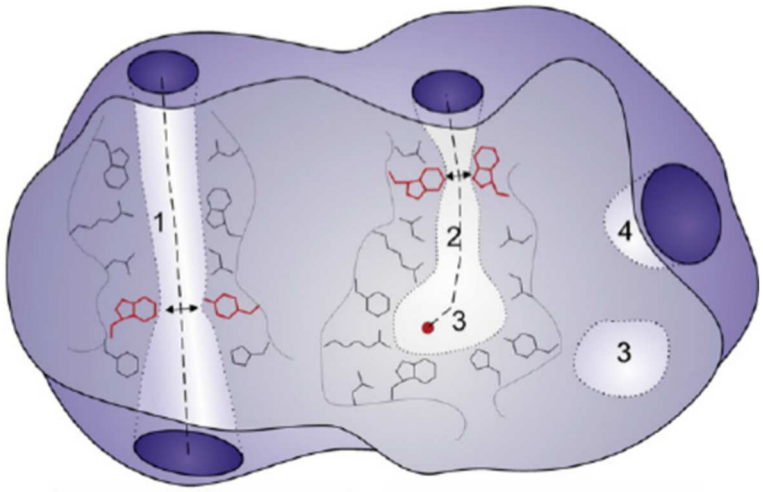

Figure 14: **Schematic representation of a protein with a channel/pore (1), a tunnel (2), a buried cavity (3) and a surface cleft/groove (4).** Figure 14 was inherited from Brezovsky *et al.*[68] Void interior is light purple, channel and tunnel entrance is dark purple, channel- and tunnel-lining residues are in black and bottleneck residues are in red. Arrows indicate a bottleneck. The red dot in the buried cavity represents the starting point for the tunnel calculation.

3.1 Multi-functional enzymes

A very well studied multi-functional class 6 enzyme is the carbamoyl phosphate synthetase (CPS).[73] CPS catalyses the synthesis of carbamoyl phosphate from bicarbonate, glutamine and 2x MgATP (Adenosintriphosphate). Two out of three intermediates, ammonia and carbamate, migrate from the site of generation to the site of utilisation through a permanent intramolecular tunnel with a total length of almost 100 Å and ~3.3 Å in diameter connecting three actives. Studying the structure of CPS also revealed a difference in diameter between the two tunnels spanning the actives sites, reflecting the larger tunnel needed to transport carbamate compared to ammonia.[73] The class II amidotransferase Glutamine phosphoribosylpyrophosphate amidotransferase (GPATase) catalyses the conversion of phosphoribosylpyrophosphate into phosphoribosylamine. The intramolecular tunnel of GPATase only exists transitory through binding of the right ligand to the active site and conformational changes of the protein backbone.[74] This architectural feature has also been proposed for the bifunctional enzyme Guanosine 5′- Monophosphate synthetase (GMPS).[75] An obstructed protein tunnel can be found in glucosamine 6-phosphate synthase (GlmS).[76] GlmS catalyses the conversion of D-fructose-6P (Fru6P) into D-glucosamine-6P. The tunnel connecting the two active sites of the glutaminase domain and the synthase domain is blocked by the amino acid side chain of

Trp-74. Mouilleron *et al.* illustrates the conformational change of Trp-74 to the open position through binding of a glutamine affinity analogue, and binding of Fru6P triggers the closed state (***Figure 15***).[76] Glutamate synthase also shows a substrate-induced conformational change of amino acids affecting the nature of the molecular tunnel.[77]

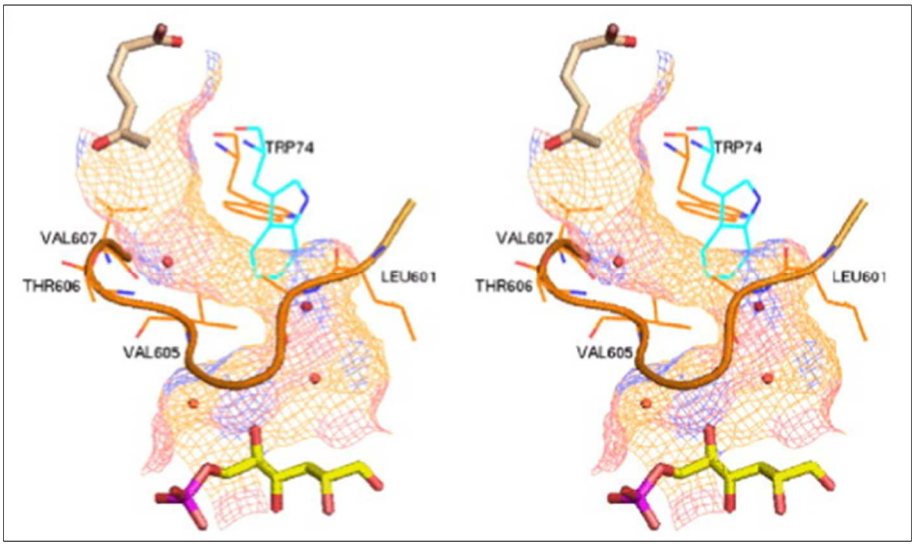

Figure 15: **Open and closed state of the substrate tunnel of glucosamine 6-phosphate synthase.** Figure 15 was inherited from Stéphane Mouilleron *et al.*[76] Superposition of the open and closed position of Trp-74 triggered (orange and blue sticks, respectively) through binding of 6-diazo-5-oxo-L-nor- leucine, a glutamine affinity analogue and Fru6P. The accessible surface of the tunnel was calculated with *Py*MOL (probe radius of 1.4 Å) and is represented as a surface mesh. Water molecules are depicted as red spheres.

3.2 Mono-functional enzymes

In mono-functional enzymes one or more molecular tunnels converge at a single active site to deliver substrates or release reactive products. A substrate-induced "gate" function of two amino acids in a molecular tunnel was suggested for the flavoenzyme cholesterol oxidase.[78] The monomeric enzyme catalyses the reversible chemical reaction of cholesterol + O_2 ⇌ cholest-4-en-3-one + H_2O_2. A putative hydrophobic O_2 tunnel has been proposed for cholesterol oxidase with an arginine and glutamate controlling the access of molecular oxygen to the active site. Conformational changes of the amino acids alter the nature of the tunnel to an open or closed state.[78] Klvana *et al.* has shown through MD simulations that the substrate and product exchange between the active site and the protein surface in DhaA haloalkane dehalogenase occurs via permanent tunnels, transient tunnels and migration through the protein matrix.[79] Lipoxygenases catalyse the dioxygenation of polyunsaturated fatty acids (PUFAs) into hydroperoxide derivatives.[63] The iron-containing active site is deeply buried inside the

enzyme. The two substrates, PUFA and O_2, become merged at the catalytic centre through two permanent hydrophobic tunnels (***Figure 16***).[67]

Firstly, in the case of Pa-LOX, I will illustrate in this study that one of the tunnels is occupied by a PUFA and the second hydrophobic tunnel might be used as O_2 transport pathway directly leading to the catalytic centre. These results are supported by mutational studies showing that the widening of the second substrate tunnel alters the catalytic specificity of the enzyme. Here, the biochemical experiments were provided from Swathi Banthiya in the laboratory of Prof. Hartmut Kühn (Charité - Universitätsmedizin Berlin, Institut für Biochemie). Several molecular tunnels can also be observed in hydrogenases. The hydrophobic tunnels provide substrate for the reversible catalytic reaction $H_2 \rightleftharpoons H^- + H^+ \rightleftharpoons 2e^- + 2H^+$.[6,22,80] Secondly, I will present in this thesis the results of tunnel calculations from various O_2-sensitive and O_2-tolerant [NiFe] hydrogenases with detailed insights and a focus on the O_2-tolerant *Re*MBH. Additionally, to the hydrophobic tunnels found in *Re*MBH a hydrophilic tunnel might release water produced in the reactivation reaction $2H_2 + O_2 = 2H_2O$. One of the hydrophobic tunnels does not show an entrance at the protein surface in the calculations and seems to act as storage for the gaseous substrates [80]

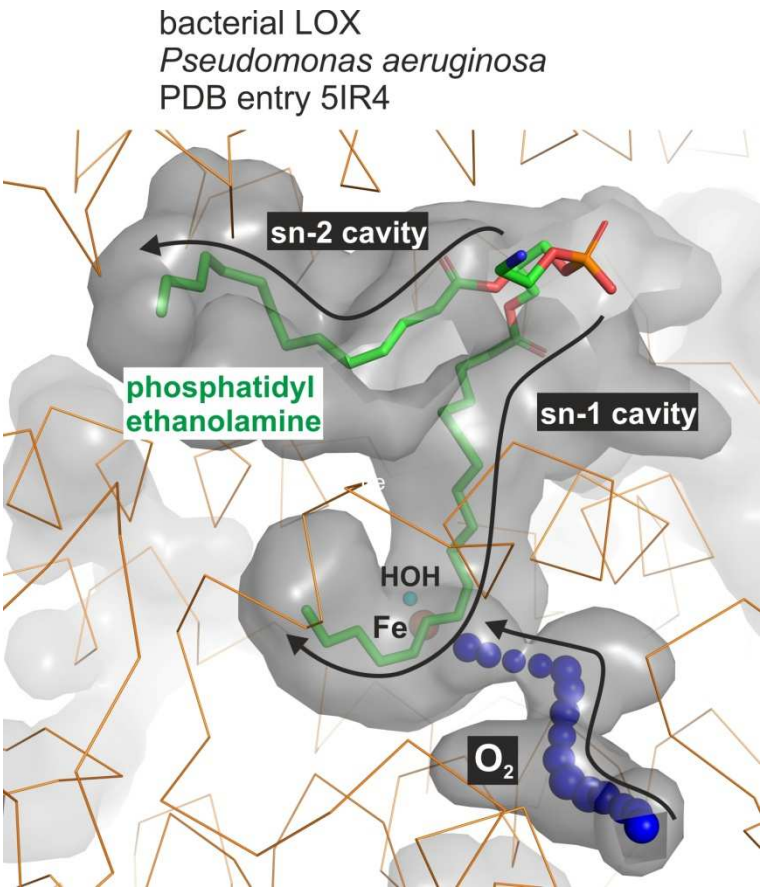

Figure 16: **Hydrophobic substrate tunnels of bacterial wild-type lipoxygenase from *Pseudomonas aeruginosa*.** Protein cα-backbone depicted as orange ribbon. Internal surface calculations with *Py*MOL are shown in grey. O_2 tunnel calculations with *Caver 3.0* are illustrated as blue spheres. Substrate sn-1 and sn-2 cavity are occupied by the endogenous ligand phosphatidylethanolamine. All tunnels are indicated by black arrows. The active site iron ion and the coordinating water molecule are depicted as orange and cyan spheres, respectively.

3.3 Tunnel calculation

There are several geometry-based software tools for the calculation and analysis of protein channels and tunnels. An overview of advantages and disadvantages of various software tools has recently been provided by Brezovsky *et al.*[68] The software CAVER [72,81], MOLE [82] and MOLAXIS [83] can be used for the calculation and analysis of protein tunnels. Channels or pores can be studied with HOLE [84], MOLAXIS, CHUNNEL [85] and POREWALKER [86]. For the analysis of overall voids the programs HOLLOW [87] and 3V [88] are available. In this work, the molecular tunnels of the two enzymes, *Re*MBH and Pa-LOX have been studied, and therefore the tunnel analysis software tools CAVER, MOLE and MOLAXIS will be compared.

For reasons of simplification the applications will calculate the tunnels using an internal cavity as starting point instead of starting at the protein surface. All three Voronoi-based programs describe all possible pathways between the internal cavities and the protein exterior through the preceding prediction of internal voids.[89] For the calculation they also employ the Delaunay triangulation to draw the vertices and edges of the Voronoi diagram (***Figure 17***) [72] and the Dijkstra's algorithm[90] to find the tunnel pathways.

The Voronoi diagram can be described as followed: *(i)* A Voronoi diagram is a separation of a plane into *n* regions based on the distance of a discrete set of specified points also called sites. In case of a protein, these sites are the centres of the amino acid atoms depicted as spheres. *(ii)* Edges and vertices form the delimitation of the regions. Each point on an edge is halfway of exact two sites and each vertex is halfway of at least three sites. *(iii)* Each point within a region is closer to the site of that region then to any other site of the Voronoi diagram. *(iv)* Each edge belongs to two vertices and in turn each vertex has at least three edges. *(v)* The regions are polygons. *(vi)* Each edge belongs to exactly two of the *n* regions.[89] The Voronoi diagram with a limited number of sites and the Delaunay triangulation are duals. The Delaunay triangulation can be described with the empty-circle method: Three sites of the Voronoi diagram form a triangle in the Delaunay triangulation. The circumcircle of this triangle should be empty of other sites (***Figure 17B***, red circle). The circumcentre is a vertex of the Voronoi diagram and Delaunay edges are orthogonal to the corresponding Voronoi edges.[89]

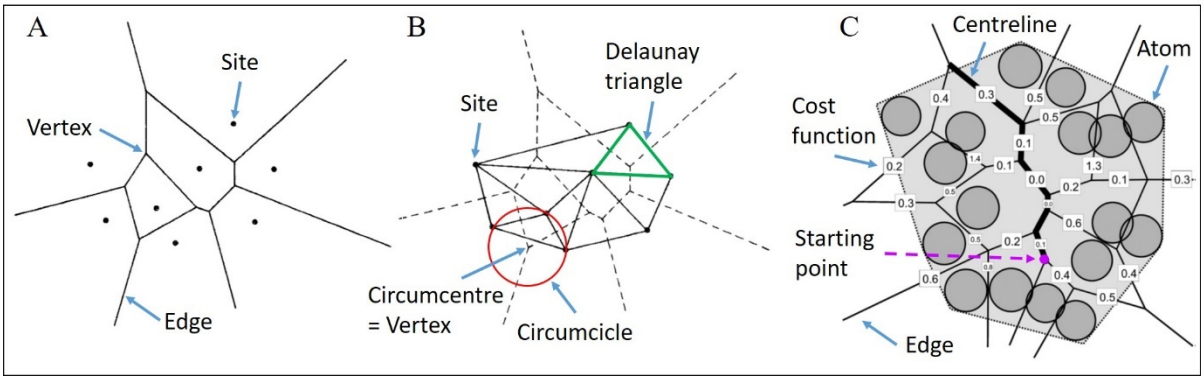

Figure 17: Voronoi diagram (A), Voronoi diagram with Delaunay triangulation (B) and 2D Voronoi diagram for tunnel search in proteins (C). Figure 17 A+B are inherited and modified from Franz Aurenhammer.[89] Figure 17 C is inherited and modified from Martin Petřek *et al*.[82] **(A)** shows a Voronoi diagram with 8 sites, 8 regions, 8 vertices and the corresponding edges. **(B)** shows a Delaunay triangulation of the Voronoi diagram from A with Delaunay triangles (one Delaunay triangle is marked in green) connecting three sites and a red circumcircle of a Delaunay triangle. **(C)** The scheme shows a 2D Voronoi diagram of a molecule presented as atoms (spheres). The edges (thin lines) are evaluated by the cost function (numbers) with the ideal path (thick centreline) found by the Dijkstra's algorithm. The starting point is marked as purple circle.

The algorithm of the three software tools can be described in the following steps: *(i)* The protein is represented by van der Waals spheres defining the molecule atom centres. In all applications, the spheres have a fixed size with the radius of the smallest atom in the structure. MOLE applies the fixed-size sphere to all atoms and deems the errors arising from this procedure as insignificant as most atoms in biomolecules have van der Waals radii between 1.6 – 2.1 Å.[82] However, including hydrogen atoms in the calculation of the Voronoi diagram can increase the error up to 2 Å. MOLAXIS and CAVER avoid this error by approximating larger atoms through a set of equally sized spheres.[68] *(ii)* Construction of the Voronoi diagram. *(iii)* Manual definition of the starting point for the tunnel calculation by the user or automatically by applying the centre of the largest cavity (MOLAXIS) or using residues from the Catalytic Site Atlas (CAVER, MOLE).[68,91] Additionally, optimisation of the starting point to prevent collision with surrounding atoms in CAVER and MOLE. *(iv)* For determining the surface between the protein and the solvent CAVER draws outer boundary points by rolling a probe around the protein surface. MOLE approximates a convex hull and MOLEAXIS defines a simplified protein surface by applying a large sphere.[68] *(v)* All computational applications calculate molecular tunnels on the basis of the cost function. The cost function evaluates each Voronoi edge by its length and width, but the width determination differs between the software tools. CAVER calculates a very detailed path by measuring the distances between several points on the surface of the closest atom to points on the Voronoi edge. MOLE only measures one distance between the surface of the closest atom and the Voronoi edge. MOLEAXIS uses

the average of the two distances from the surface of the closest atom and the two vertices of the Voronoi edge, assuming the whole edge has the same width.[68] *(vi)* The route of a pathway with the lowest cost is finally determined with the Dijsktra's algorithm.[90] The "cheapest" pathway will be characterised by its length and its width. The shortest pathway as well as the widest tunnel will have the lowest cost.[72]

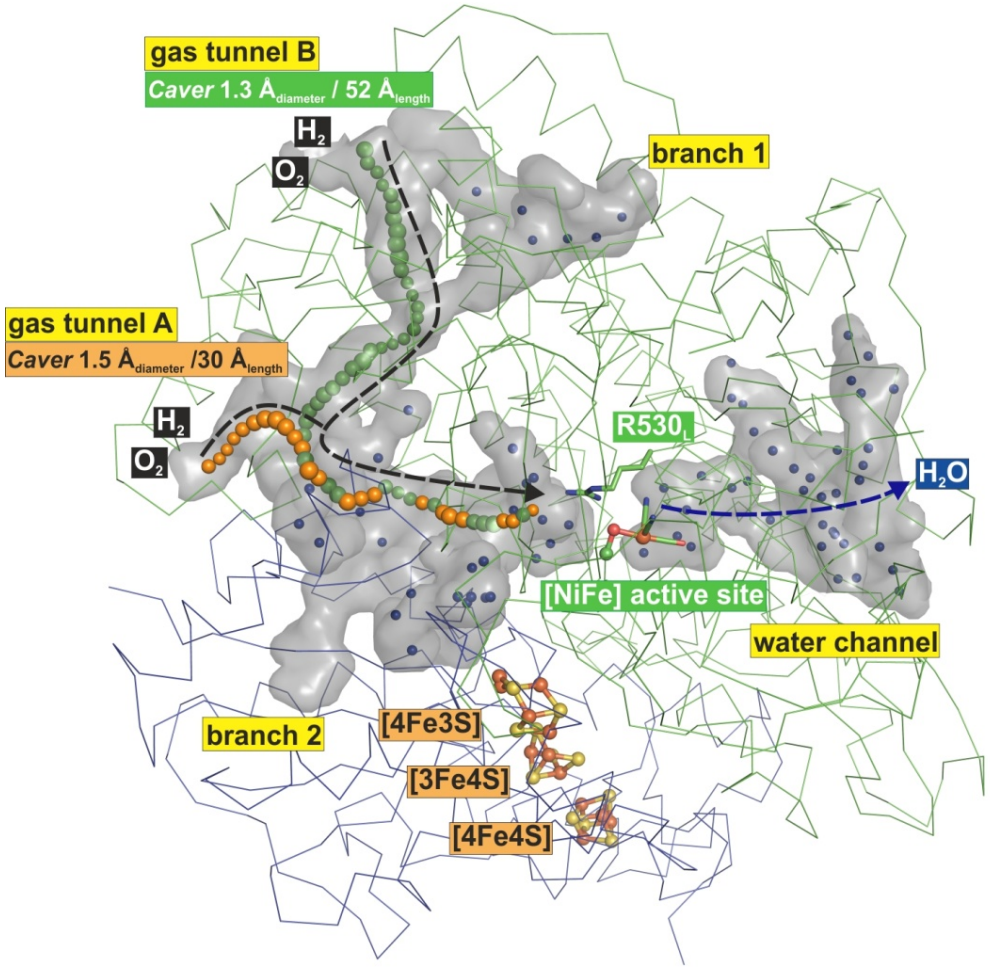

Figure 18: Tunnel network of *Re*MBH. The large and small subunits of *Re*MBH are depicted as ribbon in green and blue, respectively. The initial starting point for the *Caver 3.0* tunnel calculations is the highly conserved $R530_L$ (green sticks). The calculated tunnels are shown in chains of spheres in orange for gas tunnel A and green for gas tunnel B. Water molecules are illustrated as blue spheres with a high occupancy in the water channel. The [NiFe] active site as well as the [FeS]-clusters are in ball/stick representation. The proposed direction of the gas substrate and the water product are indicated as arrows in black and blue, respectively.

In this study, the program *Caver 3.0* was used as *Py*MOL plugin for the calculation of molecular tunnels in *Re*MBH (***Figure 18***) and Pa-LOX.

4 From crystal to structure

The section 'from crystal to structure' focuses on the basic theory of protein X-ray crystallography. More detailed information can be found in literature of Bernhard Rupp 'Biomolecular Crystallography: Principles, Practice, and Application to Structural Biology'[92], Terese M. Bergfors 'Protein Crystallization'[93] or Jan Drenth 'Principles of Protein X-Ray Crystallography'[94].

To obtain a diffracting crystal from an irregularly shaped protein is an important not alone difficult step in the process of determining a protein structure. Considering that a protein in its natural environment of a cell preferably not aggregates or periodically assembles with other proteins, it is even more challenging to achieve that in a crystallisation experiment. Additionally, proteins with their non-regular surface with flexible side chains and loops have only a few locations of weak intermolecular interactions which are involved in connecting the proteins for the growth of a crystal. Finding the right crystallisation condition is the first step towards the protein structure. Following, the obtained single protein crystal with its sharp edges can be harvested from the crystallisation drop, cooled in liquid nitrogen (LN_2) for the reduction of radiation damage and a data set with X-rays can be collected (***Figure 19***). From the resulting reflections on each frame an electron density can be calculated via Fourier transform techniques. Now the protein model can be built into the electron density. Eventually, after several rounds of refinement, model building and structure validation the final protein structure can be deposited online (***Figure 19***).

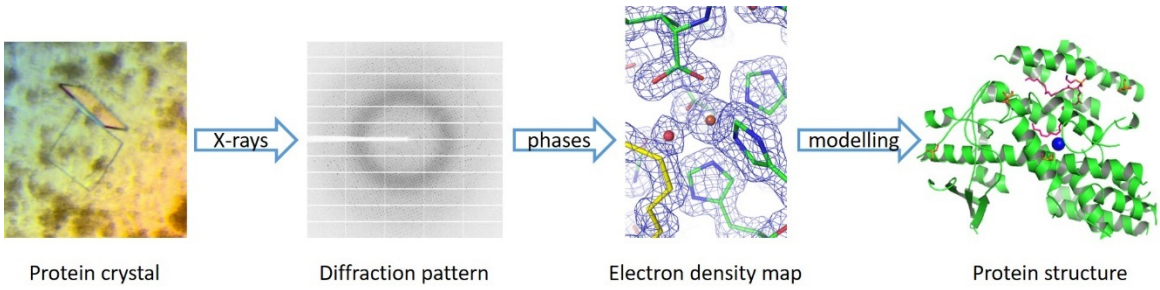

Figure 19: Workflow of structure determination from an example protein of this study. The flow chart shows the plate shaped crystal from Pa-LOX (lipoxygenase from *Pseudomonas aeruginosa*), followed by its diffraction patter received during data collection. After Fourier transformation, the protein was modelled into the calculated electron density map resulting in a 3D protein structure of Pa-LOX (PDB entry 5IR4).[63]

4.1 Protein crystallisation

4.1.1 Crystallisation kinetics

For the success of the crystallisation experiment the protein needs to change its phase from soluble to supersaturated to form crystallisation nuclei. The reduction of solubility can be achieved by adding precipitant and/or dehydrate the protein solution. Additionally, temperature, pH, protein concentration, additives and change of the buffer conditions can benefit the supersaturation process, thus nucleation and crystal growth. The driving force of crystal growth is the strong entropic gain mainly obtained through the release of free water molecules during crystal formation. On the opposite, there is the entropy loss from the loss of motional freedom (flexible side chains), which is, however, lower than the entropic gain. The enthalpic contribution in crystallisation is instead negligible. This leads to a negative value of the free energy, which is required for a spontaneous self-assembly of proteins to a crystal. The experiment starts with the protein in solution in the stable region. Through the change of parameters like the increase of precipitant and protein concentration the protein solubility decreases and reaches the supersaturated region in the diagram (***Figure 20***). In this region, a phase separation occurs into a protein-rich phase (crystal nuclei, protein crystal, precipitate, liquid protein 'oil' phases) and a saturated protein solution. In the homogenous nucleation zone assembled proteins reach a critical size and form nuclei. This will reduce the concentration of the soluble protein and the system preferably is displaced into the heterogenous nucleation zone, where crystal growth takes place. In this metastable region, transient nuclei form and disappear, but they are likely not to reach the critical size and external nuclei are needed. Crossing the instability curve the protein will precipitate in this unstable region. A visual description of the crystallisation process is presented in the protein crystallisation diagram (***Figure 20***). To achieve the supersaturation of the protein several crystallisation techniques are available.

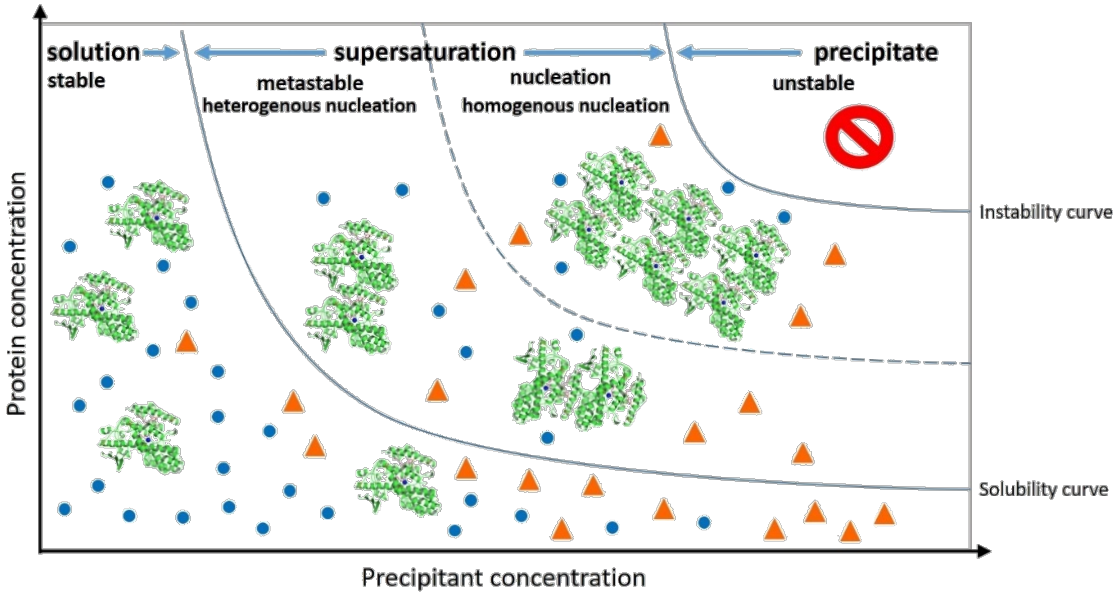

Figure 20: Protein crystallisation diagram. The diagram shows three phases. **(1)** In the stable zone the protein is in solution. **(2)** The metastable/ nucleation zone, where the supersaturation of the protein leads to spontaneous formation of crystallisation nuclei (homogenous nucleation). In the lower supersaturated region heterogenous nucleation takes place. This, however, requires seeds for crystal growth for example microcrystals. **(3)** If protein or precipitant reaching a high concentration and crossing the instability curve the protein will precipitate (unstable region). The protein is depicted as ribbon in green. Water molecules are shown as blue spheres and precipitant as orange triangles.

4.1.2 Crystallisation techniques

The most popular crystallisation technique is the vapour diffusion method (***Figure 21***). In the crystallisation setup, the protein solution is mixed with the precipitant solution e.g. in a ratio 1:1. The mixture will be either placed on a siliconized cover slide (hanging drop) or in a crystallisation well of a crystallisation plate (sitting drop). The reservoir of the crystallisation plate contains the precipitant solution with a higher concentration then in the protein/precipitant mixture. In the sealed system, aqueous vapour diffuses from the crystallisation drop into the reservoir increasing the concentration of the protein and precipitant preferably reaching the region for homogenous nucleation followed by crystal growth in the metastable region (***Figure 20***). Also very common are the microbatch and microdialysis methods (***Figure 21***). In the microbatch crystallisation technique the protein/precipitant solution is placed onto an oil-covered well of a crystallisation plate. The drop will sink to the bottom of the well and be covered by the oil. To reach protein supersaturation in this method, the precipitant solution has to have a higher concentration or the oil used, is water-permeable and the concentrations in the crystallisation drop can change. The microdialysis crystallisation method is based on the passing of crystallisation reagents towards the lower concentration through a semi-permeable membrane until reaching an equilibrium. The protein/precipitant solution will be placed in a

chamber of the dialysis button and covered by the membrane. In case the protein supersaturation does not reach the homogenous nucleation zone micro-seeds can be added to the crystallisation solution to induce crystal growth. In this micro-seeding method crushed crystals, microcrystals or tiny particles serve as micro-seeds and can be added to the crystallisation drop by streaking or adding a diluted solution.

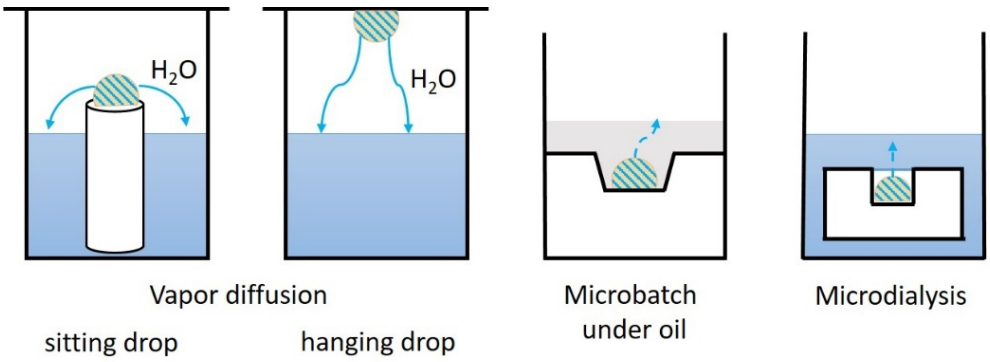

Figure 21: Crystallisation techniques. The most common crystallisations methods are vapour diffusion as sitting or hanging drop, microbatch under oil or microdialysis. The precipitant solution is shown in blue. The protein/precipitant solution is depicted as blue-orange-striped drop. The grey area in the microbatch method illustrates the oil used to cover the crystallisation drop.

4.2 Theory of X-ray diffraction

Determining the molecular structure of a protein, high energy electromagnetic waves (~10^4 keV), X-rays, with wavelengths in the atomic range (~10^{-10} = 0.1 nm = 1 Å) are needed. The X-rays interact with the electrons of the atoms in the crystal and through induction of oscillation at the electrons, they further emit electromagnetic waves of the same frequency (elastic scattering). Superposition of the emitted electromagnetic waves leads to constructive and destructive interference. Constructive interference of the scattered waves is recorded in a diffraction pattern as reflections on a detector. The condition of constructive interference is described by Bragg's law:

Equation 2

$$n\lambda = 2d \sin\theta$$

The Bragg equation describes the scattering of X-rays on discrete lattice planes with an interplanar distance d which is related to the scattering angle θ. Is the path difference $2d \sin\theta$ from one lattice plane to the other, a multiple integer n of the wavelength λ, constructive interference occurs (***Figure 22***).

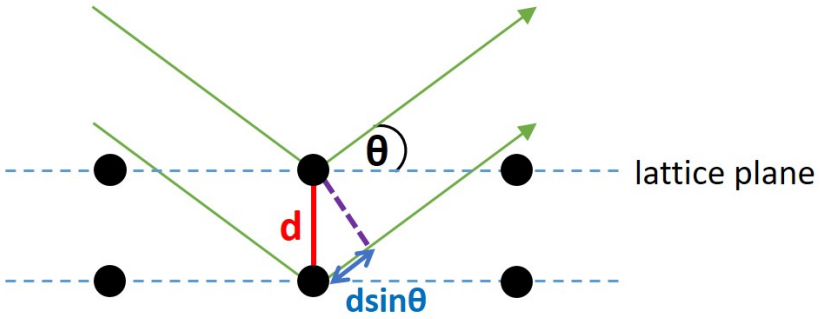

Figure 22: Bragg diffraction. Schematic interpretation of Bragg's law with X-ray diffraction at two distinct lattice planes (blue dashed lines) with d as interplanar distance (red line), the scattering angle θ and the path difference 2d *sin* θ (blue double arrow). The green line and arrows illustrate the incident and scattered electromagnetic waves. The black spheres depict the schematic positions of atoms in the crystal lattice.

The occurrence of reflections can be described with the Ewald construction. ***Figure 23*** shows the Ewald sphere with the crystal (purple) at the centre, the reciprocal lattice and its origin O. The radius of the Ewald sphere depends on the wavelength of the incident beam (1/λ). In order to obtain reflection spots the reciprocal lattice points (green spheres) need to cross exactly at the Ewald sphere. This is given when Bragg's law is fulfilled. To increase the number of reciprocal lattice points intersecting with the Ewald sphere, thus increase the amount of reflections, the crystal needs to be rotated. Is the wavelength λ of the incident X-ray beam larger than the greatest interplanar distance d in the crystal lattice no reciprocal lattice point will meet the Ewald sphere and no diffraction can be detected.

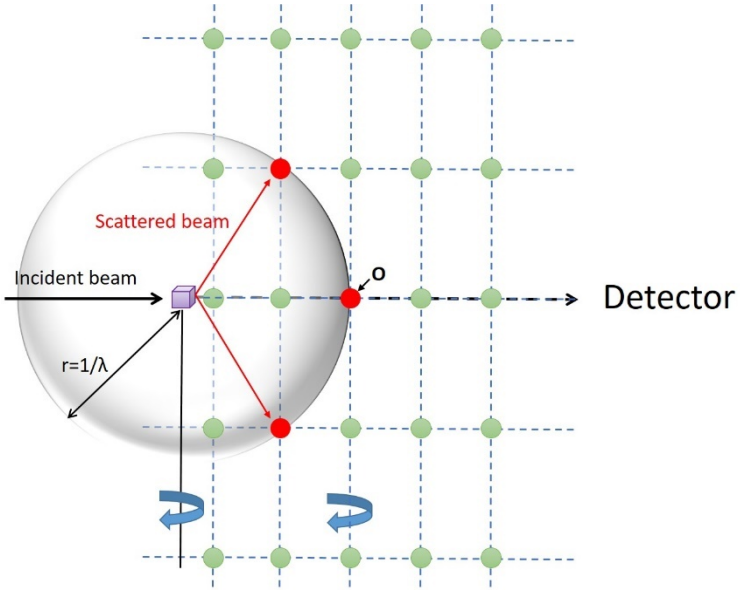

Figure 23: Ewald Construction. When the X-ray (incident) beam impinges on the protein crystal (purple) the photons are scattered at the electrons of the amino acid atoms. Reflections can be detected when the reciprocal lattice points (green spheres) cross the Ewald sphere, which is given when the Bragg's law is fulfilled. During data collection the crystal will be rotated to collect a full data set of the protein crystal. The size of the Ewald sphere depends on the wavelength of the X-ray beam (1/λ).

4.3 Data collection

If now the conditions of *(a)* the reciprocal lattice points intersecting with the Ewald sphere, *(b)* the scattered beam hits the detector and *(c)* the reciprocal lattice points in the Ewald sphere lie within the resolution limit of the crystal, X-ray diffraction data can be collected. Through the rotation of the crystal in small increments, a number of diffraction images are collected and compose the data set. Crucial for the positive outcome of a protein structure model is a highly complete data set of good quality. During the rotation, reflections will be recorded on the detector. In the first step, a software program determines the unit cell constants from the distances of the reflections, resolution of the crystal, specifies a space group from the first initial images and will provide a data collection strategy. If there is no collection strategy possible because of lattice disorder, no reflection spots or low resolution the crystal might be moved to a different position (in case of needles or large crystals on a microfocus beamline) or exchanged for a new crystal. The time needed for collecting a data set can vary immense between a synchrotron (seconds – minutes - hours) and laboratory X-ray generators (hours – days) and even between the technical setups of the synchrotron beamlines (generation of the synchrotron, detector models).

4.4 Structure factor & Electron density

For the reconstruction of the electron density two terms are needed: 1st the structure factor amplitudes $|F_{hkl}|$, which are directly accessible from the intensity of each reflection ($I_{hkl} \sim |F_{hkl}|^2$) and 2nd the phase $\varphi(hkl)$, which needs to be determined through further phasing experiments. These terms are implemented in the mathematical function of the structure factor $F_{(hkl)}$ with the structure factor indices (hkl) describing a plane in the crystal lattice.

Equation 3

$$F_{(hkl)} = |F_{hkl}| \cdot exp[i\varphi(hkl)]$$

The reversible method of Fourier transformation (FT) is then performed to convert the reciprocal space (structure factors, $F_{(hkl)}$) into the real space (electron density, $\rho_{(x,y,z)}$) shown in equation 4 with V as the volume of the unit cell.

Equation 4

$$\rho_{(x,y,z)} = \frac{1}{V} \sum_{h=-\infty}^{+\infty} \sum_{k=-\infty}^{+\infty} \sum_{l=-\infty}^{+\infty} F_{(hkl)} \cdot exp[-2\pi i(hx + ky + zl)]$$

4.5 Phasing

Missing the phase in the initial experiment leaves us with the "phase problem", which can be solved through molecular replacement or several experimental phasing methods. Following, the most popular phasing methods are described.

4.5.1 Molecular Replacement

The increasing number of available crystal structures through the PDB, molecular replacement is getting the most popular phasing method. The limitation in this method is the sequence homology of around 30 % or larger between the known structure and the unknown structure, where phase information is needed for. Through rotation-translation fitting of the known search model (calculated diffraction data) into the asymmetric unit of the unknown structure (observed diffraction data) phase information is obtained. There are two basic methods of placing the search model into the observed data of the target model. In the six-dimensional search method at each grid point of the asymmetric unit of the target model, all calculated structure factors of the search model are placed in different orientations[95]. The best solution is validated by the calculation of highest correlation score and the lowest *R*-value at each grid point. Searching in all six dimensions simultaneously is very time consuming. Therefore, in the method of rotation-translation searches the 3-dimensional rotation search will be followed by the 3-dimensional translation search. The search can be performed using Patterson-based methods with a further improvement through maximum likelihood functions. In the Patterson map the intramolecular distance vectors of the search model will be oriented in the position of the intramolecular distance vectors of the unknown model. The Patterson map can be constructed from Fourier coefficients, which are calculated from the squared structure factor amplitudes without phase information.[95] Further, the maximum likelihood function also considers for experiment and model error, e.g. incompleteness, coordinate errors, B-factors and occupancy, in the rotation-translation searches, which improves the finding of the right solution.

4.5.2 Isomorphous replacement

Soaking or co-crystallisation of a crystal with heavy atoms creates an isomorphous derivative crystal of the same unit cell compared to the native crystal (no heavy atoms). The phase problem can be solved by calculating the isomorphous differences of the two crystals through the differences in intensities of the heavy atoms.[96] Either one or more heavy atoms can be soaked into the crystal for single isomorphous replacement (SIR) or multi isomorphous

replacement (MIR). The differences in the structure factor amplitudes of the native ($|F_P|$) and derivative crystal ($|F_{PH}|$) are used to estimate the structure factor amplitudes for the heavy atoms ($|F_H|$) and construct the Patterson difference map. From the now known positions of the heavy atoms the corresponding phases can be calculated.[96] The complex structure factors can be visualised in an Argand diagram and the graphical representation of the phase (α) calculation with the Harker diagram, both shown in ***Figure 24***. The Harker construction for the SIR experiment (***Figure 24B***) shows two solutions for the calculated phases. To overcome this phase ambiguity, experiments with additional heavy atoms (MIR) or using the anomalous signal of the heavy atoms (single wavelength anomalous diffraction, SAD and multiple wavelength anomalous diffraction, MAD) or a combination of both (SIRAS, MIRAS) as well as density modification methods could be applied.

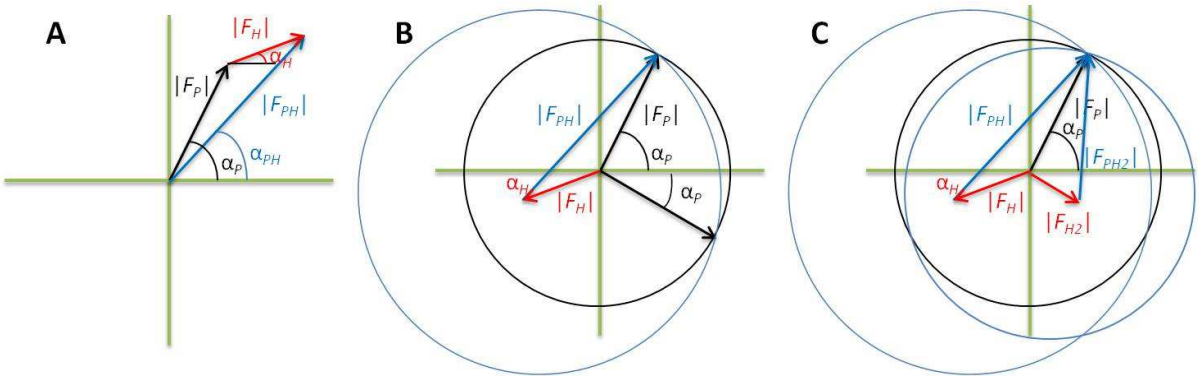

Figure 24: A) Argand diagram for SIR. B) Harker construction for SIR. C) Harker diagram for MIR with two heavy-atom derivatives. The reflection amplitudes are $|F_P|$ for the native crystal, $|F_{PH}|$ for the heavy atom derivative crystal and $|F_H|$ for the isomorphous difference. The reflection phases are $|\alpha_P|$ for the native crystal, $|\alpha_{PH}|$ for the heavy atom derivative crystal and $|\alpha_H|$ for the isomorphous difference. Both possible solutions occur for the native crystal $|F_P|$ were the two circles intersect. To overcome this phase ambiguity a second heavy atom $|F_{PH2}|$ in a MIR experiment can be introduced making only one solution possible.[92]

4.5.3 Anomalous diffraction

In the anomalous diffraction method, heavy atoms in the structure absorb X-rays at for each element very specific wavelength (absorption edge). This absorption of X-rays leads to an anomalous scattering of the same heavy atom (F_{PH}) compared to the equally scattering of all other atoms (F_P) in the molecule. As a consequence, the relationship between amplitudes and the angles of the diffraction is broken, Friedel's law is broken (***Figure 25B***). Friedel's law describes that a Friedel pair of two reflections is related by inversion through the origin of the centrosymmetrically reciprocal space of the crystal. Each pair has an equal amplitude ($|F_P|$) and opposite phase (φ) (***Figure 25A***). In case of anomalous scattering, amplitudes change, because of the absorption of the anomalous scatterer. In the experiment, first the specific scattering

factors f' (dispersive contribution) and f'' (anomalous contribution) of the heavy atom need to be determined by an X-ray absorption edge scan (***Figure 25C***, fluorescence scan of Krypton). In the next step, for example the MAD experiment, at four different wavelengths, using one crystal, data sets are collected: (1) Peak point with the largest anomalous differences, (2) inflection point has the optimal dispersive signal from f' (for dispersive differences between data sets), (3) high remote with both the anomalous and dispersive signal and (4) low remote for dispersive difference against inflection data (***Figure 25C***). Using one crystal for all the data sets has the advantage that no isomorphism errors are present, but the disadvantage of possible radiation damage to the crystal. In a SAD experiment, only one data set above the absorption edge for the heavy atom is required. In the special case of a S-SAD experiment, where sulfur atoms of the amino acids methionine and cysteine are used as anomalous scatterer, the K-edge of sulphur is too far away to be reached by a beamline so far. Additionally, the closer you get to the edge (longer wavelength) the more resolution you lose (lower energy). The problem of phase ambiguity in a SAD experiment can be solved by density modifications like solvent flattening, solvent flipping or histogram matching. In both, solvent flattening and flipping, a solvent region is defined (solvent mask) and the electron density is set to a constant value or zero, respectively. In the histogram matching the initial electron density map is compared to a theoretical electron density map, as the electron density values for a given resolution should be the same.

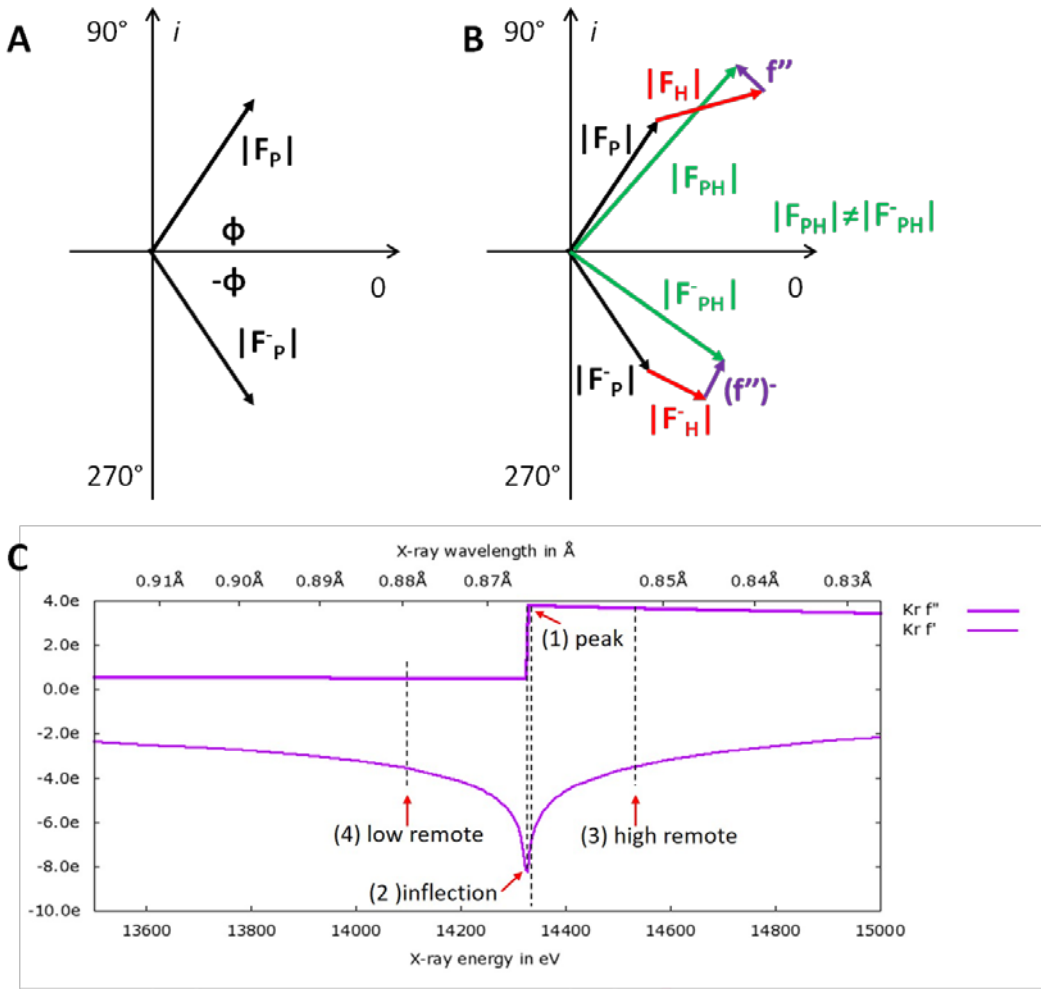

Figure 25: (A) Friedel's law. All members of a Friedel pair have an equal amplitude ($(|F_P| = (|F^-_P|)$, but an opposite phase ($\varphi = -\varphi$). **(B) Breakdown of Friedel's law.** Structure factor amplitudes of the derivatised crystal (F_{PH}) and the anomalous scatterer (F_H). **(C) MAD phasing.** All four wavelengths are marked for data set collecting in a MAD experiment on the example of a krypton fluorescence scan (theoretical values calculated using http://skuld.bmsc.washington.edu/scatter, 18.12.2016).

4.6 Model building, refinement & validation

Model building, refinement and validation are strongly intertwined. The model building starts with either an experimental electron density map or a map obtained through molecular replacement (MR). However, through MR the electron density map might be highly biased from a poor starting model, which is incomplete or low in sequence identity, and needs further bias minimisation. The model will be built manually from scratch or with an automated model building program in real space whereas the refinement takes place in reciprocal space. Solvent molecules, side-chain conformations, loops, ions and ligands are built into the electron density map. Still existing stereochemical errors are corrected during restraint refinement including parameters like bond lengths, bond angles, torsion angles, non-bonded interactions and chirality. Following every cycle of model rebuilding and restrained refinement to overall fit

between observed structure factor amplitudes F_{obs} (from the diffraction experiment) and the calculated structure factor amplitudes F_{calc} (from the computed model) can be tracked by the *R*-value. To determine model quality a free data set, which is excluded from the refinement, is used as cross-validation. The overall fit of the data and model is computed independently for the free data set R_{free} and the working data set R_{work} (Equation 5). The R_{free} value is further a good indicator for overfitting of the model (introduction of additional model information most likely happening through the extensive insertion of water molecules) and potentially optimisation of restraint weights. Discrepancy from the most favourable model is indicated through an increase in the gap between R_{free} and R_{work}.

Equation 5

$$R = \frac{\sum_{hkl} |F_{obs} - F_{calc}|}{\sum_{hkl} F_{obs}}$$

Additional validation programs like MolProbity[97], WHAT IF[98], PDB validation server[99] and RAMPAGE[100] help with examining geometry errors, close contacts, side-chain flips, ligand binding, water molecules with no protein interaction and thus, the improvement of the protein model. Finally, when the structure has no further interpretable positive or negative difference density, no major geometry errors can be found and the model is biochemically plausible, the model rebuilding and refinement can be finished.

Methods

5 Hydrogenase *Re*MBH

All *Re*MBH protein solutions were expressed and purified by Dr. Stefan Frielingsdorf and kindly provided by the group of Dr. Oliver Lenz from the Institut für Chemie at the Technische Universität Berlin.

5.1 Krypton derivatisation

5.1.1 Crystallisation

*Re*MBH was crystallized with a concentration of about 10 mg ml^{-1} at 277 K. Crystallisation was performed with the sitting-drop vapour diffusion method in 24-well Linbro plates (Jena Bio- science). The reservoir solution contained 20-30 % polyethylene glycol 3350, 100 mM Bis-(2-hydroxy- ethyl)-amino-tris(hydroxymethyl)-methane buffer at pH 5.5. Precipitants and protein solution were mixed in different ratios (7 - 8 µl) into micro-bridges (Hampton Research). After 2-4 days, the dark-brown *Re*MBH crystals were directly flash cooled in liquid nitrogen (***Figure 26***).

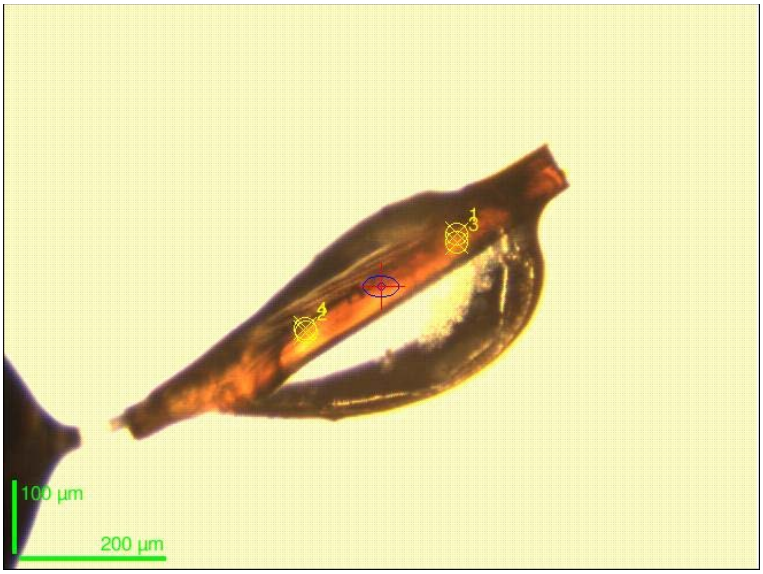

Figure 26: Wild-type *Re*MBH crystal in a nylon loop. The *Re*MBH crystal is mounted at a synchrotron beamline under LN_2.

5.1.2 Data Collection and structure analysis

Diffraction data was collected at the synchrotron radiation facility ERSF in Grenoble, France. Several native and anomalous data sets were collected with the program *MxCUBE*[101] at the tunable beamline ID 23-1[102] with a PILATUS 6M-F detector at a wavelength of λ = 0.976 Å and λ = 0.861 Å, respectively. An optimized data collection strategy was automatically calculated from four test pictures employing the program *EDNA* using four test images.[103] The collection was performed at 100 K, a detector distance of 200 - 400 mm and a rotation increment of 0.1° with an exposure time of 0.04 s for each frame. The images of the best data sets were indexed, integrated and scaled using the *XDS* program package and the CCP4 program *SCALA*.[104,105] Crystals belong to orthorhombic space group $P2_12_12_1$ (approximately unit cell constants: a = 73 Å, b = 96 Å, c = 120 Å; α = β = γ = 90.00°). Initial phases for *Re*MBH were obtained by molecular replacement using the structure of native *Re*MBH (PDB entry 4IUC) as initial search model. Molecular replacement was achieved through the CCP4 program *PHASER*.[106–108] Subsequently, several refinement strategies (real-space refinement, individual B-factors, occupancies) as well as simulated-annealing and search for water molecules are calculated with the program *PHENIX*.[109] The anomalous electron density was calculated with the program *FFT* of the CCP4 package. The crystal structure was finalized by the CCP4 program *REFMAC5*.[110] Manual rebuilding of the krypton-derivatized *Re*MBH model and electron density interpretation was performed after each refinement cycle using the program *COOT*.[111] The final models, native and anomalous, have agreement factors R_{free} / R_{work} of 15.1 % / 13.3 % and 16.9 % / 13.1 %, respectively.[112] Structure validation was performed with the programs of the RCSB PDB Validation server[99], Molprobity[97] and WHAT IF server[98]. All molecular graphics representations were created using *Py*MOL[113].

5.1.3 Caver tunnel analysis

The *Caver 3.0*[72,81] program was used as *Py*MOL plugin. The settings in the program have been changed manually. The initial starting point (NH_2 of the guanidine-group of the arginine, e.g. $R530_L$ for *Re*MBH), shell depth (2 Å), shell radius (3 Å), cluster threshold (3.5 Å) and the desired radius (5 Å) maintained constant for all calculations. The minimum probe radius varied from 1.2 - 1.6 Å and calculations were performed in 0.1 Å steps. The maximum distance was adjusted from 3 Å to 4 Å with an increasing probe radius and up to 9 Å in the amino acid substitutions of the proposed active site gate of *Df*-hydrogenase. The maximum distance specifies the maximal distance of the tunnel calculation starting point from the initial starting

point (arginine). The bottleneck radius is the narrowest part of a given tunnel and corresponds to the minimum probe radius.

5.2 Oxygen derivatisation

5.2.1 Crystallisation

*Re*MBH was crystallized with the sitting-drop vapour diffusion method in 24-well Linbro plates (Jena Bioscience) at a concentration of about 10 mg ml^{-1} and at 277 K. The reservoir solution contained 20-30 % polyethylene glycol 3350, 100 mM Bis-(2-hydroxy-ethyl)-amino-tris(hydroxylmethyl)-methane buffer at pH 5.5. Precipitants and protein solution were mixed in different ratios (7 - 8 µl) into micro-bridges (Hampton Research). After 2-4 days, the dark-brown needle shaped *Re*MBH crystals were directly used for high-pressure cooling and O_2 derivatisation experiments or were cryo-protected in 15 % glycerol and flash cooled in liquid nitrogen (LN_2) for native data set collection.

5.2.2 High-pressure cryo-cooling

The cryo-protectant free cooling of the *Re*MBH crystals was performed using a high-pressure cooling system recently developed at the ESRF in Grenoble (***Figure 27***).[114] The needle shaped crystals were directly harvested from the crystallization drop with specific pluggable sample supports (MiTeGen, Ithaca) and transferred into the pressurizing drop tubes at room temperature. The lower parts of the drop tubes are then cooled in LN_2 and the crystals are pressurized with 2000 bar of helium. Following, the crystals were dropped into the bottom of the tube and cooled at 77 K. Finally, the system was depressurized, the crystals handled in liquid nitrogen and stored under LN_2 for further X-ray experiments. Four crystals were high-pressure cooled at the same time.

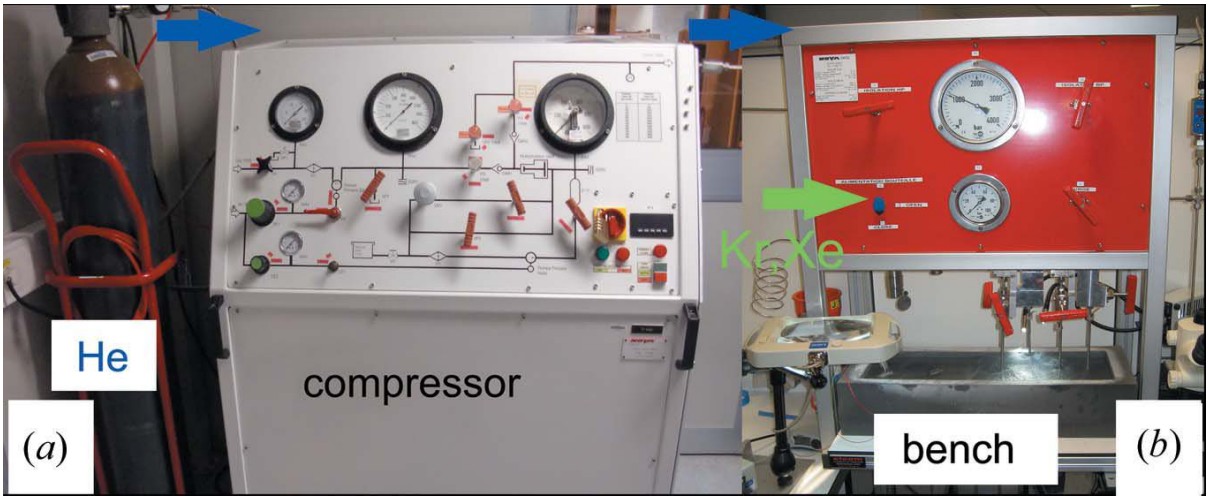

Figure 27: Photograph of high-pressure cooling device. Figure 27 was inherited from van der Linden *et al.*[114] **(a)** shows the Helium (He) cylinder followed by a two-stage compressor. **(b)** shows the cooling bench, with four sample drop tubes (250 mm length, 2.4 mm diameter). It also provides a Xe/Kr cylinder for noble gas derivative preparation.

5.2.3 Oxygen derivatisation

The *Re*MBH crystals were derivatised with O_2 gas in a cryogenic oxygen pressure cell newly developed at the ESRF in Grenoble.[115] Each time one crystal was harvested from the crystallization drop with a specific pluggable sample support (MiTeGen, Ithaca) being surrounded by mother liquor including 15 % glycerol. The crystal was then loaded into the pressurising drop tube at room temperature. The *Re*MBH crystals were pressurized at 56 bar (5600 kPa) and 70 bar (7000 kPa) in a time frame of 15 - 77 min. Still under pressure the crystal was dropped into the bottom of the tube and cooled at 77 K. After depressurizing the system, the crystal was handled with a specially designed cryo-toolkit and stored under liquid nitrogen for further experiments (***Figure 28***).

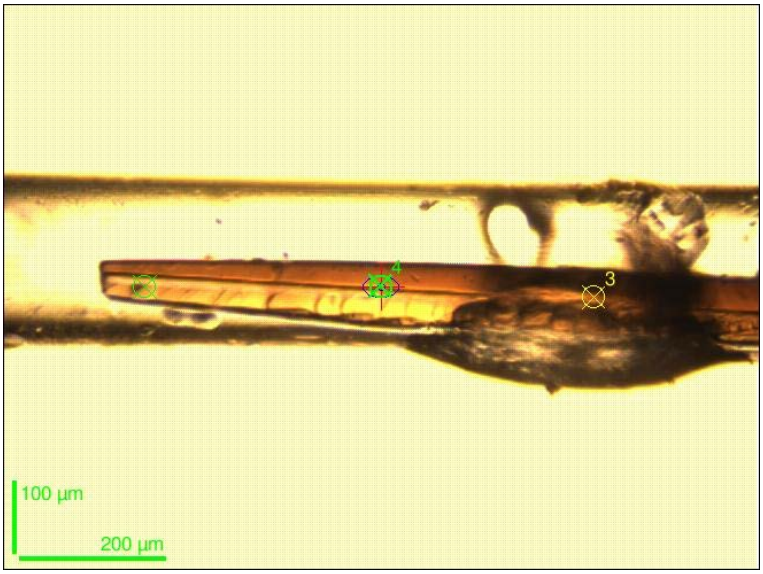

Figure 28: O_2 derivatised *Re*MBH in a capillary. The derivatised *Re*MBH crystal is mounted in the capillary at a synchrotron beamline under LN_2.

5.2.4 Data Collection and structure analysis

Diffraction data was collected at the synchrotron radiation facility ESRF in Grenoble, France. The best high-pressure (HP) data set was collected at the tuneable beamline ID29[116] with a PILATUS 6M-F detector at a wavelength of 0.976 Å. The best O_2 derivatised (OxD) and reference (REF) data set were collected at the tuneable beamline ID30B with a PILATUS 6M-F detector at a wavelength of 0.976 Å. All data sets were measured using data collection and

strategy software packages *MxCube*[101] and *EDNA*.[103] The data collection was carried out in the helical rotation mode at 100 K, a rotation increment of 0.05 ° with an exposure time of 0.037 s for each frame (3000 images) and a detector-to-crystal distance of 191 mm, 163 mm and 256 mm for the HP, OxD and REF data set, respectively. The images of the best data set were indexed, integrated and scaled using the *XDS* 2 package[104] and the CCP4 program *SCALA*[105].[106,107] All crystals belong to orthorhombic space group $P2_12_12_1$ (approximately unit cell constants HP: 121.57 a = 73.39 Å, b = 95.70 Å, c = 121.57 Å; α = β = γ = 90.00 °, approximately unit cell constants OxD: a = 73.13Å, b = 95.57 Å, c = 119.69 Å; α = β = γ = 90.00 °, approximately unit cell constants REF: a = 73.11 Å, b = 95.57 Å, c = 119.83 Å; α = β = γ = 90.00 °). Initial phases for *Re*MBH (HP, OxD, REF) were obtained by molecular replacement based on the crystal structure of the reduced state *Re*MBH (PDB entry 4TTT) as initial search model using the CCP4 program *PHASER*.[106,108] Subsequently, different refinement strategies (inter alia real-space refinement, B-factor refinements) and simulated-annealing (slow cooling protocol, maximum likelihood target function, energy minimization) were carried out. The search for water molecules was performed with the *PHENIX* program.[109] The crystal structure was finalized with the CCP4 program *REFMAC5*.[110] Manual rebuilding of HP, OxD and REF models and electron density interpretation were performed after each refinement cycle using the program *COOT*.[111] The final OxD model has agreement factors R_{free} / R_{work} of 13.2 % / 16.3 %.[112] Structure validations were performed with the programs of the RCSB PDB Validation server[99], MolProbity server[97] and WHAT IF server[98]. All molecular graphics representations were created using *Py*MOL.[113]

5.2.5 Caver tunnel analysis

The *Caver 3.0* program was used as *Py*MOL plugin.[72,113] The settings in the program have been changed manually. The initial starting point (NH_2 of the guanidine-group of the arginine, i.e. $R530_L$ for *Re*MBH), shell depth (2 Å), shell radius (3 Å), cluster threshold (3.5 Å), desired radius (5 Å) and the maximum distance (3 Å) maintained constant for all calculations. The maximum distance specifies the maximal distance of the tunnel calculation starting point from the initial starting point (arginine). The bottleneck radius is the narrowest part of a given tunnel and corresponds to the minimum probe radius. The tunnels itself are ordered due to specific cost function, e.g. two tunnels with equal radii the one with the shorter distances has a lower cost. The tunnel with the lowest cost will be the primary tunnel.

6 Lipoxygenase Pa-LOX

All Pa-LOX protein solutions were expressed and purified by Swathi Banthiya and kindly provided by the group of Prof. Hartmut Kühn from the Institut für Biochemie at the Charité - Universitätsmedizin Berlin.

6.1 Pa-LOX wild-type

6.1.1 Crystallisation

Pa-LOX was crystallized in two different crystallization buffers leading to two crystal forms. Crystallizations were performed with the sitting-drop vapour diffusion method in 24-well Linbro plates (Jena Biosciences, Jena, Germany) and a protein concentration of about 15 mg ml^{-1} at 293 K. The first crystallization condition (crystal form 1) was obtained over a reservoir solution containing 10 % polyethylene glycol (PEG) 3350, 50 mM magnesium chloride ($MgCl_2$) and 100 mM HEPES buffer at pH 5. Precipitants and protein solution were mixed in a 1.5/2 µl ratio into micro-bridges (Hampton Research, Aliso Viejo, USA). After 6–8 weeks the needle shaped Pa-LOX crystals were cryo-cooled in liquid nitrogen using 20 % glycerol. The reservoir solution of the second crystallization condition (crystal form 2) contained 12 % PEG 3350, 0.2 M $MgCl_2$ and 0.1 M tris(hydroxymethyl) aminomethane at pH 1. Precipitants, protein solution and seeding stock in a ration 1.0 : 1.5 : 0.5 were mixed into micro-bridges (Hampton Research, Aliso Viejo, USA) according to the Microseed Matrix Seeding (MMS) protocol from Hampton Research. The protocol describes the crushing of crystals in 50 µl of the crystallisation buffer with a seed bead, followed by a preparation of differently diluted stock solutions (1/10, $1/10^2$, $1/10^3$, $1/10^4$, $1/10^5$) (***Figure 29***). After 3–6 weeks the plate-shaped crystals were cryo-cooled in liquid nitrogen using 25 % glycerol as cryo-protectant. The cryo-protectant was mixed to the crystallization buffer in 5 % steps (15 %, 20 % and 25 %).

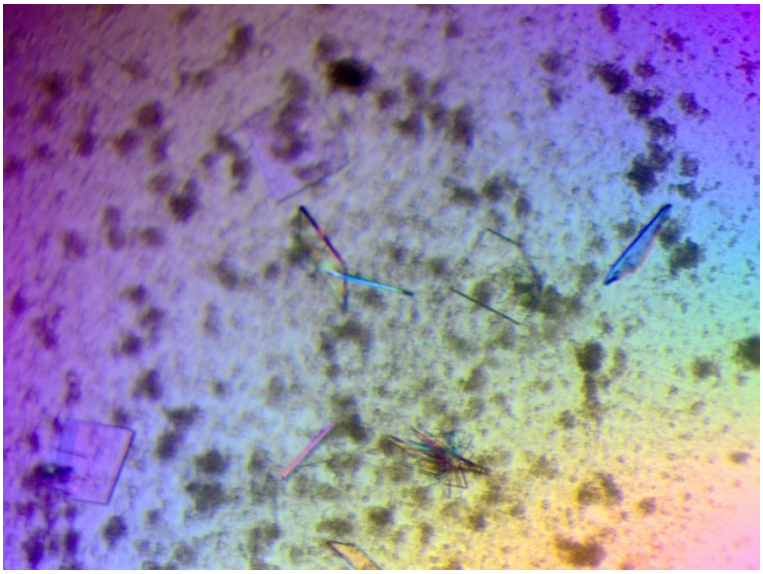

Figure 29: Plate-shaped crystals of Pa-LOX. Pa-LOX crystals in a vapour diffusion sitting drop after microseeding.

6.1.2 Data collection and structure analysis

Diffraction data were collected at 100 K using synchrotron X-ray sources from BESSY II (Berlin, Germany) and ESRF (Grenoble, France). The best diffraction datasets of both Pa-LOX crystal forms were collected at synchrotron beamline ID23-1[102] at ESRF with a Pilatus 6M-F detector at 0.972 nm wavelength. The data collection and strategy software packages *MxCuBE*[101] and *EDNA*[103] were used. The data collection of the first crystal form (needle shape – crystal form 1 was performed with a crystal-to-detector distance of 284 mm and a rotation increment of 0.1° with 0.04 s exposure time for each frame (1200 images). 1500 images of the second crystal form (plate shape – crystal form 2 were collected with a crystal-to-detector distance of 215 mm and a rotation increment of 0.1° with an exposure time of 0.04 s for each frame. The images of each data set were indexed, integrated and scaled using the *XDS*[104] program package and the CCP4[106] program *SCALA*[105]. The crystal form 1 belongs to the orthorhombic space group $P2_12_12$ (approximately unit cell constants: a = 133.09 Å, b = 116.35 Å, c = 42.72 Å, α = β = γ= 90.00°). The crystal form 2 belongs to the orthorhombic space group $C222_1$ (a = 83.74 Å, b = 97.39 Å, c = 153.84 Å, α = β = γ= 90.00°). Initial phases for both crystal forms of wild-type Pa-LOX were obtained by the conventional molecular replacement protocol (rotation, translation, rigid-body fitting) using the crystal structure of the phospholipid-lipoxygenase complex from *Pseudomonas aeruginosa* (PDB entry 4G32) as initial search model, which was used in the program *PHASER*[108] of the CCP4 software package[106,107]. A simulated-annealing procedure with the resulting models were performed using a slow-cooling protocol and a maximum likelihood target function, energy minimization

and B-factor refinements by the program *PHENIX*[109], which were carried out in the resolution range of 43.80 – 1.90 Å for the crystal form 1 and 48.97 – 1.48 Å for the crystal form 2, respectively. After the first round of refinements, phospholipid substrates in the ligand-binding pockets were clearly visible in the electron density of both σA-weighted 2*Fo-Fc* maps, as well as in the σA-weighted simulated annealing omitted density maps for both crystal forms of Pa-LOX. Both Pa-LOX crystal forms were modelled with TLS refinement (TLS - for Translation, Libration (small movements) and Screw-rotation of a group of atoms) using anisotropic temperature factors for all atom.[117] Restrained, individual B-factors were refined, and the crystal structure was finalized by the CCP4 program *REFMAC5*[110] and other programs of the CCP4 suite[106,107]. The final model has agreement factors R_{free} and R_{work} of 18.2 % and 14.4 %, for wild-type Pa-LOX crystal form 1 and 15.5 % and 13.6 %, for wild-type Pa-LOX crystal form 2, respectively. Manual rebuilding of the wild-type Pa-LOX crystal form 1 and 2 models and electron density interpretation were performed after each refinement cycle using the program COOT[111]. Structure validation was performed with the programs *PHENIX*[109], RCSB PDB Validation server[99], MolProbity[97], SFCHECK[118], PROCHECK[119], WHAT IF server[98] and RAMPAGE[100]. All crystal structure superpositions of backbone α-carbon traces were performed using the CCP4 program LSQKAB[106]. All molecular graphics representations in this work were created using the *Py*MOL[113] software package.

6.2 Pa-LOX Ala420Gly mutant

6.2.1 Crystallisation

Purified Ala420Gly mutant was crystallized with the sitting-drop vapour diffusion method in 24-well Linbro plates (Jena Biosciences, Jena, Germany) at a protein concentration of about 15 mg ml^{-1} at 293 K. The reservoir solution contained 12 % PEG 3350, 0.2 M MgCl2 and 0.1 M tris(hydroxymethyl)-aminomethane at pH 7.1. Precipitants, protein solution and seeding stock were mixed into micro-bridges (Hampton Re-search, Aliso Viejo, USA) according to the Microseed Matrix Seeding (MMS) protocol from Hampton Research. After 2-3 weeks the plate-shaped crystals were cryo-cooled in liquid nitrogen using 25 % glycerol as cryo-protectant. The cryo-protectant was mixed with the crystallization buffer in 5 % steps (15 %, 20 %, 25 %).

6.2.2 Data collection and structure analysis

Diffraction data was collected at the synchrotron radiation facility ERSF in Grenoble, France. The best data set was collected at the tuneable beamline ID 23-1[102] with a PILATUS 6M-F detector at a wavelength of λ = 0.972 Å using the data collection and strategy software packages *MxCube*[101] and *EDNA*[103]. The collection was performed at 100 K, a crystal-to-detector distance of 261 mm and a rotation increment of 0.15° with an exposure time of 0.04 s for each frame (1000 images). The images of the best data set were indexed, integrated and scaled using the *XDS* program package[104] and the CCP4 program *SCALA*[105,106]. Crystals show the orthorhombic space group $C222_1$ (approximately unit cell constants: a = 84 Å, b = 97 Å, c = 156 Å; α = β = γ = 90.00°). Initial phases for Pa-LOX Ala420Gly mutant were obtained by molecular replacement based on the crystal structure of the phospholipid-lipoxygenase complex from *Pseudomonas aeruginosa* (PDB entry 5IR4) as initial search model using the CCP4 program *PHASER*[108]. Subsequently, different refinement strategies (inter alia real-space refinement, B-factor refinements) and simulated-annealing (slow cooling protocol, maximum likelihood target function, energy minimization) were carried out. The search for water molecules was performed with the *PHENIX* program[109]. The crystal structure was modelled with TLS refinement using anisotropic temperature factors for all atoms.[117] The crystal structure was finalized with the CCP4 program *REFMAC5*[110]. Manual rebuilding of the Pa-LOX Ala420Gly mutant model and electron density interpretation was performed after each refinement cycle using the program *COOT*[111]. The final model has agreement factors R_{free} / R_{work} of 17.1 % / 13.9 %.[112] Structure validations were performed with the programs of the RCSB PDB Validation server[99], MolProbity server[97] and WHAT IF server[98]. All molecular graphics representations were created using *Py*MOL.[113]

6.2.3 Structural modelling of enzyme – fatty acid complexes

The crystal structure of the Pa-LOX Ala420Gly mutant, described here, contains a phosphatidylethanolamine molecule bound at the substrate-binding pocket. The two fatty acid moieties of this endogenous ligand occupy two adjacent fatty acid binding sub-cavities, which are connected by a lobby, which harbours the polar head group of the phospholipid. The sub-cavity that contains the sn1 fatty acid involves the catalytic non-heme iron. Linoleic acid and arachidonic acid molecules were modelled into this sub-cavity on the basis of the electron density of the endogenous ligand. Both structures of the two fatty acids were obtained from the *COOT*[111] small molecule library and directly fitted into the electron density via several steps

of rotation, translation and real space refinement. The model-complex structure was finalized using the structure idealization procedure of the CCP4 program *REFMAC5*[110], following a refinement of geometric restrains in *COOT*[111].

6.2.4 Caver tunnel analysis

The *Caver 3.0*[72] program was used from the plugin of the program *Py*MOL[113]. The settings in the program have been changed manually. The C11 and C15 carbon atom of the docked arachidonic acid as well as the C9 and C13 of linoleic acid served as initial starting point in the crystal structures of both Pa-LOX wild-type (PDB entry 5IR4) and Ala420Gly mutant (PDB entry 5LC8). The shell depth (4 Å), shell radius (3 Å), cluster threshold (3.5 Å), the maximum distance (3-4 Å) and the desired radius (5 Å) maintained constant for all calculations. The maximum distance specifies the maximal distance of the tunnel calculation starting point from the initial starting point. The minimum probe radius was defined by the largest value showing tunnel within the given parameters.

Results

7 Hydrogenase *Re*MBH

i. Krypton Derivatization of an O2-Tolerant Membrane-Bound [NiFe] Hydrogenase Reveals a Hydrophobic Tunnel Network for Gas Transport.

Kalms J*, Schmidt A, Frielingsdorf S, van der Linden P, von Stetten D, Lenz O, Carpentier P, Scheerer P. ***Angew Chem Int Ed Engl.*** 2016 Apr 25; 55(18):5586-90.

[NiFe] Hydrogenase

International Edition: DOI: 10.1002/anie.201508976
German Edition: DOI: 10.1002/ange.201508976

Krypton Derivatization of an O_2-Tolerant Membrane-Bound [NiFe] Hydrogenase Reveals a Hydrophobic Tunnel Network for Gas Transport

*Jacqueline Kalms, Andrea Schmidt, Stefan Frielingsdorf, Peter van der Linden, David von Stetten, Oliver Lenz, Philippe Carpentier, and Patrick Scheerer**

Abstract: *[NiFe] hydrogenases are metalloenzymes catalyzing the reversible heterolytic cleavage of hydrogen into protons and electrons. Gas tunnels make the deeply buried active site accessible to substrates and inhibitors. Understanding the architecture and function of the tunnels is pivotal to modulating the feature of O_2 tolerance in a subgroup of these [NiFe] hydrogenases, as they are interesting for developments in renewable energy technologies. Here we describe the crystal structure of the O_2-tolerant membrane-bound [NiFe] hydrogenase of Ralstonia eutropha (ReMBH), using krypton-pressurized crystals. The positions of the krypton atoms allow a comprehensive description of the tunnel network within the enzyme. A detailed overview of tunnel sizes, lengths, and routes is presented from tunnel calculations. A comparison of the ReMBH tunnel characteristics with crystal structures of other O_2-tolerant and O_2-sensitive [NiFe] hydrogenases revealed considerable differences in tunnel size and quantity between the two groups, which might be related to the striking feature of O_2 tolerance.*

The transport of reactants from the protein exterior to a buried active site or between multiple catalytic centers via protein tunnels is common to all six enzyme classes.[1,2] A particular remarkable example for the tunneling of intermediates is the class 6 enzyme carbamoyl phosphate synthetase. The three active sites are connected by two substrate tunnels spanning a total distance of almost 100 Å.[3] The access of the substrate to a buried active site has been studied in various enzymes, for example, bacteriorhodopsin, lipoxygenase, photosystem II, and hydrogenase.[4–9] Hydrogenases are metalloenzymes that catalyze the reaction $H_2 \rightleftharpoons H^- + H^+ \rightleftharpoons 2e^- + 2H^+$. They are widespread in all three domains of life and are classified according to the metal located at the active site. Members of the class of [Fe] hydrogenases catalyze a crucial step of methanogenesis in hydrogenotrophic archaea.[10] The [FeFe] hydrogenases are mostly involved in H_2 production under strictly anaerobic conditions, whereas [NiFe] hydrogenases are primarily H_2-oxidising enzymes.[11] [NiFe] hydrogenases can be further subdivided into O_2-sensitive and O_2-tolerant enzymes. O_2-sensitive hydrogenases are irreversibly inactivated in the presence of O_2, which is presumably caused by the reaction of reactive oxygen species with the metal cofactor(s).[12] In contrast, O_2-tolerant hydrogenases retain their enzymatic function in the presence of O_2,[13] which makes them attractive for biotechnological applications.[14] The feature of O_2 tolerance is related to the capability of the enzymes to use some of the electrons generated by H_2 oxidation for the complete reduction of O_2 to harmless water.[13,15] Prominent members of the O_2-tolerant enzymes belong to the group 1 membrane-bound [NiFe] hydrogenases (MBHs), which are made up of three subunits. The large subunit contains the [NiFe] active site where hydrogen splitting occurs and the small subunit harbors three [FeS] clusters that establish an electronic connection between the catalytic center and the third subunit, a membrane-integral cytochrome b_{562}. In this study we employed the catalytically active *Re*MBH heterodimer lacking cytochrome b_{562}.

According to the nature of the gas molecule approaching the [NiFe] active site via a hydrophobic tunnel, different enzymatic reactions take place. During the catalytic cycle H_2 is oxidized to protons and electrons. Protons are transported to the protein surface via protonatable amino acids and water molecules.[16] Electrons are guided through a relay composed of several iron–sulfur clusters to the primary electron acceptor.[17] In the event of O_2 approach, an additional reaction is proposed to occur at the [NiFe] active site. In this catalytic reactivation process, electrons are delivered from the electron relay to reduce O_2 with the aid of protons to H_2O, which then is released to the protein surface through a nearby water channel (Figure 1). Under aerobic conditions the [4Fe3S] cluster of the electron relay can undergo two redox transitions at physiological potential and transfers a second electron to the active site. In this two-electron mode structural changes occur at this cluster and one iron ion (Fe4) changes its binding partners (iron shift).[18] The crystal structures available so far for *Re*MBH[17,18] revealed plausible pathways for electron transport and water release, while both the proton pathways and gas transport routes remained largely unde-

[*] J. Kalms, A. Schmidt, Dr. P. Scheerer
Institut für Medizinische Physik und Biophysik (CC2)
Group Protein X-ray Crystallography and Signal Transduction
Charité – Universitätsmedizin Berlin
Charitéplatz 1, 10117 Berlin (Germany)
E-mail: patrick.scheerer@charite.de
Dr. S. Frielingsdorf, Dr. O. Lenz
Institut für Chemie, Sekr. PC14
Technische Universität Berlin
Strasse des 17. Juni 135, 10623 Berlin (Germany)
P. van der Linden, Dr. D. von Stetten, Dr. P. Carpentier
ESRF—European Synchrotron Radiation Facility
71 Avenue des Martyrs, Grenoble Cedex 9, 38043 (France)

Supporting information for this article can be found under http://dx.doi.org/10.1002/anie.201508976.

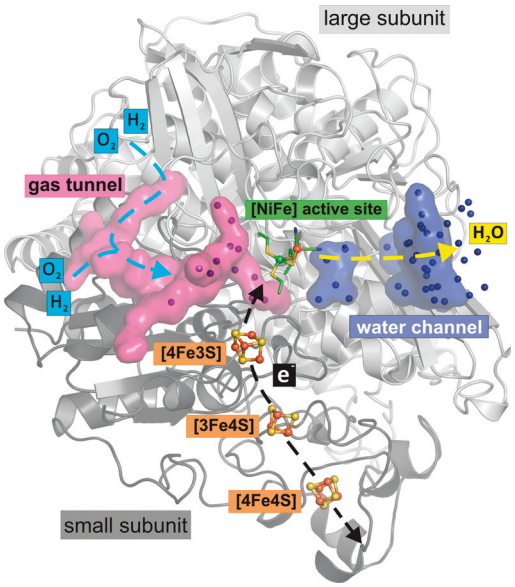

Figure 1. Ribbon representation of the large and small subunit of *Re*MBH (PDB entry: 3RGW) with the [NiFe] active site and its [FeS] clusters (proximal: [4Fe3S], medial: [3Fe4S], distal: [4Fe4S]) shown as balls and sticks. The gas tunnel (magenta) and the water channel (blue) are depicted as surfaces (calculated for all figures with PyMOL).[20] Water molecules (spheres) of the tunnel and channel are shown in the corresponding color (magenta/blue). The routes for H_2/O_2 and H_2O through the tunnels/channels are indicated by the light-blue and yellow arrows, respectively. The electron flow is represented by black arrows.

fined. Efficient gas transport to the deeply buried active site requires a tunnel that connects the protein exterior with the catalytic center.[19]

In 1997, a gas tunnel was proposed based on the derivatization with xenon (Xe) gas in crystals of O_2-sensitive [NiFe] hydrogenase from *Desulfovibrio fructosovorans* (*Df*).[9] Here we present high-resolution X-ray data of the O_2-tolerant *Re*MBH with multiple krypton (Kr) binding sites according to which a hydrophobic gas tunnel was defined. The hydrophobicity and high atomic number of noble gases like Kr and Xe make them favorable for the investigation of hydrophobic gas tunnels in pressurization experiments and X-ray studies.[4,6–9] A comparison of the gas tunnel architectures derived from crystal structures of O_2-sensitive and O_2-tolerant [NiFe] hydrogenases of various organisms uncovered significant differences, which are discussed in light of the O_2 tolerance of some [NiFe] hydrogenases.

In order to track the location of the hydrophobic gas tunnel we used the efficient method of noble gas derivatization of *Re*MBH crystals. Several native and anomalous data sets were collected (high-resolution and anomalous datasets at 1.47 Å and 2.52 Å resolution, respectively; see Table S1 in the Supporting Information). The overall protein structure of the krypton-derivatized *Re*MBH, including the four metal cofactors, is structurally identical to that of the as-isolated ("oxidized state 2") wildtype enzyme.[18] The [NiFe] active site resides in the so-called Ni_r-B state, characterized by an OH^- ligand bridging the two metals. The corresponding Ni–Fe distance is 2.85 Å. The structure of the [4Fe3S] cluster, however, shows some heterogeneity as the iron ion (Fe_4) involved in the iron-shift was found in a double conformation, which is reflected by an extended electron density (Figure S1). The increased flexibility might be caused by the noble gas derivatization method. However, the cluster structure is certainly no mixture of the previously reported H_2-reduced and "oxidized state 2", because both Fe_4 positions in the current structure are close to the position found in the "oxidized state 2".[18] The *Re*MBH structure contains 19 Kr sites with different occupancies located in tunnels and cavities (Table S2 and Figure S2). 15 out of 19 krypton atoms form an apparent hydrophobic gas tunnel network that connects the protein surface with the [NiFe] active site (Figure 2). Water

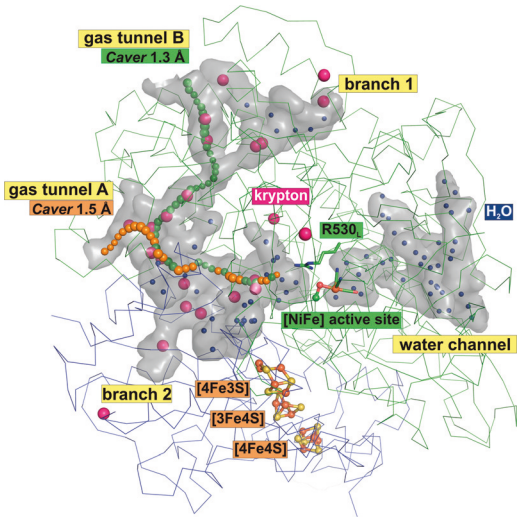

Figure 2. Stick representation of the large and small subunit of krypton-derivatized *Re*MBH (PDB entry: 5D51). The [NiFe] active site and the [FeS] clusters are shown as balls and sticks. The hydrophobic gas tunnel and the water channel are depicted as gray surfaces. Krypton atoms (magenta) and water molecules (blue) are shown as single spheres. $R530_L$ served as the initial starting point for *Caver* calculations. The results are represented by green and orange chains with a bottleneck radius of 1.3 Å and 1.5 Å, respectively.

molecules are located in hydrophilic cavities that form a water channel, which links the catalytic center with the protein exterior (Figure 2). The gas can enter the hydrophobic tunnel network through two openings, gas tunnels A and B, at the enzyme surface (Figure 2). Montet et al.[9] showed previously two main inlets for Xe and H_2 in the *Df*-[NiFe] hydrogenase, which are partially in agreement with the tunnel entrances of *Re*MBH. The proposed main inlet in channel b-a of *Df*-hydrogenase was found blocked in *Re*MBH (branch 2), whereas the second entrance located in channel c corresponds to the gas tunnel A entrance in our structure (Figure 2). The second gas tunnel opening in *Re*MBH (gas tunnel B) refers to channel f-d in the *Df* enzyme, which was reported as a functionally unimportant path for gas diffusion.[9] The 10 Xe sites identified by Montet et al. appear to occupy the same hydrophobic pathways that were revealed by krypton derivatization in our study.

To further support our experimental results, tunnel calculations were conducted with the program *Caver*.[20] We

performed the analysis with a minimal probe radius of 1.2 Å, which corresponds to the van der Waals radius of hydrogen (Table S3). The tunnel prediction with *Caver* was carried out in 0.1 Å steps up to 1.6 Å, which was the largest value showing tunnels. The invariant amino acid residue $R530_L$ (*Re*MBH nomenclature: L = large and S = small subunit), which is located in close proximity to the [NiFe] active site, served as the initial starting point for the tunnel calculations (Figure 2). This particular arginine is conserved among the [NiFe] hydrogenases known so far.[17,21]

The calculations revealed two plausible tunnel pathways in *Re*MBH, which are in agreement with the position of the krypton atoms (Figure 2). Gas tunnel A is 30 Å in length with a maximum bottleneck radius (narrowest part of a given tunnel)[20] of 1.5 Å. The gas tunnel B is 50 Å long with a bottleneck radius of 1.3 Å (Figure 2 and Table S4). The calculated routes are in full agreement with the chain of krypton atoms in the *Re*MBH structure. Subsequently, we examined the crystal structures of various group 1 hydrogenases for the presence of possible gas tunnels calculated with *Caver*. For that purpose the O_2-tolerant enzymes from *Ralstonia eutropha* (*Re*), *Escherichia coli* (*EcHyd-1*), *Hydrogenovibrio marinus* (*Hm*), and *Salmonella enterica* (*Se*) were compared to the O_2-sensitive hydrogenases from *Desulfovibrio gigas* (*Dg*), *Desulfovibrio desulfuricans* (*Dd*), *Desulfovibrio vulgaris* (*Dv*), *Desulfovibrio fructosovorans* (*Df*), and *Allochromatium vinosum* (*Av*) (Tables S4 and S5). A comparison of gas tunnel networks of O_2-tolerant and O_2-sensitive hydrogenases is exemplified by *Re*MBH and *Dv* hydrogenase (Figure 3). Although substantial sections of the gas tunnel network seem to be conserved (Figure 3), there are significant differences between the hydrogenases regarding the number of tunnels leading to the protein surface (see Tables S4 and S5). O_2-tolerant hydrogenases contain on average only two tunnels; the only exception is *Hm*MBH,[22] which harbors three and four tunnel openings for the H_2-reduced and air-oxidized states, respectively. The tunnel bottleneck radii range between 1.2 Å and 1.5 Å. Thus, there is a remarkable congruence concerning the number of gas tunnels (ca. two) in O_2-tolerant [NiFe] hydrogenases. A similar consistency holds true for O_2-sensitive enzymes. Except for *Dd* hydrogenase[23] with only two tunnels, the other four analyzed enzymes contain at least five tunnel openings. The corresponding bottleneck radii range between 1.2 Å and 1.6 Å.

In conclusion, the occurrence of hydrophobic tunnels and openings in O_2-sensitive hydrogenases is on average two times higher than in their O_2-tolerant counterparts (Tables S4 and S5). Although *Hm*MBH, *Ec*Hyd-1,[24] and *Dd* hydrogenase show a tunnel network similar to that of their consensus counterparts, there is a considerable difference in the number of tunnel openings. Branches 1 and 2 (Figure 2), which are open for gas access in all studied O_2-sensitive enzymes (Figure 3), are blocked in *Dd* hydrogenase. O_2-tolerant *Hm*MBH contains openings for the two gas tunnels at the end of branches 1 and 2. According to the calculations, *Ec*Hyd-1 has only one opening located at gas tunnel A (Figure 4). The fact that gas tunnel A seems to be present in all O_2-tolerant and O_2-sensitive [NiFe] hydrogenases leads to the conclusion that this tunnel is mainly used for gas transport

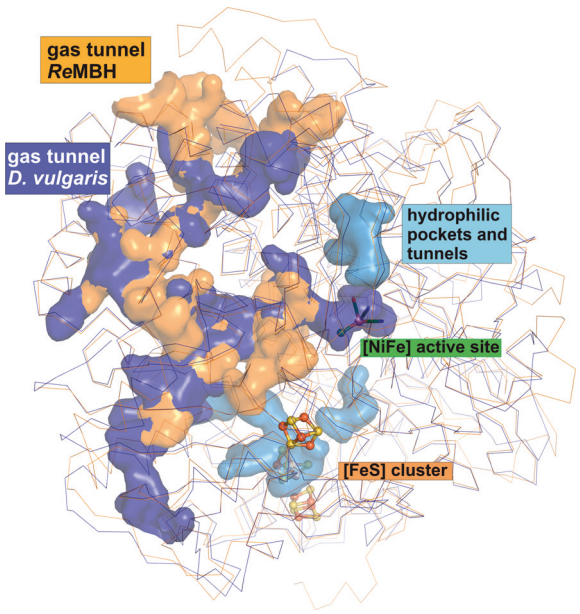

Figure 3. Stick representation of the O_2-tolerant *Re*MBH (PDB entry: 3RGW, orange) and O_2-sensitive *Dv* hydrogenase[27] (PDB entry: 1WUL, dark blue). The [FeS] clusters and the [NiFe] active site are illustrated as balls and sticks. The hydrophobic gas tunnels in *Re*MBH (in orange) and *Dv* (in dark blue) are also shown. Hydrophilic pockets and tunnels of *Dv* hydrogenase are depicted in light blue.

(Figure 2). Differences between the hydrogenases are also manifested in the gas tunnel dimensions. The majority of the tunnels present in O_2-tolerant and O_2-sensitive enzymes feature a bottleneck radius of 1.2 Å (37.5%) and 1.3 Å

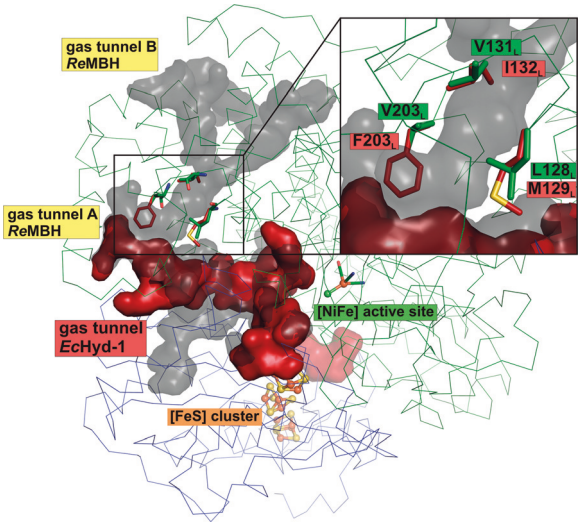

Figure 4. Superposition of the hydrophobic tunnels from *Re*MBH (PDB entry: 3RGW, gray) and *Ec*Hyd-1 (PDB entry: 3UQY, dark red). The protein backbone of *Re*MBH and the four metal cofactors shown as balls and sticks. The superposed gas tunnels are depicted as surfaces. Close-up view: The three *Ec*Hyd-1 amino acids ($M129_L$, $I132_L$, $F203_L$) blocking gas tunnel B are shown as dark-red sticks. They are superposed with the *Re*MBH amino acids $L128_L$, $V131_L$, $V203_L$ (green sticks).

(43.5%), respectively, and they span distances of 28–76 Å between the protein surface and the reactive center. However, on average the tunnels with the largest bottleneck have the shortest length. As evident in Figure 2, the *Re*MBH gas tunnel A has the largest bottleneck radius of 1.5 Å and a short length of 30 Å; in contrast, gas tunnel B is 50 Å in length and has a bottleneck radius of just 1.3 Å. The gas tunnel dimensions in all other studied structures (except *Dv* hydrogenase[25]) show a similar relation. As mentioned above, there is a considerable conformity of the gas tunnel architecture in O_2-tolerant and O_2-sensitive [NiFe] hydrogenases, particularly in close proximity to the active site. According to our calculations, the calculated starting point of the tunnel is situated 3–4 Å away from the conserved arginine residue ($R530_L$ in the case of *Re*MBH; Figure 2). An increase in the bottleneck radius would lead to a greater maximum distance between initial and calculated starting point. This implies that the end of the gas tunnel close to the active site is getting narrower. Such an effect has already been observed for *Df* hydrogenase carrying amino acid substitutions at the proposed active site gate (Table S6).[26] Moreover, a previous study demonstrated that an expansion by site-directed amino acid replacements of the potential gas tunnel of the H_2-sensing regulatory hydrogenase of *Re* yielded variants that are sensitive to inhibition by O_2.[27] In *Df* hydrogenase, replacement of the highly conserved residues, $V74_L$ and $L122_L$, by $M74_L/M122_L$ (PDB entry: 3CUR) and $I74_L/F122_L$ (PDB entry: 3CUS) led to a shift of the calculated starting point of the tunnel of 9 Å away from $R530_L$, due to the steric bulk of the amino acid side groups (Figure S3).[26] We used the corresponding crystal structures to calculate a virtual gas tunnel at 3 Å maximum distance to the conserved arginine. This calculation revealed a tunnel bottleneck radius of only 1 Å, which makes it rather difficult for O_2 and even H_2 to reach the active site.

This assumption is indeed reflected by a substantial increase in the Michaelis constant for H_2 in the case of the $V74_LI/L122_LF$ ($K_mH_2 = 50$ μM) and $V74_LM/L122_LM$ ($K_mH_2 = 200$ μM) variants compared to the native *Df* hydrogenase ($K_mH_2 = 10$ μM).[26] The single amino acid substitutions led to a maximum distance similar to that of the native structure (Table S6). The crystal structures indicate a slightly larger distance between the conserved gate residues, valine and leucine, in O_2-tolerant hydrogenases than in O_2-sensitive enzymes. This is mainly due to conformational differences of residue $L125_L$ (*Re*MBH nomenclature) (Figure S4). The experimental data of double-exchange variants of *Df* hydrogenase and the *Caver* calculations demonstrate that an exchange of the active-site gate amino acids to bulkier residues and the diameter of the gas tunnel ending have a major impact on the gas flow to the active site. Intriguingly, there is more variability in amino acids involved in tunnel formation within the group of O_2-sensitive hydrogenases than we observe in O_2-tolerant hydrogenases. Both groups show an amino acid invariance of 37.4% within conserved tunnel structures (Figures S7 and S8).

Additionally, we identified a hydrophilic tunnel directly at the medial [3Fe4S] cluster exclusively in the O_2-sensitive hydrogenases. This tunnel is blocked by a tryptophan in O_2-tolerant hydrogenases, which replaces a phenylalanine present in O_2-sensitive enzymes (except for the *Av* hydrogenase[28]) (Figures S5 and S6). Blocking the [3Fe4S] cluster to solvent accessibility might influence the electrochemical potential of the cluster.[29] In the case of O_2-tolerant enzymes only *Ec*Hyd-1 shows major differences in amino acid composition of the gas tunnel network. The bulkier amino acids $F203_L$, $M129_L$, and $I132_L$ block the gas tunnel B (Figure 4, Table S7).[24] The main gas tunnel A has a bottleneck radius of 1.2 Å and is 32 Å in length.

Based on the positioning of the krypton atoms in the hydrophobic tunnels of *Re*MBH and the corresponding theoretical prediction of gas tunnel routes in both O_2-sensitive and O_2-tolerant [NiFe] hydrogenases, we hypothesize that the O_2-sensitive enzymes have a more complex tunnel network and more openings than their O_2-tolerant counterparts. This may lead to increased gas diffusion rates for both H_2 and inhibitory gases such as O_2 and CO. In comparison, the gas tunnels of O_2-tolerant hydrogenases seem narrow and have fewer openings. This property presumably limits the gas flow rate to the catalytic center, which in turn may contribute to the remarkable O_2 tolerance of these enzymes. We would like to emphasize that the results of this study are based on the analyses of static crystal structures. However, dynamic changes of the gas tunnel networks are likely affecting gas access to the active site, and molecular dynamics (MD) simulations represent an invaluable tool to investigate such effects in future studies. Our krypton-pressurized *Re*MBH crystal structure therefore represents an excellent starting point for comprehensive MD simulations in order to investigate gas diffusion processes in relation to continuous changes in the gas tunnel diameters. In addition, investigating *Re*MBH variants providing gas tunnel modifications could be helpful to further prove our hypothesis.

Experimental Section

*Re*MBH was produced and purified as described previously.[17] Optimized *Re*MBH crystals were obtained using sitting-drop vapor diffusion[17,18] and were krypton-pressurized with a high-pressure cooling system.[30] A detailed description of all experiments can be found in the Supporting Information.

Acknowledgements

We are grateful to the scientific staff of the European Synchrotron Radiation Facility (ESRF, Grenoble, France) at beamlines ID14-1, ID23-1, ID23-2, ID14-4, and ID29, where the data were collected, for continuous support. We like to thank Ciara Lally for critically reading the manuscript. This work was supported by grants from the Deutsche Forschungsgemeinschaft (SFB740-B6 to P.S.; SFB1078-B6 to P.S.), ESRF (to P.v.d.L., D.v.S., and P.C., and P.S.), DFG Cluster of Excellence "Unifying Concepts in Catalysis" (Research Field E3-1 to J.K., A.S., S.F., O.L., and P.S.).

Keywords: hydrogenases · krypton · metalloenzymes · oxygen · structural biology

How to cite: *Angew. Chem. Int. Ed.* **2016**, *55*, 5586–5590
Angew. Chem. **2016**, *128*, 5676–5680

[1] L. J. Kingsley, M. A. Lill, *Proteins Struct. Funct. Bioinf.* **2015**, *83*, 599–611.
[2] F. M. Raushel, J. B. Thoden, H. M. Holden, *Acc. Chem. Res.* **2003**, *36*, 539–548.
[3] A. Weeks, L. Lund, F. M. Raushel, *Curr. Opin. Chem. Biol.* **2006**, *10*, 465–472.
[4] N. Hayakawa, T. Kasahara, D. Hasegawa, K. Yoshimura, M. Murakami, T. Kouyama, *J. Mol. Biol.* **2008**, *384*, 812–823.
[5] J. Saam, I. Ivanov, M. Walther, H. G. Holzhütter, H. Kuhn, *Proc. Natl. Acad. Sci. USA* **2007**, *104*, 13319–13324.
[6] J. W. Murray, J. Barber, *J. Struct. Biol.* **2007**, *159*, 228–237.
[7] A. Guskov, J. Kern, A. Gabdulkhakov, M. Broser, A. Zouni, W. Saenger, *Nat. Struct. Mol. Biol.* **2009**, *16*, 334–342.
[8] A. Gabdulkhakov, A. Guskov, M. Broser, J. Kern, F. Müh, W. Saenger, A. Zouni, *Structure* **2009**, *17*, 1223–1234.
[9] Y. Montet, P. Amara, A. Volbeda, X. Vernede, E. C. Hatchikian, M. J. Field, M. Frey, J. C. Fontecilla-Camps, *Nat. Struct. Biol.* **1997**, *4*, 523–526.
[10] C. Zirngibl, W. van Dongen, B. Schwörer, R. von Bünau, M. Richter, A. Klein, R. K. Thauer, *Eur. J. Biochem.* **1992**, *208*, 511–520.
[11] W. Lubitz, H. Ogata, O. Rüdiger, E. Reijerse, *Chem. Rev.* **2014**, *114*, 4081–4148.
[12] J. C. Fontecilla-Camps, A. Volbeda, C. Cavazza, Y. Nicolet, *Chem. Rev.* **2007**, *107*, 4273–4303.
[13] P. Wulff, C. C. Day, F. Sargent, F. A. Armstrong, *Proc. Natl. Acad. Sci. USA* **2014**, *111*, 6606–6611.
[14] B. Friedrich, J. Fritsch, O. Lenz, *Curr. Opin. Biotechnol.* **2011**, *22*, 358–364.
[15] L. Lauterbach, O. Lenz, *J. Am. Chem. Soc.* **2013**, *135*, 17897–17905.
[16] V. H. Teixeira, C. M. Soares, A. M. Baptista, *Proteins Struct. Funct. Bioinf.* **2008**, *70*, 1010–1022.
[17] J. Fritsch, P. Scheerer, S. Frielingsdorf, S. Kroschinsky, B. Friedrich, O. Lenz, C. M. Spahn, *Nature* **2011**, *479*, 249–252.
[18] S. Frielingsdorf, J. Fritsch, A. Schmidt, M. Hammer, J. Löwenstein, E. Siebert, V. Pelmenschikov, T. Jaenicke, J. Kalms, Y. Rippers, F. Lendzian, I. Zebger, C. Teutloff, M. Kaupp, R. Bittl, P. Hildebrandt, B. Friedrich, O. Lenz, P. Scheerer, *Nat. Chem. Biol.* **2014**, *10*, 378–385.
[19] J. C. Fontecilla-Camps, P. Amara, C. Cavazza, Y. Nicolet, A. Volbeda, *Nature* **2009**, *460*, 814–822.
[20] B. Kozlíková, E. Šebestová, V. Šustr, J. Brezovský, O. Strnad, L. Daniel, D. Bednář, A. Pavelka, M. Maňák, M. Bezděka, P. BeneŠ, M. Kotry, A. W. Gora, J. Damborský, J. Sochor, *Bioinformatics* **2014**, *30*, 2684–2685.
[21] C. Greening, A. Biswas, C. R. Carere, C. J. Jackson, M. C. Taylor, M. B. Stott, G. M. Cook, S. E. Morales, *ISME J.* **2016**, *10*, 761–777.
[22] Y. Shomura, K. S. Yoon, H. Nishihara, Y. Higuchi, *Nature* **2011**, *479*, 253–256.
[23] P. M. Matias, C. M. Soares, L. M. Saraiva, R. Coelho, J. Morais, J. Le Gall, M. A. Carrondo, *J. Biol. Inorg. Chem.* **2001**, *6*, 63–81.
[24] A. Volbeda, P. Amara, C. Darnault, J. M. Mouesca, A. Parkin, M. M. Roessler, F. A. Armstrong, J. C. Fontecilla-Camps, *Proc. Natl. Acad. Sci. USA* **2012**, *109*, 5305–5310.
[25] H. Ogata, S. Hirota, A. Nakahara, H. Komori, N. Shibata, T. Kato, K. Kano, Y. Higuchi, *Structure* **2005**, *13*, 1635–1642.
[26] F. Leroux, S. Dementin, B. Burlat, L. Cournac, A. Volbeda, S. Champ, L. Martin, B. Guigliarelli, P. Bertrand, J. C. Fontecilla-Camps, M. Rousset, C. Léger, *Proc. Natl. Acad. Sci. USA* **2008**, *105*, 11188–11193.
[27] T. Buhrke, O. Lenz, N. Krauss, B. Friedrich, *J. Biol. Chem.* **2005**, *280*, 23791–23796.
[28] H. Ogata, P. Kellers, W. Lubitz, *J. Mol. Biol.* **2010**, *402*, 428–444.
[29] A. Dey, F. E., Jr. Jenney, M. W. Adams, E. Babini, Y. Takahashi, K. Fukuyama, K. O. Hodgson, B. Hedman, E. I. Solomon, *Science* **2007**, *318*, 1464–1468.
[30] P. van der Linden, F. Dobias, H. Vitoux, U. Kapp, J. Jacobs, S. Mc Sweeney, C. Mueller-Dieckmann, P. Carpentier, *J. Appl. Crystallogr.* **2014**, *47*, 584–592.

Received: September 24, 2015
Revised: December 17, 2015
Published online: February 23, 2016

Angewandte Chemie
Eine Zeitschrift der Gesellschaft Deutscher Chemiker

Supporting Information

Krypton Derivatization of an O_2-Tolerant Membrane-Bound [NiFe] Hydrogenase Reveals a Hydrophobic Tunnel Network for Gas Transport

*Jacqueline Kalms, Andrea Schmidt, Stefan Frielingsdorf, Peter van der Linden, David von Stetten, Oliver Lenz, Philippe Carpentier, and Patrick Scheerer**

anie_201508976_sm_miscellaneous_information.pdf

Jacqueline Kalms[a], Andrea Schmidt[a], Dr. Stefan Frielingsdorf[b], Peter van der Linden[c],

Dr. David von Stetten[c], Dr. Oliver Lenz[b], Dr. Philippe Carpentier[c], and Dr. Patrick Scheerer[a],*

[a] Institut für Medizinische Physik und Biophysik (CCO), Group Protein X-ray Crystallography and Signal Transduction, Charité – Universitätsmedizin Berlin, Charitéplatz 1, 10117 Berlin, Germany

[b] Institut für Chemie, Sekr. PC14, Technische Universität Berlin, Straße des 17. Juni 135, 10623 Berlin, Germany

[c] ESRF, 71 Avenue des Martyrs, Grenoble Cedex 9, 38043, France

*To whom correspondence should be addressed: patrick.scheerer@charite.de

Table of contents

Experimental Section

Protein expression and purification. Native *Re*MBH was expressed and purified in the as-isolated (air-oxidized) state as described elsewhere.[1,2]. In brief, *R. eutropha* strain HF649 was grown in modified FGN medium containing 0.05 % (w/v) fructose and 0.4 % (w/v) glycerol. Buffled Erlenmeyer flasks were filled to 80 % of their capacity and shaken at 120 rpm at 30 °C for up to 10 days. The cell pellets were resuspended in 50 mM potassium phosphate (K-PO_4) buffer pH 7.2 containing Complete EDTA-free protease inhibitor mixture (Roche), and DNase I (Roche). The cell suspension was subsequently disrupted in a French pressure cell (SLM Aminco) via two passages at 1,241 bar. Cell debris was removed by low-speed centrifugation (4,000 g at 4 °C for 20 min). Subsequently, $K_3[Fe(CN)_6]$ was added to a final concentration of 50 mM, and membrane and soluble fractions were separated by ultracentrifugation (100,000 g at 4 °C for 60 min). The membrane pellet was resuspended in an appropriate volume of buffer (50 mM K-PO_4, pH 7.2; 150 mM NaCl) and ultra-centrifuged again (100,000 g at 4 °C, 35 min). Membrane proteins were solubilized in 10 ml solubilization buffer (50 mM K-PO_4, pH 7.2; 150 mM NaCl; 2 % (w/v) Triton X-114; complete protease inhibitor mixture) per 1 g of membrane pellet and the suspension was then stirred on ice for 2 h. After ultracentrifugation (100,000 g, 4 °C, 40 min), the supernatant was loaded on Strep-Tactin Superflow columns (IBA, Göttingen, Germany). The columns were washed with 10 bed volumes of washing buffer (50 mM K-PO4, 150 mM NaCl), and proteins were eluted with three bed volumes of elution buffer (washing buffer, 3 mM desthiobiotin, 10 % (w/v) glycerol). MBH-containing fractions were pooled and concentrated using a centrifugal filter device (Amicon Ultra-15 (PL-30), Millipore). Aliquots of the resulting concentrate were frozen in liquid N_2 and stored therein. Protein concentrations were determined using a BCA kit (Pierce, USA) using BSA as standard.

Crystallization. *Re*MBH was crystallized with a concentration of about 10 mg ml^{-1} at 277 K. Crystallization was performed with the sitting-drop vapour diffusion method in 24-well Linbro plates (Jena Bioscience). The reservoir solution contained 20-30 % polyethylene glycol 3350, 100 mM Bis-(2-hydroxy-

ethyl)-amino-tris(hydroxymethyl)-methane buffer at pH 5.5 - 6.5. Precipitants and protein solution were mixed in different ratios (7 - 8 µl) into micro-bridges (Hampton Research). After 2-4 days the dark-brown *Re*MBH crystals were directly flash cooled in liquid nitrogen.

High-pressure krypton derivatization. Krypton derivatization was performed using a high-pressure cooling system recently developed at the ESRF in Grenoble.[3] The crystals were harvested with specific pluggable sample supports (MiTeGen, Ithaca) and transferred into the high pressure sample cell. After 10 min of pressurization under 80 bar of krypton gas, the krypton-containing crystals were directly flash-cooled, then depressurized and handled in liquid nitrogen.[3]

Structure analysis. Diffraction data was collected at the synchrotron radiation facility ERSF in Grenoble, France. Several native and anomalous data sets were collected with the program MXCUBE[4] at the tunable beamline ID 23-1[5] with a PILATUS 6M-F detector at a wavelength of λ = 0.976 Å and λ = 0.861 Å, respectively. An optimized data collection strategy was automatically calculated employing the program EDNA.[6] The collection was performed at 100 K, a detector distance of 200 - 400 mm and a rotation increment 0.1° with an exposure time of 0.04 s for each frame. The images of the best data sets were indexed, integrated and scaled using the XDS program package and the CCP4 program SCALA.[7,8] Crystals belong to orthorhombic space group $P2_12_12_1$ (approximately unit cell constants: a = 73 Å, b = 96 Å, c = 120 Å; $\alpha = \beta = \gamma = 90.00°$). Supplementary Table S1 summarizes the statistics for crystallographic data collection and structural refinement. Initial phases for *Re*MBH were obtained by molecular replacement using the structure of native *Re*MBH (PDB entry 4IUC) as initial search model. Molecular replacement was achieved through the CCP4 program PHASER.[9,10] Subsequently, several refinement strategies (real-space refinement, individual B-factors, occupancies) as well as simulated-annealing and search for water molecules are calculated with the program PHENIX.[11] The anomalous electron density was calculated with the program FFT of the CCP4 package. The crystal structure was finalized by the CCP4 program REFMAC5.[12] Manual rebuilding of the krypton-derivatized *Re*MBH model and electron density interpretation was performed after each refinement cycle using the program COOT.[13] The final models,

native and anomalous, have agreement factors R_{free} / R_{work} of 15.1 % / 13.3 % and 16.9 % / 13.1 %, respectively.[14] Structure validation was performed with the programs of the RCSB PDB Validation server[15], Molprobity[16] and WHAT IF server[17]. All molecular graphics representations were created using *Py*MOL[18].

Caver tunnel analysis. The *Caver*[19] program was used as *Py*MOL plugin. The settings in the program have been changed manually. The initial starting point (NH_2 of the guanidine-group of the arginine, e.g. $R530_L$ for *Re*MBH), shell depth (2 Å), shell radius (3 Å), cluster threshold (3.5 Å) and the desired radius (5 Å) maintained constant for all calculations. The minimum probe radius varied from 1.2 - 1.6 Å and calculations were performed in 0.1 Å steps. The maximum distance was adjusted from 3 Å to 4 Å with an increasing probe radius and up to 9 Å in the amino acid substitutions of the proposed active site gate of *Df*-hydrogenase. The maximum distance specifies the maximal distance of the tunnel calculation starting point from the initial starting point (arginine). The bottleneck radius is the narrowest part of a given tunnel and corresponds to the minimum probe radius. All tunnel results (quantity, bottleneck radius, length and maximum distance) of the different crystal structures are listed in the Supplementary Tables S4 to S6.

Supplementary Table S1. Data collection and refinement statistics.

	KR_native (PDB entry 5D51)	KR_anomalous
Data collection		
Beamline	ESRF; ID23.1 (Grenoble, France)	
Space group	*P 2₁ 2₁ 2₁*	*P 2₁ 2₁ 2₁*
Unit cell (a, b, c [Å]; α, β, γ [°])	73.39, 95.57, 119.75; 90.00, 90.00, 90.00	73.55, 95.71, 120.21; 90.00, 90.00, 90.00,
Wavelength [Å]	0.976	0.861
R_{pim} [20]	0.030 (0.324)	0.019 (0.026)
R_{merge} [20]	0.073 (0.796)	0.039 (0.057)
I/σ (I)[21]	12.2 (2.3)	32.4 (22.0)
Completeness [%]	99.2 (98.3)	99.7 (98.7)
Redundancy	6.8 (6.9)	6.6 (6.9)
SigAno		0.8
Refinement		
Resolution [Å]	47.79 - 1.47 (1.55 – 1.47)*	47.85 - 2.52 (2.65 – 2.52)*
R_{work} [%]	13.3	13.1
R_{free} [%]	15.1	16.9
No. of krypton atoms	19	18
Ramachandran favoured [%][22]	97.8	97.4
Ramachandran allowed [%][22]	2.2	2.6
Ramachandran outlier [%][22]	0.0	0.0

*Number of crystals for native and anomalous data set: 1

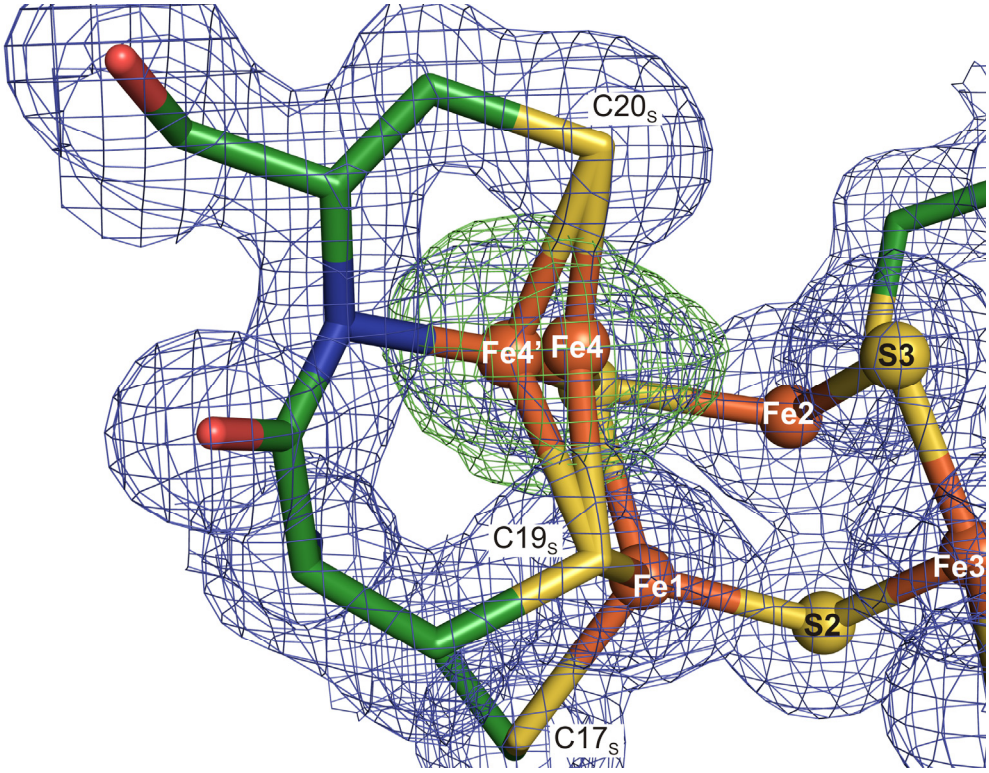

Supplementary Figure S1. Double conformation of the shifting iron ion, Fe4, in *Re*MBH. The positive *Fo-Fc* electron density map calculated without the proximal cluster and contoured at 3 σ is shown as green mesh. The Fe4 is coordinated by C19s and C20s and the backbone nitrogen of C20s. Final 2*Fo-Fc* electron density map contoured at 1 σ (blue mesh) is illustrated for the proximal cluster. The cluster structure is represents no mixture of the previously reported H_2-reduced and oxidized state 2, because both Fe4 positions in the current structure are close to the position found in the oxidized state 2 crystal structure.

Supplementary Table S2. Krypton atoms. 19 Krypton atoms with single and double conformation and various occupancies in the crystal structure of *Re*MBH after krypton derivatization (PDB entry 5D51)

Krypton sites	*Occupancy [%]*
1	45 / 45
2	60
3	84
4	55
5	60
6	25
7	35
8	35
9	55 / 25
10	45
11	45
12	45 / 25
13	35 / 20
14	30
15	30
16	40
17	45
18	25
19	15

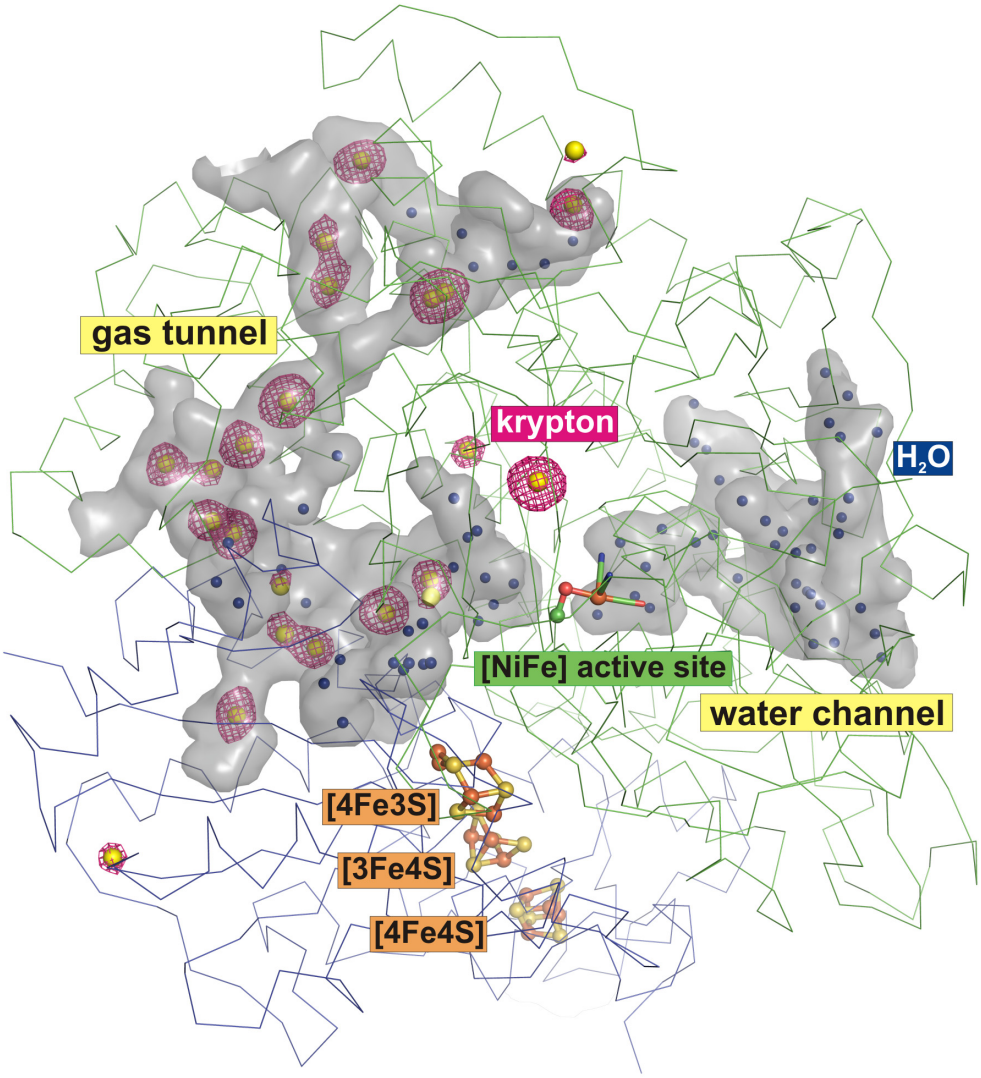

Supplementary Figure S2. Ribbon representation of the air-oxidized krypton-derivatized *Re*MBH (PDB entry 5D51). 19 krypton atoms (yellow) shown as spheres and an anomalous electron density map contoured at 3.5 σ (coloured in magenta). The [NiFe] active site and the three [FeS]-clusters are shown as ball and stick. The channels and tunnels are depicted as grey surfaces (calculated with *Py*MOL) and water molecules as blue spheres.

Supplementary Table S3. Theoretical radii of atoms and molecules.

Atom	*Covalent radius [pm]*[23]	*Molecular covalent radius [pm]*[24]	*van der Waals radius [pm]*[25]
Oxygen	66	$57_{\text{double bond}}$	152
Hydrogen	31	$32_{\text{single bond}}$	120
Krypton	116		202
Xenon	140		216

Supplementary Table S4. Gas tunnel comparison of O_2-tolerant [NiFe]-hydrogenases.

Hydrogenase	*PDB entry*	*Total number of gas tunnels*	*Number of gas tunnels referred to bottleneck radius*	*Bottleneck radius [Å]*	*Length [Å]*	*Maximum distance [Å]*
MBH from *Ralstonia eutropha*	**3RGW**[1] H_2-reduced	2	1 1	1.3 1.5	52.7 30.9	3 4
	4IUC[26] air-oxidized	2	1 1	1.3 1.5	51.1 28.9	3 4
	5D51(this study) air-oxidized	2	1 1	1.3 1.5	50.4 29.9	3 4
MBH from *Hydrogenovibrio marinus*	**3AYX**[27] H_2-reduced	3	1 1 1	1.2 1.3 1.4	68.7 54.4 35.5	3 3 3
	3AYZ[27] air-oxidized	4	1 2 1	1.2 1.3 1.4	66.2 57.0 / 37.7 35.7	3 3 3
*Ec*Hyd-1 from *Escherichia coli*	**3UQY**[28] H_2-reduced	1	1	1.2	32.1	3
	3USE[28] air-oxidized	2	2	1.2	32.2 / 30.9	3
	4UE3not published $R509_LK$ mutant	2	2	1.2	34.4 / 34.3	3
Hyd-5 from *Salmonella enterica*	**4C3O**[29] reduced state	2	1 1	1.2 1.5	75.6 32.2	3 4

Supplementary Table S5. Gas tunnel comparison of O_2-sensitive [NiFe]-hydrogenases.

Hydrogenase	*PDB entry*	*Total gas number of tunnels*	*Number of gas tunnels referred to bottleneck radius*	*Bottleneck radius [Å]*	*Length [Å]*	*Maximum distance [Å]*
MBH from *Allochromatium vinosum*	**3MYR**[30] oxidized state	5	2 1 1 1	1.2 1.3 1.4 1.5	76.4 / 59.1 32.6 49.5 27.4	3 3 3 4
MBH from *Desulfovibrio gigas*	**2FRV**[31] oxidized state	5	2 2 1	1.3 1.4 1.6	68.3 / 35.1 66.9 / 52.0 36.5	3 3 4
MBH from *Desulfovibrio desulfuricans*	**1E3D**[32] oxidized state	2	1 1	1.2 1.3	68.5 31.7	3 3
MBH from *Desulfovibrio vulgaris* str. 'Miyazaki F'	**1WUK**[33] oxidized state	5	1 3 1	1.2 1.3 1.4	37.9 51.4 / 33.6 / 31.5 59.9	3 3 4
	1WUL[33] reduced state	5	1 3 1	1.2 1.3 1.4	37.1 49.2 / 31.8 / 30.0 65.2	3 3 4
MBH from *Desulfovibrio fructosovorans*	**4URH**[34] partially oxidized	6	1 3 1 1	1.2 1.3 1.4 1.5	74.0 62.2 / 61.8 / 33.6 41.1 47.2	3 3 3 4

Supplementary Table S6. Gas tunnel comparison of O_2-sensitive *Desulfovibrio fructosovorans* active site gate substitutions.

Amino acid substitutions	*PDB entry*	*Total number of gas tunnels*	*Number of gas tunnels referred to bottleneck radius*	*Bottleneck radius [Å]*	*Maximum distance [Å]*
Ni-A Ni-SOX $L122_LA$	**4UQL**[34]	5	1 2 2	1.2 1.3 1.4	3 3 3
$L122_LA$ after air exposure	**4UQP**[34]	5	1 1 3	1.2 1.3 1.4	3 3 3
$V74_LM$	**3H3X**[35]	6	6	1.2	3
$V74_LM$, $L122_LM$	**3CUR**[36]	5	2 2 1	1.2 1.3 1.4	9 9 9
$V74_LI$, $L122_LF$	**3CUS**[36]	7	2 4 1	1.2 1.3 1.4	9 9 9

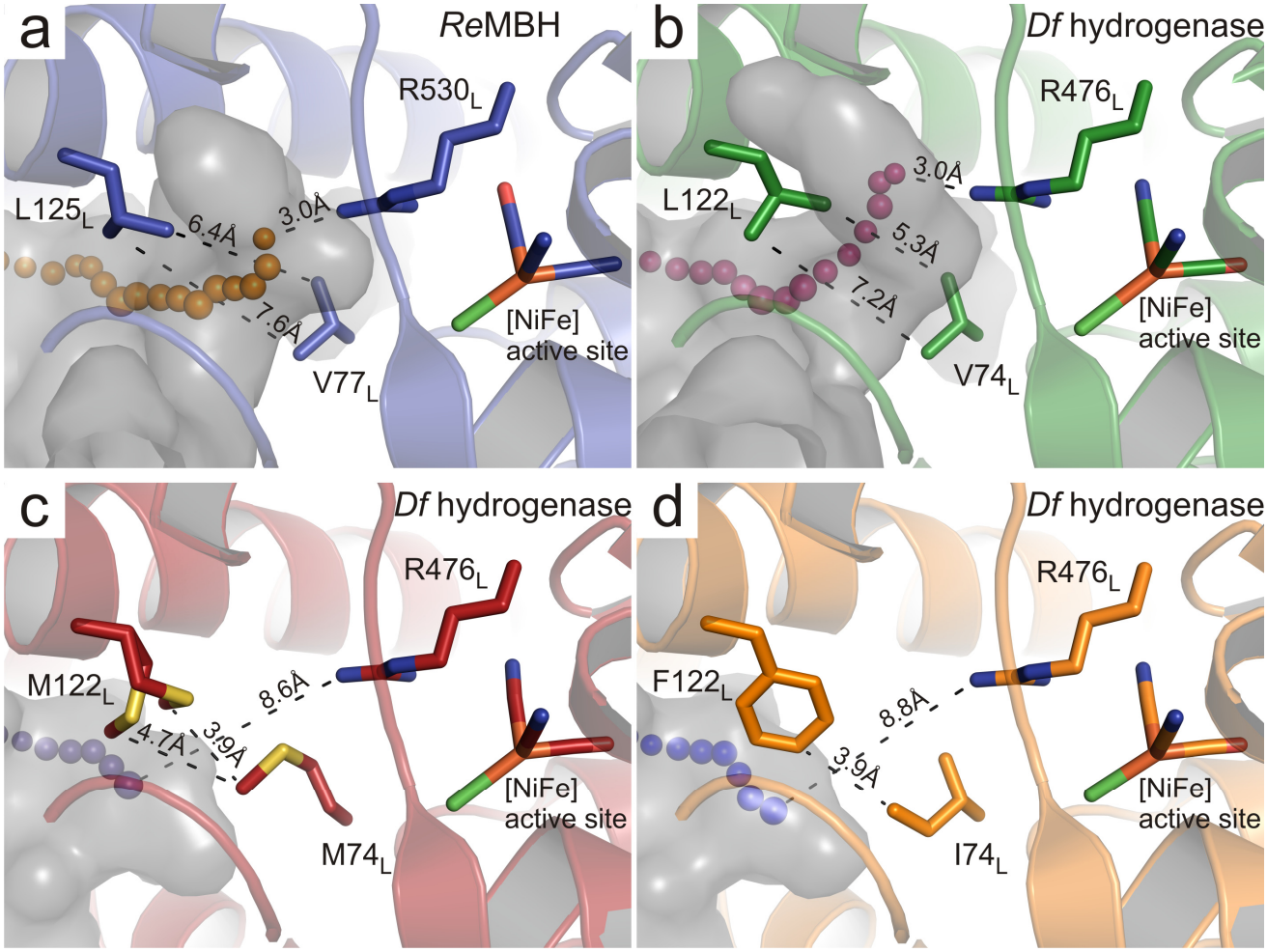

Supplementary Figure S3. Distances of active site gate amino acids and distances between initial and calculation starting point (*Caver*) of O_2-tolerant *Re*MBH and O_2-sensitive *Df*-hydrogenase. (a) *Re*MBH (PDB entry 3RGW). (b) native *Df*-hydrogenase (PDB entry 4URH). (c) $M74_L/M122_L$ mutant *Df* hydrogenase (PDB entry 3CUR). (d) $I74_L/F122_L$ mutant *Df*-hydrogenase (PDB entry 3CUS). Active site gate amino acids, [NiFe] active site and arginine (*Caver*: initial starting point) are illustrated as sticks. Calculation starting point is depicted as first sphere of a tunnel chain. Surfaces were calculated with *Py*MOL and are shown in grey.

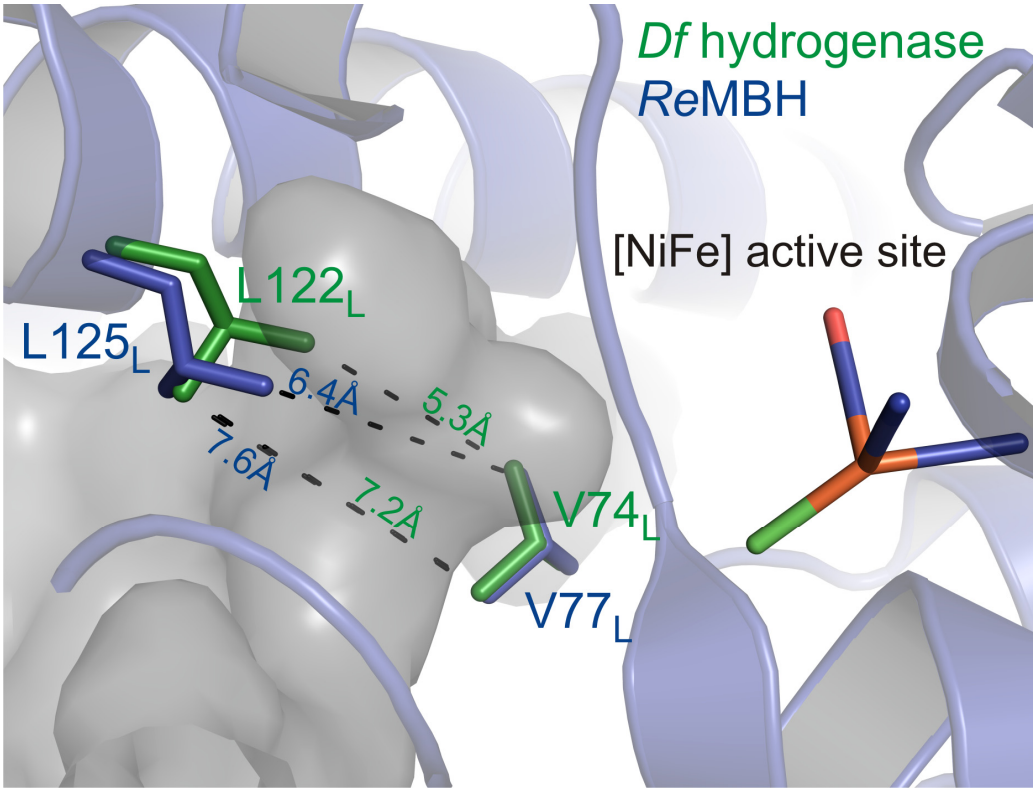

Supplementary Figure S4. Superposition of active site gate amino acids $V77_L$ and $L125_L$ of *Re*MBH (PDB entry 3RGW in blue) and $V74_L$ and $L122_L$ of *Df*-hydrogenase (PDB entry 4URH in green) with distances. Cartoon representation of O_2-tolerant *Re*MBH. Active site gate amino acids and [NiFe] active site are illustrated as sticks. Surfaces were calculated with *Py*MOL and are shown in grey.

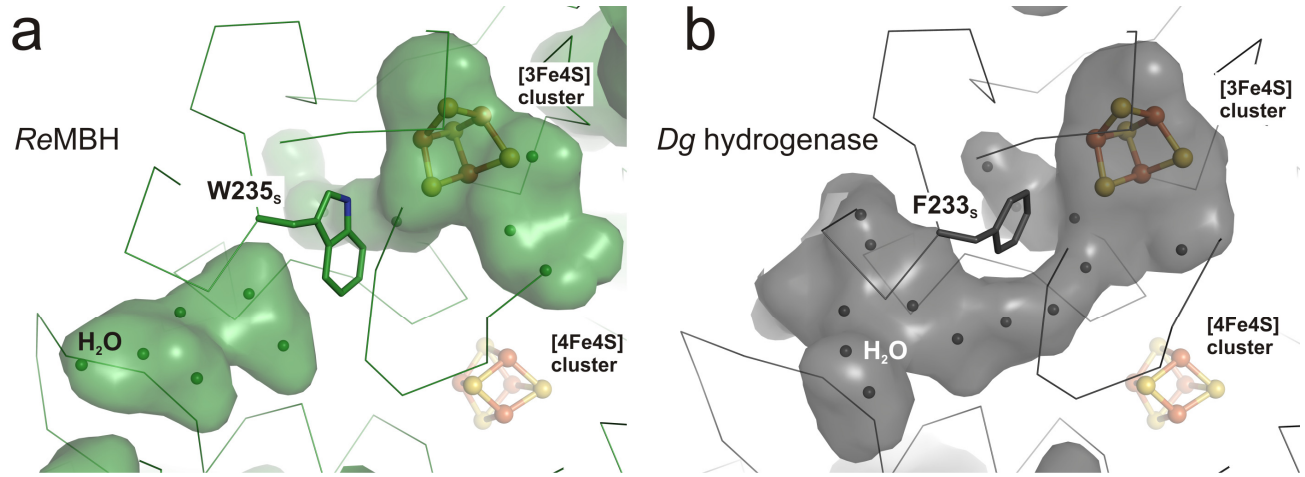

Supplementary Figure S5. Surface representation of (a) O_2-tolerant *Re*MBH (PDB entry 3RGW, coloured in green) and (b) O_2-sensitive *Dg*-hydrogenase (PDB entry 2FRV, coloured in grey). The medial [3Fe4S] and distal [4Fe4S] clusters are depicted in ball and stick representation. Water molecules are shown as spheres. $W235_S$ from O_2-tolerant *Re*MBH shows a blocking of the hydrophilic medial cluster tunnel compared to O_2-sensitive *Dg*-hydrogenase.

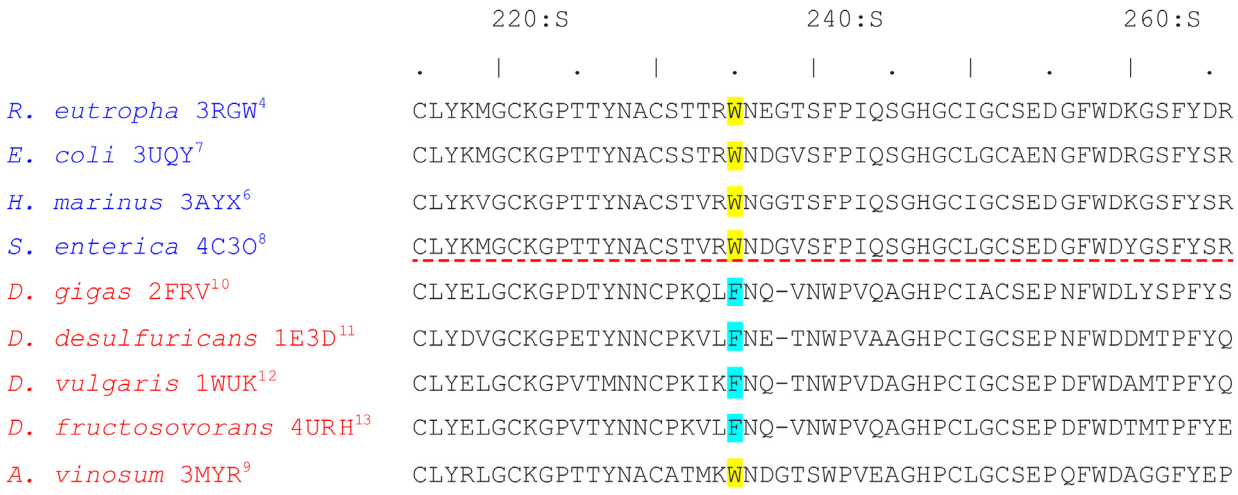

Supplementary Figure S6. Small subunit (215-266 aa) sequence alignment. Alignment section of all analyzed O_2-tolerant (blue) and O_2-sensitive (red) [NiFe]-hydrogenases, which contain either a tryptophan (yellow) or a phenylalanine (blue) at the position of the medial cluster tunnel, respectively (except of O_2-sensitve *Av*-hydrogenase). The blocking of the medial cluster tunnel is exemplarily shown for *Re*MBH and *Dg*-hydrogenase in Supplementary Figure 5.

Supplementary Table S7. *E. coli* amino acids (yellow highlighted) blocking gas tunnel B. Three different amino acids involved in gas tunnel B formation (*Re*MBH nomenclature) in the large subunit of O_2-tolerant and O_2-sensitive [NiFe]-hydrogenases.

O_2-tolerant				*O_2-sensitive*				
R. eutropha 3RGW[1]	*E. coli 3UQY*[28]	*H. marinus 3AYX*[27]	*S. enterica 4C3O*[29]	*A. vinosum 3MYR*[30]	*D. gigas 2FRV*[31]	*D. desulfuricans 1E3D*[32]	*D. vulgaris 1WUK*[33]	*D. fructosovorans 4URH*[34]
L128	M129	L129	L129	L1114	L118	L124	L134	L125
V131	I132	V132	V132	V1117	V121	V127	V137	V128
V203	F203	V204	V203	V1188	T193	T199	T209	T202

Supplementary Figure S7. Large subunit sequence alignment. Alignment from O_2-tolerant (blue) and O_2-sensitive (red) hydrogenases with amino acids of the *Re*MBH hydrophobic gas tunnel (yellow).

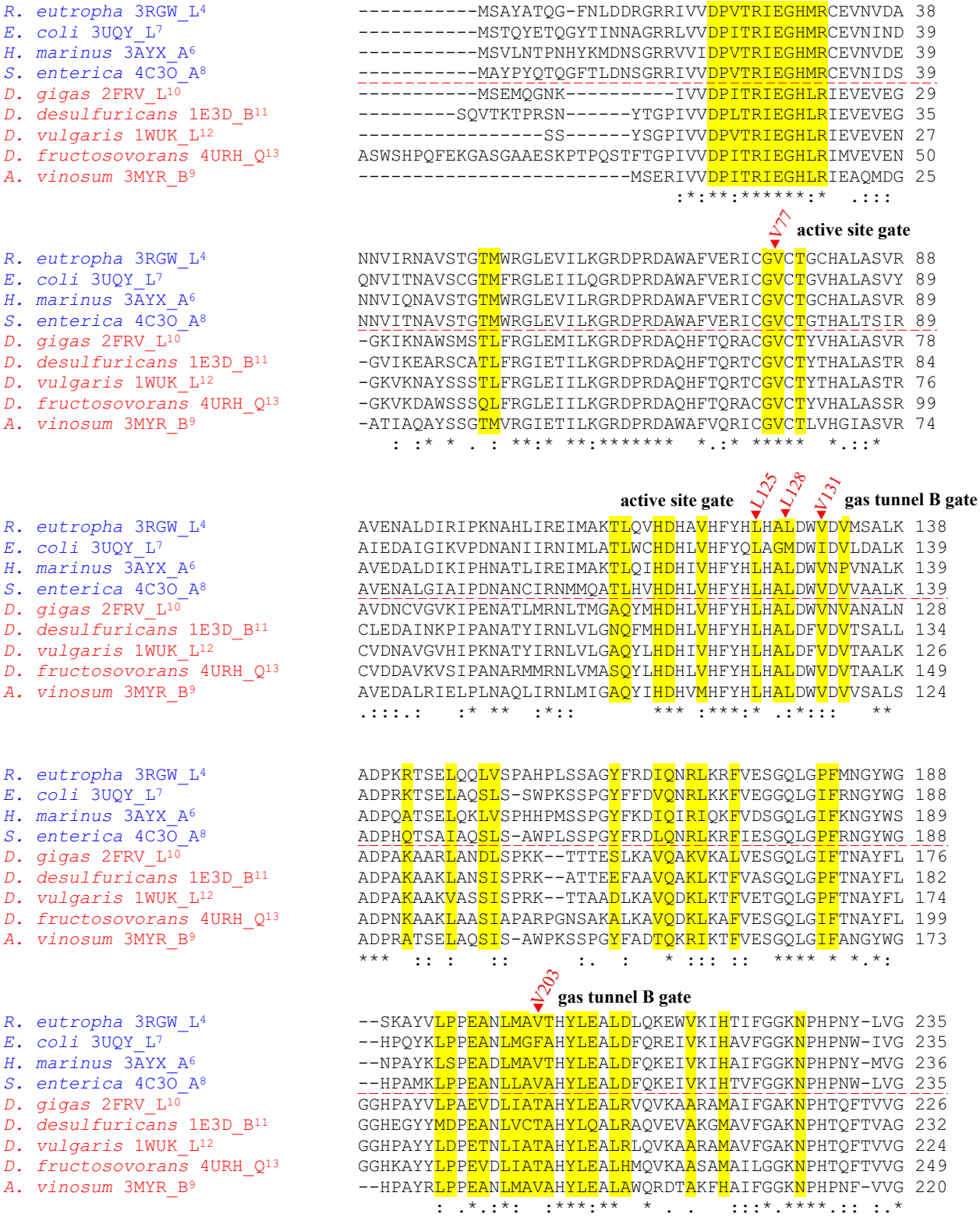

```
R. eutropha 3RGW_L[4]          GVPCAINLDGIGAASAPVNMERLSFVKARIDEIIEFNKNVYVPDVLAIGT 285
E. coli 3UQY_L[7]              GMPCAINIDESGAVGA-VNMERLNLVQSIITRTADFINNVMIPDALAIGQ 284
H. marinus 3AYX_A[6]           GVPCAINIDGDMAAGAPINMERLNFVKSLIEQGRTFNTNVYVPDVIAIAA 286
S. enterica 4C3O_A[8]          GVPCAINLDETGAVGA-VNMERLNLVSSIIQKARQFCEQVYLPDVLLIAS 284
D. gigas 2FRV_L[10]            GCTNYDSLRP----------ERIAEFRKLYKEVREFIEQVYITDLLAVAG 266
D. desulfuricans 1E3D_B[11]    GVTCYEALTP----------ERIKQFRELYVKARAFIEEVYIPDLLLVAS 272
D. vulgaris 1WUK_L[12]         GVTCYDALTP----------QRIAEFEALWKETKAFVDEVYIPDLLVVAA 264
D. fructosovorans 4URH_Q[13]   GCSNYQGLTK----------NPLANYLALSKEVCQFVNECYIPDLLAVAG 289
A. vinosum 3MYR_B[9]           GVPSPIDLDSDSALNA----KRLAEVRNLIQSMRTFVDQVYVPDTLAIAG 266
                               * .    :            : :           *  :  :.* : :.

R. eutropha 3RGW_L[4]          LYKQAGWLYGGGLAATNVLDYGEYPNVA----YNKSTDQLPGGAILNGNW 331
E. coli 3UQY_L[7]              FNKP-WSEIGTGLSDKCVLSYGAFPDIAN--DFGEKSLLMPGGAVINGDF 331
H. marinus 3AYX_A[6]           FYR--DWLYGGGLSATNVMDYGAYPKTP----YDKSTDQLPGGAIINGDW 330
S. enterica 4C3O_A[8]          YYKD-WAKIGGGLSSMNLLAYGEFPDNPN--DYSASNLLLPRGAIINGRF 331
D. gigas 2FRV_L[10]            FYKN-WAGIG---KTSNFLTCGEFPTD----EYDLNSRYTPQGVIWGNDL 308
D. desulfuricans 1E3D_B[11]    YYKD-WGKIG---GTNNFMAFGEFPAP--GGERDLNSRWYKPGVIYDRKV 316
D. vulgaris 1WUK_L[12]         AYKD-WTQYG---GTDNFITFGEFPK----DEYDLNSRFFKPGVVFKRDF 306
D. fructosovorans 4URH_Q[13]   FYKD-WGGIG---GTSNYLAFGEFATDDSSPEKHLATSQFPSGVITGRDL 335
A. vinosum 3MYR_B[9]           FYKD-WGERGEGLG--NFLCYGDLPTGAS---LDPATFLFPRGAILDRDL 310
                                 :      *        :  *  .           .     *.:

R. eutropha 3RGW_L[4]          DEVFPVDPRDSQQVQEFVSHSWYKYAD--ESVGLHPWDGVTEPNYVLGAN 379
E. coli 3UQY_L[7]              NNVLPVDLVDPQQVQEFVDHAWYRYPN--DQVGRHPFDGITDPWYNPGD- 378
H. marinus 3AYX_A[6]           GKIHPVDPRDPEQVQEFVTHSWYKYPD--ETKGLHPWDGITEPNYELGSK 378
S. enterica 4C3O_A[8]          DEIHPVDLTAPDEIQEFVTHSWYTYGNGNNDKGLHPWDGLTEPQLVMGEH 381
D. gigas 2FRV_L[10]            SKVDDFN---PDLIEEHVKYSWYEGAG-----AHHPYKGVTKP------- 343
D. desulfuricans 1E3D_B[11]    GSVQPFD---PSKIEEHVRHSWYEG------KARAPFEGETNP------- 350
D. vulgaris 1WUK_L[12]         KNIKPFD---KMQIEEHVRHSWYEGA-----EARHPWKGQTQP------- 341
D. fructosovorans 4URH_Q[13]   GKVDNVD---LGAIYEDVKYSWYAPGG----DGKHPYDGVTDP------- 371
A. vinosum 3MYR_B[9]           STIHEVDLEATGEIQEFVNHSWYEYSVG-NDRGLHPYEGQTNLEYDRRG- 358
                                 :  .:      : * * ::**         .  *:.* *.

R. eutropha 3RGW_L[4]          TKGTRTRIEQIDESAKYSWIKSPRWRGHAMEVGPLSRYILAYAHARSGNK 429
E. coli 3UQY_L[7]              VKGSDTNIQQLNEQERYSWIKAPRWRGNAMEVGPLARTLIAYHKG----- 423
H. marinus 3AYX_A[6]           TKGSRTNIIEIDESAKYSWIKSPRWRGHAVEVGPLARYILAYAQG----- 423
S. enterica 4C3O_A[8]          YKGTKTFIEQVDESAKYSWIKSPRWKGHAMEVGPLARYLIGYHQN----- 426
D. gigas 2FRV_L[10]            ------KWTEFHGEDRYSWMKAPRYKGEAFEVGPLASVLVAYAKK----- 382
D. desulfuricans 1E3D_B[11]    ------HFTFMGDTDKYSWNKAPRYDGHAVETGPLAQMLVAYGHN----- 389
D. vulgaris 1WUK_L[12]         ------KYTDLHGDDRYSWMKAPRYMGEPMETGPLAQVLIAYSQG----- 380
D. fructosovorans 4URH_Q[13]   ------KYTKLDDKDHYSWMKAPRYKGKAMEVGPLARTFIAYAKG----- 410
A. vinosum 3MYR_B[9]           --GVAPPYKQLDVSDGYSWLKAPRWKGRSVEVGPLARVLMLYATG----- 401
                                         .     *** *:**: *...*.***:  :: *

R. eutropha 3RGW_L[4]          YAERPKEQLEYSAQMINSAIPKALGLPETQYT-LKQLLPSTIGRTLARAL 478
E. coli 3UQY_L[7]              -----DAATVESVDRMMSALNLPLSG----------IQSTLGRILCRAH 457
H. marinus 3AYX_A[6]           -VEYVKTQVHTSLNRFN-AVCRLLDPNHKDITDLKAFLGSTIGRTLARAL 471
S. enterica 4C3O_A[8]          -----KPEFKEPVDQLLSVLKLPKEA----------LFSTLGRTAARAL 460
D. gigas 2FRV_L[10]            -----HEPTVKAVDLVLKTLGVGPEA----------LFSTLGRTAARGI 416
D. desulfuricans 1E3D_B[11]    -----HKTIKPTIDAVLGKLNLGPEA----------LFSTLGRTAARGI 423
D. vulgaris 1WUK_L[12]         -----HPKVKAVTDAVLAKLGVGPEA----------LFSTLGRTAARGI 414
D. fructosovorans 4URH_Q[13]   -----QPDFKKVVDMVLGKLSVPATA----------LHSTLGRTAARGI 444
A. vinosum 3MYR_B[9]           -----HDQARELVDSTLSRLDLPVDA----------LYSTLGRTAARAL 435
                                     .      :     :                : **:**  .*.

R. eutropha 3RGW_L[4]          ESQYCGEMMHSDWHDLVANIRAGDTATANVDKWDPATWPLQAKGVGTVAA 528
E. coli 3UQY_L[7]              EAQWAAGKLQYFFDKLMTNLKNGNLATASTEKWEPATWPTECRGVGFTEA 507
H. marinus 3AYX_A[6]           ESEYCGDMMLDDFNQLISNIKNGDSSTANTDKWDPSSWPEHAKGVGTVAA 521
S. enterica 4C3O_A[8]          ESVWAGNTLQYFFDRLMRNLKSGDTATANVTLWEPDTWPTSAKGVGFSEA 510
D. gigas 2FRV_L[10]            QCLTAAQEVEVWLDKLEANVKAG-----KDDLYTDWQYPTESQGVGFVNA 461
D. desulfuricans 1E3D_B[11]    QTLVIAQQMENWLNEYENNIVK------DKQIVEDYAVPTSARGVGFADV 467
D. vulgaris 1WUK_L[12]         ETAVIAEYVGVMLQEYKDNIAKG-----DNVICAPWEMPKQAEGVGFVNA 459
D. fructosovorans 4URH_Q[13]   ETAIVCANMEKWIKEMADSG-AK-----DNTLCAKWEMPEESKGVGLADA 488
A. vinosum 3MYR_B[9]           ESKILVDAMQGWYDGLIANVKSGDTKTFNETLWEPSSWPSRAQGVGIMEA 485
                               :      :    .    .         .         *  ..***   .
```

Supplementary Figure S8. Small subunit sequence alignment. Alignment from O_2-tolerant (blue) and O_2-sensitive (red) hydrogenases with amino acids of the *Re*MBH hydrophobic gas tunnel (yellow).

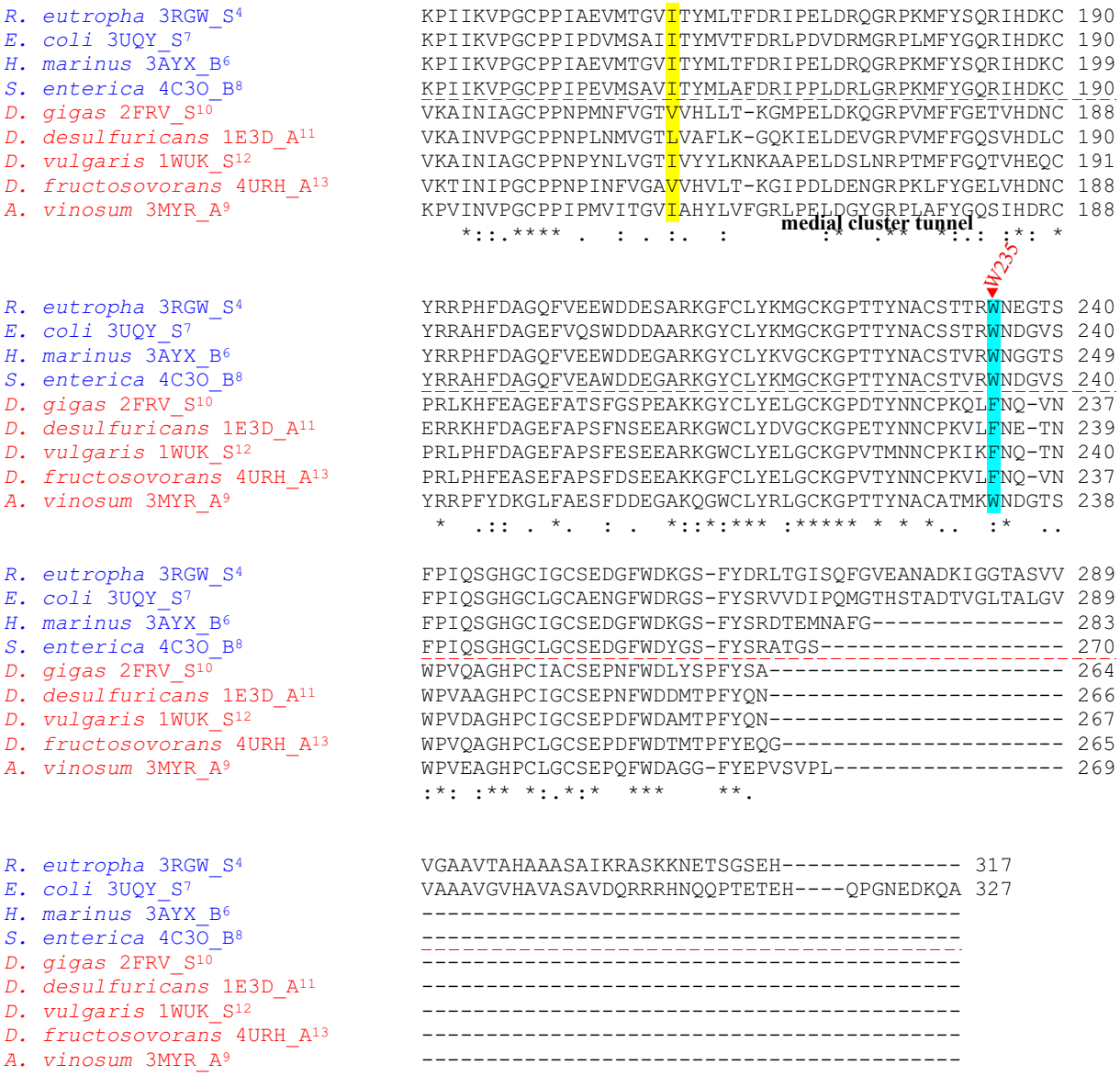
R. eutropha 3RGW_S4 KPIIKVPGCPPIAEVMTGVITYMLTFDRIPELDRQGRPKMFYSQRIHDKC 190
E. coli 3UQY_S7 KPIIKVPGCPPIPDVMSAIITYMVTFDRLPDVDRMGRPLMFYGQRIHDKC 190
H. marinus 3AYX_B6 KPIIKVPGCPPIAEVMTGVITYMLTFDRIPELDRQGRPKMFYSQRIHDKC 199
S. enterica 4C3O_B8 KPIIKVPGCPPIPEVMSAVITYMLAFDRIPPLDRLGRPKMFYGQRIHDKC 190
D. gigas 2FRV_S10 VKAINIAGCPPNPMNFVGTVVHLLT-KGMPELDKQGRPVMFFGETVHDNC 188
D. desulfuricans 1E3D_A11 VKAINVPGCPPNPLNMVGTLVAFLK-GQKIELDEVGRPVMFFGQSVHDLC 190
D. vulgaris 1WUK_S12 VKAINIAGCPPNPYNLVGTIVYYLKNKAAPELDSLNRPTMFFGQTVHEQC 191
D. fructosovorans 4URH_A13 VKTINIPGCPPNPINFVGAVVHVLT-KGIPDLDENGRPKLFYGELVHDNC 188
A. vinosum 3MYR_A9 KPVINVPGCPPIPMVITGVIAHYLVFGRLPELDGYGRPLAFYGQSIHDRC 188
medial cluster tunnel
W235
R. eutropha 3RGW_S4 YRRPHFDAGQFVEEWDDESARKGFCLYKMGCKGPTTYNACSTTRWNEGTS 240
E. coli 3UQY_S7 YRRAHFDAGEFVQSWDDDAARKGYCLYKMGCKGPTTYNACSSTRWNDGVS 240
H. marinus 3AYX_B6 YRRPHFDAGQFVEEWDDEGARKGYCLYKVGCKGPTTYNACSTVRWNGGTS 249
S. enterica 4C3O_B8 YRRAHFDAGQFVEAWDDEGARKGYCLYKMGCKGPTTYNACSTVRWNDGVS 240
D. gigas 2FRV_S10 PRLKHFEAGEFATSFGSPEAKKGYCLYELGCKGPDTYNNCPKQLFNQ-VN 237
D. desulfuricans 1E3D_A11 ERRKHFDAGEFAPSFNSEEARKGWCLYDVGCKGPETYNNCPKVLFNE-TN 239
D. vulgaris 1WUK_S12 PRLPHFDAGEFAPSFESEEARKGWCLYELGCKGPVTMNNCPKIKFNQ-TN 240
D. fructosovorans 4URH_A13 PRLPHFEASEFAPSFDSEEAKKGFCLYELGCKGPVTYNNCPKVLFNQ-VN 237
A. vinosum 3MYR_A9 YRRPFYDKGLFAESFDDEGAKQGWCLYRLGCKGPTTYNACATMKWNDGTS 238
R. eutropha 3RGW_S4 FPIQSGHGCIGCSEDGFWDKGS-FYDRLTGISQFGVEANADKIGGTASVV 289
E. coli 3UQY_S7 FPIQSGHGCLGCAENGFWDRGS-FYSRVVDIPQMGTHSTADTVGLTALGV 289
H. marinus 3AYX_B6 FPIQSGHGCIGCSEDGFWDKGS-FYSRDTEMNAFG---------- 283
S. enterica 4C3O_B8 FPIQSGHGCLGCSEDGFWDYGS-FYSRATGS---------- 270
D. gigas 2FRV_S10 WPVQAGHPCIACSEPNFWDLYSPFYSA---------- 264
D. desulfuricans 1E3D_A11 WPVAAGHPCIGCSEPNFWDDMTPFYQN---------- 266
D. vulgaris 1WUK_S12 WPVDAGHPCIGCSEPDFWDAMTPFYQN---------- 267
D. fructosovorans 4URH_A13 WPVQAGHPCLGCSEPDFWDTMTPFYEQG---------- 265
A. vinosum 3MYR_A9 WPVEAGHPCLGCSEPQFWDAGG-FYEPVSVPL---------- 269
R. eutropha 3RGW_S4 VGAAVTAHAAASAIKRASKKNETSGSEH---------- 317
E. coli 3UQY_S7 VAAAVGVHAVASAVDQRRRHNQQPTETEH----QPGNEDKQA 327
H. marinus 3AYX_B6 ----------
S. enterica 4C3O_B8 ----------
D. gigas 2FRV_S10 ----------
D. desulfuricans 1E3D_A11 ----------
D. vulgaris 1WUK_S12 ----------
D. fructosovorans 4URH_A13 ----------
A. vinosum 3MYR_A9 ----------

Supplementary References

1. Fritsch, J.; Scheerer, P.; Frielingsdorf, S.; Kroschinsky, S.; Friedrich, B.; Lenz, O.; Spahn C. M. The crystal structure of an oxygen-tolerant hydrogenase uncovers a novel iron-sulphur centre. *Nature*. **479(7372),** 249-252 (2011).
2. Goris, T.; Wait, A. F.; Saggu, M.; Fritsch, J.; Heidary, N.; Stein, M.; Zebger, I.; Lendzian, F.; Armstrong, F. A.; Friedrich, B.; Lenz, O. A unique iron-sulfur cluster is crucial for oxygen tolerance of a [NiFe]-hydrogenase. *Nat Chem Biol.* **7(5),** 310-318 (2011).
3. van der Linden, P.; Dobias, F.; Vitoux, H.; Kapp, U.; Jacobs, J.; Mc Sweeney, S.; Mueller-Dieckmann, C. and Carpentier, P. Towards a high-throughput system for high-pressure cooling of cryoprotectant-free biological crystals. *J. Appl. Cryst.* **47,** 584-592 (2014).
4. Gabadinho, J.; Beteva, A.; Guijarro, M.; Rey-Bakaikoa, V.; Spruce, D.; Bowler, M. W.; Brockhauser, S.; Flot, D.; Gordon, E. J.; Hall, D. R.; Lavault, B.; McCarthy, A. A.; McCarthy, J.; Mitchell, E.; Monaco, S.; Mueller-Dieckmann, C.; Nurizzo, D.; Ravelli, R. B.; Thibault, X.; Walsh, M. A.; Leonard, G. A.; McSweeney, S. M. MxCuBE: a synchrotron beamline control environment customised for macromolecular crystallography experiments. *J. Synch. Rad*. **17,** 700-707 (2010).
5. Nurizzo, D.; Mairs, T.; Guijarro, M.; Rey, V.; Meyer, J.; Fajardo, P.; Chavanne, J.; Biasci, J.C.; McSweeney, S. and Mitchell, E. The ID23-1 structural biology beamline at the ESRF. *J. Synchrotron Rad*. **13(Pt 3),** 227-238 (2006).
6. Incardona, M.-F.; Bourenkov, G. P.; Levik, K.; Pieritz, R. A.; Popov, A. N. and Svensson, O. EDNA: a framework for plugin-based applications applied to X-ray experiment online data analysis. *J. Synchrotron Rad*. **16,** 872-879 (2009).
7. Kabsch, W. XDS. *Acta Cryst*. **D66,** 125-132 (2010).
8. CCP4. The CCP4 suite programs for protein crystallography. *Acta Crystallogr. D Biol. Crystallogr*. **50,** 760–763 (1994).
9. Winn, M. D.; Ballard, C. C.; Cowtan, K. D.; Dodson, E. J.; Emsley, P.; Evans, P. R.; Keegan, R. M.; Krissinel, E. B.; Leslie, A. G. W.; McCoy, A.; McNicholas, S. J.; Murshudov, G. N.; Pannu, N. S.; Potterton, E. A.; Powell, H. R.; Read, R. J.; Vagin, A., Wilson, K. S. Overview of the CCP4 suite and current developments. *Acta. Cryst*. **D67,** 235-242 (2011).
10. McCoy, A. J.; Grosse-Kunstleve, R. W.; Adams, P. D.; Winn, M. D.; Storoni, L. C. and Read, R. J. Phaser crystallographic software. *J. Appl. Cryst.* **40,** 658-674 (2007).
11. Adams, P. D.; Afonine, P. V.; Bunkóczi, G.; Chen, V. B.; Davis, I. W.; Echols, N.; Headd, J. J.; Hung, L.-W.; Kapral, G. J.; Grosse-Kunstleve, R. W.; McCoy, A. J.; Moriarty, N. W.; Oeffner, R.; Read, R. J.; Richardson, D. C.; Richardson, J. S.; Terwilliger, T. C. and Zwart, P. H. PHENIX: a comprehensive Python-based system for macromolecular structure solution. *Acta Cryst*. **D66,** 213-221 (2010).
12. Murshudov, G. N.; Vagin, A. A. and Dodson, E. J. Refinement of Macromolecular Structures by the Maximum-Likelihood method. *Acta Cryst*. **D53,** 240-255 (1997).
13. Emsley, P.; Lohkamp, B.; Scott, W.G.; Cowtan, K. Features and development of Coot. *Acta Crystallogr D Biol Crystallogr*. **66(Pt 4),** 486-501 (2010).
14. Brünger, A. T. Free R value: a novel statistical quantity for assessing the accuracy of crystal structures. *Nature*. **355(6359),** 472-475 (1992).

15. Berman, H. M.; Westbrook, J.; Feng, Z.; Gilliland, G.; Bhat, T. N.; Weissig, H.; Shindyalov, I. N.; Bourne, P. E. The Protein Data Bank. *Nucleic Acids Res*. **28(1),** 235-242 (2000).

16. Davis et al. MolProbity: all-atom contacts and structure validation for proteins and nucleic acids. *Nucleic Acids Research*. **35,** W375-W383 (2007).

17. Rodriguez, R.; Chinea, G.; Lopez, N.; Pons, T.; Vriend, G. Homology modeling, model and software evaluation: three related resources. *CABIOS*. **14,** 523-528 (1998).

18. Schrodinger, L.L.C. The PyMOL Molecular Graphics System, Version 1.3.

19. Kozlíková, B.; Šebestová, E.; Šustr, V.; Brezovský, J.; Strnad, O.; Daniel, L.; Bednář, D.; Pavelka, A.; Maňák, M.; Bezděka, M.; Beneš, P.; Kotry, M.; Gora, A. W.; Damborský, J. and Sochor, J. CAVER Analyst 1.0: Graphic tool for interactive visualization and analysis of tunnels and channels in protein structures. *Bioinformatics*. **30(18),** 2684-2685 (2014).

20. Weiss, M.S. Global indicators of X-ray data quality. *J. Appl. Cryst*. **34,** 130-135 (2001).

21. Einspahr, H. M.; Weiss, M. S. Quality indicators in macromolecular crystallography: definitions and applications. In *International Tables for Crystallography*: *Volume F: Crystallography of Biological Macromolecules*. Rossmann, M. G. et al. New York, NY: Wiley, (IUCr Series. International Tables for Crystallography). - ISBN 978-0-470-66078-2, p. 64-74 (2011).

22. Lovell, S.C.; Davis, I.W.; Arendall, W.B., III; de Bakker, P.I.W.; Word, J.M.; Prisant, M.G.; Richardson, J.S. and Richardson, D.C. Structure validation by Ca geometry: f/y and Cb deviation. *Proteins: Structure, Function & Genetics*. **50,** 437-450 (2002).

23. Cordero, B.; Gómez, V.; Platero-Prats, A. E.; Revés, M.; Echeverría, J.; Cremades, E.; Barragán, F.; Alvarez, S. Covalent radii revisited. *Dalton Trans*. **21,** 2832-2838 (2008).

24. Pyykkö, P.; Atsumi, M. Molecular double-bond covalent radii for elements Li-E112. *Chemistry*. **15(46),** 12770-12779 (2009).

25. Bondi, A. van der Waals Volumes and Radii. *J. Phys. Chem*. **68 (3),** 441–451 (1964).

26. Frielingsdorf, S.; Fritsch, J.; Schmidt, A.; Hammer, M.; Löwenstein, J.; Siebert, E.; Pelmenschikov, V.; Jaenicke, T.; Kalms, J.; Rippers, Y.; Lendzian, F.; Zebger, I.; Teutloff, C.; Kaupp, M.; Bittl, R.; Hildebrandt, P.; Friedrich, B.; Lenz, O.; Scheerer, P. Reversible [4Fe-3S] cluster morphing in an O(2)-tolerant [NiFe] hydrogenase. *Nat Chem Biol*. **10(5),** 378-385 (2014).

27. Shomura, Y.; Yoon, K. S.; Nishihara, H.; Higuchi, Y. Structural basis for a [4Fe-3S] cluster in the oxygen-tolerant membrane-bound [NiFe]-hydrogenase. *Nature*. **479(7372),** 253-256 (2011).

28. Volbeda, A.; Amara, P.; Darnault, C.; Mouesca, J. M.; Parkin, A.; Roessler, M. M.; Armstrong, F. A.; Fontecilla-Camps, J. C. X-ray crystallographic and computational studies of the O2-tolerant [NiFe]-hydrogenase 1 from Escherichia coli. *PNAS*. **109(14),** 5305-5310 (2012).

29. Bowman, L.; Flanagan, L.; Fyfe, P. K.; Parkin, A.; Hunter, W. N.; Sargent, F. How the structure of the large subunit controls function in an oxygen-tolerant [NiFe]-hydrogenase. *Biochem J*. **458(3),** 449-458 (2014).

30. Ogata, H.; Kellers, P.; Lubitz, W. The crystal structure of the [NiFe] hydrogenase from the photosynthetic bacterium Allochromatium vinosum: characterization of the oxidized enzyme (Ni-A state). *J Mol Biol*. **402(2),** 428-444 (2010).

31. Volbeda, A.; Garcin, E.; Piras, C.; de Lacey, A. L.; Fernandez, V. M.; Hatchikian, E. C.; Frey, M. and Fontecilla-Camps, J. C. Structure of the [NiFe] Hydrogenase Active Site: Evidence for Biologically Uncommon Fe Ligands. *J. Am. Chem. Soc.* **118 (51),** 12989–12996 (1996).

32. Matias, P. M.; Soares, C. M.; Saraiva, L. M.; Coelho, R.; Morais, J.; Le Gall, J.; Carrondo, M. A. [NiFe] hydrogenase from Desulfovibrio desulfuricans ATCC 27774: gene sequencing, three-dimensional structure determination and refinement at 1.8 A and modelling studies of its interaction with the tetrahaem cytochrome c3. *J Biol Inorg Chem*. **6(1),** 63-81 (2001).

33. Ogata, H.; Hirota, S.; Nakahara, A.; Komori, H.; Shibata, N.; Kato, T.; Kano, K.; Higuchi, Y. Activation process of [NiFe] hydrogenase elucidated by high-resolution X-ray analyses: conversion of the ready to the unready state. *Structure*. **13(11),** 1635-1642 (2005).

34. Volbeda A, Martin L, Barbier E, Gutiérrez-Sanz O, De Lacey AL, Liebgott PP, Dementin S, Rousset M, Fontecilla-Camps JC. Crystallographic studies of [NiFe]-hydrogenase mutants: towards consensus structures for the elusive unready oxidized states. *J Biol Inorg Chem.* **20(1),** 11-22 (2015).

35. Dementin S, Leroux F, Cournac L, de Lacey AL, Volbeda A, Léger C, Burlat B, Martinez N, Champ S, Martin L, Sanganas O, Haumann M, Fernández VM, Guigliarelli B, Fontecilla-Camps JC, Rousset M. Introduction of methionines in the gas channel makes [NiFe] hydrogenase aerotolerant. *J Am Chem Soc.* **131(29),** 10156-10164 (2009).

36. Leroux, F.; Dementin, S.; Burlat, B.; Cournac, L.; Volbeda, A.; Champ, S.; Martin, L.; Guigliarelli, B.; Bertrand, P.; Fontecilla-Camps, J. C.; Rousset, M. and Léger, C. Experimental approaches to kinetics of gas diffusion in hydrogenase. *PNAS*. **105(32),** 11188-11193 (2008).

ii. Tracking the route of molecular oxygen in membrane-bound [NiFe] hydrogenase of Ralstonia eutropha. ***– Preprint***

This is a preprint of Kalms J*, Schmidt A, Frielingsdorf S, Utesch T, Gotthard G, von Stetten D, van der Linden P, Royant A, Mroginski MA, Carpentier P, Lenz O, and Scheerer P. ***Proc Natl Acad Sci U S A.*** 2018 Mar 6;115(10):E2229-E2237.

Tracking the route of molecular oxygen in O_2-tolerant membrane-bound [NiFe] hydrogenase

Jacqueline Kalms [1,#], Andrea Schmidt [1,#], Stefan Frielingsdorf [2], Tillmann Utesch [2], Guillaume Gotthard [3], David von Stetten [3], Peter van der Linden [3], Antoine Royant [3,4], Maria Andrea Mroginski [2], Philippe Carpentier [3,5,6,7], Oliver Lenz [2], and Patrick Scheerer [1,*]

[1] Institut für Medizinische Physik und Biophysik (CC2), Group Protein X-ray Crystallography and Signal Transduction, Charité - Universitätsmedizin Berlin, Charitéplatz 1, 10117, Berlin, Germany.

[2] Institut für Chemie, Sekr. PC14, Technische Universität Berlin, Strasse des 17. Juni 135, 10623, Berlin, Germany.

[3] ESRF-European Synchrotron Radiation Facility, 71 Avenue des Martyrs, Grenoble Cedex 9, 38043, France

[4] Institut de Biologie Structurale, Université Grenoble Alpes, CNRS, CEA, Grenoble, 38044, France.

[5] CEA/DRF/BIG/CBM/BioCat, 17 Avenue des Martyrs, Grenoble Cedex 9, 38054, France.

[6] CNRS UMR 5249, LCBM, Grenoble, France.

[7] Université Grenoble Alpes, LCBM, Grenoble, France.

[#] Both authors contributed equally to this work.

* Correspondence and requests for materials should be addressed to Dr. Patrick Scheerer (phone: 49-450-524178; E-mail: patrick.scheerer@charite.de)

Summary

[NiFe] hydrogenases catalyse the reversible splitting of H_2 into protons and electrons. H_2 travels through a dedicated gas tunnel network to reach the deeply buried catalytic centre. The same network is presumably accessible for other gases, such as inhibitory O_2. Although most [NiFe] hydrogenases are either reversibly or irreversibly inactivated by O_2, it is still unclear, whether O_2 actually reaches the catalytic centre. A small subgroup of [NiFe] hydrogenases, including the membrane-bound hydrogenase of *Ralstonia eutropha* (MBH), are able to overcome this attack by reducing O_2 to water. The key feature of O_2 tolerance relies on a special [4Fe3S]-cluster that is capable to release two electrons upon O_2 attack. Here, the route that is taken by O_2 within the MBH gas tunnel network is traced by a novel 'soak-and-freeze' method, accompanied by protein X-ray crystallography and computational studies. This combined approach led to the detection of several preferred residence sites of O_2 molecules within the MBH. The occupancy of these sites was related to the O_2 concentration used for MBH crystal derivatization.

Introduction

In many enzymes the catalytic centres are deeply buried within the protein matrix. In these cases, substrate access as well as the transport of intermediates and product release are often facilitated by dedicated molecular tunnels.[1] A sheltered active site in combination with molecular tunnels can have several advantages for the enzyme: *(i)* an increase of the catalytic efficiency compared to free diffusion, *(ii)* protection of the active site from reactive and inhibitory compounds, *(iii)* protection of unstable intermediates, *(iv)* improved transport time between active sites, *(v)* increased substrate selectivity and *(vi)* regio- and/or stereospecific control.[1,2] In multi-functional enzymes molecular tunnels connect the different sites of reaction intermediate generation and utilisation. A very well-studied enzyme with multiple active sites is the class I amidotransferase carbamoyl phosphate synthetase (CPS). The intermediates ammonia and carbamate migrate through a permanent tunnel with a length of almost 100 Å. The CPS structure also revealed a difference in tunnel diameter adjusting to the dimensions of the intermediate.[3] The intramolecular tunnel of glutamine phosphoribosylpyrophosphate amidotransferase (GPATase) shows a different architectural feature. GPATase catalyses the conversion of phosphoribosylpyrophosphate into phosphoribosylamine. Here, the intermediate tunnel between the two active sites only exists temporarily upon binding of the correct ligand to the active site and that induces consecutive conformational changes of the protein backbone.[4] In other enzymes like glutamate synthase and glucosamine 6-phosphate synthase, the substrate tunnel is obstructed and switches between an open and closed state through substrate-induced conformational changes of amino acids, which act as a gate.[5,6]

In other enzymes the molecular tunnels connect the protein exterior with the active site deeply buried within the protein matrix. Such tunnels can serve as permanent or gated substrate pathways as found in DhaA haloalkane dehalogenase or cholesterol oxidase, respectively.[7,8] In

lipoxygenases two permanent hydrophobic tunnels that might be used individually by the two substrates, lipid and dioxygen merge at the active site.[9,10]

A recent study on the gas tunnel network O_2-tolerant [NiFe] hydrogenases and their O_2-sensitive counterparts revealed major structural differences in dimension and complexity.[11] In the O_2-tolerant membrane-bound [NiFe] hydrogenase (MBH) of *Ralstonia eutropha* the protein exterior and the [NiFe] active site are connected via two hydrophobic gas tunnels (Figure 1, black dashed arrow).[11,12] MBH is composed of three subunits, the large subunit harbours the deeply buried active site where the reversible catalytic reaction $H_2 \rightleftharpoons 2e^- + 2H^+$ takes place. The small subunit contains an electron relay consisting of three [FeS]-clusters (Figure 1, light blue, dashed arrow) that transfer the electrons derived from H_2 oxidation at the active site to the third subunit, a membrane-integral cytochrome b_{562}. The cytochrome itself is connected to the quinone pool of the respiratory chain.[12,13] The majority of [NiFe] hydrogenases becomes inactivated by O_2. The MBH is one of few examples that can overcome the O_2 attack by redirecting electrons from the [FeS]-clusters back to the [NiFe] active site where they are used to reduce O_2 completely to harmless water (Figure 1, black and light blue dashed arrow).[13,14,15] The water molecules are released by a nearby water channel (Figure 1, yellow dashed arrow).[12] Experimental determination of O_2 migration pathways in proteins by X-ray crystallography has always been challenging due to the weak interaction of O_2 with the amino acids, the high mobility of the gas and the low electron count. Thus, O_2 pathways were mainly identified by either computational studies or by using noble gas molecules like krypton to mimic O_2.[11,16,17] Here, we present the crystal structure of MBH prepared by the novel "soak-and-freeze" method that reveals defined O_2 sites in two hydrophobic tunnels and a cavity. These observations are in good agreement with molecular dynamics (MD) simulations suggesting O_2 “hopping” process through these tunnels.

Results and Discussion

In our protein crystallography experiments we applied the novel 'soak-and-freeze' method recently established at the ESRF in order to investigate whether O_2 reaches the [NiFe] active site through the hydrophobic tunnels previously defined by krypton-derivatised MBH crystals.[18] MBH crystals were grown and subsequently exposed to molecular oxygen in a gas pressure cell at 56 bar and 70 bar, which is equivalent to a dissolved O_2 concentration of 72.8 mM and 91 mM, respectively. After incubation for time periods from 15-70 minutes, the derivatised crystals were flash frozen in liquefied O_2 at 77 K (Table 1). Subsequently, the gas pressure cell was depressurised and the crystals were transferred to liquid nitrogen for analysis at the synchrotron beamline. For all O_2-derivatised crystals a non-derivatised reference data set was collected using MBH crystals from the same crystallisation batch (Table 2). The O_2 positions were determined by examining the $Fo^{O_2} - Fo^{reference}$ electron density map calculated using structure factors of the O_2-derivatised and reference data sets, respectively. With the 'soak-and-freeze' technique we identified four O_2 binding sites (Oxy1-4) in the best data set, three of which were located within the gas tunnel system of MBH. One O_2 molecule (Oxy2) resided in a hydrophobic pocket surrounded by amino acids $M30_L$, $V46_L$, $S47_L$, $F569_L$, $E570_L$, $L573_L$ and $L591_L$ (subscript indicates subunit: L = large subunit, S = small subunit) (Figure 1 and 2, Table 3). Owing to the 2D representation of Figures 1 and 2, Oxy2 appears to be close to the [NiFe] active site, but the actual distance is 16.3 Å. Apart from the four O_2 residence sites illustrated in Fig. 2, three further O_2 molecules were identified in the tunnel on the basis of the $Fo^{O_2} - Fo^{reference}$ electron density map. As the occupancies of the additional O_2 molecules were less than 40 %, they were not modelled in the structure. Superposition of the O_2-derivatised with the krypton-derivatised MBH structures illustrates, however, that all seven O_2 molecules share their location with those of the krypton atoms (Supplementary Figure 1). The maximum occupancy with 100 % was observed for Oxy1 (at the same position as

krypton 1 with an occupancy of 100 %) at 70 bar after 15 minutes of soaking in pressurized O_2 before freezing. Using Oxy1 as benchmark, we can clearly deduce a correlation of O_2 occupancy with pressure and incubation time (Table 1). In order to inspect the positions of the O_2 molecules in respect of the gas tunnel network, the latter was calculated with the program *Caver 3.0*[19] using the highly conserved residue $R530_L$ as initial starting point. The program predicts two subunit-crossing tunnels, which merge before reaching the [NiFe] active site. Tunnel A with a minimal diameter (d_{min}) of ~ 1.4 Å and a length of ~ 33 Å is categorised as primary gas tunnel, whereas tunnel B (d_{min} ~ 1.3 Å, length ~ 52 Å) serves as putative secondary pathway. Approximately 56 % of the amino acids forming the tunnel surface are of hydrophobic character (Supplementary Figure 2). The hydrophobic tunnel entrances presumably facilitate the access of the gaseous substrates. The highest occupied O_2 molecule (Oxy1) is located in branch 1, which does not have a direct connection the protein exterior and might serve as substrate storage cavity. A similar storage cavity has been proposed by Montet and coworkers for the O_2-sensitive hydrogenase from *Desulfovibrio gigas* assuming that some of the hydrophobic cavities serve as gas reservoirs.[20] They suggested that the concentration of the gaseous substrate in the enzyme effects the gas metabolism. Comparable conclusions have been drawn from the MD simulation results from [NiFeSe] hydrogenase.[21] Baltazar and colleagues deduce from cavities with trapped H_2 molecules that they either hinder H_2 transport to the active site or promote access by storing gas molecules. Considering that the H_2 concentrations usually needed for catalytic activity in hydrogenases are above ambient level, the MBH gas reservoir might play an important role in enzyme metabolism.[22] To further verify a gas reservoir feature, MD simulations of simultaneous H_2 and O_2 transport in the corresponding ratio through the tunnel network as well as tunnel mutation studies might shed further light on this topic. Oxy3 is located within tunnel B near the bottleneck (smallest tunnel diameter) consisting of the amino acids $A127_L$, $V131_L$ and $A202_L$. Oxy4 in tunnel A is the O_2 molecule closest to the active site

(Figure 2), near the bottleneck of tunnel A. It is composed of amino acids including $E27_L$, $R530_L$, $P596_L$ and $C597_L$ with a distance < 3 Å from the bottleneck.

The observations based on the crystallographic structure were compared with MD simulations of MBH in aqueous solution described in further detail in the Method section. The resulting 300 ns long trajectories showing the diffusion of O_2 and H_2 molecules suggested a "hopping"-like movement of O_2 and H_2 molecules (movies 1-4 of O_2 trajectories) through the main tunnels (Figures 3, 4, Supplementary Figure 1, 3, 4). Notably, no permanent tunnel opening was observed in the simulations while diffusion outside the tunnel system was detected, which is in agreement with previous calculations performed on a structurally similar O_2-sensitive "standard" [NiFe] hydrogenase.[15] Diffusion of gas molecules through the previously proposed water channel[13] was predicted to be unfavourable compared to the gas diffusion through tunnels A and B. O_2 diffusion ("hopping" process) through the gas tunnel network (Figure 3) resulted in high densities at the Oxy1 and Oxy3 sites (molecule occupancies of > 75 %) (Supplementary Figure 1B), which is in excellent agreement with the results of the "soak-and-freeze" experiment. Furthermore, O_2 molecules were detected in the vicinity of all other experimentally proposed binding sites as well as within a 3 Å radius from the active site. Due to the side chain flexibility at room temperature, the positions of the O_2 binding sites change in the course of the simulations, particularly in tunnel A. This impedes a direct comparison with the experimentally determined values. The assignment of these sites, however, was computationally predicted on the basis of residence times and site occupancies by O_2 molecules (Supplementary Figure 1). Analysis of transition probabilities between the preferred O_2-binding sites showed that, except for Oxy2, all O_2 positions in the MBH were connected by the tunnel network predicted by *Caver 3.0* (Supplementary Figure 1). In addition, Oxy5 and Oxy6, located close to the proposed tunnel entries, showed the highest transition probabilities (28.6 and 23.2 %, respectively) to the "bulk region" (solvent and undefined regions within the protein) making

these positions potential entry sites for O_2 (Figure 3, Table 6). The probability for a transition from the bulk region to branch 1 (Oxy1 and Oxy7) was much lower compared to transitions from the bulk to positions Oxy5 and Oxy6 at the potential entry points (Table 6). Deeply buried sites, such as Oxy3 and the branch 1 region showed higher self-transition probabilities (Table 6) and occupancies (Supplementary Figure 1B) than regions close to the protein surface (Oxy5 and Oxy6) indicating longer residence times for O_2 at these sites. The only discrepancy between MD simulations and *Caver 3.0* predictions was that in the MD simulations the observed O_2 densities in tunnel A were lower than in tunnel B (Supplementary Figure 1B), while the *Caver* predictions on the crystallographic structure identified tunnel A as main access pathway (Figure 1). This finding may result from the increased flexibility of the amino acid side chains narrowing tunnel A in the simulations.

The spatial probability density of H_2 in the gas tunnel network was similar to that predicted for O_2 (Supplementary Figure 4). However, distinct differences in the diffusion properties of H_2 and O_2 were encountered. For the H_2 diffusion, tunnel A was strongly favoured over tunnel B as reflected by (a) the high transition probabilities between Oxy5 and Oxy4 (Supplementary Table 1), and (b) the increased occupancies of these sites (Supplementary Figure 4). Concomitantly, the low occupancy of Oxy3 (45.7 vs 76.9 % for H_2 and O_2, respectively) reflects a reduced diffusion of H_2 through tunnel B. Because of the smaller size and lower molecular weight of H_2 compared to O_2, higher H_2 densities were found in close vicinity (2.7 Å distance) to the active site as well as outside the MBH tunnel system in the MBH (Supplementary Figure 3). To investigate whether the pressure treatment, which comes along with the 'soak and freeze' method, had an impact on the overall structure of MBH and its gas tunnels, we compared the O_2-derivatised structure and a structure obtained after high-pressure (2000 bar of helium) treatment of MBH crystals with the non-derivatised reference structure of MBH at ambient pressure.[23] The structures were aligned using the program *Py*MOL[24], and we

obtained root mean square deviations (RMSD) of 0.043 Å and 0.195 Å when comparing the O_2-derivatised structure and the high-pressure structure with the reference MBH structure, respectively (Supplementary Figure 5). The greater differences with the high-pressure structure are also reflected by the B-factors (temperature factors). The B-factor comparison between the three structures were visualised using *Py*MOL in a range between 10-50 $Å^2$ (Figure 5). Intriguingly, the structure of the O_2-derivatised MBH revealed generally lower temperature factors when compared to the reference data set. Thus, a pressure of 70 bar seems to stabilize flexible parts at the enzyme surface, in particular regions close to the gas tunnel openings. A further increase of the pressure to 2000 bar, however, led to a marked rise in the temperature factors. The pressure-induced higher flexibility of amino acids even led to an unresolved disordered loop structure close to the entrance of tunnel A and in an enlargement of the surrounding area (Figure 5). Furthermore, branch 1 of the hydrophobic tunnel is capped by a surface-located alpha helix, which does not show an increase in flexibility through pressurisation. This supports the proposal of branch 1 being mainly a dead end and not a transient gas tunnel with a lockable lid. Notably, the [NiFe] active site as well as the medial [3Fe4S]-cluster and the distal [4Fe4S]-cluster of the electron relay maintained their spatial structure upon pressurisation. In all three MBH structures the Ni and Fe atoms have a distance of 2.9 Å (Table 5), and they are bridged by a hydroxide ligand, which is entirely in line with the oxidation state of the catalytic center.[12,13] They also showed the typical open conformation of the proximal [4Fe3S]-cluster with a bond length of ~2.1 Å between iron 4 and the backbone nitrogen of cysteine 20 (Supplementary Figure 6), which is compatible with the as-isolated, superoxidised state of the enzyme.[13] However, the [4Fe3S]-cluster of the O_2-derivatised MBH showed two further structural features when compared to the reference structure. First, the carboxylate functional group of $E76_S$ is shifted towards Fe4 of the cluster (Supplementary Figure 7) and second, Fe1 carries a hydroxyl ligand (Supplementary Figure 8).[13,25] While the

distance of E76S and Fe4 amounted to 3.4 Å and 3.2 Å in the reference and high-pressure structure, respectively, it was reduced to 2.6 Å in the O_2-derivatised MBH (Table 2, 5, Supplementary Figure 7). The E76S-shift towards the proximal cluster was observed in all O_2-derivatised MBH structures (Tables 1 and 2). In the as-isolated structure of the membrane-bound O_2-tolerant [NiFe]-hydrogenase 1 from *Escherichia coli* (*Ec*Hyd-1) the E76S was found in a double conformation with distances of 4.9 Å and 2.4 Å of one glutamate-derived carboxylate Oε to Fe4.[22] Volbeda and coworkers proposed that E76S functions as base for the deprotonation of the carboxamido N of cysteine 20, which further enables the Fe4 to bind to the backbone of cysteine 20 and thus stabilizes the high-potential form of the [4Fe3S]-cluster. A similar cluster stabilization was proposed for the Fe1-bound hydroxyl ligand in MBH.[13] The presence of this ligand with a Fe-O distance of 1.8 Å between the hydroxyl oxygen and the Fe1 was confirmed in the O_2-derivatised MBH structures. The hydroxyl ligand has an average occupancy of ~ 34 % with no obvious relation to the O_2 concentration (Table 1). In the reference data sets, however, Fe1-bound hydroxyl ligand was not visible. In the previously published crystal structures of as-isolated, superoxidized MBH, the hydroxyl ligand occurred with a high variation in occupancy, reaching from 0 % in PDB entry 4TTT, 30 % in PDB entry 4IUC (B-factor: 9 $Å^2$), up to 88 % in PDB entry 4IUB (B-factor: 11 $Å^2$).[13] At present it remains unclear whether the Fe1-bound hydroxyl ligand and the E76S-shift are related to the 5+/4+ redox state transition of the [4Fe3S]-cluster or represent damages caused by high O_2 concentrations. However, it is important to note that no remarkable damage due to high O_2 pressure and/or radiation was observed for the remaining metal cofactors in the MBH.

The novel technique of crystal derivatisation ('soak-and-freeze') enables unprecedented insight into the accessibility of the MBH tunnel network for gas molecules. Our data show that MBH contains several hydrophobic tunnels that can be traced on the basis of O_2 molecules residing at defined sites. Remarkably, the positions of all detected O_2 molecules match with

those previously determined in krypton-derivatised MBH, which makes, at least in this case, krypton a good mimic for O_2. Molecular dynamics simulations further manifest the pathways used by the gas molecules travelling from the protein surface to the deeply buried active site. Furthermore, the MD simulations indicate that O_2 and the much smaller H_2 molecules likely use the same route within the gas tunnel network. However, the simulations also revealed differences in the distribution of O_2 and H_2. O_2 occupies the two transition sites of tunnel A to a much lesser extent than H_2 does. O_2 might instead be directed towards branch 1 of gas tunnel B which is located far away from the vulnerable [NiFe] active site. Direct contact of O_2 with active site can, however, not be excluded, and the current model of O_2 tolerance implies that O_2 is reduced at the [NiFe] active site with the aid of electrons delivered by the fully reduced proximal [4Fe3S]-cluster.[15] Understanding the architecture of the tunnel network in MBH is crucial for future modifications of the enzyme functions through engineering of the tunnel characteristics. Site-directed amino acid exchanges allow either expansion or constriction as well as changing the physical properties like hydrophobicity of the tunnel. These modifications may have an influence on both the access of the substrate H_2 to the active site and the susceptibility of the enzyme toward O_2.

Full Methods

Protein expression and purification. Native MBH was produced and purified in the as-isolated (air-oxidized) state as described elsewhere.[12,26]

Crystallisation. MBH was crystallized with the sitting-drop vapor diffusion method in 24- well Linbro plates (Jena Bioscience) at a concentration of about 10 mg ml^{-1} and at 277 K. The reservoir solution contained 20-30 % polyethylene glycol 3350, 100 mM Bis-(2-hydroxy-ethyl)-amino-tris(hydroxylmethyl)-methane buffer at pH 5.5 - 6.5. Precipitants and protein solution were mixed in different ratios (7 - 8 µl) into micro-bridges (Hampton Research). After 2-4 days the dark-brown needle shaped MBH crystals were directly used for high-pressure cooling and O_2 derivatisation experiments or were cryo-protected in 15 % glycerol and flash cooled in liquid nitrogen (LN2) for native data set collection.

High-pressure cryo-cooling. The cryo-protectant free cooling of the MBH crystals was performed using a high-pressure cooling system recently developed at the ESRF in Grenoble.[20] The needle shaped crystals were directly harvested from the crystallization drop with specific pluggable sample supports (MiTeGen, Ithaca) and transferred into the pressurizing drop tubes at room temperature. The lower parts of the drop tubes were then cooled in LN2 and the crystals were pressurized with 2000 bar of helium. Thereafter the crystals were dropped into the bottom of the tube and flash-cooled at 77 K. Finally, the system was depressurized, the crystals handled in liquid nitrogen and stored under LN2 for further X-ray experiments. Four crystals could be high-pressure cooled at the same time.

O_2 derivatisation. The MBH crystals were derivatised with O_2 gas in a cryogenic oxygen pressure cell newly developed at the ESRF in Grenoble.[18] Each time one crystal was harvested from the crystallization drop with a specific pluggable sample support (MiTeGen, Ithaca) being surrounded by mother liquor including 15 % glycerol. The crystal was then loaded into the pressurising drop tube at room temperature. The MBH crystals were pressurized at 56 bar (5600

kPa) and 70 bar (7000 kPa) in a time frame from 15 to77 min. Still under pressure the crystal was dropped into the bottom of the tube and flash-cooled at 77 K. After depressurizing the system, the crystal was handled in LN2 with a specially designed cryo-toolkit and stored in liquid nitrogen for further X-ray experiments.

Structure analysis. Diffraction data was collected at the synchrotron radiation facility ESRF in Grenoble, France. The best high-pressure (HP) data set was collected at the tunable beamline ID29[27] with a PILATUS 6M-F detector at a wavelength of 0.976 Å. The best oxygen derivatised (OxD) and reference (REF) data set were collected at the tunable beamline ID30B[28] with a PILATUS 6M-F detector at a wavelength of 0.976 Å. All data sets were measured using data collection and strategy software packages MxCube[29] and EDNA.[30] The data collection was carried out in the helical rotation mode at 100 K, a rotation increment of 0.05 ° with an exposure time of 0.037 s for each frame (3000 images collected) and a detector-to-crystal distance of 191 mm, 163 mm and 256 mm for the HP, OxD and REF data set, respectively. The images of the best data set were indexed, integrated and scaled using the XDS program package[31] and the CCP4[32] program SCALA.[33] All crystals belong to orthorhombic space group $P2_12_12_1$ (unit cell constants HP: a = 73.39 Å, b = 95.70 Å, c = 121.57 Å; α = β = γ = 90.00°, unit cell constants OxD: a = 73.13Å, b = 95.57 Å, c = 119.69 Å; α = β = γ = 90.00°, unit cell constants REF: a = 73.11 Å, b = 95.57 Å, c = 119.83 Å; α = β = γ = 90.00°). Initial phases for MBH (HP, OxD, REF) were obtained by molecular replacement based on the crystal structure of the reduced state MBH (PDB entry 4TTT) as initial search model using the CCP4 program PHASER.[34,35] Subsequently, different refinement strategies (inter alia real-space refinement, B-factor refinements) and simulated-annealing (slow cooling protocol, maximum likelihood target function, energy minimization) were carried out. The search for water molecules was performed with the PHENIX suite.[36] The crystal structure was finalized with the CCP4 program REFMAC5.[37] Manual rebuilding of HP, OxD and REF models and electron density

interpretation were performed after each refinement cycle using the program COOT.[38] The final OxD model has agreement factors R_{free} / R_{work} of 13.2 % / 16.3 %.[39] Structure validations were performed with the programs of the RCSB PDB Validation server[40], MolProbity server[41] and WHAT IF server[42]. All molecular graphics representations were created using *Py*MOL.[24] Table 4 summarizes the statistics for crystallographic data collection and structural refinement.

Caver tunnel calculation. The program *Caver* 3.0 was used as *Py*MOL plugin.[19,24] The settings in the program were manually adjusted. The initial starting point (NH_2 of the guanidine- group of the arginine, i.e. $R530_L$ for MBH), shell depth (2 Å), shell radius (3 Å), cluster threshold (3.5 Å), desired radius (5 Å) and the maximum distance (3 Å) were maintained constant for all calculations. The maximum distance specifies the furthest point (from the initial arginine) to start a tunnel calculation. The bottleneck radius is the narrowest part of a given tunnel and corresponds to the minimum probe radius. The tunnel analysis provides a list of calculated tunnels (residues) with their bottleneck residues which were used to draw Figure 2 and Supplementary Figure 2. The tunnels are ranked according to a specific cost function (*e.g.* two tunnels with equal radii the one with the shorter distances has a lower cost).[19] The tunnel with the lowest cost is the primary tunnel.

Molecular dynamics simulations. Classical molecular dynamics (MD) simulations were performed to investigate the diffusion of O_2 and H_2 within MBH. For this, the coordinates of reduced MBH (PDB entry 3RGW) were used as starting configuration.[12] While the protein was described with the Gromos53a6 united force field[43], the inorganic ligands ([NiFe] active site and [FeS] clusters) were treated as rigid bodies using the Lincs algorithm.[44] Their partial charges were adopted from an earlier work.[45] The protein-cofactor model was solvated in a cubic pre-equilibrated SPC water box[46] under ca. 25 mM NaCl. Additionally, O_2 (or H_2) molecules mimicking a concentration of ca. 225 mM were inserted randomly replacing bulk water molecules. The high concentration of oxygen was used to increase the interaction with

MBH similar as it was done for the standard hydrogenase.[17] Both gas molecules were simulated as three-site model described in literature.[17]

After stepwise energy minimizing and thermally equilibrating the model at 300 K, the system was subjected to a 300 ns long production run. During the simulation carried out with Gromacs 4.6.5[47], a time step of 2 fs was enabled by constraining all bonds containing hydrogen atoms by the Lincs algorithm.[41] The NPT ensemble (constant number of particles, pressure (p=1 atm) and temperature (T=300 K)) under periodic boundary conditions was realized by the Berendsen pressure[48] and v-rescale temperature[49] methods applying pressure and temperature coupling constants of $\tau_p = 1.0$ ps and $\tau_T = 0.1$ ps, respectively. Electrostatic interactions beyond a cut- off of 1.4 nm were modelled by the Particle Mesh Ewald summation[50] and van der Waals interactions were truncated beyond 1.2 nm.

Gas transition models. The diffusion of O_2 and H_2 within the MBH was described by a simple transition model based on the O_2 (H_2) dynamics extracted from the MD simulations. In total, eight regions were defined. Seven regions correspond to spheres of 5 Å around the amino acids surrounding oxygen molecules (Oxy1-Oxy7) in the crystal structure. Bulk solvent (or region 0) contained all gas molecules outside these six defined spheres (solvent and undefined positions in MBH). Based on this model, transitions between these regions were analysed for all O_2 (H_2) molecules using a time resolution of 20 ps. Furthermore, occupancies were calculated taking the last 150 ns of the trajectory into account.

References

1. Raushel, F. M., Thoden, J. B. & Holden, H. M. Enzymes with molecular tunnels. *Acc. Chem. Res.* **36,** 539–548 (2003).
2. Huang, X., Holden, H. M. & Raushel, F. M. Channeling of substrates and intermediates in enzyme-catalyzed reactions. *Annu. Rev. Biochem* **70,** 149–80 (2001).
3. Thoden, J. B., Holden, H. M., Wesenberg, G., Raushel, F. M. & Rayment, I. Structure of carbamoyl phosphate synthetase: A journey of 96 Å from substrate to product. *Biochemistry* **36,** 6305–6316 (1997).
4. Krahn, J. M. *et al.* Coupled formation of an amidotransferase interdomain ammonia channel and a phosphoribosyltransferase active site. *Biochemistry* **36,** 11061–11068 (1997).
5. Van Den Heuvel, R. H. H. *et al.* Structural studies on the synchronization of catalytic centers in glutamate synthase. *J. Biol. Chem.* **277,** 24579–24583 (2002).
6. Mouilleron, S., Badet-Denisot, M. A. & Golinelli-Pimpaneau, B. Glutamine binding opens the ammonia channel and activates glucosamine-6P synthase. *J. Biol. Chem.* **281,** 4404–4412 (2006).
7. Klvana, M. *et al.* Pathways and Mechanisms for Product Release in the Engineered Haloalkane Dehalogenases Explored Using Classical and Random Acceleration Molecular Dynamics Simulations. *J. Mol. Biol.* **392,** 1339–1356 (2009).
8. Coulombe, R., Yue, K. Q., Ghisla, S. & Vrielink, A. Oxygen Access to the Active Site of Cholesterol Oxidase through a Narrow Channel Is Gated by an Arg-Glu Pair. *J. Biol. Chem.* **276,** 30435–30441 (2001).
9. Banthiya, S. *et al.* Structural and functional basis of phospholipid oxygenase activity of bacterial lipoxygenase from Pseudomonas aeruginosa. *Biochim. Biophys. Acta - Mol. Cell Biol. Lipids* **1861,** 1681–1692 (2016).
10. Kalms, J. *et al.* The crystal structure of Pseudomonas aeruginosa lipoxygenase Ala420Gly mutant explains the improved oxygen affinity and the altered reaction specificity. *Biochim. Biophys. Acta - Mol. Cell Biol. Lipids* **accepted** (2017).
11. Kalms, J. *et al.* Krypton Derivatization of an O2-Tolerant Membrane-Bound [NiFe] Hydrogenase Reveals a Hydrophobic Tunnel Network for Gas Transport. *Angew. Chemie - Int. Ed.* **55,** 5586–5590 (2016).
12. Fritsch, J. *et al.* The crystal structure of an oxygen-tolerant hydrogenase uncovers a novel iron-sulphur centre. *Nature* **479,** 249–252 (2011).
13. Frielingsdorf, S. *et al.* Reversible [4Fe-3S] cluster morphing in an O(2)-tolerant [NiFe] hydrogenase. *Nat. Chem. Biol.* **10,** 378-385 (2014).
14. Fritsch, J., Lenz, O. & Friedrich B. Structure, function and biosynthesis of O_2-tolerant hydrogenases. *Nat. Rev. Microbiol.* **11,** 106-114 (2013).
15. Wulff, P., Day, C. C., Sargent, F. & Armstrong, F. A. How oxygen reacts with oxygen-tolerant respiratory [NiFe]-hydrogenases. *Proc. Natl. Acad. Sci. U. S. A.* **111,** 6606–11 (2014).
16. Cohen, J., Olsen, K. W. & Schulten, K. Finding gas migration pathways inproteins using implicit ligand sampling. *Methods in Enzymology* **437,** 439–457 (2008).
17. Wang, P., Best, R. B. & Blumberger, J. Multiscale simulation reveals multiple pathways for H2 and O2 transport in a [NiFe]-hydrogenase. *J. Am. Chem. Soc*. **133,** 3548-3556. (2011).
18. Lafumat, B. *et al.* Gas-sensitive biological crystals processed in pressurized oxygen and krypton atmospheres: deciphering gas channels in proteins using a novel `soak-and-freeze' methodology. *J. Appl. Crystallogr.* **49,** 1478-1487 (2016).

19. Chovancova, E. *et al.* CAVER 3.0: A Tool for the Analysis of Transport Pathways in Dynamic Protein Structures. *PLoS Comput. Biol.* **8,** 23–30 (2012).
20. Montet, Y. *et al*. Gas access to the active site of Ni-Fe hydrogenases probed by X-ray crystallography and molecular dynamics. *Nature* **4**, 523-526 (1997).
21. Baltazar, C. S., Teixeira, V. H. & Soares, C. M. Structural features of [NiFeSe] and [NiFe] hydrogenases determining their different properties: a computational approach. *J. Biol. Inorg. Chem.* **17**, 543-555 (2012).
22. Conrad, R., Aragno, M., & Seiler, W. The inability of hydrogen bacteria to utilize atmospheric hydrogen is due to threshold and affinity for hydrogen. *FEMS Microbiol. Lett.* **18**, 207–210 (1983).
23. Van Der Linden, P. *et al.* Towards a high-throughput system for high-pressure cooling of cryoprotectant-free biological crystals. *J. Appl. Crystallogr.* **47,** 584–592 (2014).
24. The PyMOL Molecular Graphics System, Version 1.8 Schrödinger, LLC.
25. Volbeda, A. *et al.* X-ray crystallographic and computational studies of the O2-tolerant [NiFe]-hydrogenase 1 from Escherichia coli. *Proc. Natl. Acad. Sci.* **109,** 5305–5310 (2012).
26. Goris, T. *et al.* A unique iron-sulfur cluster is crucial for oxygen tolerance of a [NiFe]-hydrogenase. *Nat. Chem. Biol.* **7,** 310–318 (2011).
27. De Sanctis, D. *et al.* ID29: A high-intensity highly automated ESRF beamline for macromolecular crystallography experiments exploiting anomalous scattering. *J. Synchrotron Radiat.* **19,** 455–461 (2012).
28. Theveneau, P. *et al.* The Upgrade Programme for the Structural Biology beamlines at the European Synchrotron Radiation Facility – High throughput sample evaluation and automation. *J.Phys.: Conf. Ser.* **425,** 012001 (2013).
29. Gabadinho, J. *et al.* MxCuBE: A synchrotron beamline control environment customized for macromolecular crystallography experiments. *J. Synchrotron Radiat.* **17,** 700–707 (2010).
30. Incardona, M. F. *et al.* EDNA: A framework for plugin-based applications applied to X-ray experiment online data analysis. *J. Synchrotron Radiat.* **16,** 872–879 (2009).
31. Kabsch, W. Xds. *Acta Crystallogr. Sect. D Biol. Crystallogr.* **66,** 125–132 (2010).
32. Project, C. C. The CCP4 suite: Programs for protein crystallography. *Acta Crystallogr. Sect. D Biol. Crystallogr.* **50,** 760–763 (1994).
33. Evans, P. Scaling and assessment of data quality. *Acta Crystallogr. Sect. D Biol. Crystallogr.* **62,** 72–82 (2006).
34. Winn, M. D. *et al.* Overview of the CCP4 suite and current developments. *Acta Crystallogr. Sect. D Biol. Crystallogr.* **67,** 235–242 (2011).
35. McCoy, A. J. *et al.* Phaser crystallographic software. *J. Appl. Crystallogr.* **40,** 658–674 (2007).
36. Adams, P. D. *et al.* PHENIX: A comprehensive Python-based system for macromolecular structure solution. *Acta Crystallogr. Sect. D Biol. Crystallogr.* **66,** 213–221 (2010).
37. Murshudov, G. N., Vagin, A. A. & Dodson, E. J. Refinement of macromolecular structures by the maximum-likelihood method. *Acta Crystallogr. Sect. D Biol. Crystallogr.* **53,** 240–255 (1997).
38. Emsley, P., Lohkamp, B., Scott, W. G. & Cowtan, K. Features and development of Coot. *Acta Crystallogr. Sect. D Biol. Crystallogr.* **66,** 486–501 (2010).
39. Brünger, A. T. Free R value: a novel statistical quantity for assessing the accuracy of crystal structures. *Nature* **355,** 472–475 (1992).
40. Berman, H. M. *et al.* The Protein Data Bank. *Nucleic Acids Res.* **28,** 235–242 (2000).
41. Davis, I. W. *et al.* MolProbity: All-atom contacts and structure validation for proteins

and nucleic acids. *Nucleic Acids Res.* **35,** 375–383 (2007).
42. Rodriguez, R., Chinea, G., Lopez, N., Pons, T. & Vriend, G. Homology modeling, model and software evaluation: three related resources. *Bioinformatics* **14,** 523–528 (1998).
43. Oostenbrink, C., Soares, T. A., Van Der Vegt, N. F. A. & Van Gunsteren, W. F. Validation of the 53A6 GROMOS force field. *Eur. Biophys. J.* **34,** 273–284 (2005).
44. Hess, B., Bekker, H., Berendsen, H. J. C. & Fraaije, J. G. E. M. LINCS: A linear constraint solver for molecular simulations. *J. Comput. Chem.* **18,** 1463–1472(1997).
45. Rippers, Y., Utesch, T., Hildebrandt, P., Zebger, I. & Mroginski, M. A. Insights into the structure of the active site of the O2-tolerant membrane bound [NiFe] hydrogenase of R. eutropha H16 by molecular modelling. *Phys. Chem. Chem. Phys.* **13,** 16146–16149 (2011).
46. Berendsen, H. J. C., Postma, J. P. M., Gunsteren, W. F. van & Hermans, J. in *Intermolecular Forces* (ed. Pullman, B.) 331–342 (1981).
47. Van Der Spoel, D. *et al.* GROMACS: Fast, flexible, and free. *J. Comput. Chem.* **26,** 1701–1718 (2005).
48. Berendsen, H. J. C., Postma, J. P. M., van Gunsteren, W. F., DiNola, a & Haak, J. R. Molecular dynamics with coupling to an external bath. *J. Chem. Phys.* **81,** 3684–3690 (1984).
49. Bussi, G., Donadio, D. & Parrinello, M. Canonical sampling through velocity rescaling. *J. Chem. Phys.* **126,** 014101 (2007).
50. Darden, T., York, D. & Pedersen, L. Particle mesh Ewald: An N·log(N) method for Ewald sums in large systems. *J. Chem. Phys.* **98,** 10089 (1993).
51. Weiss, M. S. Global indicators of X-ray data quality. *J. Appl. Cryst.* **34,** 130–135 (2001).
52. Einspahr, H. M. & Weiss, M. S. in *International Tables for Crystallography* 64–74 (2012).
53. Lovell, S. C. *et al.* Structure validation by C alpha geometry: phi,psi and C beta deviation. *Proteins-Structure Funct. Genet.* **50,** 437–450 (2003).

Supplementary Information accompanies this manuscript.

Acknowledgements We are grateful to Uwe Müller, Manfred Weiss and the scientific staff of the BESSY-MX/Helmholtz Zentrum Berlin für Materialien und Energie at beamlines BL14.1, BL14.2 and BL14.3 operated by the Joint Berlin MX-Laboratory at the BESSY II electron storage ring (Berlin-Adlershof, Germany) and the scientific staff of the European Synchrotron Radiation Facility (ESRF, Grenoble) at beamlines ID30A-3, ID30B, ID23-1, ID23-2 and ID29, where the data were collected, for continuous support. The authors acknowledge the "Norddeutscher Verbund für Hoch- und Höchstleistungsrechnen" (HLRN) for providing HPC resources. This work was supported by grants from the ESRF (to G.G., D.v.S., P.v.d.L., A.R. and P.C.), the Deutsche Forschungsgemeinschaft (SFB740 to P.S..; SFB1078 to P.S.), and DFG Cluster of Excellence 'Unifying Concepts in Catalysis' (Research Field D3/E3- 1 to J.K., A.S., S.F., T.U., M.A.M., O.L. and P.S.).

Author Contributions

J.K., A.S., P.C. and P.S. designed the idea and the experiments of the project; O.L. and P.S. coordinated the project; S.F. prepared the MBH protein sample; J.K., A.S., D.v.S. and P.S. performed crystallographic data collection and refinement; J.K., A.S., G.G. and D.v.S. prepared the crystal samples; P.v.d.L. and P.C. designed the high pressure freezing system; P.v.d.L., A.R. and P.C. designed the "soak-and-freeze" methodology; P.v.d.L and P.C. handled the pressure cells; T.U. and M.A.M performed and coordinated the MD simulations; J.K., A.S., T.U., S.F.,

O.L. and P.S. analysed the data, drafted and illustrated the manuscript with contributions from all co-authors.

Accession codes The atomic coordinates and structure factors have been deposited in the Protein Data Bank under accession codes 5MDL, 5MDJ, 5MDK and 4TTT.

Conflict of interest statement The authors declare no competing financial interests. Correspondence and requests for materials should be addressed to P.S. (patrick.scheerer@charite.de).

Figure 1 | Overview of substrate and product flow.

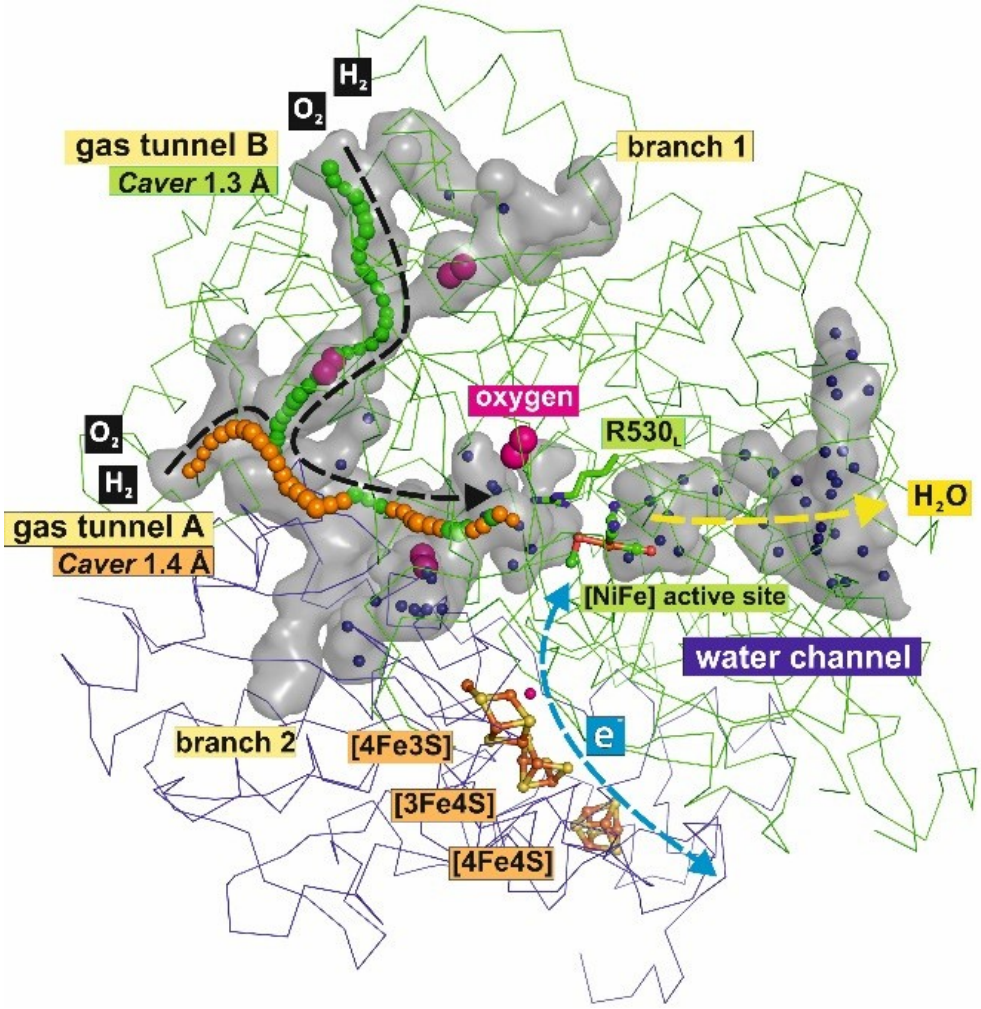

Ribbon/line representation of the large (green) and small (blue) subunit of O_2-derivatised MBH (PDB entry 5MDL). The [NiFe] active site and the three [FeS]-clusters are depicted in the balls and sticks representation. The hydrophobic gas tunnel and the hydrophilic water channel are shown as gray surfaces calculated with *Py*MOL.[24] Molecular oxygen and water molecules are shown as spheres in magenta and blue, respectively. Amino acid $R530_L$, which was used as initial starting point for the *Caver 3.0* tunnel calculation[19], is shown in stick representation. The *Caver* results are pictured as orange and green chains of spheres with a bottleneck radius of 1.4 Å and 1.3 Å, respectively. The directions of the flow of H_2/O_2 molecules, electrons and water molecules are illustrated as black, light blue and yellow dashed arrows, respectively.

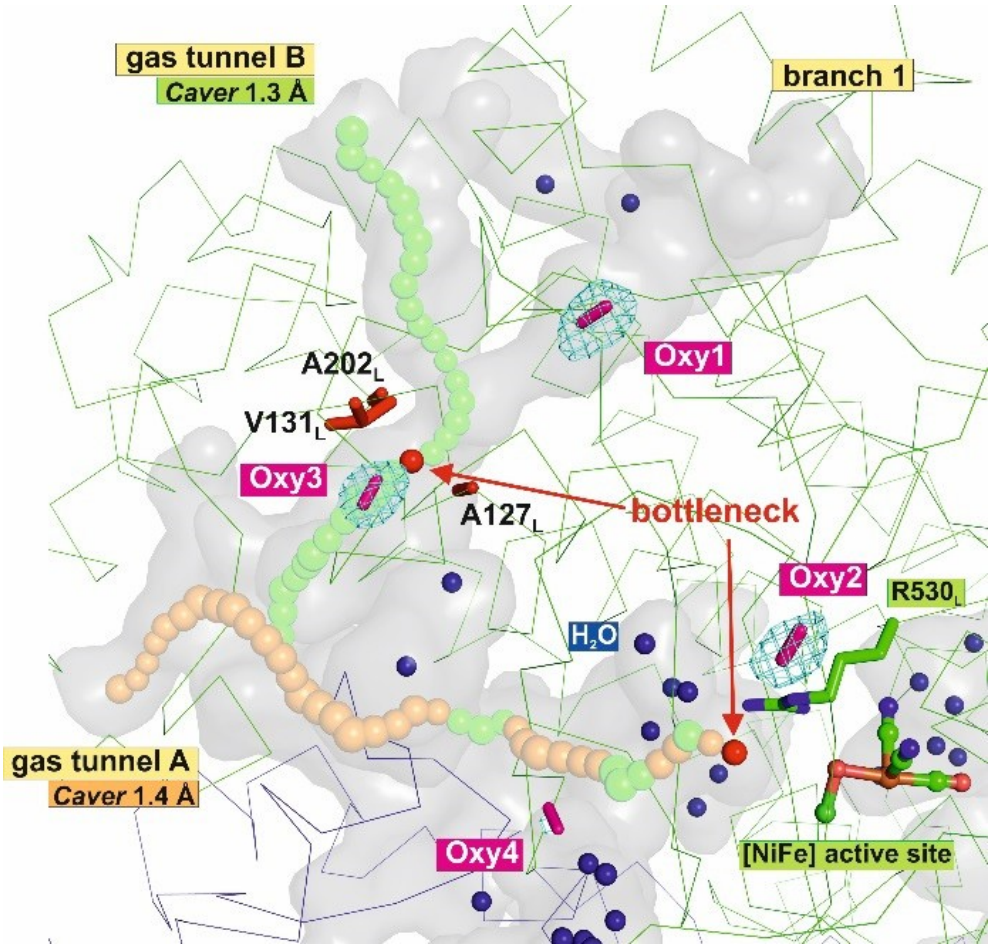

Figure 2 | O2 molecules detected in the MBH gas tunnel network.

Ribbon/line representation of MBH with the gas tunnel shown as grey surface (calculated with *Py*MOL[24]). Molecular oxygen molecules are depicted as magenta sticks with an Fo^{O_2} – $Fo^{reference}$ electron density map contoured at 3 σ (cyan mesh) and are calculated on the basis of the O_2-free reference data set. Water molecules are shown as blue spheres. $R530_L$ (stick representation) served as initial starting point for the *Caver* calculation[19] of the gas tunnels. The main gas routes are represented by orange and green chains of spheres. The bottlenecks are illustrated as red spheres and are composed of $A127_L$, $V131_L$ and $A202_L$ for tunnel B. The bottleneck for tunnel A is positioned right at the gate to the [NiFe] active site.

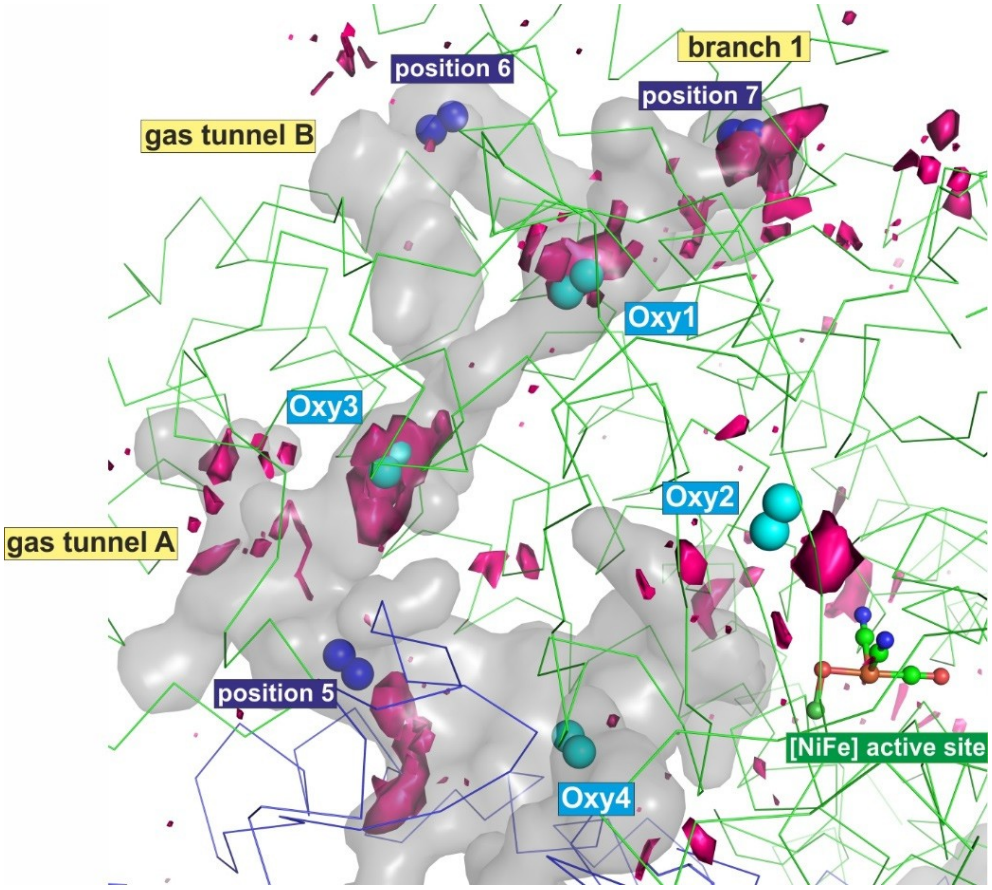

Figure 3 | Comparison of the experimentally determined O2 positions in the predicted gas tunnels with the O2 densities derived from MD simulations.

O_2 densities obtained from MD simulations (pink surface) are superimposed on the structure of O_2-derivatised MBH. The MBH tunnels calculated in *Py*MOL[24] are shown as grey surface consisting of tunnel A, tunnel B, and branch 1. O_2 positions determined by the soak-and-freeze approach are indicated as cyan and dark blue spheres. The O_2 molecules at positions 5 – 7 are only for comparison as they are not modelled in the actual MBH structure due to low occupancy. The backbone of the MBH is drawn in the ribbon representation and the active site as ball and stick model.

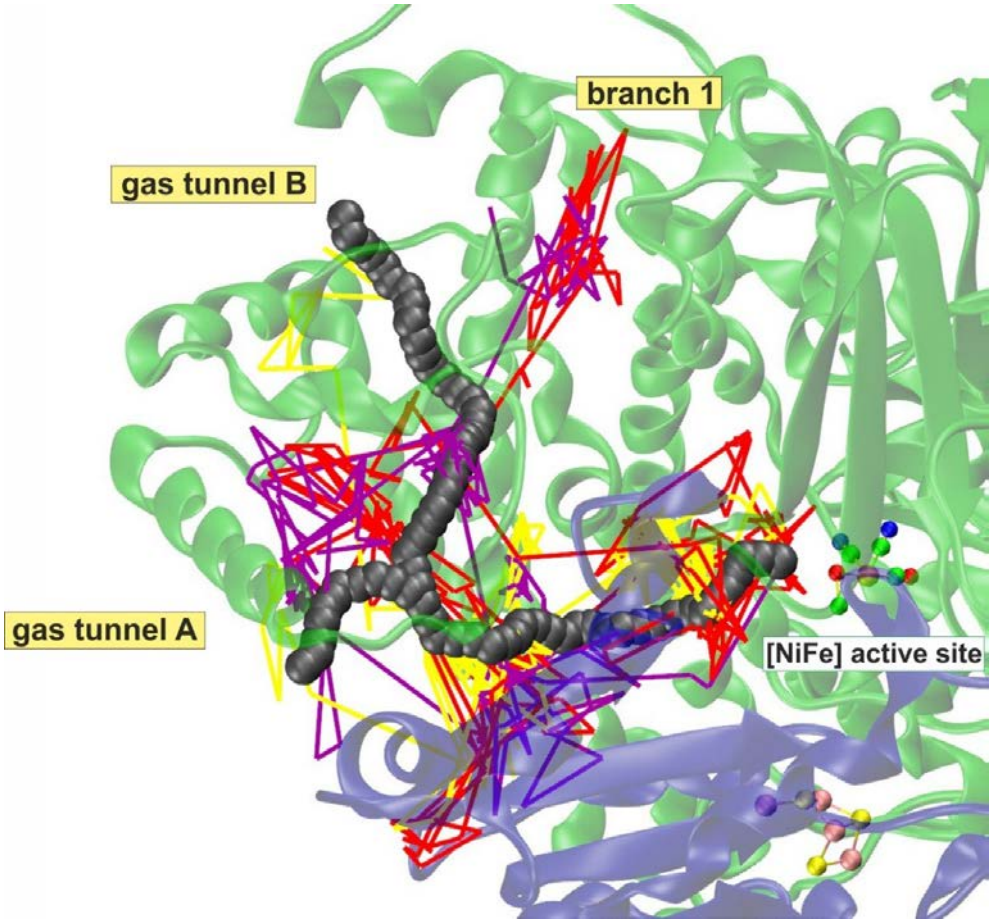

Figure 4 | Example travelling pathways for O2 through the gas tunnel network.

The diffusion pathways of three individual O_2 molecules during 3-5 ns are shown as red, purple and yellow lines. During the complete trajectories, gas molecules enter and leave the MBH at two main sites close to the calculated tunnels A and B (*Caver 3.0*, grey spheres), but to a lower content also at branch 1. The MBH large and small subunits are shown as green and blue cartoon, respectively. The active site (green, carbon; red, oxygen; blue, nitrogen; orange, iron; green, nickel) and the proximal [4Fe3S] cluster (yellow, sulphur; pink, iron) are indicated in the ball and stick representation.

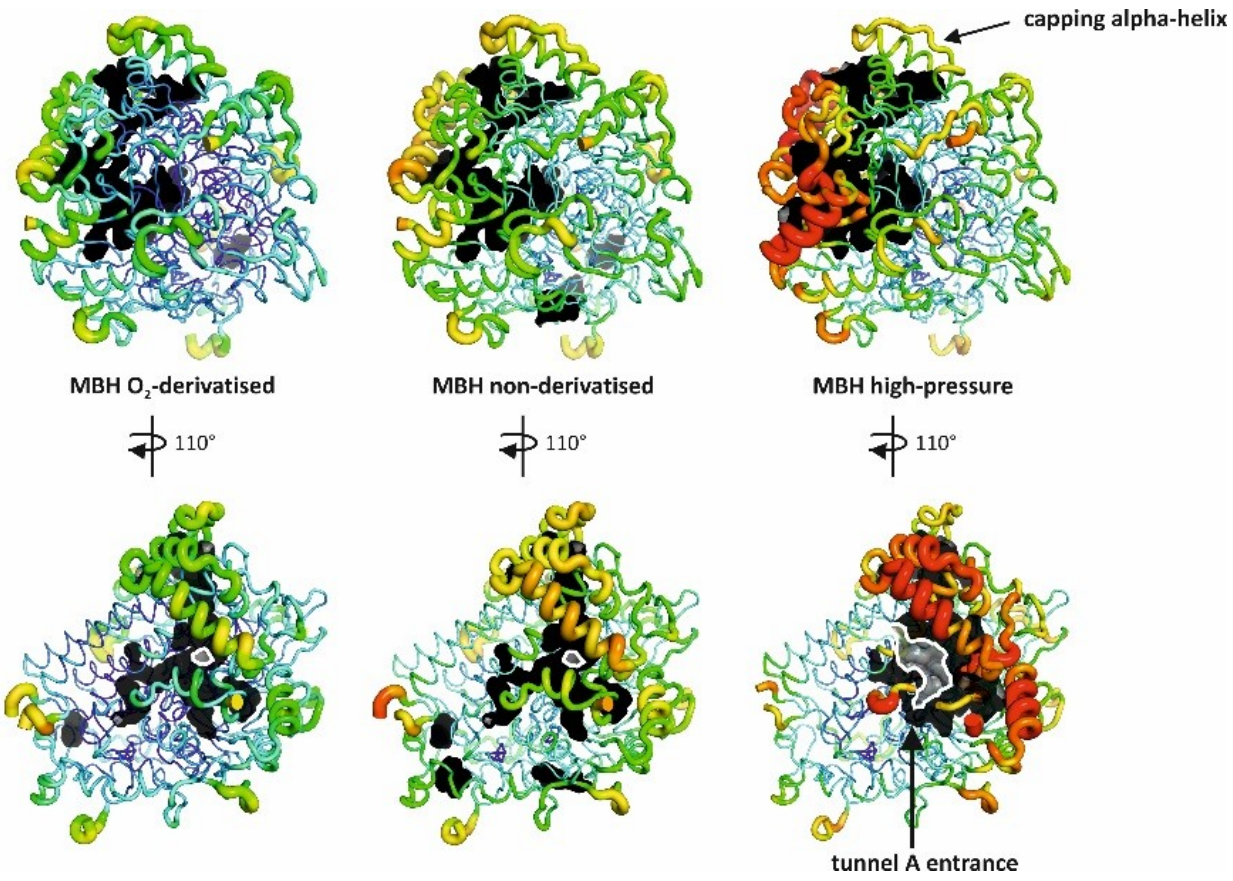

Figure 5 | Comparison of O2-derivatised, reference and high-pressure MBH structures on the basis of the B (temperature)-factors.

All structures are shown in tube representations. Low to high B-factors are represented in the range from blue to red colour and are set from 10 to 50 Å^2. The hydrophobic tunnel is illustrated in black and calculated with *Py*MOL.[24] The lower structures are rotated by 110° and provide a view on the entry of tunnel A edged by a white line.

Table 1 | Oxygen derivatisation experiments.

Data set	Pressure (bar)	Time (min)	Resolution (Å)	Occupancy Oxy1 (%)	Fe4-E76$_s$ distance (Å)	OH^- ligand (%)
1	56	15	1.35	63	2.8	31
2	56	15	1.30	72	2.8	27
3	56	15	1.42	71	3.1	36
4	56	15	1.44	80	2.8	28
6	56	30	1.31	79	2.5	22
7	56	30	1.45	73	2.8	39
8	56	30	1.27	92	2.4	35
9	56	30	1.32	91	2.5	41
10	56	60	1.55	91	2.6	72
5	56	77	1.37	62	2.9	36
11	70	15	1.41	100	2.6	45
12	70	15	1.45	91	2.7	32

Table 2 | Reference data set experiments.

Data set	Resolution (Å)	Fe4-E76s distance (Å)
1	1.40	3.37
2	1.41	3.30
3	1.38	3.50
4	1.36	3.39
5	1.50	3.43

Table 3 | Characteristics of O_2 molecules of derivatised MBH.

O2 position	Close environment (dist. < 4 Å)	$Fo^{O_2} - Fo^{reference}$ peak (σ)	Occupancy (%)	B-factor (Å^2) of O2 atoms
1	$W130_L$, $V280_L$, $I283_L$, $G284_L$, $T473_L$	14.94	100	O1: 29.61 O2: 27.98
2	$M30_L$, $V46_L$, $S47_L$, $F569_L$, $E570_L$, $L573_L$, $L591_L$	8.41	50	O1: 26.91 O2: 28.21
3	$A127_L$, $L128_L$, $V131_L$, $A202_L$, $V203_L$, $Y206_L$	11.42	62	O1: 29.99 O2: 28.47
4	$S21_S$, $E22_S$, $I25_S$, $T47_S$	3.69	56	O1: 30.72 O2: 30.92

Table 4 | Data collection and refinement statistics.

MBH	O_2-derivatised	High-pressure	Non-derivatised (as-isloated)
PDB entry	**5MDL**	**5MDJ**	**5MDK**
Data collection	ESRF, ID30B	ESRF, ID29	ESRF, ID30B
Space group	*P212121*	*P212121*	*P212121*
Cell dimensions			
a, *b*, *c* (Å)	73.13, 95.57, 119.69	73.39, 95.70, 121.57	73.11, 95.57, 119.83
α, *β*, *γ* (°)	90, 90, 90[a]	90, 90, 90[a]	90, 90, 90[a]
Resolution (Å)	47.78 - 1.41 (1.49-1.41)[b]	47.85 - 1.48 (1.56 - 1.48)[b]	47.78 - 1.50 (1.58 - 1.50)[b]
*R*merge[51]	0.064 (0.681)[b]	0.064 (0.839)[b]	0.060 (0.800)[b]
I/(σ)*I*[52]	10.7 (2.0)[b]	12.5 (2.0)[b]	12.4 (1.9)[b]
*CC1/2**	100 (89.6)[b]	100 (82.6)[b]	100 (88)[b]
Completeness (%)	96.4 (94.4)[b]	99.8 (99.4)[b]	99.8 (98.9)[b]
Redundancy	4.8 (4.6)[b]	5.6 (5.2)[b]	5.4 (5.2)[b]
Wilson B factor (Å^2)	14.4	20.7	19.9
Refinement			
Resolution (Å)	1.41	1.48	1.50
No. Reflections	147390	135294	127184
*R*work/ *R*free (%)	13.2 / 16.3	14.4 / 17.8	13.2 / 16.4
No. atoms / residues			
Large subunit (HoxG)	4774 / 601	4687 / 601	4800 / 601
Small subunit (HoxK)	2118 / 269	2057 / 268	2147 / 269
Others:			
[FeS] clusters	22 / 3	23 / 3	22 / 3
[NiFe] active site	9 / 1	9 / 1	9 / 1
Water	617 / 609	478 / 473	656 / 655
Dioxygen	8 / 4	0	0
Cl^-	1 / 1	1 / 1	5 / 3
Mg^{2+}	1 / 1	1/ 1	1 / 1
PEG	7 / 1	0	
Mean B-factor (all atoms; Å^2)	19.59	26.1	24.63
R.m.s.[c] deviations			
Bond lengths (Å)	0.008	0.010	0.007
Bond angles (°)	1.261	1.379	1.249
Ramachandran plot[d],[53]			
% most favoured	98	98	97
Allowed /Disallowed	2/ 0	2/ 0	3/ 0

[a]One crystal was used; [b]highest resolution shell is shown in parenthesis; [c]R.m.s. - root mean square;

[d]as defined in the program RAMPAGE

Table 5 | Selected cluster distances.

	O_2-derivatised	High-pressure	Reference
[NiFe] active site Ni-Fe distance (Å)	2.9	2.9	2.9
[4Fe3S]-cluster Fe4-N20 distance (Å)	2.1	2.2	2.2
[4Fe3S]-cluster Fe4-E76s distance (Å)	2.6	3.2	3.4

Table 6 | Transition matrix for the O_2 diffusion

	bulk	Oxy1	Oxy 2	Oxy 3	Oxy 4	Oxy 5	Oxy 6	Oxy 7
bulk	99.6	0.0	0.0	0.0	0.0	0.0	0.0	0.0
Oxy 1	4.2	70.9	0.0	7.2	0.0	0.0	2.9	14.8
Oxy 2	11.0	0.0	88.9	0.0	0.0	0.0	0.0	0.0
Oxy 3	9.7	6.8	0.0	71.0	7.0	5.5	0.0	0.0
Oxy 4	9.2	0.0	0.0	14.3	69.4	7.1	0.0	0.0
Oxy 5	23.2	0.0	0.1	15.6	9.3	51.8	0.0	0.0
Oxy 6	28.6	5.1	0.0	0.0	0.0	0.0	62.9	3.4
Oxy 7	11.9	15.9	0.0	0.0	0.0	0.0	2.2	70.0

All directional (column to row) gas hopping probabilities are given in %. The “bulk” region contains positions in the solvent or undefined areas in the protein.

Supplementary Information

Tracking the route of molecular oxygen in O_2-tolerant membrane-bound [NiFe] hydrogenase

Jacqueline Kalms [1,#], Andrea Schmidt [1,#], Stefan Frielingsdorf [2], Tillmann Utesch [2], Guillaume Gotthard [3], David von Stetten [3], Peter van der Linden [3], Antoine Royant [3,4], Maria Andrea Mroginski [2], Philippe Carpentier [3,5,6,7], Oliver Lenz [2], and Patrick Scheerer [1,*]

[1]Institut für Medizinische Physik und Biophysik (CC2), Group Protein X-ray Crystallography and Signal Transduction, Charité - Universitätsmedizin Berlin, Charitéplatz 1, 10117, Berlin, Germany.

[2]Institut für Chemie, Sekr. PC14, Technische Universität Berlin, Strasse des 17. Juni 135, 10623, Berlin, Germany.

[3]ESRF-European Synchrotron Radiation Facility, 71 Avenue des Martyrs, Grenoble Cedex 9, 38043, France

[4]Institut de Biologie Structurale, Université Grenoble Alpes, CNRS, CEA, Grenoble, 38044, France.

[5]CEA/DRF/BIG/CBM/BioCat, 17 Avenue des Martyrs, Grenoble Cedex 9, 38054, France.

[6]CNRS UMR 5249, LCBM, Grenoble, France.

[7]Université Grenoble Alpes, LCBM, Grenoble, France.

[#]Both authors contributed equally to this work.

*Correspondence and requests for materials should be addressed to Dr. Patrick Scheerer (phone.: 49-450-524178; E-mail: patrick.scheerer@charite.de)

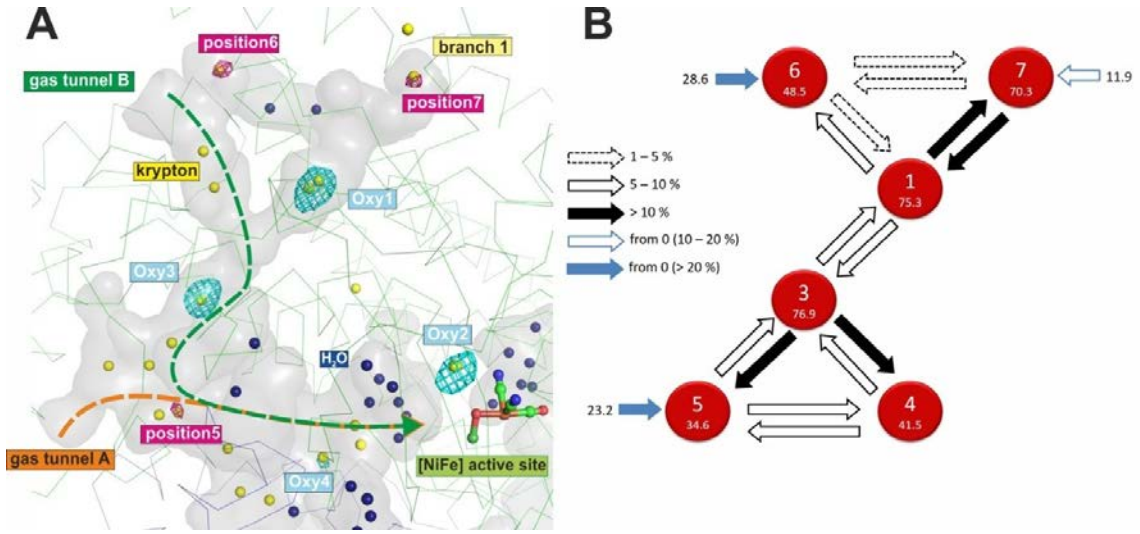

Supplementary Figure 1 | Superposition of O2 and krypton binding positions in gas-derivatised MBH and O2 transition network.

(A) Ribbon/line representation of O_2-derivatised MBH (PDB entry 5MDL) with the hydrophobic gas tunnel shown as grey surface (calculated with *Py*MOL). The [NiFe] active site is depicted as balls and sticks. Krypton atoms (PDB entry 5D51) and water molecules are shown as spheres in yellow and blue, respectively. Binding positions of molecular oxygen are illustrated as cyan mesh of the $Fo^{0_z} - Fo^{reference}$ electron density map contoured at 3 σ. Further possible O_2 binding positions are shown as magenta mesh of the $Fo^{0_z} - Fo^{reference}$ electron density map contoured at 2.5 σ. Gas tunnel A and B calculated by *Caver* are pictured as orange and green dashed arrows, respectively. (B) The transition network consists of six sites (nodes) illustrated as red circles (site 0 and Oxy2 are not shown). The percental occupancy of each site is indicated within the circles. Transitions between nodes are highlighted as arrows, weighted according to their probabilities. Blue arrows mark regions with the highest transition probability coming from state 0, the bulk region (in %).

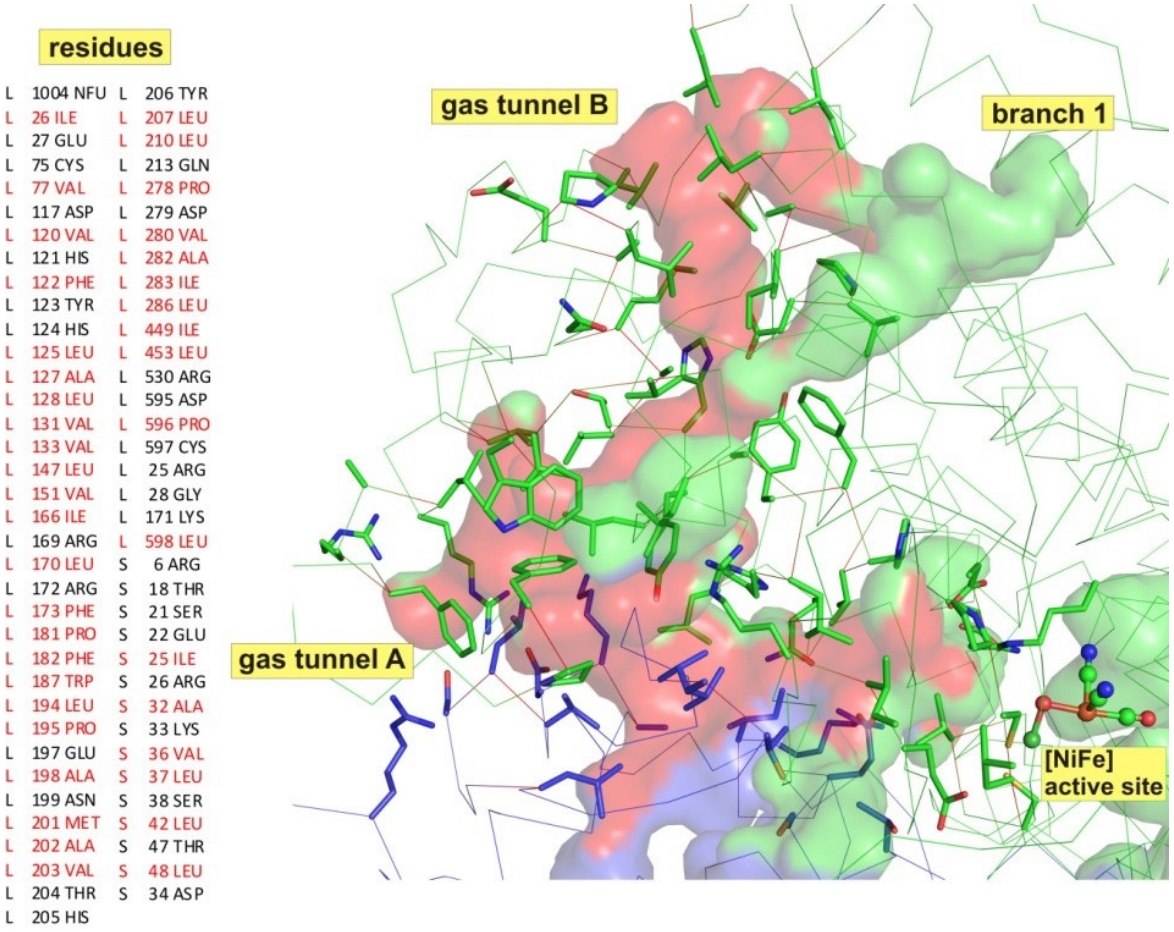

Supplementary Figure 2 | Hydrophobicity of the MBH gas tunnel network.

All amino acids are depicted as sticks in green for the large subunit and in blue for the small subunit. The tunnel is illustrated as surface calculated in *Py*MOL in green for the large subunit and in blue for the small subunit. The red surface shows all hydrophobic amino acids lining the gas tunnel A and B.

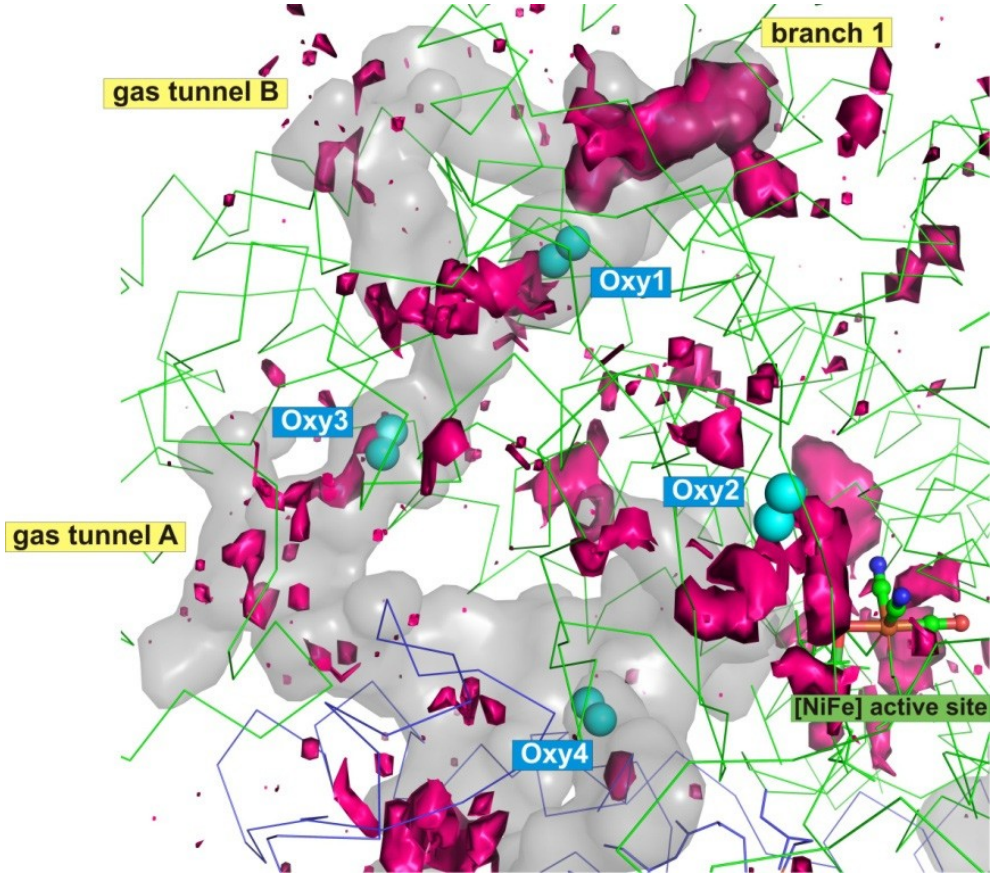

Supplementary Figure 3 | Hydrogen densities from the Molecular dynamics (MD) simulations.

Hydrogen densities obtained from the MD simulations (pink surface) are mapped on the O_2-derivatised MBH. *Py*MOL tunnel depicted as grey surface consisting of tunnel A, tunnel B and branch 1. Further, the oxygen positions determined by the soak-and-freeze approach are indicated cyan spheres. The backbone of the MBH is drawn in the ribbon representation and the active site in the stick and balls representation.

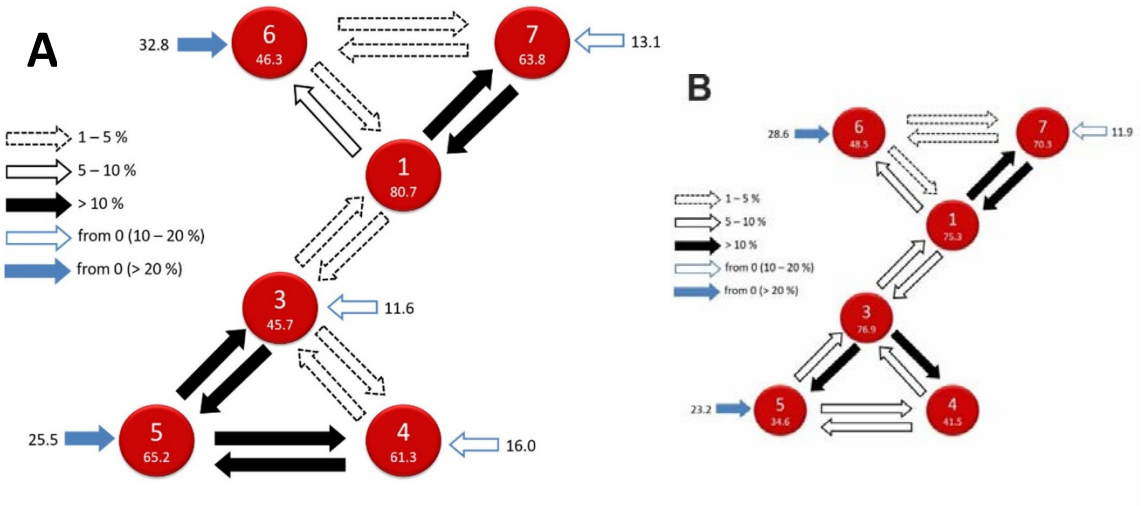

Supplementary Figure 4 | Hydrogen transition (compared to O2) network in the MBH. (A) The transition network consists of six sites (nodes) illustrated as red circles (site 0 and Oxy2 are not shown). The percental occupancy of each site is indicated within the circles. Transition between nodes are highlighted as arrows, weighted according to their probabilities. Blue arrows mark regions with the highest transition probability coming from state 0 (in %). (B) The oxygen transition network as comparison to A (described in Supplementary Figure 1 B).

Supplementary Table 1 | Transition matrix for the H2 diffusion

	bulk	Oxy1	Oxy 2	Oxy 3	Oxy 4	Oxy 5	Oxy 6	Oxy 7
bulk	99.5	0.0	0.0	0.0	0.0	0.1	0.1	0.0
Oxy 1	4.9	72.2	0.3	2.7	0.0	0.2	3.1	16.5
Oxy 2	12.7	0.4	86.4	0.0	0.0	0.5	0.0	0.0
Oxy 3	11.6	4.4	0.0	70.0	3.6	10.4	0.0	0.0
Oxy 4	16.0	0.0	0.0	4.8	57.1	22.1	0.0	0.0
Oxy 5	25.5	0.4	0.7	10.4	17.4	45.3	0.0	0.0
Oxy 6	32.8	6.2	0.0	0.0	0.0	0.0	58.4	2.5
Oxy 7	13.1	24.4	0.0	0.0	0.0	0.0	1.9	60.5

All directional (column to row) gas hopping probabilities are given in %. The "bulk" region contains positions in the solvent or undefined areas in the protein.

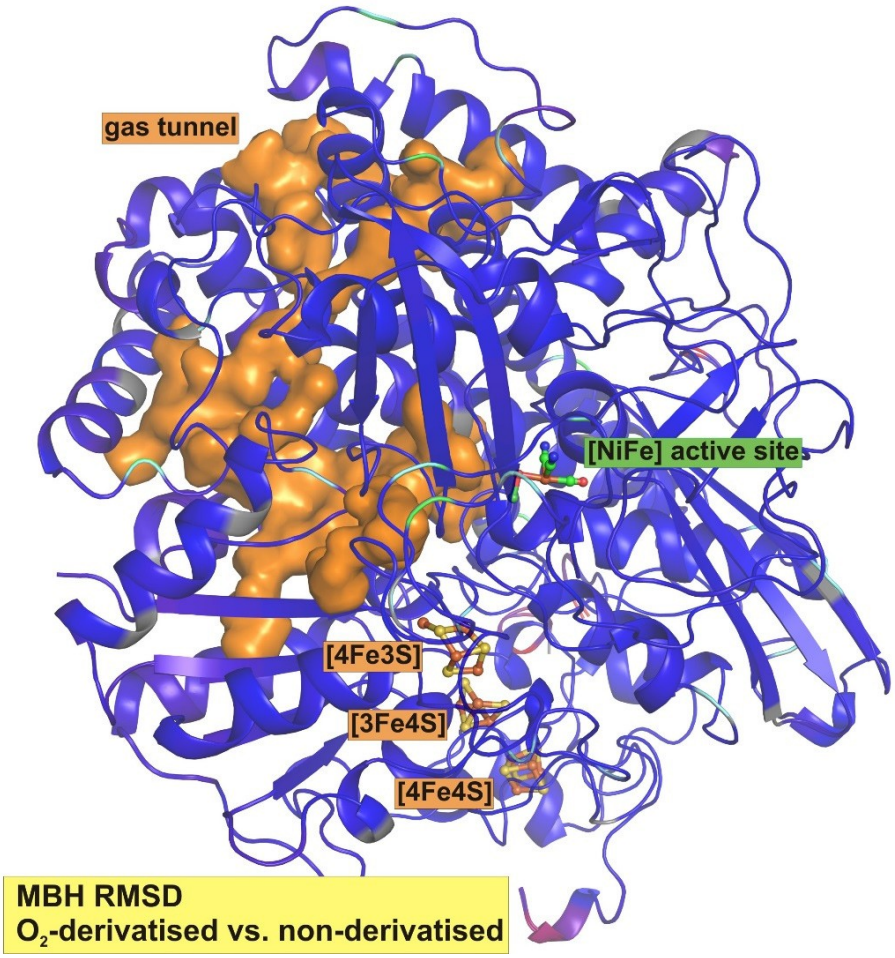

Supplementary Figure 5 | Root mean square deviation (RMSD) of O2-derivatised and non-derivatised MBH.

Ribbon representation of the MBH small and large subunits. [NiFe] active site and [FeS]-clusters are shown in ball and stick representation. The hydrophobic tunnel network is shown as orange surface calculated with *Py*MOL.[21] The two structures were aligned with the program *Py*MOL and the corresponding structural differences were coloured from blue to red. With blue colour specifies the minimum and red maximum pairwise RMSD.

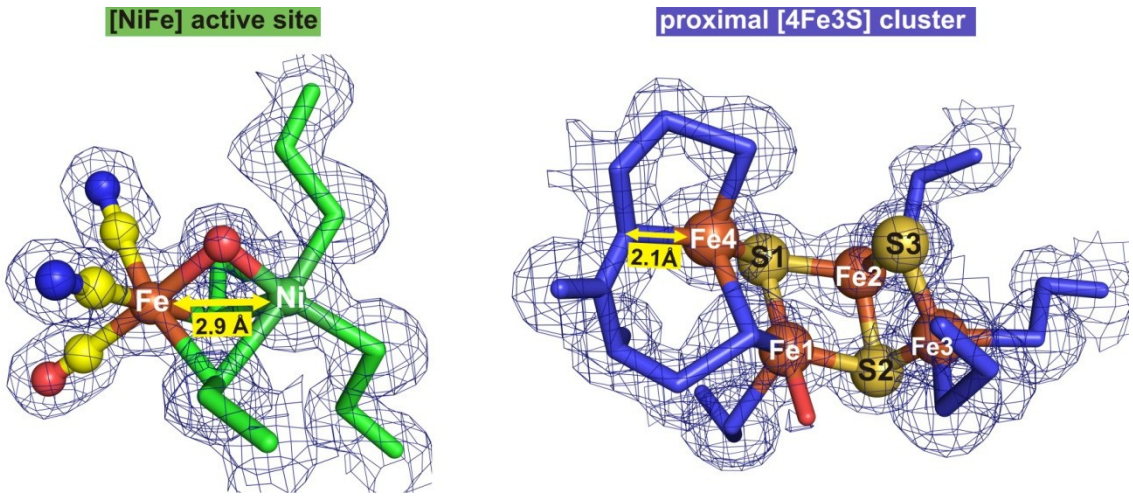

Supplementary Figure 6 | [NiFe] active site and the proximal [4Fe3S] cluster of the O2-derivatised MBH.

The [NiFe] active site and the proximal [4Fe3S] cluster are depicted as ball and stick. The nickel ion is coordinated by four cysteine residues of which two are bound terminally and the other two bridging with the iron atom. Additionally, the iron atom is bound to three diatomic ligands (2x CN^-, CO). In the oxidised state the Ni and Fe are bridged by a hydroxide ligand (red sphere) and have a distance of 2.9 Å. The proximal cluster is shown in its open conformation in the oxidised state where the Fe4 is bound to the backbone nitrogen of cysteine 20 with a bond distance of 2.1 Å. Furthermore, we can find a hydroxyl ligand at the Fe1. For both centers the 2*Fo-Fc* electron density map is depicted as blue mesh and contoured at 1σ.

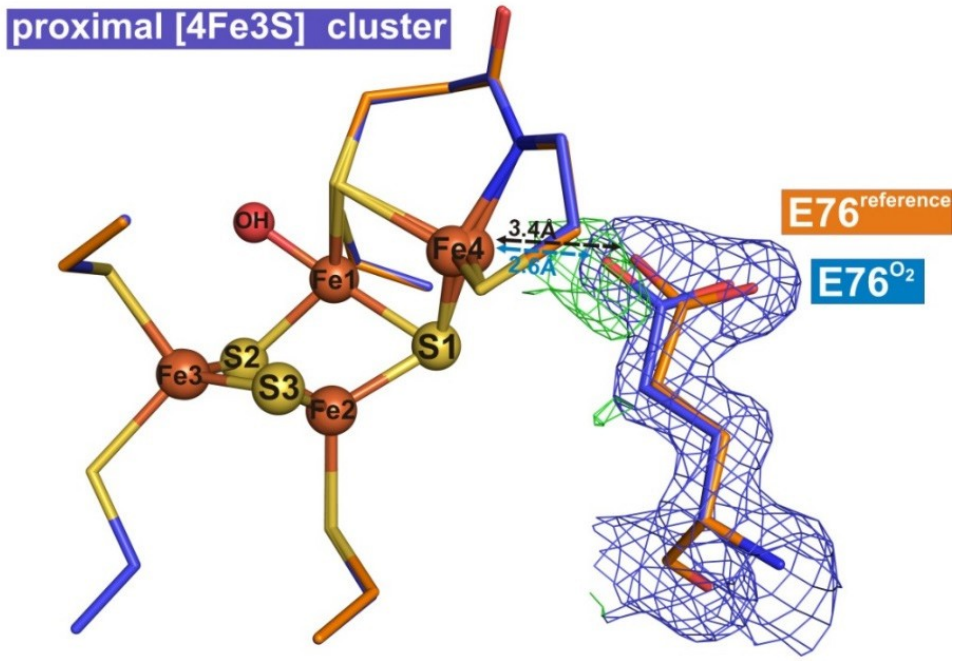

Supplementary Figure 7 | Proximal [4Fe3S] cluster and amino acid E76S of O2-derivatised and non-derivatised MBH.

The proximal cluster of O_2-derivatised (PDB entry 5MDL, blue) and non-derivatised (PDB entry 5MDK, orange) MBH is shown as balls and sticks in its as-isolated state with an open conformation. The 2*Fo-Fc* electron density map of $E76^{reference}$ is illustrated as blue mesh and contoured at 1σ. The $Fo^{0_z} - Fo^{reference}$ electron density map is depicted as green mesh and contoured at 3σ.

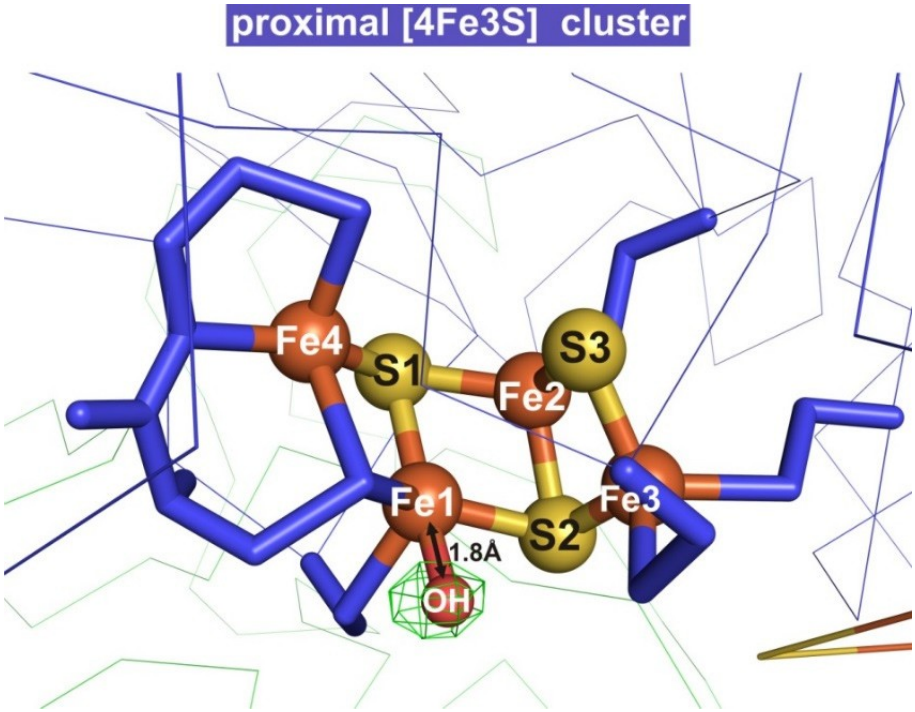

Supplementary Figure 8 | Proximal [4Fe3S] cluster and hydroxyl ligand of the O2-derivatised MBH.

The proximal cluster is shown in its superoxidised state with an open conformation and the hydroxyl ligand bound to Fe1 with a distance of 1.8 Å. The positive *Fo-Fc* electron density map of the hydroxyl ligand is illustrated as green mesh and contoured at 3σ.

8 Lipoxygenase PA-LOX

iii. Structural and functional basis of phospholipid oxygenase activity of bacterial lipoxygenase from Pseudomonas aeruginosa.

Banthiya S, Kalms J*, Galemou Yoga E, Ivanov I, Carpena X, Hamberg M, Kuhn H, Scheerer P. ***Biochim Biophys Acta.*** 2016 Nov; 1861(11):1681-1692.

Biochimica et Biophysica Acta 1861 (2016) 1681–1692

Contents lists available at ScienceDirect

Biochimica et Biophysica Acta

journal homepage: www.elsevier.com/locate/bbalip

Structural and functional basis of phospholipid oxygenase activity of bacterial lipoxygenase from *Pseudomonas aeruginosa*

Swathi Banthiya [a,1], Jacqueline Kalms [b,1], Etienne Galemou Yoga [b], Igor Ivanov [a], Xavi Carpena [c,d], Mats Hamberg [e], Hartmut Kuhn [a,*], Patrick Scheerer [b,**]

[a] Institut für Biochemie, Charité - Universitätsmedizin Berlin, Charitéplatz 1, D-10117 Berlin, Germany
[b] Institut für Medizinische Physik und Biophysik, Group Protein X-ray Crystallography and Signal Transduction, Charité – Universitätsmedizin Berlin, Charitéplatz 1, D-10117 Berlin, Germany
[c] Institut de Biologia Molecular de Barcelona (IBMB-CSIC), Parc Científic de Barcelona, 08028 Barcelona, Spain
[d] XALOC beamline, ALBA synchrotron (CELLS), 08290 Cerdanyola del Vallès, Spain
[e] Department of Medical Biochemistry and Biophysics, Karolinska Institutet, Stockholm, Sweden

ARTICLE INFO

Article history:
Received 19 May 2016
Received in revised form 29 July 2016
Accepted 3 August 2016
Available online 5 August 2016

Keywords:
Eicosanoids
Bacteria
Biomembranes
Protein X-ray crystallography
Protein structure
Inflammation
Infection

ABSTRACT

Pseudomonas aeruginosa expresses a secreted LOX-isoform (PA-LOX, LoxA) capable of oxidizing polyenoic fatty acids to hydroperoxy derivatives. Here we report high-level expression of this enzyme in *E. coli* and its structural and functional characterization. Recombinant PA-LOX oxygenates polyenoic fatty acids including eicosapentaenoic acid and docosahexaenoic acid to the corresponding (n-6)*S*-hydroperoxy derivatives. This reaction involves abstraction of the pro*S*-hydrogen from the n-8 bisallylic methylene. PA-LOX lacks major leukotriene synthase activity but converts 5*S*-HETE and 5*S*,6*R*/*S*-DiHETE to anti-inflammatory and pro-resolving lipoxins. It also exhibits phospholipid oxygenase activity as indicated by the formation of a specific pattern of oxygenation products from different phospholipid subspecies. Multiple mutagenesis studies revealed that PA-LOX does not follow classical concepts explaining the reaction specificity of mammalian LOXs. The crystal structure of PA-LOX was solved with resolutions of up to 1.48 Å and its polypeptide chain is folded as single domain. The substrate-binding pocket consists of two fatty acid binding subcavities and lobby. Subcavity-1 contains the catalytic non-heme iron. A phosphatidylethanolamine molecule occupies the substrate-binding pocket and its sn1 fatty acid is located close to the catalytic non-heme iron. His377, His382, His555, Asn559 and the C-terminal Ile685 function as direct iron ligands and a water molecule (hydroxyl) completes the octahedral ligand sphere. Although the biological relevance of PA-LOX is still unknown its functional characteristics (lipoxin synthase activity) implicate this enzyme in a bacterial evasion strategy aimed at downregulating the hosts' immune system.

1. Introduction

Mammalian lipoxygenases (LOXs) have been implicated in the biosynthesis of bioactive lipids and in cell differentiation but also play a role in the pathogenesis of hyperproliferative, cardiovascular and neurodegenerative diseases [1,2]. The human genome involves six functional LOX genes (ALOX15, ALOX15B, ALOX12, ALOX12B, ALOXE3, ALOX5) whereas in mice seven different ALOX-isoforms (Alox15, Alox15b, Alox12, Alox12b, Alox5, Aloxe3, Aloxe12) exist [3]. However, LOXs are not only expressed in mammals but also occur in lower organisms [4,5] including bacteria [6,7]. Among all bacterial genomes sequenced so far, <0.5% contain LOX-like sequences, which are likely to encode for functional LOX-isoforms. These data suggest that LOXs are not essential for the survival of bacteria [4]. In fact, most human pathogenic bacteria do not carry LOX genes and thus, for many specific bacterial infections, pathogen LOXs may not play a major role for disease development. Bacterial species, which contain putative LOX sequences include firmicutes, different types of proteobacteria, cyanobacteria, actinobacteria and representatives of the CFB group [4]. Bacterial LOXs exhibit different reaction specificity when acting on different fatty acid substrates. For instance, LOX from *Nostoc* sp. *PCC 712* oxygenates linoleic acid preferentially to 9*R*-HpODE [8], whereas the enzyme from *Anabaena* sp. exhibits a variable specificity [8,9]. The LOX from *Acaryochloris marina*, constitutes a fusion protein consisting of an N-terminal heme-domain with a sequence homology to catalase and a C-terminal LOX-domain [10]. When the LOX-domain was separately expressed in *E. coli*, it oxygenated ω-3 fatty acids at the n-7 position with *R* stereo-specificity [11].

* Correspondence to: H. Kuhn, Institut für Biochemie (CC2), Charité – Universitätsmedizin Berlin, Charitéplatz 1, D-10117 Berlin, Germany.
** Correspondence to: P. Scheerer, Institut für Medizinische Physik und Biophysik (CC2), Group Protein X-ray Crystallography and Signal Transduction, Charité – Universitätsmedizin Berlin, Charitéplatz 1, D-10117 Berlin, Germany.
E-mail addresses: hartmut.kuehn@charite.de (H. Kuhn), patrick.scheerer@charite.de (P. Scheerer).
[1] S.B. and J. K. contributed equally to this work.

http://dx.doi.org/10.1016/j.bbalip.2016.08.002
1388-1981/

In 2004 [6] the first bacterial LOX was characterized in the facultative pathogen *Pseudomonas aeruginosa*. This enzyme was named LoxA and we refer to it as PA-LOX throughout this paper. This LOX-isoform has been expressed as recombinant protein and was later on well characterized [6,12,13] with respect to its protein chemical and enzymatic properties. Interestingly, when purified from natural sources it exhibited different protein-chemical and enzymatic properties, which might be related to posttranslational modification of the enzyme [14]. Recombinant PA-LOX was crystallized and its crystal structure revealed remarkable structural differences in comparison to eukaryotic LOX-isoforms. The polypeptide chain is folded into a single domain and thus, the enzyme does not show the classical two-domain structure of eukaryotic LOXs [15–18]. Moreover, the substrate-binding pocket of the recombinant enzyme is large enough to allow the binding of a complete phospholipid molecule. In fact, the crystal structure indicated a phosphatidylethanolamine molecule bound at the active site, which carries one C18 (sn1 position) and one C14/16 (sn2 position) fatty acid [12]. This ligand was spontaneously incorporated into the holoenzyme during recombinant expression and was retained throughout the entire purification procedure. Recently, two additional papers were published about this enzyme. We have reported that pure recombinant PA-LOX is capable of oxygenating intact erythrocyte membranes, which leads to hemolysis and to the formation of specifically oxygenated phospholipids [19]. An even more recent report challenged this hypothesis but implicated the enzyme in biofilm growth in association with the host airway epithelium [20].

Although a number of enzymatic properties of PA-LOX have been explored in the past [13,20], little is known about its reaction specificity with complex substrates. Moreover, no targeted mutagenesis studies have been carried out to alter the enzymatic properties [21–24]. Here we report structural and functional characterization of PA-LOX, which includes the crystal structure of the enzyme in two different space groups at 1.48 Å and 1.90 Å resolution and multiple mutagenesis studies to test the applicability of different mechanistic concepts explaining the reaction specificity of mammalian LOXs.

2. Materials and methods

2.1. Chemicals

The chemicals used were obtained from the following sources: arachidonic acid and linoleic acid from Sigma (Taufkirchen, Germany); HPLC standards of 5(±)-HETE, 12*S*-HETE, 12(±)-HETE, 15*S*-HETE, 15(±)-HETE, 13*S*-HODE and 13(±)-HODE from Cayman Chem. (distributed by Biomol, Hamburg, Germany); sodium borohydride from Life Technologies, Inc. (Eggenstein, Germany); HPLC solvents from Baker (Deventer, The Netherlands); antibiotics and isopropyl-β-thiogalactopyranoside (IPTG) from Carl Roth GmbH (Karlsruhe, Germany); restriction enzymes from Thermo Fisher Scientific-Fermentas (Schwerte, Germany); the *E. coli* strain BL21 (DE3) pLysS from Invitrogen (Carlsbad, USA); *E. coli* strain XL-1 blue from Stratagene (La Jolla, USA). Oligonucleotide synthesis was performed at BioTez (Berlin, Germany). Phospholipid substrates (1-palmitoyl-2-linoleoyl phosphatidylethanolamine, L-phosphatidylionositol sodium salt, 2-linoleoyl-palmitoyl-sn-glycero-3 phosphatidylcholine, 1-palmitoyl-2-linoleoyl-sn-glcero-3-phospho-L-serine sodium salt) 1,2-dilinoleoyl-sn-glycero-3-phosphatidylethanolamine were purchased from Santa Cruz (Heidelberg, Germany), Sigma Aldrich (Schnelldorf, Germany) and Avanti Polar Lipids (Alabama, USA; distributed by Otto Norel, Hamburg, Germany). Nucleic acid sequencing was carried out at Eurofins MWG Operon (Ebersberg, Germany). Native rabbit ALOX15 (rabALOX15) was prepared to apparent electrophoretic homogeneity from a reticulocyte-rich hemolysate supernatant by sequential ammonium sulfate precipitation, anion exchange chromatography and isoelectric focusing [25]. [11*R*-^{2}H]-linoleic acid (pro*R*; 24% deuterated) and [11*S*-^{2}H]-linoleic acid (pro*S*; 98% deuterated) were prepared as earlier described [26,27].

2.2. Bacterial expression, purification and site-directed mutagenesis

Recombinant expression (*E. coli*) and affinity purification of PA-LOX were carried out as described before [19]. Site-directed mutagenesis was performed using the Pfu Ultra II Hotstart 2XPCR Mastermix (Agilent Technologies, California, USA) according to the instructions of the manufacturer. 5–10 bacterial clones were picked for each mutant, plasmids were prepared using NucleoSpin Plasmid Easy Pure kit (Macherey-Nagel, Düren, Germany) and positive clones were identified by nucleotide sequencing (Eurofins Genomics, Ebersberg, Germany). The mutant proteins, which include PA-LOX Glu369Ala, Leu612Val, Met434Val, Phe435Leu, Met434Val + Phe435Leu (Triad concept) and Glu604Tyr + Lys605His (Jisaka concept) were then expressed, purified and used for enzymatic characterization.

2.3. Fatty acid oxygenase activity assays

Linoleic acid and arachidonic acid oxygenase activities of PA-LOX and rabbit ALOX15 were determined either spectro-photometrically using a Shimadzu instrument (Shimadzu UV-2102 PC spectrophotometer, Shimadzu, Duisburg, Germany) or oxygraphically with a Clarke-type oxygen electrode (Hansatech, Norfolk, UK). To quantify the fatty acid oxygenase activity of the other polyenoic fatty acid isomers, aliquots of the enzyme preparations (PA-LOX, rabbit ALOX15) were incubated in 1 ml of PBS (pH 7.4) containing 0.1 mM of different polyenoic fatty acids as substrates. After a three-minute incubation period, the formed hydroperoxy compounds were reduced with sodium borohydride and after acidification, 1 ml of ice-cold methanol was added. The protein precipitate was spun down and aliquots of the clear supernatant were injected to RP-HPLC for identification and quantification of the oxygenation products.

2.4. GC/MS analysis of reaction products

To identify the chemical structure of the major fatty acid oxygenation products of the different polyenoic fatty acids the dominant conjugated dienes were prepared by RP-HPLC, silylated with BSTFA and further analyzed by GC/MS on a Hewlett Packard 5890 Series II Plus gas chromatograph coupled with Hewlett Packard 5971 detector and equipped with a 19091A 101HP-Ultra 1 column (12 m × 0.2 mm, coating thickness 0.33 μm). The injector and ion source temperatures were set at 280 °C and 200 °C, respectively. The derivatized fatty acids were eluted with the following temperature program: isothermically at 70 °C for 3 min and then from 70 to 300 °C at a rate 30 °C/min.

2.5. Determination of iron content

The iron content of the expressed and purified wild-type PA-LOX was computed by atom absorbance spectroscopy on a Perkin-Elmer Life Sciences AA800 instrument equipped with an AS800 auto sampler. The value of the iron content obtained was related to the PA-LOX that was measured spectro-photometrically (1 mg/ml pure PA-LOX gives an absorbance of 1.1 at 280 nm).

2.6. Phospholipid oxygenase activity assay

To quantify the phospholipid oxygenase activity of both, PA-LOX and rabbit ALOX15, aliquots of the enzyme preparations were incubated with phospholipid vesicles as model membranes. The volume of the assay system was adjusted to 1 ml and different membrane and enzyme concentrations were initially tested. After the time periods indicated, the reaction was stopped by the addition of sodium borohydride. Following acidification, the total lipids were extracted from the reaction mixtures [28], the solvent was evaporated and the remaining ester lipids were reconstituted in 1 ml of a 1:1 mixture of chloroform and methanol. Aliquots of this mixture were then either subjected to HPLC

separation of the major phospholipid classes or to alkaline hydrolysis. For this purpose, the solvent was evaporated and the remaining lipids were reconstituted in 0.85 ml methanol. 0.15 ml of 40% KOH was added and the ester lipids were hydrolyzed at 60 °C for 20 min under argon atmosphere. Then the samples were cooled down, acidified with 0.15 ml acetic acid and aliquots of this mixture were injected into RP-HPLC for quantification of the 13-HODE + 15-HETE/linoleic acid + arachidonic acid ratio [29].

2.7. Lipid analytics

HPLC analysis of the LOX products was performed on a Shimadzu instrument equipped with a Hewlett-Packard diode array detector 1040 A by recording the absorbance at 235 nm. Reverse phase-HPLC was carried out on a Nucleodur C18 Gravity column (Marchery-Nagel, Düren, Germany; 250 × 4 mm, 5 μm particle size) coupled with a guard column (8 × 4 mm, 5 μm particle size). A solvent system of methanol/water/acetic acid (85/15/0.1, by volume) was used at a flow rate of 1 ml/min. Normal phase-HPLC (SP-HPLC) was performed on a Nucleosil 100-5 column (250 × 4 mm, 5 μm particle size) with the solvent system n-hexane/2-propanol/acetic acid (100/2/0.1, by volume) and a flow rate of 1 ml/min. Hydroxy fatty acid enantiomers (15-HETE, 13-HODE) were separated by chiral phase HPLC (CP-HPLC) on a Chiralcel OD column (Daicel Chem. Ind., Ltd., Osaka, Japan) using a solvent system consisting of hexane/2-propanol/acetic acid (100/5/0.1, by volume) and a flow rate of 1 ml/min.

2.8. Crystallization of PA-LOX

PA-LOX was crystallized in two different crystallization buffers leading to two crystal forms. Crystallizations were performed with the sitting-drop vapour diffusion method in 24-well Linbro plates (Jena Biosciences, Jena, Germany) and a protein concentration of about 15 mg/ml at 293 K. The first crystallization condition (crystal form 1) was obtained over a reservoir solution containing 10% polyethylene glycol (PEG) 3350, 50 mM magnesium chloride ($MgCl_2$) and 100 mM HEPES buffer at pH 7.5. Precipitants and protein solution were mixed in a 1.5/2 μl ratio into micro-bridges (Hampton Research, Aliso Viejo, USA). After 6–8 weeks the needle shaped PA-LOX crystals were cryo-cooled in liquid nitrogen using 20% glycerol. The reservoir solution of the second crystallization condition (crystal form 2) contained 12% PEG 3350, 0.2 M $MgCl_2$ and 0.1 M tris(hydroxymethyl) aminomethane at pH 7.1. Precipitants, protein solution and seeding stock were mixed into micro-bridges (Hampton Research, Aliso Viejo, USA) according to the Microseed Matrix Seeding (MMS) protocol from Hampton Research. After 3–6 weeks the plate-shaped crystals were cryo-cooled in liquid nitrogen using 25% glycerol as cryo-protectant. The cryo-protectant was mixed to the crystallization buffer in 5% steps (15%, 20% and 25%).

2.9. Data collection and structure analysis

Diffraction data were collected at 100 K using the synchroton X-ray source at BESSY II (Berlin, Germany) and ESRF (Grenoble, France). More detailed information on data collection and evaluation of the X-ray data is given in the supplement. All molecular graphics representations in this work were created using the *PyMOL* software package.

2.10. Structural modeling of enzyme substrate complexes

Both structures of the wild-type PA-LOX enzyme present a phosphatidylethanolamine molecule (ZPE in the PDB entry) in two connected hydrophobic pockets of which one is close to the active site (subcavity 1). We used the electron density of the endogenous ligand to model linoleic acid and arachidonic acid in both PA-LOX structures. Structures of arachidonic acid and linoleic acid were provided by the *COOT* library and were directly modeled into the (positive difference) F_o-F_c electron density map of the ZPE-ligand *via* several steps of rotation, translation and real space refinement. The model-complex structures were finalized using the restrained refinement procedure of the CCP4 program *REFMAC5* and a last refinement of geometric restrains using *COOT* [30]. The structure of 5,8,11-eicosatrienoic acid was created with *PyMOL* using arachidonic acid as template since both fatty acids only differ in the double bond between C14 and C15.

3. Results

3.1. Enzyme preparation and purification

PA-LOX was routinely expressed as N-terminal polyhistidine-tag fusion protein after elimination of the secretion sequence of the native enzyme. After cell lysis the supernatant was loaded on a Ni-agarose column. The majority of the PA-LOX was typically recovered in the elution fractions 1, 2 and 3 (Fig. 1A). Since SDS-PAGE indicated a >90% homogeneity, aliquots of these fractions were employed for most of our experiments as PA-LOX preparation. Applying this expression and purification strategy we typically obtained 3.2 ± 0.3 mg of purified recombinant protein per 50 ml liquid culture ($n = 10$), which corresponds to an expression level of 66 mg pure protein/l bacterial culture fluid. This expression level is 5-fold higher than that achieved in a previous study with a different bacterial expression system [20]. Here an expression level of 12 mg pure protein/l culture fluid was obtained. In SDS-PAGE recombinant PA-LOX migrated with an apparent molecular weight of 70 kDa. Its iron content was 106 ± 3 mol% indicating that the iron supply of the expression system was not critical. In the Deschamps study [20] an iron content of 67% was reported. With fresh enzyme preparations we determined for linoleic acid oxygenation at pH 7.4 a molecular turnover rate of 165 s^{-1} at 165 μM substrate concentration. After freezing and thawing of the enzyme we carried out more detailed kinetic studies for the oxygenation of linoleic acid and arachidonic acid. The Lineweaver-Burk diagrams are shown in Figs. S1 and S2 (see supplement) and the numeric values for the basic kinetic parameters are given in Table 1. The data suggest that under our experimental conditions there is no major preference of the enzyme for either of the two fatty acids (similar kcat/Km ratios) and this conclusion is consistent with previous literature [20]. There is, however, a clear difference between the kcat/Vmax ratios calculated in our study and the Deschamps paper [20]. For instance, for arachidonic acid we obtained a kcat/Km ratio of 0.48 at pH 7.4 but in a previous paper [20] a value of 6.6 $(\mu M\ s)^{-1}$was determined (pH 7.5). Formally, these data suggest that our enzyme preparation may be of lower quality. However, our activity assays were carried out in the absence of any detergents whereas 0.01% of TX-100 was used in the previous study [20]. When we carried out comparative activity assays in the presence and absence of a detergent (deoxycholate) we observed a significant increase in the catalytic activity (Fig. S3). Thus, because of the different assay conditions the kinetic constants calculated in the two studies cannot directly be compared.

3.2. PA-LOX oxidizes linoleic acid and arachidonic acid to the n-6 hydroperoxy derivatives

As indicated above the two major polyenoic fatty acids of mammalian cells (linoleic acid, arachidonic acid) are suitable substrates for PA-LOX. When the recombinant enzyme was incubated *in vitro* separately with linoleic acid and arachidonic acid 13*S*-HpODE (Fig. 1B, I + II) and 15*S*-HpETE (Fig. 1C, I + II) were formed as major oxygenation products. These results are consistent with previous literature data [6,12,20].

3.3. Stereochemistry of PA-LOX catalyzed fatty acid oxygenation

To explore the stereochemistry of fatty acid oxygenation we first analyzed the enantiomer composition of the major products of linoleic

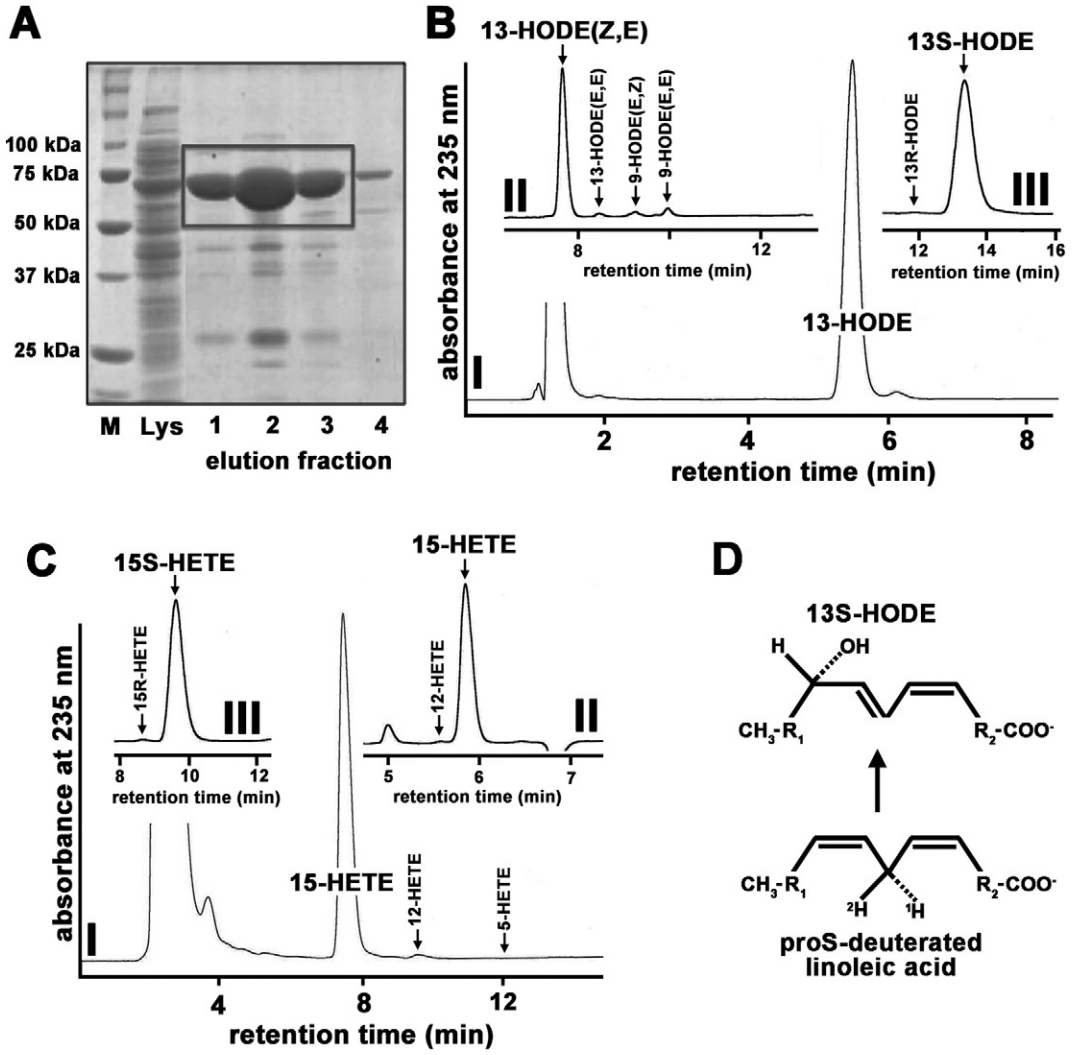

Fig. 1. Recombinant expression of PA-LOX in *E. coli*. Recombinant PA-LOX was expressed as polyhistidine-tag fusion protein in a 50 ml liquid culture. After washing the bacterial pellet was reconstituted in 5 ml of PBS, the cells were lyzed by sonication, debris was spun down. A) An aliquot (1 μl) of the lysis supernatant was applied to SDS-PAGE (Lys). The remaining lysis supernatant was subjected to affinity chromatography on a Ni-agarose column and the polyhistidine-tag fusion proteins were eluted with elution buffer containing 200 mM imidazole. Fractions of 0.3 ml were collected and aliquots of the elution fractions were analyzed by SDS-PAGE. M – molecular weight markers, Lys – lysis supernatant (1 μl), elution fractions 1–4 (2 μl). The gel was stained with Coomassie blue. B) An aliquot (0.1 μl) of the elution fraction 2 was incubated for 5 min in PBS containing 165 μM linoleic acid. The reaction products were prepared as described in Materials and methods and analyzed by RP-, SP- and CP-HPLC. I) RP-HPLC, II) SP-HPLC of linoleic acid oxygenation products. III) CP-HPLC of linoleic acid oxygenation product. C) An aliquot (0.1 μl) of the elution fraction 2 was incubated for 5 min in PBS containing 165 μM arachidonic acid. The reaction products were prepared as described in Materials and methods and analyzed by RP-, SP- and CP-HPLC. I) RP-HPLC, II) SP-HPLC of arachidonic acid oxygenation products. III) CP-HPLC of arachidonic acid oxygenation product. D) Stereochemistry of linoleic acid oxygenation by pure PA-LOX. The pro*S*-hydrogen from C11 of linoleic acid is abstracted and oxygen is introduced antarafacially (13*S*-H(p)ODE formation).

acid and arachidonic acid oxygenation. As indicated in Fig. 1 (III in panels B and C) we found that for 13-H(p)ODE and 15-H(p)ETE the *S*-enantiomers strongly prevailed. Thus, according to the antarafacial character of the LOX reaction the pro*S*-hydrogen should be abstracted from the bisallylic methylene C11 of linoleic acid. To prove abstraction of this hydrogen, we employed 11*S*- (pro*S*) and 11*R*- (pro*R*) deuterated linoleic acids as substrates (Fig. 1D). The major oxygenation product [13-H(p)ODE] was isolated by SP-HPLC and its deuterium content was determined by GC/MS. Employing pro*R*-deuterated linoleic acid, 88.5 ± 1.5% of the deuterium was retained in the reaction product

Table 1
Basic kinetic parameters for linoleic acid and arachidonic acid oxygenation by pure PA-LOX. Pure PA-LOX was incubated in PBS (2.1 μg/ml) in the presence of arachidonic acid or linoleic acid at five different substrate concentrations (10 μM, 20 μM, 50 μM, 100 μM, 165 μM) and the increase in absorbance at 235 nm was measured spectro-photometrically (double readings at each substrate concentration). The data were used to construct Lineweaver-Burk plots and the kinetic parameters were extracted from these diagrams.

Substrate	Vmax (μM/min)	Km (μM)	kcat/Km (μM s^{-1})
Arachidonic acid	42.3	48.9	0.48
Linoleic acid	117.8	174.0	0.38

Table 2
Stereospecific hydrogen abstraction during linoleic acid oxygenation by PA-LOX and rabbit ALOX15. PA-LOX (0.32 μg/ml for [11*R*-^{2}H]-labeled substrate, 3.2 μg/ml for [11*S*-^{2}H]-labeled substrate) and rabbit ALOX15 (3.5 μg/ml for [11*R*-^{2}H]-labeled substrate, 35 μg/ml for [11*S*-^{2}H]-labeled substrate) were incubated for 5 min with the two substrates (50 μM final concentration) and the linoleate oxygenase reaction was followed spectro-photometrically. The hydroperoxy compounds formed were reduced, the major oxygenation product was prepared by sequential RP- and SP-HPLC and analyzed by GC/MS. Because of the kinetic isotopic effect 10-fold higher enzyme concentrations were used for the incubations with [11*S*-^{2}H]-deuterated substrate.

LOX-isoform	Deuterated substrate	Deuterium retention (%)	Deuterated substrate	Deuterium retention (%)
PA-LOX	[11*R*-^{2}H]	88.5 ± 1.5	[11*S*-^{2}H]-	3.3 ± 0.6
rabALOX15		89.0 ± 0.0		3.0 ± 0.0

(Table 2). In contrast, when we used pro*S*-deuterated substrate only 3.3 ± 0.6% of the label was retained. These data indicate that PA-LOX abstracts the pro*S*-hydrogen from C-11 of linoleic acid and thus, the enzyme follows the antarafacial concept of the LOX reaction. Similar results were obtained for the rabbit enzyme when taken through the same experimental protocol (Table 2).

3.4. Storage stability of purified PA-LOX

To explore the stability of recombinant PA-LOX the enzyme was incubated at 4 °C for different time sets in the absence or presence of glycerol. The enzymatic activity (spectro-photometric assay) was determined as suitable readout parameter. As indicated in Fig. 2A the enzyme loses about 60% of its activity during the first 24 h of incubation independent of the presence or absence of glycerol. At longer incubation periods the decrease in catalytic activity was much less rapid.

3.5. Temperature profile and activation energy

Next, we explored the temperature dependence of the catalytic activity and calculated the activation energy. From Fig. 2B it can be seen that the catalytic activity of PA-LOX increases with temperature until 35 °C but then a sudden drop was observed. In previous studies on the temperature dependence of PA-LOX it was found that 25 °C was the optimal temperature of fatty acid oxygenation [13,20]. These data suggest that our enzyme preparation is functionally more resistant against elevated temperatures. The loss in activity above 35 °C is likely to be due to thermal denaturation and these activity data have not been considered for calculation of the activation energy. The activity data obtained between 5 °C and 35 °C were employed to construct the Arrhenius-plot (Fig. 2C) and from the slope of the linear regression curve an activation energy of 33.8 kJ/mol × K was calculated. Comparative experiments for native rabbit ALOX15 under identical experimental conditions indicated that thermal denaturation was already initiated at temperatures above 25 °C and that the activation energy for this enzyme (calculated for the temperature range between 5 °C and 25 °C) was significantly lower (14.3 kJ/mol × K).

3.6. Substrate specificity for different polyenoic fatty acids

The ω-6 polyenoic fatty acids linoleic acid and arachidonic acid are the dominating polyenoic fatty acids in mammalian cells. To explore whether ω-3 or ω-9 fatty acids are also oxygenated by PA-LOX we determined the relative oxygenation rate of different polyenoic fatty acids as well as the structures of the major oxygenation products formed. From Table 3 it can be seen that all ω-6 and ω-3 fatty acids are oxygenated at the n-6th carbon atom regardless of the presence or absence of an additional double bond in the methyl terminus of the fatty acid. In contrast, the n-9 fatty acid C20:Δ5,8,11 was not well oxygenated. In fact, in our standard spectro-photometric assay we were unable to record any increase in absorbance at 235 nm and thus, no kinetic parameters could be determined. However, when we analyzed the reaction products prepared from a large scale incubation the corresponding 5-hydro(pero)xy derivative was identified as major reaction product (Fig. 3A–C) as

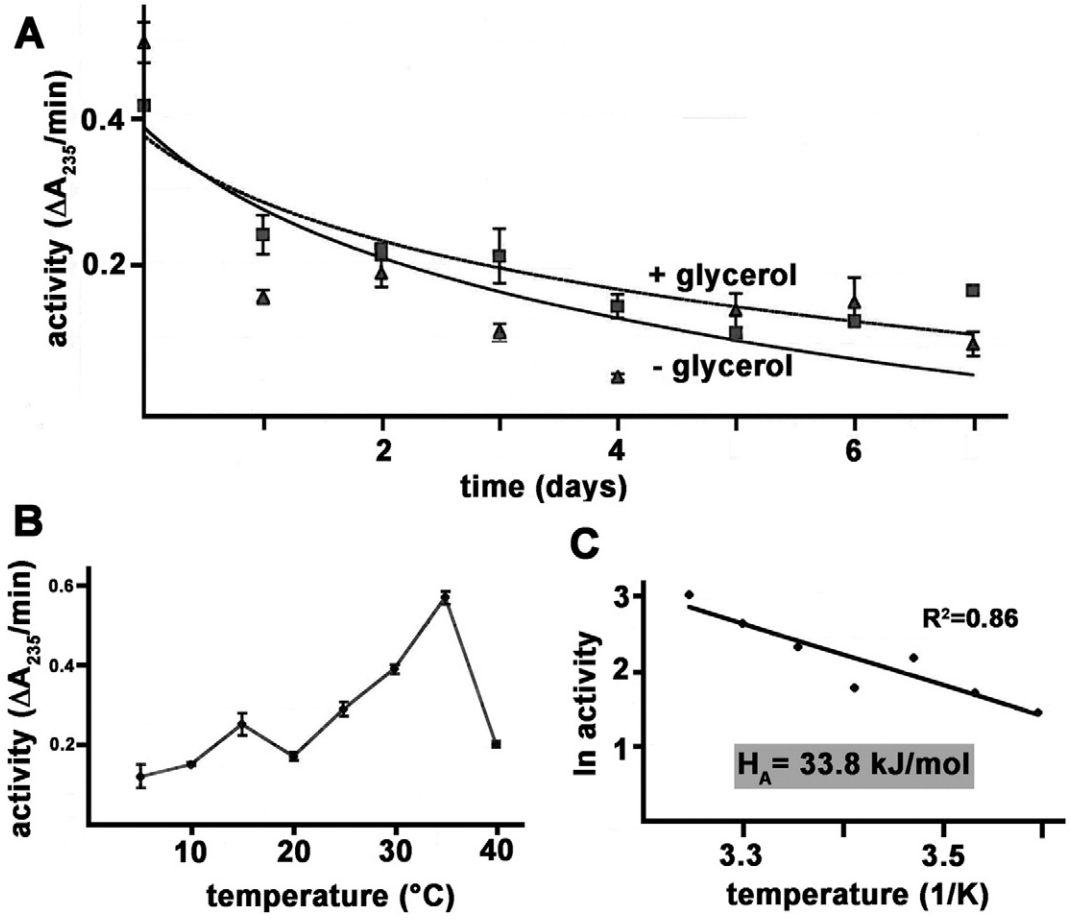

Fig. 2. Long-term stability and temperature profile of linoleic acid oxygenation by recombinant PA-LOX. A) Long-term stability: A solution of recombinant PA-LOX (16.7 mg/ml PBS) was incubated in the presence and absence of 10% glycerol at 4 °C. Aliquots were taken at the time points, diluted and linoleic acid oxygenase activity was assayed spectro-photometrically at room temperature in triplicate. B) Temperature profile: Linoleic acid oxygenase activity of purified recombinant PA-LOX was assayed spectro-photometrically at different temperatures in triplicate. The initial rates of the kinetic progress curves were used to plot the temperature profile. C) Activation energy: The catalytic activities of recombinant PA-LOX from the temperature profile in the range between 5 °C and 35 °C were taken to construct the Arrhenius plot. The activation energy was calculated from the slope of the linear regression curve.

Table 3
Fatty acid oxygenase activity of PA-LOX with different polyenoic fatty acids.

Chain length	Class	Substrate fatty acid	Rel. catalytic efficiency (%)	Position of oxygenation	Most informative key ions in MS *m/z* (rel. abundance)
C18	ω-6	C18:Δ9,12	50	n-6 (C_{13})	n.a.
		C18:Δ6,9,12	11	n-6 (C_{13})	173 (100), 367 (10.7) α-cleavage, 438 (0.1, M^+)
	ω-3	C18:Δ9,12,15	11	n-6 (C_{13})	171 (84.1), 369 (8.8), α-cleavage, 438 (0.4, M^+)
		C18:Δ6,9,12,15	6	n-6 (C_{13})	171 (82.3), 367 (2.0), α-cleavage, 436 (0.2, M^+)
C20	ω-9	C20:Δ5,8,11	n.d.	n-15 (C_5)	261 (100, α-cleavage), 466 (0.2, M^+)
	ω-6	C20:Δ11,14	66	n-6 (C_{15})	173 (100, α-cleavage), 468 (0.7, M^+)
		C20:Δ8,11,14	428	n-6 (C_{15})	173 (100, α-cleavage), 466 (0.7, M^+)
		C20:Δ5,8,11,14	100	n-6 (C_{15})	173 (90.9, α-cleavage), 464 (0.5, M^+)
	ω-3	C20:Δ8,11,14,17	39	n-6 (C_{15})	171 (90.9, α-cleavage), 464 (0.2, M^+)
		C20:Δ5,8,11,14,17	6	n-6 (C_{15})	171 (69.3, α-cleavage), 462 (0.4, M^+)
C22	ω-3	C22:Δ4,7,10,13,16,19	367	n-6 (C_{17})	171 (48.0, α-cleavage), 488 (0.2, M^+)

n.a. – not analyzed, n.d. – undetectably low in the spectro-photometric assay.

indicated by the key ions at *m/z* 261 (relative abundance of 100%) and the molecular ion at *m/z* 466 (relative abundance of 0.2%). Thus, with a polyenoic fatty acid lacking the n-8th bisallylic methylene the enzyme exhibits 5-lipoxygenating activity. However, the rate of 5-lipoxygenation is much lower than that of 15-lipoxygenation of arachidonic acid. Among the fatty acids tested, C20:Δ8,11,14 (ω-6) and C22:Δ4,7,1,0,13,16,19 (ω-3) (DHA) were most effectively oxygenated under our experimental conditions whereas C20:Δ5,8,11,14,17(ω-3) (EPA) was not a good substrate. Among the C18 fatty acids linoleic acid turned out to be the best substrate. Here the presence of an additional double bond impaired the catalytic efficiency. Similar experiments were carried out in a previous study [20] but different results on the substrate specificity of the enzymes were obtained. For instance, the most preferred substrate in the Deschamps study was arachidonic acid (C20:Δ5,8,11,14). Linoleic acid (C18:Δ9,12), eicosapentaenoic acid (C20:Δ5,8,11,14,17), docosahexaenoic acid (C22:Δ4,7,10,13,16,19) and di-homo-gamma-linoleic acid (C20:Δ8,11,14) were less effectively oxygenated. We found that among the fatty acids tested di-homo-gamma-linoleic acid (C20:Δ8,11,14) was the best substrate followed by docosahexaenoic acid (C22:Δ4,7,10,13,16,19), arachidonic acid (C20:Δ5,8,11,14), linoleic acid (C18:Δ9,12) and linolenic acid (C18:Δ6,9,12) and (C18:Δ9,12,15). Eicosapentaenoic acid (C20:Δ5,8,11,14,17) was much less effectively oxygenated under our experimental conditions. The reasons for these conflicting results remain unclear but the different substrate concentrations (10 μM in the Deschamps [20] study *vs.* 0.1 mM in our study) and the differences in the assay conditions [20] (pH 7.0 *vs.* 7.4) may contribute. Interestingly, there were no major differences in the product patterns indicating that the reaction specificity did not depend on the variable assay conditions.

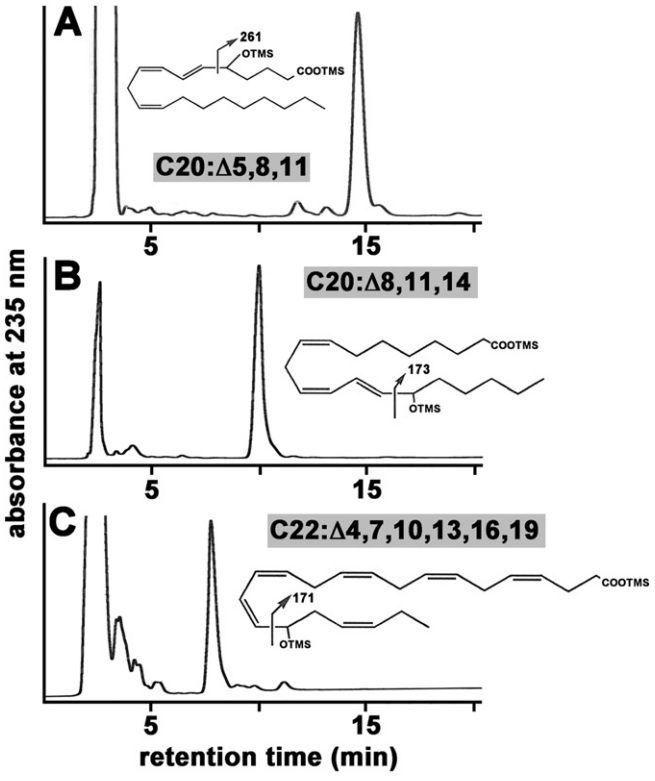

Fig. 3. Profile of oxygenation products formed from selected polyenoic fatty acids by recombinant PA-LOX. Bacterial lysate supernatant PA-LOX (2–11 μg/ml) was incubated in PBS with the different fatty acids as described in the legend of Table 2. The major reaction products were prepared by RP-HPLC, silylated and further analyzed by GC/MS. The indicative fragmentation pattern is given in the insets. A) C20:Δ5,8,11 (ω-9), 11 μg; B) C20:Δ8,11,14 (ω-6), 5.5 μg; C) C22:Δ4,7,10,13,16,19 (ω-3), 2.2 μg.

3.7. Leukotriene and lipoxin synthase activity

Rabbit ALOX15 exhibits a 14,15-epoxyleukotriene synthase activity converting 15*S*-HpETE to 14,15-epoxyleukotriene A4 [31] and a lipoxin synthase activity [32]. To test whether PA-LOX does also exhibit such catalytic activities we first incubated the enzyme with low 15*S*-HpETE concentrations and analyzed the conjugated trienes by RP-HPLC. As reference enzyme (positive control) pure native rabbit ALOX15 was used. With the rabbit enzyme we observed the formation of significant amounts of conjugated trienes (Fig. 4A). These compounds were not formed with 15*S*-HETE suggesting their origin as double oxygenation products. Thus, they should be formed *via* the 14,15-epoxy leukotriene pathway. Interestingly, these products could only be detected in small amounts if PA-LOX was used for the incubation under identical conditions (Fig. 4A). This data is consistent with the results reported in a previous study [20] showing that 15-HpETE may not be a good substrate for PA-LOX. Moreover, when we quantified the amounts of 15-H(p)ETE that was not converted during the incubation period we found that compared to non-enzyme control incubations most of the substrate was recovered for PA-LOX. In contrast, with rabbit ALOX15 <10% of the substrate was found. These data indicate that 15-HpETE was not converted by PA-LOX.

Lipoxins are anti-inflammatory eicosanoids, which can be biosynthesized *via* transcellular mechanisms involving various LOX-isoforms [33,34]. To examine the lipoxin synthase activity of PA-LOX we incubated the enzyme either with 5*S*-HETE (Fig. 4B) or with a 1:1 mixture of 5*S*,6*S*- and 5*S*,6*R*-DiHETE (Fig. 4C), which constitute major reaction products of the ALOX5 pathways. Then we analyzed the formation of conjugated tetraenes by recording the chromatogram at 300 nm. As indicated in Fig. 4B + C PA-LOX formed a mixture of conjugated tetraene isomers indicating its lipoxin synthase activity. It should, however, been stressed that quantitative evaluation of the chromatograms indicated that the lipoxin synthase activity was 2.5-orders of magnitude lower than arachdonic acid oxygenase activity. We added 2.5-fold more enzyme and analyzed 260-fold lower amounts of products. In a previous study [20] the authors concluded that PA-LOX does not exhibit a lipoxin synthase activity, which conflicts with our HPLC analyses.

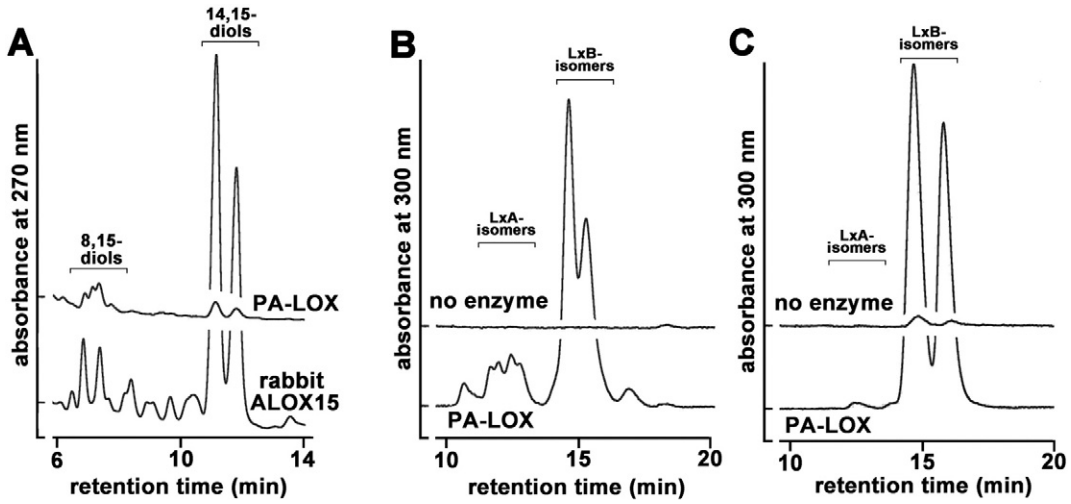

Fig. 4. Leukotriene synthase and lipoxin synthase activity of PA-LOX. A) Leukotriene synthase activity: Purified PA-LOX (52 μg/ml) was incubated in PBS with 25 μM 15-HpETE for 10 min. The reaction products were reduced with sodium borohydride and analyzed by RP-HPLC recording the absorbance at 270 nm. For comparison leukotriene formation by rabbit ALOX15 (similar arachidonic acid oxygenase activity) was analyzed. B + C) Lipoxin synthase activity: Purified PA-LOX (2 μg/ml) was incubated with in PBS with 30 μM of 5*S*-HETE (panel B) and 5,6-DiHETE (panel C) for 10 min. The reaction products were reduced with sodium borohydride and analyzed by RP-HPLC recording the absorbance at 300 nm.

3.8. Phospholipid oxygenase activity

The previous crystal structure of PA-LOX revealed that a phospholipid molecule occupies the putative substrate-binding pocket [12] and recent experiments with erythrocyte membranes indicated the capability of PA-LOX to oxygenate membrane phospholipids and to destroy intact red blood cells [19]. However, the efficiency of phospholipid oxygenation has not been quantified and the structures of the oxygenation products have not been determined. To address these questions we incubated PA-LOX and rabbit ALOX15 with different phospholipid preparations and quantified the oxygenation efficiency analyzing the extent of product formation within a 5 min incubation period. For this purpose, we reduced the reaction products after the incubation period with borohydride, extracted the lipids, hydrolyzed the phospholipids under alkaline conditions and quantified the conjugated dienes by RP-HPLC. Fig. 5A shows that conjugated dienes, which co-migrated with authentic standards of 13-HODE and 15-HETE (not separated under these conditions) were formed. These products could not be detected when the substrate was incubated in the absence of the LOX. Next, we prepared the major conjugated dienes by RP-HPLC and further analyzed them by SP-HPLC (Fig. 5B). Here we found that the majority of the conjugated dienes co-migrated with authentic standards of 13-HODE(Z,E). 9-HODE (E,Z) and the corresponding all-E-isomers were only formed in small amounts. Chiral phase HPLC (Fig. 5C) indicated a strong preponderance of 13*S*-HODE. Taken together, these data indicate a specific phospholipid oxygenase activity of PA-LOX. In order to quantify this catalytic activity and to compare it with the phospholipid oxygenase activity of rabbit ALOX15 we carried out comparative experiments of the two enzymes with different phospholipid substrates and compared it with the linoleic acid oxygenase activity of the two enzymes. The corresponding results are summarized in Table 4 and the following conclusions can be drawn: i) For both enzymes the linoleic acid oxygenase activity is much higher than the phospholipid oxygenase activity. ii) When normalized to a similar linoleic acid oxygenase activity rabbit ALOX15 exhibits a higher phospholipid oxygenase activity than PA-LOX. iii) Among the different phospholipids, phosphatidylethanolamine appears to be the preferred substrate for both enzymes. iv) For all substrates specific product patterns were analyzed indicating that the stereochemistry of the oxygenation reaction was tightly enzyme controlled. Only for PS oxygenation by PA-LOX a relatively high share of unspecific oxygenation products are formed, suggesting incomplete enzyme control.

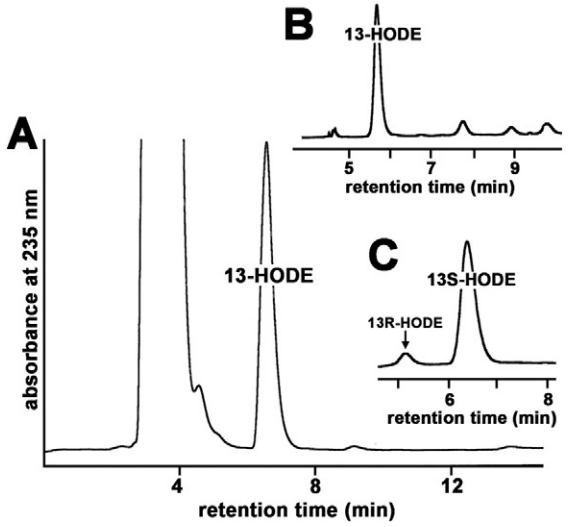

Fig. 5. Product specificity of PA-LOX catalyzed oxygenation of 1-palmitoyl-2-linoleoyl-phosphatidylethanolamine. Purified PA-LOX (50 μg/ml) was incubated in PBS with 165 μM of 1-palmitoyl-2-linoleoyl-phosphatidylethanolamine for 5 min in the presence 0.5% sodium cholate. The reaction products were reduced with sodium borohydride, hydrolyzed under alkaline conditions and analyzed by RP-HPLC recording the absorbance at 235 nm. B) The conjugated dienes were collected, the solvent was evaporated and the remaining lipids were further analyzed by SP-HPLC. C) To obtain information of the enantiomer composition the 13-HODE formed was purified by SP-HPLC and analyzed by CP-HPLC.

Table 4
Comparison of phospholipid oxygenase activity of PA-LOX and rabbit ALOX15. Aliquots of native purified rabbit ALOX15 and recombinant PA-LOX (Ni-agarose elution fraction 2) were incubated with the different phospholipids in PBS at room temperature for 15 min. The phospholipid concentration were normalized to a linoleic acid content of 165 μM. The oxygenation products were reduced, the lipids were extracted and hydrolyzed under alkaline conditions. 13-HODE was prepared by RP-HPLC and further analyzed by CP-HPLC.

Substrate	PA-LOX		Rabbit ALOX15	
	Rel. activity (%)	13*S*/13*R*-ratio (%)	Rel. activity (%)	13*S*/13*R*-ratio (%)
Linoleic acid	100	99:1	100	95:5
PE	0.06	93:7	8.3	95:5
PS	0.04	64:36	<0.01	83:17
PI	0.05	95:5	0.5	88:12
PC	0.02	78:22	0.5	77:23

Table 5
Reaction specificity of LOX mutants with arachidonic acid. The mutants indicated were created, the proteins were expressed and aliquots of the Ni-agarose elution fraction 2 were incubated with arachidonic acid for 5 min. The reaction products were prepared and analyzed by RP-HPLC. For comparison the literature data for rabALOX15 are given [22].

Determinant	Rabbit ALOX15			PA-LOX		
	Mutant	12-HETE (%)	15-HETE (%)	Mutant	12-HETE (%)	15-HETE (%)
Borngräber I	F353A	80	20	E369A	0	100
Sloane	I418A	92	8	M434V	0	100
Sloane	M419A	12	88	F435L	0	100
Borngräber II	I593A	45	55	L612V	0	100
Jisaka [39][#]	D602Y + V603H	70[*]	30	E604Y + K605H	0[*]	100

[#] Human ALOX15B.
[*] 8-HETE.

In an additional set of experiments we compared monolinoleoyl-PE with a dilinoleoyl-PE as substrate for PA-LOX. Here we found that the formation of 13S-HODE from dilinoleoyl-PE was 7.2 ± 1.0-fold higher suggesting that the dilinoleoyl derivative is a better substrate for this enzyme. Taken together our experiments with phospholipids as LOX-substrates indicate that PA-LOX exhibits a phospholipid oxygenase activity, which is however, more then 3 orders of magnitude lower than the linoleic acid oxygenase activity. In a previous study [20] the authors suggested that PA-LOX does not exhibit a phospholipid oxygenase activity. This conclusion conflicts with our HPLC analyses and with our previous findings that pure PA-LOX *in vitro* induces lysis of red cells [19]. Moreover, the capability of the enzyme to bind a phospholipid in the crystal structure [12] provides a plausible explanation for the phospholipid oxygenase activity of the enzyme. However, as observed for the lipoxin synthase activity the phospholipid oxygenase activity is much lower than the fatty acid oxygenase activity of the enzyme.

3.9. Mutagenesis studies of reaction specificity determinants

Mammalian ALOX15 orthologs follow the triad concept [22,35], which explains the reaction specificity of these enzymes. Corresponding mutagenesis studies on rabbit and human ALOX15 convert these enzymes into 12-lipoxygenating isoforms [22,36]. On the other hand, the 12-lipoxygenating ALOX15 isoforms of pigs [37], mice [38] and rhesus monkeys [24] can be converted to 15-lipoxygenating enzyme species by mutagenesis of the triad determinants. To test the applicability of the triad concept for PA-LOX we performed multiple mutagenesis studies and tested the reaction specificity of the mutants. As indicated in Table 5 neither of the mutants exhibited a major 12-lipoxygenating activity and thus, the triad concept may not be applicable for PA-LOX.

PA-LOX shares a similar degree of amino acid conservation with human ALOX15B (31.2% amino acid identity) as it does with human ALOX15 (26.1% amino acid identity). Previous studies suggested that the triad concept is not applicable to human ALOX15B [24]. Instead, Asp603 and Val604 have been identified as sequence determinants of human ALOX15B and simultaneous mutagenesis of these residues (Asp603Tyr + Val604His) altered the reaction specificity of this enzyme in favor of 8-lipoxygenation [39]. A sequence alignment of human ALOX15B and PA-LOX indicated that in PA-LOX Glu604 and Lys605 occupy these positions. When we mutated these residues in PA-LOX (Glu604Tyr + Lys605His) we did not observe major alterations in the reaction specificity (Table 5). Thus, the enzyme does not follow this concept either.

3.10. Crystal structures of PA-LOX

Three PA-LOX crystal structures have recently been solved at 1.75 Å resolution (wild-type; PDB entry 4G32; SG: $P2_12_12$), 2.0 Å resolution (wild-type; PDB entry 4G33, SG: $C222_1$) [12] and 1.6 Å resolution (Gly188Glu mutant, PDB entry 4RPE, SG: $C2$). In all of these structures a phosphatidylethanolamine molecule (ZPE) is bound at the active site. The phosphate group of the endogenous ligand in the Gly188Glu mutant differs somewhat from the crystal structure in space group $C222_1$ due to the amino acid substitution at the entrance of the substrate-binding pocket. When we crystallized our recombinant PA-LOX we also obtained two different crystal forms and solved the corresponding crystal structures at a resolution of 1.9 Å (crystal form 1; PDB entry 5IR5; SG: $P2_12_12$) and 1.48 Å (crystal form 2; PDB entry 5IR4; SG: $C222_1$), respectively. Data collection and refinement statistics of our crystallization studies are given in Table 6 and the main results can briefly be summarized as follows: i) The overall structure (Fig. 6A–D) indicates a single polypeptide monomer, which does not fold into the classical two-domain structure of eukaryotic LOXs. ii) In all crystal structures the putative substrate-binding pocket involves a phosphatidylethanolamine molecule (ZPE of the PDB nomenclature). This pocket consists of three different parts (Fig. 6C + D). The two fatty acid moieties of the phospholipid occupy two different subcavities. The sn1 fatty acid arm is localized in the catalytic subcavity, which also contains the catalytic non-heme iron. The sn2 fatty acid arm is localized in subcavity 2 and does not have direct access to the metal ion. In the "lobby" the polar head group of the phospholipid is arrested. In the structure of the crystal form 1 (SG: $P2_12_12$) the phosphate group interacts with Arg422 *via* a hydrogen bond and the terminal amino group of the ethanolamine moiety forms a salt bridge with Asp190 (Fig. 7A/inset). iii) The N-terminal β-barrel domain of eukaryotic LOX-isoforms is absent, but a cluster of helices may function as lid structure covering the entrance into the substrate binding pocket (Fig. 7A). iv) This lid is differently oriented with respect to the catalytic domain (slight rotation by approximately 5°) in the two crystal forms suggesting a certain degree of motional flexibility. v) In both crystal forms the catalytic center involves the non-heme iron, which is monodentate ligated by three conserved histidines (in PA-LOX: His377, His382, His555), Asn559, the C-terminal Ile685 and a water molecule or a hydroxyl, which completes

Table 6
Data collection and refinement statistics of PA-LOX crystal structures.

	PA-LOX, crystal form 1 PDB entry 5IR5	PA-LOX, crystal form 2 PDB entry 5IR4
Beamline	ESRF; ID23-1 (Grenoble, France)	ESRF; ID23-1 (Grenoble, France)
Number of crystals	1	1
Space group	$P2_12_12$	$C222_1$
Unit cell (a, b, c [Å] α, β, γ [°])	133.09, 116.35, 42.72; 90.00, 90.00, 90.00	83.74, 97.39, 153.84; 90.00, 90.00, 90.00
Wavelength [Å]	0.97242	0.97242
Resolution [Å]	43.8–1.9 (2.0–1.9)	48.97–1.48 (1.56–1.48)
R_{pim}	0.034 (0.249)	0.035 (0.355)
R_{merge}	0.065 (0.471)	0.076 (0.774)
I/σ (I)	13.1 (2.8)	14.5 (2.0)
Completeness [%]	99.6 (99.8)	99.8 (99.0)
Redundancy	4.4 (4.4)	5.6 (5.6)
R_{work} [%]	14.4	13.6
R_{free} [%]	18.2	15.5
Ramachandran favoured [%]	94.2	94.7
Ramachandran allowed [%]	5.8	5.3
Ramachandran outlier [%]	0.0	0.0
RMSD superpose (*LSQKAB*)	0.118 (PDB entry 4G32)	0.364 (PDB entry 4G33)

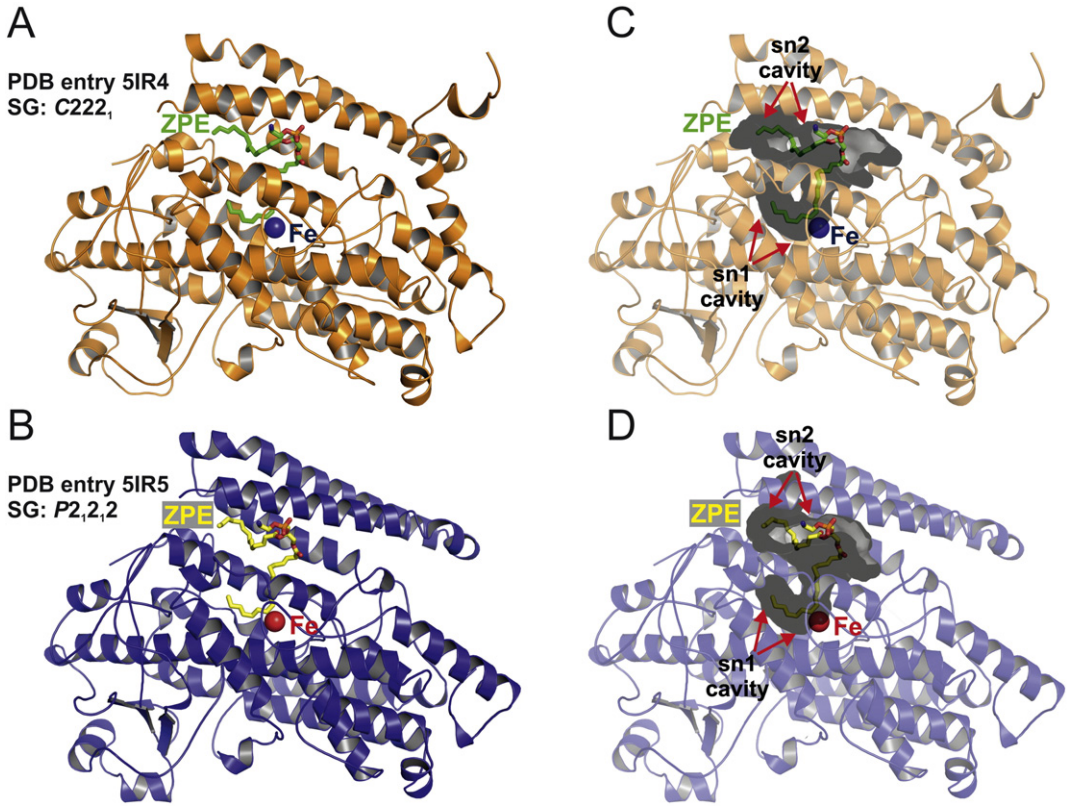

Fig. 6. Crystal structures of PA-LOX with endogenous ligand at the active site. Overall structure of PA-LOX are shown as cartoon representations for the two different crystal forms ((A) crystal form 2, SG: $C222_1$, PDB entry 5IR4, 1.48 Å resolution, depicted in orange color and (B) crystal form 1, SG: $P2_12_12$, PDB entry 5IR5, 1.9 Å resolution, depicted in blue color). The endogenous ligand phosphatidylethanolamine is shown as sticks in green or yellow color as well as the active site iron atom is shown as sphere in blue and red color for the two crystal forms, $C222_1$ and $P2_12_12$ respectively. In C (for crystal form 2) and D (for crystal form 1) surface representations of the substrate cavity with the bound endogenous ligand 1-vaccenyl-2-palmitoyl phosphatidylethanolamine (ZPE) are depicted which illustrate the entrance for the substrate calculated with the program *PyMOL* and colored in grey. The sn1 fatty acid (probably vaccenic acid) is bound in subcavity 1, the sn2 fatty acid (myristoyl or palmitoyl acid) in subcavity 2 and the glycerol moiety including the polar head group occupies the lobby.

the octahedral ligand sphere (Fig. 7B). Similar to the crystal structure of human ALOX5 [15] one of the His ligands (His377 in PA-LOX) shows a different stereochemical orientation when compared with the other two His ligands [40]. For His377 the angle between the plane of the imidazole ring and the iron was >10°. In contrast, the corresponding angle for the other His iron ligands (His382, His555) was close to 0°. A very similar situation has been observed for human ALOX5 where the corresponding His might function as mobile iron ligand, which has been implicated in the catalytic cycle [40]. The water (hydroxyl), which is in hydrogen bond distance to the iron (2.2 Å), forms a hydrogen bridge to the carboxylate oxygen of C-terminal Ile685 (Fig. 7B). The bottom of subcavity 1 is sealed by the amino acids Glu373, Met374, Leu424, Ile431, Met434, Phe430, Phe435, Gln562, Ile608 and Tyr609. The bottom of subcavity 2 is surrounded by amino acids Ile117, Phe120, Val189, Ala196, Ser197, Ile192, Leu193, Leu600, Leu603, Glu604 as well as Phe430 and Ile608, which form a hydrophobic barrier between the

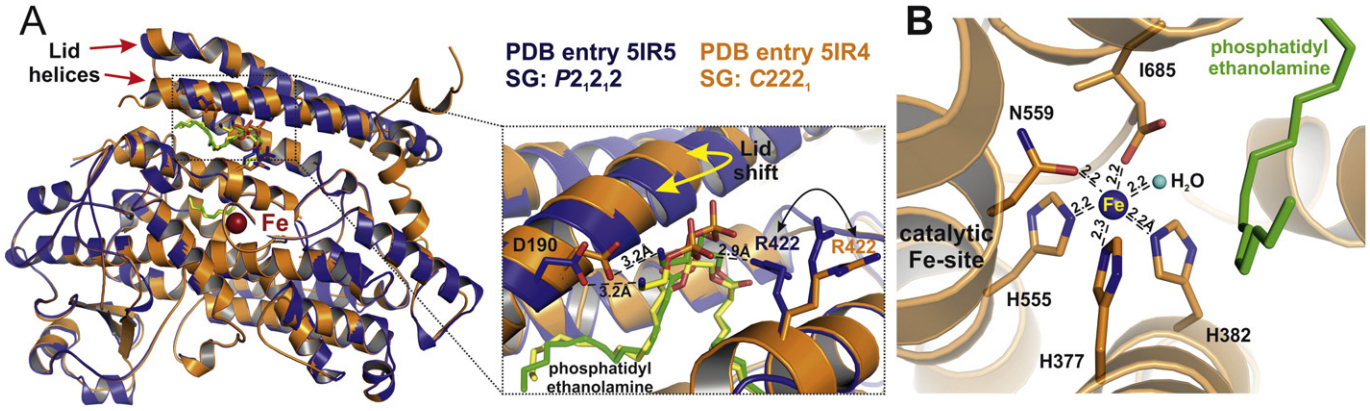

Fig. 7. Structural comparison of PA-LOX crystal structures. (A) Cartoon representation of the superimposed PA-LOX crystal structures in two different crystal forms (crystal form 1, $P2_12_12$, depicted in blue color and crystal form 2, SG: $C222_1$, depicted in orange). Phosphatidylethanolamine (ZPE) shown as sticks in green (crystal form 2) or yellow (crystal form 1) color. The active site iron depicted as sphere in red. Inset: Close-up view of substrate entrance site: The phosphatidylethanolamine head group is coordinated by D190 and R422 via hydrogen bonds in crystal form 1 whereas in crystal form 2 the lid helical structure is shifted away (indicated by a yellow arrow) and the ligand head group has no interaction with R422 (indicated by a black arrow). (B) The catalytic active site iron atom (shown as blue sphere) is coordinated by five amino acids (shown as sticks) and a water molecule (shown as cyan sphere).

two subcavities. vi) When we superimposed the X-ray structures of the two crystal forms (PDB entries 4G32/4G33) described in the literature [12] with the crystallographic data obtained here we found a high degree of similarity. In fact, except for minor structural differences in the cavity the structures are virtually identical with a root-mean-square deviation (RMSD) of 0.12 and 0.36 for the crystal structures of the space groups $P2_12_12$ and $C222_1$, respectively.

3.11. Structural modeling of PA-LOX fatty acid complexes

The endogenous ligand (ZPE) does not carry a bisallylic methylene and thus, is not a good oxygenation substrate. To explore the structural basis for the stereo-selective hydrogen abstraction (Table 2) we modeled the ligand structures of linoleic acid and arachidonic acid into the PA-LOX crystal structures on the basis of the *Fo-Fc* electron density of the endogenous ligand (ZPE). Here we found (Fig. 8A) that linoleic acid is oriented at the active site in such a way that the pro*S*-hydrogen atom at C11 of the linoleic acid backbone is localized in close proximity (2.2 Å) to the active site water (hydroxyl). In contrast, the pro*R*-hydrogen is more distant (3.7 Å) and this data is consistent with preferential abstraction of the pro*S*-hydrogen during PA-LOX catalyzed linoleic acid oxygenation (Table 2). The methyl tail of arachidonic acid (Fig. 8B) is similarly aligned at the active site as that of linoleic acid so that the pro*S*-hydrogen at C13 is located in close proximity (2.3 Å) to the active site water (hydroxyl). The alignment is consistent with the observed 15*S*-lipoxygenating activity of the enzyme (Fig. 1). 5,8,11-eicosatrienoic acid is not a good substrate for PA-LOX (Table 3). When we modeled the structure of the enzyme-fatty acid complex (Fig. 8C) we found a very similar orientation of the methyl terminus of the substrate fatty acid as for linoleic acid and arachidonic acid. The two bisallylic methylenes of 5,8,11-eicosatrienoic (C10, C7) are far distant from the active site water molecule and for the C10 hydrogens the following distances have been determined: C10-pro*S* – 5.7 Å, C10-pro*R* – 5.5 Å. Thus, the two C10-hydrogens are >5 Å apart from the active site water so that abstraction of either of them is unlikely. This conclusion is consistent with our observation that 5,8,11-eicosatrienoic acid is not a suitable substrate for PA-LOX.

4. Discussion

LOX-isoforms have been identified in two of the three domains of terrestrial life but apparently do not occur in archaea and viruses [4]. In bacteria, LOX rarely occur (<0.5% of all bacteria contain putative lipoxygenase sequences) but certain bacteria including *Pseudomonas aeruginosa* have acquired such sequences *via* horizontal gene transfer [41] and have retained them as functional genes for millions of years. Thus, there appears to be an evolutionary pressure on these sequences preventing inactivating mutations.

Although PA-LOX has been discovered >10 years ago [6] its biological role remains to be explored. Since bacteria do not carry large amounts of polyenoic fatty acids the major substrates for the secreted enzyme should come from the host cells. On the basis of the currently available data three different mechanistic scenarios for the biological relevance of PA-LOX may be discussed: i) Role of PA-LOX in biofilm formation. *In vitro* cell culture experiments recently suggested that PA-LOX is required for biofilm formation when *Pseudomonas aeruginosa* interacts with host cells [20]. In contrast, the enzyme was not essential for biofilm formation in abiotic *in vitro* systems. Although the authors suggest that expression of PA-LOX might alter lipid signaling during host cell pathogen interaction, which may impact biofilm formation, the molecular basis for these observations remain to be clarified. It remains to be worked out, which PA-LOX products are responsible for triggering biofilm formation and how exactly the triggering process proceeds. ii) Role of PA-LOX in *PA* infectiousness and invasiveness: Introduction of PA-LOX into the *PA* genome might have improved the invasiveness of the bacteria to make them more infectious [6]. Our finding that the enzyme is capable of oxygenating membrane phospholipids (Table 4) supports this hypothesis. Moreover, the ability of the enzyme to induce hemolysis when incubated *in vitro* with human red blood cells [19] is also consistent with this hypothesis. iii) Role of PA-LOX in bacterial evasion to silence the host immune response: *PA* infections induce an immune response in the host to counteract bacterial multiplication. Secretion of PA-LOX and its catalytic activity outside the bacteria might be part of an evasion strategy aimed at downregulating the host immune response to prolong bacterial life and to enable more rapid multiplication. LOXs have been implicated in the biosynthesis of pro- [42] and anti-inflammatory mediators [43]. To test whether PA-LOX might be involved in the biosynthesis of pro-inflammatory mediators, which are likely to upregulate the host immune response, we determined the leukotriene synthase [31] activity of this enzyme. In comparison with rabbit ALOX15 we found that PA-LOX does not exhibit major leukotriene synthase activity (Fig. 4). Next, we tested the capacity of PA-LOX for the biosynthesis of anti-inflammatory lipoxins. Since lipoxins are synthesized *in vivo* by transcellular mechanisms involving arachidonic acid 5- and 12/15-lipoxygenating enzymes [44] we incubated pure PA-LOX with 5*S*-HETE (arachidonic acid oxygenation product) and 5*S*,6*S*/*R*-DiHETE (LTA_4-hydrolysis products), two major products of the ALOX5 pathways. Here we found that when normalized to similar

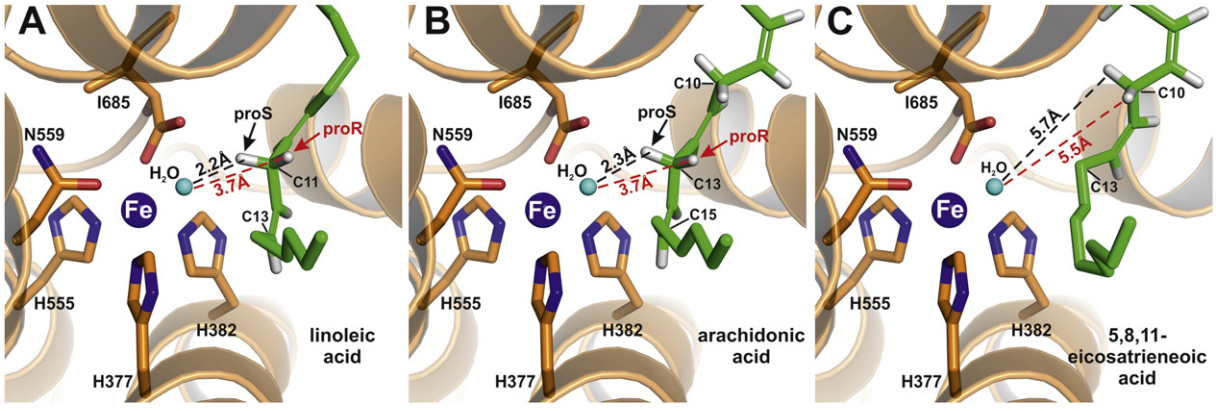

Fig. 8. Structural models of PA-LOX substrate complexes. The enzyme-substrate complexes were modeled on the basis of the X-ray structure coordinates of the PA-LOX phosphatidylethanolamine complex as described in Materials and methods. The active site amino acids and the ligand are shown as sticks and the protein is depicted as orange cartoon. The iron atom and water molecule are illustrated as spheres in blue and cyan, respectively. (A) PA-LOX-linoleic acid complex model: Linoleic acid was modeled into the position of the endogenous ligand. (B) PA-LOX-arachidonic acid complex model: Arachidonic acid was modeled into the position of the endogenous ligand. (C) PA-LOX-5,8,11-eicosatrienoic acid complex model: 5,8,11-eicosatrienoic acid is modeled into the position of the endogenous ligand. The hydrogens at the bisallylic methylenes (C10, C7) have larger distances to the active site water, which explains the low oxygenation rate.

arachidonic acid oxygenase activity PA-LOX and rabbit ALOX15 exhibit similar lipoxin synthase activities. These data suggest that PA-LOX might constitute part of an evasion strategy of the bacteria to silence the inflammatory host reaction.

When our manuscript was in the review process Deschamps and coworkers [20] reported that a recombinant version of PA-LOX does neither exhibit phospholipid oxygenase nor lipoxin synthase activity. This conclusion was mainly based on kinetic *in vitro* data and on the observation that at enzyme concentrations, which are sufficient for polyenoic fatty oxygenation, phospholipid oxygenase activity and lipoxin synthase activity are virtually indetectable. In contrast, at higher enzyme concentrations we were able to show that in principle PA-LOX exhibits both, phospholipid oxygenase and lipoxin synthase activity. However, the biologically most important question that needs to be answered in the future is whether the high enzyme concentrations required for phospholipid oxygenation and lipoxin formation are actually reached *in vivo*. Moreover, it remains to be explored whether red blood cells prepared from patients suffering from *P. aeruginosa* sepsis contain specific PA-LOX-related phospholipid oxygenation products in their membrane lipids as it was shown after *in vitro* incubation of pure PA-LOX with human red blood cells [19]. These questions can hardly be answered on the basis of the currently available experimental data. Local enzyme concentrations have not been quantified so far in any *P. aeruginosa in vivo* infection model and there are no literature data on local PA-LOX concentrations in human disease. The availability of specific antibodies against this enzyme may help to answer these questions in the future.

Another possible reason for the partly conflicting enzyme characteristics (different substrate specificity, different pH and temperature dependence) reported here and in the previous study [20] may be the different protein chemical properties of the enzyme. Our enzyme preparation migrated in SDS-PAGE at a molecular weight of 70 kDa. In the other study [20] a molecular weight of 76 kDa was determined. This difference in molecular mass may be related to the fact that during construction of the expression plasmid 29 additional amino acid have been introduced between the his tag and the native PA-LOX sequence. In our expression system this artificial sequence was kept to a minimum (11 amino acids). In other words, the two enzymes are not identical and the differences in protein chemistry might contribute to the functional differences observed in the two studies. The only way to sort this out is to compare the functional enzyme characteristics in side-by-side experiments.

When PA-LOX was purified from the periplasm of native bacteria it was reported to exhibit major oleic acid oxygenase activity [14] and a similar catalytic activity was later on reported for the recombinant enzyme [45]. Thus, in the databases this enzyme is frequently referred to as oleic acid 10-lipoxygenase. We carried out oxygraphic measurements with the pure recombinant PA-LOX but did not detect major oleic acid oxygenase activity. In fact, when we compared the oxygen uptake in the presence of linoleic acid and oleic acid we hardly detected any oxygen consumption with oleic acid. We are well aware of the fact that oxygraphic measurements are not very sensitive to completely exclude an oleic acid oxygenase activity of the enzyme but in our hand PA-LOX as mammalian LOXs strongly prefers polyenoic fatty acids over monoenoic ones.

In our PA-LOX crystal structure the two fatty acid residues of the bound phosphatidylethanolamine occupy two different subcavities. The sn1 fatty acid is buried in the catalytic cavity (sn1 cavity), which involves the catalytic non-heme iron. The sn2 fatty acid is located in sn2 cavity and has no access to the iron. The polar head group of the phospholipid is surface exposed and forms 2 ionic bonds with charged surface amino acids. Its phosphate group interacts with Arg422 and the terminal amino group of the ethanolamine moiety forms a salt bridge with Asp190. These interactions, which have also been observed in the previous 1.75 Å structure [12], arrest the phospholipid molecule at the active site of the enzyme. Thus, from the structural point of view it seems unlikely that the sn2 fatty acid can occupy the catalytic cavity (subcavity 1). However, in mammalian membrane phospholipids polyunsaturated fatty acid are overwhelmingly bound at the sn2 position whereas saturated fatty acids are usually localized at the sn1 position. When we compared the phospholipid oxygenase activity of PA-LOX with 1-palmitoyl,2-linoleyl phosphatidylethanolamine with that of 1-linoleoyl,2-linoleoyl phosphatidylethanolamine we found that the latter phospholipid is much more effectively oxygenated by PA-LOX than the former one. This data is consistent with preferential binding of the sn1 fatty acid in the catalytic cavity. However, it remains to be worked out by docking studies or co-crystallization experiments whether the binding of other phospholipids (PC, PI, PS) is less selective so that the two fatty acid moieties may randomly be bound in the two sub-pockets.

List of non-standard abbreviations

PA	*Pseudomonas aeruginosa*
LOX	lipoxygenase
12*S*-H(p)ETE	12*S*-hydro(pero)xy-5Z,8Z,10E,14Z-eicosatetraenoic acid
15*S*-H(p)ETE	15*S*-hydro(pero)xy-5Z,8Z,11Z,13E-eicosatetraenoic acid
13*S*-HODE	13*S*-hydro(pero)xy-9Z,11E-octadecadienoic acid
9*S*-HODE	9*S*-hydro(pero)xy-10E,12Z-octadecadienoic acid
LTA4	leukotriene A4
BSTFA	*N,O-Bis*(trimethylsilyl)trifluoroacetamide

Conflict of interest

The authors declare that they do not have any conflicts of interest with the content of this article.

Transparency Document

The Transparency Document associated with article can be found, in online version.

Acknowledgements and funding

We are grateful to Uwe Müller, Manfred Weiss and the scientific staff of the BESSY-MX/Helmholtz Zentrum Berlin für Materialien und Energie at beamlines BL14.1, BL14.2 and BL14.3 operated by the Joint Berlin MX-Laboratory at the BESSY II electron storage ring (Berlin-Adlershof, Germany) and the scientific staff of the European Synchrotron Radiation Facility (ESRF, Grenoble) at beamlines ID14-1, ID14-4, ID23-2, ID30A-3, ID30B and ID23-1, where the data were collected, for continuous support. This work was financially supported by grants from the Deutsche Forschungsgemeinschaft - DFG (GRK1673 to H.K.; Ku961/11-1 to H.K.; SFB740 to P.S.; SFB1078 to P.S.) and DFG - Cluster of Excellence 'Unifying Concepts in Catalysis' (Research Field D3/E3-1 to J.K. and P.S.). The authors would like to thank Dr. R. Tauber from the Institute of Laboratory Medicine, Clinical Chemistry and Pathobiochemistry, Charite - Universitätsmedizin Berlin for continuous support of our work.

Author contributions

S.B. carried out preparation, and functional characterization of the enzyme. J.K. performed crystal trials and X-ray diffraction data collection. J.K., E.G.Y. and P.S. performed structural refinement and structural modeling. I.I. analyzed the fatty acid oxygenation products by GC/MS (Table 3). X.C. provided the expression plasmid. M.H. provided the deuterated linoleic acid isomers and carried out GC/MS analysis of the oxygenation products obtained from these substrates. H.K. and P.S. planned the study, designed and coordinated the experiments. Together with S.B., H.K. also carried out HPLC analysis of the lipids. All authors contributed to ms writing.

Data deposition

The atomic coordinates and structure factor amplitudes have been deposited in the Protein Data Bank, www.pdb.org (PDB ID codes: 5IR4, 5IR5).

Appendix A. Supplementary data

Supplementary data to this article can be found online at http://dx.doi.org/10.1016/j.bbalip.2016.08.002.

References

[1] J.Z. Haeggstrom, C.D. Funk, Lipoxygenase and leukotriene pathways: biochemistry, biology, and roles in disease, Chem. Rev. 111 (2011) 5866–5898.
[2] H. Kuhn, S. Banthiya, K. van Leyen, Mammalian lipoxygenases and their biological relevance, Biochim. Biophys. Acta 1851 (2015) 308–330.
[3] C.D. Funk, X.S. Chen, E.N. Johnson, L. Zhao, Lipoxygenase genes and their targeted disruption, Prostaglandins Other Lipid Mediat. 68-69 (2002) 303–312.
[4] T. Horn, S. Adel, R. Schumann, S. Sur, K.R. Kakularam, A. Polamarasetty, P. Redanna, H. Kuhn, D. Heydeck, Evolutionary aspects of lipoxygenases and genetic diversity of human leukotriene signaling, Prog. Lipid Res. 57C (2014) 13–39.
[5] A.R. Brash, W.E. Boeglin, M.S. Chang, B.H. Shieh, Purification and molecular cloning of an 8R-lipoxygenase from the coral *Plexaura homomalla* reveal the related primary structures of R- and S-lipoxygenases, J. Biol. Chem. 271 (1996) 20949–20957.
[6] R.E. Vance, S. Hong, K. Gronert, C.N. Serhan, J.J. Mekalanos, The opportunistic pathogen *Pseudomonas aeruginosa* carries a secretable arachidonate 15-lipoxygenase, Proc. Natl. Acad. Sci. U. S. A. 101 (2004) 2135–2139.
[7] J. Hansen, A. Garreta, M. Benincasa, M.C. Fuste, M. Busquets, A. Manresa, Bacterial lipoxygenases, a new subfamily of enzymes? A phylogenetic approach, Appl. Microbiol. Biotechnol. 97 (2013) 4737–4747.
[8] T. Koeduka, T. Kajiwara, K. Matsui, Cloning of lipoxygenase genes from a cyanobacterium, *Nostoc punctiforme*, and its expression in *Escherichia coli*, Curr. Microbiol. 54 (2007) 315–319.
[9] A.Z. Andreou, M. Vanko, L. Bezakova, I. Feussner, Properties of a mini 9R-lipoxygenase from *Nostoc* sp. PCC 7120 and its mutant forms, Phytochemistry 69 (2008) 1832–1837.
[10] B. Gao, W.E. Boeglin, Y. Zheng, C. Schneider, A.R. Brash, Evidence for an ionic intermediate in the transformation of fatty acid hydroperoxide by a catalase-related allene oxide synthase from the cyanobacterium *Acaryochloris marina*, J. Biol. Chem. 284 (2009) 22087–22098.
[11] B. Gao, W.E. Boeglin, A.R. Brash, Omega-3 fatty acids are oxygenated at the n-7 carbon by the lipoxygenase domain of a fusion protein in the cyanobacterium *Acaryochloris marina*, Biochim. Biophys. Acta 1801 (2010) 58–63.
[12] A. Garreta, S.P. Val-Moraes, Q. Garcia-Fernandez, M. Busquets, C. Juan, A. Oliver, A. Ortiz, B.J. Gaffney, I. Fita, A. Manresa, X. Carpena, Structure and interaction with phospholipids of a prokaryotic lipoxygenase from *Pseudomonas aeruginosa*, FASEB J. 27 (2013) 4811–4821.
[13] X. Lu, J. Zhang, S. Liu, D. Zhang, Z. Xu, J. Wu, J. Li, G. Du, J. Chen, Overproduction, purification, and characterization of extracellular lipoxygenase of *Pseudomonas aeruginosa* in *Escherichia coli*, Appl. Microbiol. Biotechnol. 97 (2013) 5793–5800.
[14] M. Busquets, V. Deroncele, J. Vidal-Mas, E. Rodriguez, A. Guerrero, A. Manresa, Isolation and characterization of a lipoxygenase from *Pseudomonas* 42A2 responsible for the biotransformation of oleic acid into (S)-(E)-10-hydroxy-8-octadecenoic acid, Antonie Van Leeuwenhoek 85 (2004) 129–139.
[15] N.C. Gilbert, S.G. Bartlett, M.T. Waight, D.B. Neau, W.E. Boeglin, A.R. Brash, M.E. Newcomer, The structure of human 5-lipoxygenase, Science 331 (2011) 217–219.
[16] M.J. Kobe, D.B. Neau, C.E. Mitchell, S.G. Bartlett, M.E. Newcomer, The structure of human 15-lipoxygenase-2 with a substrate mimic, J. Biol. Chem. 289 (2014) 8562–8569.
[17] P. Eek, R. Järving, I. Järving, N.C. Gilbert, M.E. Newcomer, N. Samel, Structure of a calcium-dependent 11R-lipoxygenase suggests a mechanism for Ca2+ regulation, J. Biol. Chem. 287 (2012) 22377–22386.
[18] W. Minor, J. Steczko, B. Stec, Z. Otwinowski, J.T. Bolin, R. Walter, B. Axelrod, Crystal structure of soybean lipoxygenase L-1 at 1.4 A resolution, Biochemistry 35 (1996) 10687–10701.
[19] S. Banthiya, M. Pekarova, H. Kuhn, D. Heydeck, Secreted lipoxygenase from *Pseudomonas aeruginosa* exhibits biomembrane oxygenase activity and induces hemolysis in human red blood cells, Arch. Biochem. Biophys. 584 (2015) 116–124.
[20] J.D. Deschamps, A.F. Ogunsola, J.B. Jameson 2nd, A. Yasgar, B.A. Flitter, C.J. Freedman, J.A. Melvin, J.V. Nguyen, D.J. Maloney, A. Jadhav, A. Simeonov, J.M. Bomberger, T.R. Holman, Biochemical and cellular characterization and inhibitor discovery of *Pseudomonas aeruginosa* 15-lipoxygenase, Biochemistry 55 (2016) 3329–3340.
[21] G. Coffa, A.R. Brash, A single active site residue directs oxygenation stereospecificity in lipoxygenases: stereocontrol is linked to the position of oxygenation, Proc. Natl. Acad. Sci. U. S. A. 101 (2004) 15579–15584.
[22] S. Borngraber, M. Browner, S. Gillmor, C. Gerth, M. Anton, R. Fletterick, H. Kuhn, Shape and specificity in mammalian 15-lipoxygenase active site. The functional interplay of sequence determinants for the reaction specificity, J. Biol. Chem. 274 (1999) 37345–37350.
[23] K. Schwarz, M. Walther, M. Anton, C. Gerth, I. Feussner, H. Kuhn, Structural basis for lipoxygenase specificity. Conversion of the human leukocyte 5-lipoxygenase to a 15-lipoxygenating enzyme species by site-directed mutagenesis, J. Biol. Chem. 276 (2001) 773–779.
[24] R. Vogel, C. Jansen, J. Roffeis, P. Reddanna, P. Forsell, H.E. Claesson, H. Kuhn, M. Walther, Applicability of the triad concept for the positional specificity of mammalian lipoxygenases, J. Biol. Chem. 285 (2010) 5369–5376.
[25] S.M. Rapoport, T. Schewe, R. Wiesner, W. Halangk, P. Ludwig, M. Janicke-Hohne, C. Tannert, C. Hiebsch, D. Klatt, The lipoxygenase of reticulocytes. Purification, characterization and biological dynamics of the lipoxygenase; its identity with the respiratory inhibitors of the reticulocyte, Eur. J. Biochem./FEBS 96 (1979) 545–561.
[26] M. Hamberg, Stereochemistry of oxygenation of linoleic acid catalyzed by prostaglandin-endoperoxide H synthase-2, Arch. Biochem. Biophys. 349 (1998) 376–380.
[27] M. Hamberg, Stereochemistry of hydrogen removal during oxygenation of linoleic acid by singlet oxygen and synthesis of 11(S)-deuterium-labeled linoleic acid, Lipids 46 (2011) 201–206.
[28] E.G. Bligh, W.J. Dyer, A rapid method of total lipid extraction and purification, Can. J. Biochem. Physiol. 37 (1959) 911–917.
[29] H. Kuhn, J. Belkner, R. Wiesner, A.R. Brash, Oxygenation of biological membranes by the pure reticulocyte lipoxygenase, J. Biol. Chem. 265 (1990) 18351–18361.
[30] A.A. Vagin, REFMAC5 dictionary: organization of prior chemical knowledge and guidelines for its use, Acta Crystallogr. D 60 (2004) 2184–2195.
[31] R.W. Bryant, T. Schewe, S.M. Rapoport, J.M. Bailey, Leukotriene formation by a purified reticulocyte lipoxygenase enzyme. Conversion of arachidonic acid and 15-hydroperoxyeicosatetraenoic acid to 14, 15-leukotriene A4, J. Biol. Chem. 260 (1985) 3548–3555.
[32] H. Kuhn, R. Wiesner, L. Alder, B.J. Fitzsimmons, J. Rokach, A.R. Brash, Formation of lipoxin B by the pure reticulocyte lipoxygenase via sequential oxygenation of the substrate, Eur. J. Biochem./FEBS 169 (1987) 593–601.
[33] N. Ueda, S. Yamamoto, B.J. Fitzsimmons, J. Rokach, Lipoxin synthesis by arachidonate 5-lipoxygenase purified from porcine leukocytes, Biochem. Biophys. Res. Commun. 144 (1987) 996–1002.
[34] S. Hu, Q.L. Mao-Ying, J. Wang, Z.F. Wang, W.L. Mi, X.W. Wang, J.W. Jiang, Y.L. Huang, G.C. Wu, Y.Q. Wang, Lipoxins and aspirin-triggered lipoxin alleviate bone cancer pain in association with suppressing expression of spinal proinflammatory cytokines, J. Neuroinflammation 9 (2012) 278.
[35] I. Ivanov, D. Heydeck, K. Hofheinz, J. Roffeis, V.B. O'Donnell, H. Kuhn, M. Walther, Molecular enzymology of lipoxygenases, Arch. Biochem. Biophys. 503 (2010) 161–174.
[36] D.L. Sloane, R. Leung, J. Barnett, C.S. Craik, E. Sigal, Conversion of human 15-lipoxygenase to an efficient 12-lipoxygenase: the side-chain geometry of amino acids 417 and 418 determine positional specificity, Protein Eng. 8 (1995) 275–282.
[37] H. Suzuki, K. Kishimoto, T. Yoshimoto, S. Yamamoto, F. Kanai, Y. Ebina, A. Miyatake, T. Tanabe, Site-directed mutagenesis studies on the iron-binding domain and the determinant for the substrate oxygenation site of porcine leukocyte arachidonate 12-lipoxygenase, Biochim. Biophys. Acta 1210 (1994) 308–316.
[38] S. Borngraber, R.J. Kuban, M. Anton, H. Kuhn, Phenylalanine 353 is a primary determinant for the positional specificity of mammalian 15-lipoxygenases, J. Mol. Biol. 264 (1996) 1145–1153.
[39] M. Jisaka, R.B. Kim, W.E. Boeglin, A.R. Brash, Identification of amino acid determinants of the positional specificity of mouse 8S-lipoxygenase and human 15S-lipoxygenase-2, J. Biol. Chem. 275 (2000) 1287–1293.
[40] O. Radmark, O. Werz, D. Steinhilber, B. Samuelsson, 5-Lipoxygenase, a key enzyme for leukotriene biosynthesis in health and disease, Biochim. Biophys. Acta 1851 (2015) 331–339.
[41] H. Porta, M. Rocha-Sosa, Lipoxygenase in bacteria: a horizontal transfer event? Microbiology 147 (2001) 3199–3200.
[42] S. Feltenmark, N. Gautam, A. Brunnstrom, W. Griffiths, L. Backman, C. Edenius, L. Lindbom, M. Bjorkholm, H.E. Claesson, Eoxins are proinflammatory arachidonic acid metabolites produced via the 15-lipoxygenase-1 pathway in human eosinophils and mast cells, Proc. Natl. Acad. Sci. U. S. A. 105 (2008) 680–685.
[43] M.O. Freire, T.E. Van Dyke, Natural resolution of inflammation, Periodontology 2000 (63) (2013) 149–164.
[44] B.D. Levy, M. Romano, H.A. Chapman, J.J. Reilly, J. Drazen, C.N. Serhan, Human alveolar macrophages have 15-lipoxygenase and generate 15(S)-hydroxy-5,8,11-cis-13-trans-eicosatetraenoic acid and lipoxins, J. Clin. Invest. 92 (1993) 1572–1579.
[45] J. Vidal-Mas, M. Busquets, A. Manresa, Cloning and expression of a lipoxygenase from *Pseudomonas aeruginosa* 42A2, Antonie Van Leeuwenhoek 87 (2005) 245–251.

SUPPLEMENTARY INFORMATION

Structural and functional basis of phospholipid oxygenase activity of bacterial lipoxygenase from *Pseudomonas aeruginosa*

Swathi Banthiya[1]*, Jacqueline Kalms[2]*, Etienne Galemou Yoga[2], Igor Ivanov[1], Xavi Carpena[3], Mats Hamberg[4], Hartmut Kuhn[1§], and Patrick Scheerer[2§]

[1]Institut für Biochemie, Charite - Universitätsmedizin Berlin, Charitéplatz 1, D-10117 Berlin, Germany.
[2]Institut für Medizinische Physik und Biophysik, Group Protein X-ray Crystallography and Signal Transduction, Charité – Universitätsmedizin Berlin, Charitéplatz 1, D-10117 Berlin, Germany.
[3] Institut de Biologia Molecular, Parc Científic de Barcelona, Barcelona, Spain.
[4]Department of Medical Biochemistry and Biophysics, Karolinska Institutet, Stockholm, Sweden

* S.B. and J. K. contributed equally to this work

[§]Corresponding authors:

Dr. Hartmut Kuhn, Institut für Biochemie (CC2) - Charité – Universitätsmedizin Berlin, Charitéplatz 1, D-10117 Berlin, Germany, phone: +49-30-450-528040, fax: +49-30-450-528905, *email:* hartmut.kuehn@charite.de;

Dr. Patrick Scheerer, Institut für Medizinische Physik und Biophysik (CC2) - Group Protein X-ray Crystallography and Signal Transduction, Charité – Universitätsmedizin Berlin, Charitéplatz 1, D-10117 Berlin, Germany, phone: +49-30-450-524178, fax: +49-30-450-524952, *email:* patrick.scheerer@charite.de

1. Supplementary methodological information

Data collection and structure analysis - Diffraction data were collected at 100 K using synchrotron X-ray sources from BESSY II (Berlin, Germany) **(1)** and ESRF (Grenoble, France). The best diffraction datasets of both *PA-LOX* crystal forms were collected at synchrotron beamline ID23-1 **(2)** at ESRF with a Pilatus 6M-F detector at 0.972 nm wavelength. The data collection and strategy software packages *MxCuBE* **(3)** and *EDNA* **(4)** were used. The data collection of the first crystal form (needle shape – crystal form 1) was

performed with a crystal-to-detector distance of 284 mm and a rotation increment of 0.1° with 0.04 s exposure time for each frame (1200 images). 1500 images of the second crystal form (plate shape – crystal form 2) were collected with a crystal-to-detector distance of 215 mm and a rotation increment of 0.1° with an exposure time of 0.04 s for each frame. The images of each data set were indexed, integrated and scaled using the *XDS* **(5)** program package and the CCP4 program *SCALA* **(6, 7).**The crystal form 1 belongs to the orthorhombic space group $P2_12_12$ (approximately unit cell constants: a = 133.09 Å, b = 116.35 Å, c = 42.72 Å, α = β = γ= 90.00°). The crystal form 2 belongs to the orthorhombic space group $C222_1$ (a = 83.74 Å, b = 97.39 Å, c = 153.84 Å, α = β = γ= 90.00°). **Table 5** summarizes the statistics for crystallographic data collection and structural refinement. Initial phases for both crystal forms of wild-type *PA-LOX* were obtained by the conventional molecular replacement protocol (rotation, translation, rigid-body fitting) using the crystal structure of the phospholipid-lipoxygenase complex from *Pseudomonas aeruginosa* (PDB entry 4G32) as initial search model, which was used in the program *Phaser* **(8)** of the CCP4 software package **(6)**. A simulated-annealing procedure with the resulting models were performed using a slow-cooling protocol and a maximum likelihood target function, energy minimization and B-factor refinements by the program *PHENIX* **(9),** which were carried out in the resolution range of 43.80 – 1.90 Å for the crystal form 1 and 48.97 – 1.48 Å for the crystal form 2, respectively. After the first round of refinements, phospholipid substrates in the ligand-binding pockets were clearly visible in the electron density of both σ_A-weighted 2*Fo-Fc* maps, as well as in the σ_A-weighted simulated annealing omitted density maps for both crystal forms of *PA-LOX*. Both *PA-LOX* crystal forms were modeled with TLS refinement (TLS - for Translation, Libration (small movements) and Screw-rotation of a group of atoms) using anisotropic temperature factors for all atom **(10)**. Restrained, individual B-factors were refined, and the crystal structure was finalized by the CCP4 program *REFMAC5* **(11)** and other programs of the CCP4 suite **(6)**. The final model has agreement factors R_{free} and R_{cryst} of 18.2 % and 14.4 %, for wild-type *PA-LOX* crystal form 1 and 15.5 % and 13.6 %, for wild-type *PA-LOX* crystal form 2, respectively. Manual rebuilding of the wild-type *PA-LOX* crystal form 1 and 2 models and electron density interpretation were performed after each refinement cycle using the program *COOT* **(12)**. Structure validation was performed with the programs *PHENIX* **(9),** RCSB PDB Validation server **(13)**, *MolProbity* **(14),** *SFCHECK* **(15)**, *PROCHECK* **(16)**, *WHAT_CHECK* **(17)** and *RAMPAGE* **(18)**. All crystal structure superpositions of backbone α-carbon traces were performed using the CCP4 program *LSQKAB* **(6)**. All molecular graphics representations in this work were created using the *PyMol* software package.

2. Supplementary experimental data

To analyze the oxygenation kinetics of arachidonic acid and linoleic acid by pure PA-LOX we carried out detailed kinetic measurements. For this purpose pure PA-LOX was incubated with arachidonic acid and linoleic acid at 5 different substrate concentrations (10 µM, 20 µM, 50 µM, 100 µM, 165 µM) in PBS (pH 7.4) in the absence of any detergent and the increase in absorbance at 235 nm were recorded. Double readings were taken for each substrate concentration and the means ± standard errors were calculated. The means were subsequently used to construct Lineweaver-Burk diagrams and from these diagrams the basic kinetic constants Km and Vmax were extracted. These parameters were then used to calculate the kcat/Km ratio, which mirrors the catalytic efficiency with the two substrates.

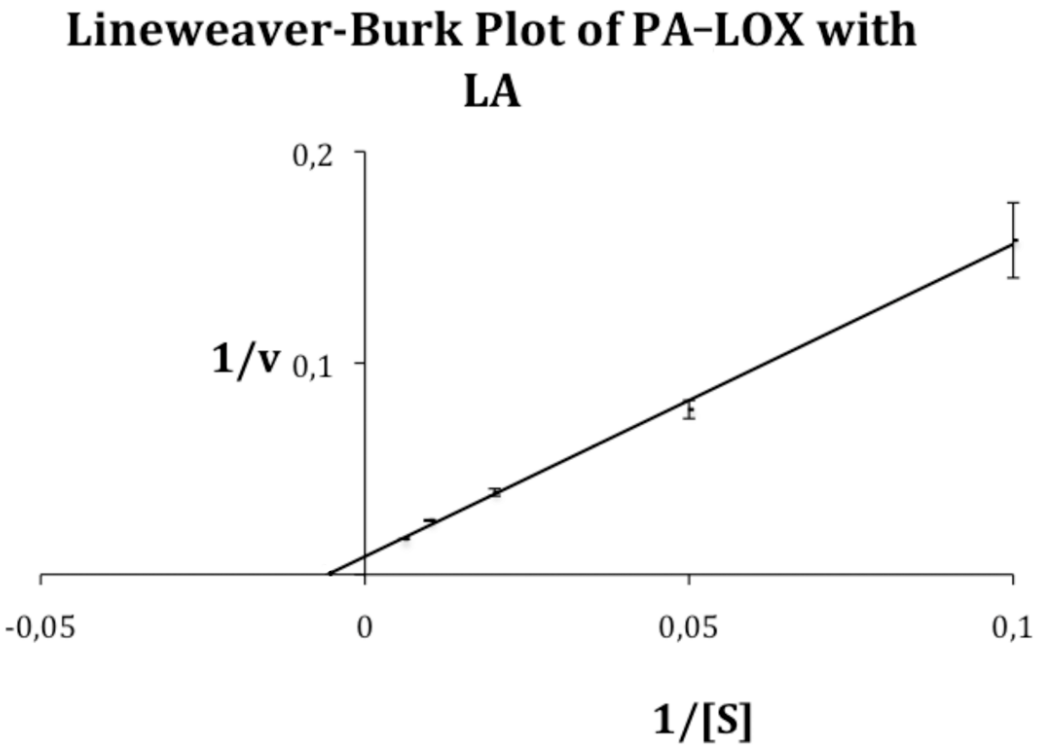

FigS1. Lineweaver-Burk plot of linoleic acid oxygenation by pure PA-LOX. Pure PA-LOX (2.1 µg/ml) was incubated in PBS (pH 7.4) in the presence of different substrate concentrations (10 µM, 20 µM, 50 µM, 100 µM, 165 µM) and the increase in absorbance at 235 nm was followed spectrophotometrically (double readings). From the experimental raw data the means of the rates were calculated and these values were used to construct the Lineweaver-Burk diagram.

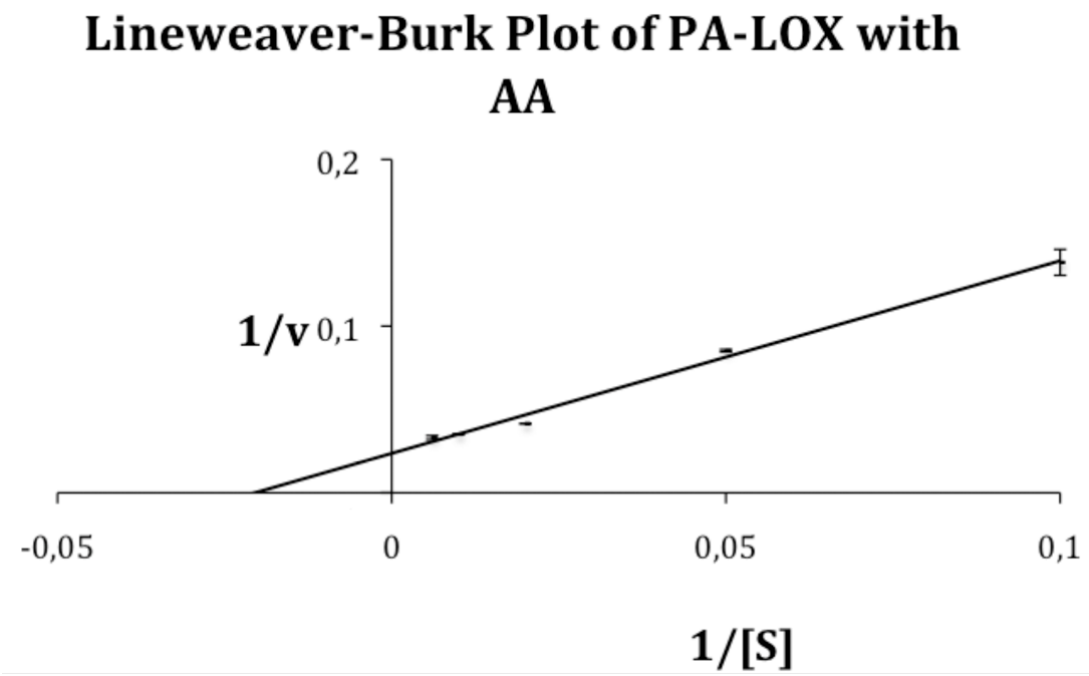

FigS2. Lineweaver-Burk plot of arachidonic acid oxygenation by pure PA-LOX. Pure PA-LOX (2.1 µg/ml) was incubated in PBS (pH 7.4) in the presence of different substrate concentrations (10 µM, 20 µM, 50 µM, 100 µM, 165 µM) and the increase in absorbance at 235 nm was followed spectrophotometrically (double readings). From the experimental raw data the means of the rates were calculated and these values were used to construct the Lineweaver-Burk diagram.

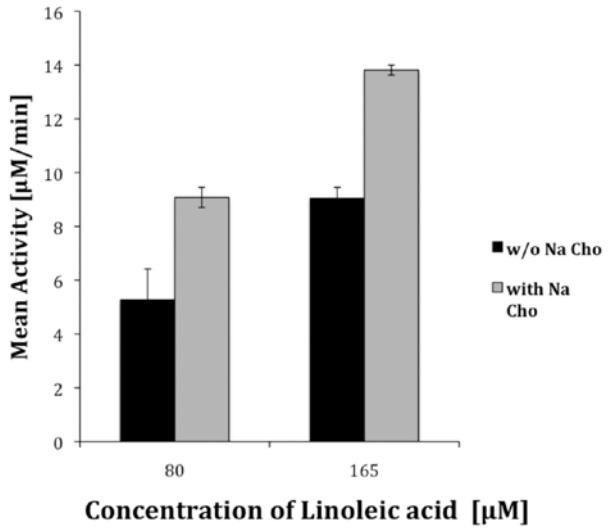

FigS3. Impact of detergents (sodium cholate) on linoleic acid oxygenation by PA-LOX. Pure PA-LOX (0.4 µg/ml) was incubated with linoleic acid in PBS (pH 7.4) in the presence (0.02 %) or absence of sodium deoxycholate at two different (80 µM, 1605 µM) substrate concentrations. The increase in absorbance at 235 nm was recorded spectrophotometrically

(double readings). From the experimental raw data the means of the rates were calculated and these values were used to construct the Lineweaver-Burk diagram. In the presence of detergents the oxygenation rate was significantly higher.

References

1. Mueller, U., Förster, R., Hellmig, M., Huschmann, F. U., Kastner, A., Malecki, P., Pühringer, S., Röwer, M., Sparta, K., Steffien, M., Ühlein, M., Wilk, P., and Weiss, M. S. (2015) The macromolecular crystallography beamlines at BESSY II of the Helmholtz-Zentrum Berlin: Current status and perspectives. *Eur. Phys. J. Plus*. **130**, 141

2. Nurizzo, D., Mairs, T., Guijarro, M., Rey, V., Meyer, J., Fajardo, P., Chavanne, J., Biasci, J.-C. C., McSweeney, S., and Mitchell, E. (2006) The ID23-1 structural biology beamline at the ESRF. *J. Synchrotron Radiat.* **13**, 227–238

3. Gabadinho, J., Beteva, A., Guijarro, M., Rey-Bakaikoa, V., Spruce, D., Bowler, M. W., Brockhauser, S., Flot, D., Gordon, E. J., Hall, D. R., Lavault, B., McCarthy, A. A., McCarthy, J., Mitchell, E., Monaco, S., Mueller-Dieckmann, C., Nurizzo, D., Ravelli, R. B. G., Thibault, X., Walsh, M. A., Leonard, G. A., and McSweeney, S. M. (2010) MxCuBE: A synchrotron beamline control environment customized for macromolecular crystallography experiments. *J. Synchrotron Radiat.* **17**, 700–707

4. Incardona, M.-F. F., Bourenkov, G. P., Levik, K., Pieritz, R. A., Popov, A. N., and Svensson, O. (2009) EDNA: a framework for plugin-based applications applied to X-ray experiment online data analysis. *J. Synchrotron Radiat.* **16**, 872–879

5. Kabsch, W. (2010) Xds. *Acta Crystallogr. Sect. D Biol. Crystallogr.* **66**, 125–132

6. Collaborative Computational Project, N. 4 (1994) The CCP4 suite: programs for protein crystallography. *Acta Crystallogr. D. Biol. Crystallogr.* **50**, 760–763

7. Evans, P. (2006) Scaling and assessment of data quality. *Acta Crystallogr. D. Biol. Crystallogr.* **62**, 72–82

8. McCoy, A. J., Grosse-Kunstleve, R. W., Adams, P. D., Winn, M. D., Storoni, L. C., and Read, R. J. (2007) Phaser crystallographic software. *J. Appl. Crystallogr.* **40**, 658–674

9. Adams, P. D., Afonine, P. V., Bunkóczi, G., Chen, V. B., Davis, I. W., Echols, N., Headd, J. J., Hung, L.-W. W., Kapral, G. J., Grosse-Kunstleve, R. W., McCoy, A. J., Moriarty, N. W., Oeffner, R., Read, R. J., Richardson, D. C., Richardson, J. S., Terwilliger, T. C., and Zwart, P. H. (2010) PHENIX: a comprehensive Python-based system for macromolecular structure solution. *Acta Crystallogr. D. Biol. Crystallogr.* **66**, 213–221

10. Winn, M. D., Isupov, M. N., and Murshudov, G. N. (2001) Use of TLS parameters to model anisotropic displacements in macromolecular refinement. *Acta Crystallogr. Sect. D Biol. Crystallogr.* **57**, 122–133

11. Vagin, A. A., Steiner, R. A., Lebedev, A. A., Potterton, L., McNicholas, S., Long, F., and Murshudov, G. N. (2004) REFMAC5 dictionary: Organization of prior chemical

knowledge and guidelines for its use. *Acta Crystallogr. Sect. D Biol. Crystallogr.* **60**, 2184–2195

12. Emsley, P., Lohkamp, B., Scott, W. G., and Cowtan, K. (2010) Features and development of Coot. *Acta Crystallogr. D. Biol. Crystallogr.* **66**, 486–501

13. Berman, H. M., Westbrook, J., Feng, Z., Gilliland, G., Bhat, T. N., Weissig, H., Shindyalov, I. N., and Bourne, P. E. (2000) The Protein Data Bank. *Nucleic Acids Res.* **28**, 235–242

14. Davis, I. W., Leaver-Fay, A., Chen, V. B., Block, J. N., Kapral, G. J., Wang, X., Murray, L. W., Arendall, W. B., Snoeyink, J., Richardson, J. S., and Richardson, D. C. (2007) MolProbity: all-atom contacts and structure validation for proteins and nucleic acids. *Nucleic Acids Res.* **35**, W375–383

15. Vaguine, a a, Richelle, J., and Wodak, S. J. (1999) SFCHECK: a unified set of procedures for evaluating the quality of macromolecular structure-factor data and their agreement with the atomic model. *Acta Crystallogr. D. Biol. Crystallogr.* **55**, 191–205

16. Laskowski, R. a., MacArthur, M. W., Moss, D. S., and Thornton, J. M. (1993) PROCHECK: a program to check the stereochemical quality of protein structures. *J. Appl. Crystallogr.* **26**, 283–291

17. Hooft, R. W. W., Vriend, G., Sander, C., and Abola, E. E. (1996) Errors in protein structures. *Nature*. **381**, 272–272

18. Lovell, S. C., Davis, I. W., Adrendall, W. B., de Bakker, P. I. W., Word, J. M., Prisant, M. G., Richardson, J. S., and Richardson, D. C. (2003) Structure validation by C alpha geometry: phi,psi and C beta deviation. *Proteins-Structure Funct. Genet.* **50**, 437–450

iv. The crystal structure of Pseudomonas aeruginosa lipoxygenase Ala420Gly mutant explains its altered reaction specificity.

Kalms J*, Banthiya S, Galemou Yoga E, Hamberg M, Kuhn H, Scheerer P. ***Biochim Biophys Acta.*** 2017 May; 1862(5):463-473.

Biochimica et Biophysica Acta 1862 (2017) 463–473

Contents lists available at ScienceDirect

Biochimica et Biophysica Acta

journal homepage: www.elsevier.com/locate/bbalip

The crystal structure of *Pseudomonas aeruginosa* lipoxygenase Ala420Gly mutant explains the improved oxygen affinity and the altered reaction specificity☆

Jacqueline Kalms [a,1], Swathi Banthiya [b,1], Etienne Galemou Yoga [a,1], Mats Hamberg [c], Hermann-Georg Holzhutter [b], Hartmut Kuhn [b,*], Patrick Scheerer [a,**]

[a] Institute of Medical Physics and Biophysics (CC2), Group Protein X-ray Crystallography and Signal Transduction, Charité - University Medicine Berlin, Charitéplatz 1, 10117 Berlin, Germany
[b] Institute for Biochemistry (CC2), Charité - University Medicine Berlin, Charitéplatz 1, 10117 Berlin, Germany
[c] Department of Medical Biochemistry and Biophysics, Karolinska Institute, Stockholm, Sweden

ARTICLE INFO

Article history:
Received 25 October 2016
Received in revised form 3 January 2017
Accepted 12 January 2017
Available online 14 January 2017

Keywords:
Eicosanoids
Oxidative stress
Mutagenesis
Oxygen sensor
Catalysis

ABSTRACT

Secreted LOX from *Pseudomonas aeruginosa* (PA-LOX) has previously been identified as arachidonic acid 15*S*-lipoxygenating enzyme. Here we report that the substitution of Ala420Gly in PA-LOX leads to an enzyme variant with pronounced dual specificity favoring arachidonic acid 11*R*-oxygenation. When compared with other LOX-isoforms the molecular oxygen affinity of wild-type PA-LOX is 1–2 orders of magnitude lower (Km O_2 of 0.4 mM) but Ala420Gly exchange improved the molecular oxygen affinity (Km O_2 of 0.2 mM). Experiments with stereo-specifically deuterated linoleic acid indicated that the formation of both 13*S*- and 9*R*-HpODE involves abstraction of the pro*S*-hydrogen from C11 of the fatty acid backbone. To explore the structural basis for the observed functional changes (altered specificity, improved molecular oxygen affinity) we solved the crystal structure of the Ala420Gly mutant of PA-LOX at 1.8 Å resolution and compared it with the wild-type enzyme. Modeling of fatty acid alignment at the catalytic center suggested that in the wild-type enzyme dioxygen is directed to C15 of arachidonic acid by a protein tunnel, which interconnects the catalytic center with the protein surface. Ala420Gly exchange redirects intra-enzyme O_2 diffusion by bifurcating this tunnel so that C11 of arachidonic acid also becomes accessible for O_2 insertion.

1. Introduction

Transport of reactants from the protein surrounding to the active site or between multiple catalytic centers within a single protein via preformed protein tunnels has been reported for many enzymes including oxidoreductases [1–4]. Lipoxygenases (LOX) form a heterogeneous family of fatty acid dioxygenases [5–7], which have been implicated in cell differentiation but also play important roles in the pathogenesis of many major diseases, such as inflammation, cancer and atherosclerosis [8–13]. LOX genes are widely distributed in animals and plants but they also occur in algae, fungi, protozoa and metazoan [14]. In bacteria they have also been detected [15,16] but in this kingdom of terrestrial life they are present at much lower frequency [14]. The first bacterial LOX was identified in the facultative human pathogen *Pseudomonas aeruginosa* [15,17]. *P. aeruginosa* LOX (PA-LOX) exhibits a phospholipid oxygenase activity and destroys red blood cells when incubated with these cells in vitro [18]. The initial crystal structure of wild-type PA-LOX [7] revealed remarkable differences to eukaryotic LOX-isoforms. For most eukaryotic LOXs a two-domain structure has been identified [19–22] but for PA-LOX the polypeptide chain folds into a single domain [7,23]. There is, however, a helical lid structure in PA-LOX, which might constitute the functional equivalent of the N-terminal β-barrel domains of mammalian LOX-isoforms [7,23]. A second interesting structural peculiarity of PA-LOX is that the enzyme crystallized from recombinant sources carries an endogenous phosphatidylethanolamine ligand at the active site. The two fatty acid moieties of this endogenous ligand occupy two different sub-cavities. The cavity containing the sn1 fatty acid harbors the non-heme iron [7,23] and thus, this cavity is likely to bind the fatty acid substrate during the LOX reaction.

In general, the LOX-reaction consists of four elementary steps [5,24] and the reaction cascade is initiated by a stereo-selective hydrogen

☆ Data deposition: The atomic coordinates and structure factors (PDB entry 5LC8) have been deposited in the Protein Data Bank (http://wwpdb.org/).

* Correspondence to: H. Kuhn, Institute of Biochemistry, Charité - University Medicine Berlin, Charitéplatz 1,Virchowweg 6, D-10117 Berlin, Germany.
** Correspondence to: P. Scheerer, Institute of Medical Physics and Biophysics, Group Protein X-ray Crystallography and Signal Transduction, Charité - University Medicine Berlin, Charitéplatz 1, 10117 Berlin, Germany.
E-mail addresses: hartmut.kuehn@charite.de (H. Kuhn), patrick.scheerer@charite.de (P. Scheerer).
[1] These authors contributed equally to this work.

http://dx.doi.org/10.1016/j.bbalip.2017.01.003
1388-1981/

abstraction from a bisallylic methylene of the fatty acid substrate. This initial elementary reaction proceeds via coupled proton-electron tunneling [25,26] and leads to the formation of a carbon-centered fatty acid radical. Different LOX-isoforms exhibit different reaction specificities [4–6] but most mammalian LOX-isoforms function as *S*-LOXs, i.e. they convert polyenoic fatty acids to *S*-configured hydroperoxides. However, mammalian ALOX12B orthologs [27,28] and various LOX-isoforms from lower eukaryotes [29–31] have been identified as *R*-LOXs. Most *S*-LOXs carry an alanine at a critical position of their primary structure, but *R*-lipoxygenases have a glycine at this position [32]. Ala-to-Gly exchange in human ALOX15B transformed this enzyme from an arachidonate 15*S*- to an 11*R*-lipoxygenating enzyme. Similarly, mouse Alox15b can be converted from an 8*S*- to 12*R*-lipoxygenating protein [32] when a similar mutagenesis strategy was applied. Although the structural basis for these alterations has not directly been explored it has been suggested that the Ala side chain in 15*S*-lipoxygenating enzymes may prevent O_2 diffusion to the 11*R*-position [33,34]. More recently, detailed kinetic investigations have been carried out with wild-type and mutant soybean LOX1 [35]. The molecular oxygen affinity data obtained for the different LOX variants suggested that outside the Ala-vs-Gly concept site-directed mutagenesis may lead to closure (Ile553Trp) and/or opening (Leu496Trp) of preformed O_2 access tunnels, which alters the catalytic activity and the reaction specificity of the corresponding mutants. However, in neither of these studies direct structural data have been provided, which explain the observed functional alterations.

For most LOXs characterized so far their enantioselectivity can be described by the Ala-vs-Gly concept [33] and corresponding amino acid exchanges altered the reaction specificity of a number of *S*-LOXs [36]. However, this was not the case for zebrafish LOX-1. This arachidonic acid 12*S*-lipoxygenating enzyme carries a Gly at this critical position [37], which qualifies this enzyme as *R*-LOX according to the Ala-vs-Gly hypothesis [33]. This data challenges the applicability of the Ala-vs-Gly concept for all LOX-isoforms. To test the applicability of this concept for PA-LOX and to explore the structural basis for the possible specificity alterations we expressed and purified the Ala420Gly mutant of PA-LOX and solved its crystal structure at 1.8 Å resolution. Comparing the 3D-structure of wild-type and mutant PA-LOX we found that the Ala420Gly substitution induced 2-fold improved molecular oxygen affinity and a dual reaction specificity converting arachidonic acid to almost equal amounts of 15*S*- and 11*R*-HETE. Structural modeling of the enzyme-substrate complex suggested that the Ala420Gly exchange bifurcates the putative O_2 access tunnel so that 11*R*-lipoxygenation becomes possible in addition to 15*S*-HpETE formation.

2. Materials and methods

2.1. Chemicals

The chemicals were obtained from the following sources: arachidonic acid and linoleic acid from Sigma (Taufkirchen, Germany); HPLC standards of 11(±)-HETE, 11*S*-HETE, 15(±)-HETE, 15*S*-HETE, 13*S*-HODE, 13(±)-HODE 9(±)-HODE and 9*S*-HODE from Cayman Chem. (distributed by Biomol, Hamburg, Germany); sodium borohydride from Life Technologies, Inc. (Eggenstein, Germany); HPLC solvents from Baker (Deventer, The Netherlands); antibiotics and isopropyl-β-thiogalactopyranoside (IPTG) from Carl Roth GmbH (Karlsruhe, Germany); restriction enzymes from Thermo Fisher Scientific-Fermentas (Schwerte, Germany); the *E. coli* strain BL21 (DE3) from Invitrogen (Carlsbad, USA). Oligonucleotide synthesis was performed at BioTez (Berlin, Germany). Nucleic acid sequencing was carried out at Eurofins MWG Operon (Ebersberg, Germany). [11(*R*)-2H] linoleic acid (*proR*; 24% deuterated) and [11(*S*)-2H] linoleic acid (*proS*; 98% deuterated) were prepared as described previously [38,39].

2.2. Protein expression and purification

The prokaryotic expression plasmid pET28a(+) containing the coding sequence of PA-LOX was kindly provided by Prof. Xavi Carpena (Institut de Biologia Molecular, Parc Científic de Barcelona, Barcelona, Spain). The plasmid was amplified in *E. coli* XL-1 Blue cells and plasmid DNA was extracted using the MIDI-preparation kit (Macherey-Nagel, Düren, Germany). The PA-LOX was expressed in *E. coli* employing the Enpresso B kit (BioSilta Ltd., St. Ives, Great Britain) and the recombinant his-tag fusion protein was purified to apparent electrophoretic homogeneity by affinity chromatography on Ni-NTA (Machery Nagel, Düren, Germany). In detail, the expression strategy involved the following steps: Competent *E. coli* BL21 (DE3) cells were transformed with the pET28-PA-LOX plasmid and grown on kanamycin containing agar plates. A 2 ml bacterial preculture (LB medium with 50 μg/ml kanamycin) was inoculated and grown at 37 °C overnight. This pre-culture was then added to a 50 ml main culture as recommended by the supplier. The main culture was grown overnight at 30 °C and the culture was continuously shaken at 250 rpm in Ultra Yield flasks (BioSilta Ltd., St. Ives, Great Britain). Expression of the recombinant enzyme was induced by adding 1 mM (final concentration) IPTG to the main culture and afterwards the culture was incubated over night at 25 °C and 250 rpm. Bacteria were harvested by centrifugation and the resulting pellet was reconstituted in 5 ml PBS. Bacteria were lysed by sonication (digital sonifier, W-250D Microtip Max 70% Amp, Model 102C (CE); Branson Ultraschall, Fürth, Germany), cell debris was removed by centrifugation and the lysate supernatant was employed for further enzyme purification by affinity chromatography.

For affinity chromatography, the lysate supernatant was incubated for 1 h at 4 °C with 0.5 ml of Protino Ni-NTAagarose suspension (Machery Nagel, Düren, Germany). The gel beads were then transferred to an open bed chromatography column (Bio-Rad, Munich, Germany). To remove unspecifically bound proteins, the column was first eluted thrice with 0.8 ml washing buffer containing 10 mM imidazole. Next, the column was washed thrice with 0.8 ml elution buffer 1 containing 25 mM imidazole to elute more tightly bound proteins. Finally, the histidine-tagged (his-tag) fusion proteins were eluted by rinsing the column seven times with 0.3 ml of elution buffer 2 containing 200 mM imidazole. The majority of the PA-LOX was recovered in the elution fractions 1, 2 and 3 (200 mM imidazole).

2.3. Site-directed mutagenesis

Site-directed mutagenesis was performed using the Pfu Ultra II Hotstart 2XPCR Mastermix (Agilent Technologies, California, USA). Upon identifying the corresponding amino acids that need to be exchanged in the wild-type PA-LOX, the primers were designed and ordered according to the instructions of the manufacturer. The PCR reaction contained the template DNA, primers for the mutant and 2-fold concentrated Pfu Master-Mix. The his-tagged PA-LOX wild-type plasmid in pET-28a(+) was used as the template. The parental template DNA is then digested with Fast Digest Dpn 1 (Thermo Fischer Scientific, Massachusetts, USA). The PCR mix was then transformed into *E. coli* XL1-Blue competent cells (Invitrogen, California, USA) and plated onto kanamycin agar plates. 5–10 clones were picked and plasmid DNA was prepared using NucleoSpin Plasmid Easy Pure (Macherey-Nagel, Düren, Germany). Nucleotide sequencing (Eurofins Genomics, Ebersberg, Germany) confirmed the sequences of the mutant plasmid clones.

2.4. Fatty acid oxygenase activity assays

Linoleic acid and arachidonic acid oxygenase activities of wild-type and mutant PA-LOX were quantified spectrophotometrically using a Shimadzu UV-2102 PC spectrophotometer (Shimadzu, Duisburg, Germany). These measurements were routinely carried out to quantify

the molecular turnover rates for linoleic acid and arachidonic acid oxygenation for the different enzyme preparations. For this purpose, aliquots of the PA-LOX enzyme preparations were incubated in 1 ml of PBS containing different concentrations of linoleic acid or arachidonic acid as substrates. After the incubation period (2–5 min) the hydroperoxy compounds formed were reduced with sodium borohydride and after acidification 1 ml of ice-cold methanol was added. The protein precipitate was spun down and aliquots of the clear supernatant were injected to RP-HPLC for identification and quantification of the oxygenation products.

2.5. Activity measurements under normoxic and hyperoxic conditions

To determine the molecular oxygen affinity of wild-type PA-LOX and its Ala420Gly mutant we mixed variable volumes of hyperoxic PBS (O_2 saturated) with anaerobic PBS (argon saturated). For this purpose, 50 ml PBS was flushed for 3 h with pure oxygen or pure argon. Next, a photometric cuvette was filled with argon gas and aliquots of anaerobic PBS (0–2 ml) were added under argon atmosphere. The cuvette was closed with a plastic stopper containing two capillary holes to add additives. Then different aliquots of hyperoxic PBS (O_2 saturated) were added so that a final reaction volume of 2 ml was reached. Next, 10 μl of a methanolic solution of arachidonic acid was added and the reaction was started with 2 μl partially anaerobized enzyme solution. The increase in absorbance at 235 nm was assayed and the linear part of the kinetic progress curve was evaluated.

2.6. Determination of Km O_2

The relation between enzyme activity and dioxygen concentration was modeled according to the Hill equation

$$V = \frac{V_{max}{O_2}^n}{{S_{0.5}}^n + {O_2}^n},$$

where V_{max} is the maximal catalytic activity at O_2 saturation, $S_{0.5}$ the half-saturation concentration of dioxygen at which half-maximal rate is reached and the coefficient n takes into account positive cooperativity reflected by a sigmoidal shape of the activity-oxygen relationship. Mean values and variances of the three kinetic parameters were determined by a bootstrap procedure. Restricted data sets were generated by assigning to each dioxygen concentration randomly a single activity measurement selected from the set of repetitive measurements. Numerical values for the kinetic parameters were estimated by fitting the model to the randomly chosen restricted data set by least-square minimization. The bootstrap trials were repeated 50 times and based on the 50 bootstrap sets the parameter values (mean ± variances) were calculated.

2.7. Mass spectrometry analysis of the reaction products from stereo-specifically labeled linoleic acid

In order to determine the enrichment of deuterium in the linoleic acid-derived oxygenation products, 13*S*-HODE (wild-type enzyme and Ala420Gly mutant) and 9*R*-HODE (Ala420Gly mutant) were prepared by reduction of the corresponding hydroperoxides and isolated by a combined RP-, SP- and CP-HPLC strategy. The methyl-esterified and trimethylsilylated materials were analyzed by GC/MS using a Hewlett Packard model 5970B mass selective detector connected to a Hewlett-Packard model 5890 gas chromatograph equipped with a 5% phenylmethylsiloxane capillary column (length, 12 m; film thickness, 0.33 mm). The injector and ion source temperatures were both set at 200 °C, and the oven temperature was raised from 120 °C at a rate of 10 °C/min. The instrument was operated in the selected ion monitoring mode using the ions *m/z* 311.2 [Me_3SiO═CH—CH═CH—CH═CH—$(CH_2)_7$-$COOCH_3$] and 312.2. The integrated ion abundances were used to calculate the deuterium enrichments, setting the original deuterium content in the substrate molecule 100%.

2.8. HPLC analytics

HPLC analysis of the LOX products was performed on a Shimadzu instrument equipped with a Hewlett-Packard diode array detector 1040 A by recording the absorbance at 235 nm. Reverse phase-HPLC was carried out on a Nucleodur C18 Gravity column (Marchery-Nagel, Düren, Germany; 250 × 4 mm, 5 μm particle size) coupled with a guard column (8 × 4 mm, 5 μm particle size). A solvent system of methanol/water/acetic acid (85/15/0.1, by volume) was used at a flow rate of 1 ml/min. Normal phase-HPLC (SP-HPLC) was performed on a Nucleosil 100–5 column (250 × 4 mm, 5 μm particle size) with the solvent system n-hexane/2-propanol/acetic acid (100/2/0.1, by volume) and a flow rate of 1 ml/min. Hydroxy fatty acid enantiomers (15-HETE, 13-HODE) were separated by chiral phase HPLC (CP-HPLC) on a Chiralcel OD column (Daicel Chem. Ind., Ltd., Osaka, Japan) using a solvent system consisting of hexane/2-propanol/acetic acid (100/5/0.1, by volume) and a flow rate of 1 ml/min. To separate the enantiomers of 11*(R/S)*-HETE the reaction products were prepared by RP-HPLC, methylated with diazomethane, re-purified on SP-HPLC and finally analyzed on a Chiralcel OD column using the solvent system hexane/2-propanol/acetic acid (100/4/0.1, by volume) and a flow rate of 1 ml/min.

2.9. Crystallization

Purified Ala420Gly mutant was crystallized with the sitting-drop vapour diffusion method in 24-well Linbro plates (Jena Biosciences, Jena, Germany) at a protein concentration of about 15 mg/ml at 293 K. The reservoir solution contained 12% polyethylene glycol 3350, 0.2 M $MgCl_2$ and 0.1 M tris(hydroxymethyl)-aminomethane at pH 7.1. Precipitants, protein solution and seeding stock were mixed into micro-bridges (Hampton Research, Aliso Viejo, USA) according to the Microseed Matrix Seeding (MMS) protocol from Hampton Research. After 2–3 weeks the plate-shaped crystals were cryo-cooled in liquid nitrogen using 25% glycerol as cryo-protectant. The cryo-protectant was mixed with the crystallization buffer in 5% steps (15%, 20%, 25%).

2.10. Data collection and structure analysis

Diffraction data was collected at the synchrotron radiation facility ESRF in Grenoble, France. The best data set was collected at the tunable beamline ID23-1 [40] with a PILATUS 6M-F detector at a wavelength of λ = 0.972 Å using the data collection and strategy software packages *MxCube* [41] and *EDNA* [42]. The collection was performed at 100 K, a crystal-to-detector distance of 261 mm and a rotation increment 0.15° with an exposure time of 0.04 s for each frame (1000 images). The images of the best data set were indexed, integrated and scaled using the *XDS* program package [43] and the CCP4 program *SCALA* [44,45]. Crystals belong to orthorhombic space group $C222_1$ (approximately unit cell constants: a = 84 Å, b = 97 Å, c = 156 Å; α = β = γ = 90.00°). Initial phases for PA-LOX Ala420Gly mutant were obtained by molecular replacement based on the crystal structure of the phospholipid-lipoxygenase complex from *Pseudomonas aeruginosa* (PDB entry 5IR4) as initial search model using the CCP4 program *PHASER* [46]. Subsequently, different refinement strategies (inter alia real-space refinement, B-factor refinements) and simulated-annealing (slow cooling protocol, maximum likelihood target function, energy minimization) were carried out. The search for water molecules was performed with the *PHENIX* program [47]. The crystal structure was modeled with TLS refinement using anisotropic temperature factors for all atoms. The crystal structure was finalized with the CCP4 program *REFMAC5* [48]. Manual rebuilding of the PA-LOX Ala420Gly mutant model and electron density interpretation was performed after each refinement cycle using

the program *COOT* [49]. The final model has agreement factors R_{free}/R_{work} of 17.1%/13.9% [50]. Structure validations were performed with the programs of the RCSB PDB Validation server [51], Molprobity server [52] and WHAT IF server [53]. All molecular graphics representations were created using *PyMOL*. Table 3 summarizes the statistics for crystallographic data collection and structural refinement.

2.11. Structural modeling of enzyme fatty acid complexes

The crystal structure of the PA-LOX Ala420Gly mutant described here contains a phosphatidylethanolamine molecule (namely ZPE in the PDB entry 5LC8) bound at the substrate-binding pocket. The two fatty acid moieties of this endogenous ligand occupy two adjacent fatty acid binding sub-cavities, which are connected by a lobby, which harbors the polar head group of the phospholipid. The sub-cavity that contains the sn1 fatty acid involves the catalytic non-heme iron. Linoleic acid and arachidonic acid molecules were modeled into this sub-cavity on the basis of the endogenous ligand. Both structures of the two fatty acids were obtained from the *COOT* [54] small molecule library and directly fitted manually into the position of the endogenous ligand via several steps of rotation, translation and geometry regularization refinement. The model-complex structure was finalized using the structure geometry optimization (idealization) procedure of the CCP4 program *REFMAC5*, following a refinement of geometric restrains in *COOT*.

2.12. Caver tunnel analysis

The *Caver 3.0* [55] program was used as *PyMOL* plugin. The settings in the program have been changed manually. The C11 and C15 carbon atom of the docked arachidonic acid as well as the C9 and C13 of linoleic acid served as initial starting point in the crystal structures of both wild-type (PDB entry 5IR4) and Ala420Gly (PDB entry 5LC8) mutant PA-LOX. The shell depth (4 Å), shell radius (3 Å), cluster threshold (3.5 Å), the maximum distance (3–4 Å) and the desired radius (5 Å) maintained constant for all calculations. The maximum distance specifies the maximal distance of the tunnel calculation starting from the initial starting point. The minimum probe radius was defined by the largest value showing a tunnel within the given parameters.

3. Results

3.1. Ala420Gly exchange alters the reaction specificity of PA-LOX

Multiple amino acid sequence alignments of PA-LOX with several eukaryotic *S*- and *R*-lipoxygenases (Fig. 1) indicated that Ala420 aligns with the critical Ala residues of *S*-LOXs and with the corresponding Gly residues of *R*-LOXs. This sequence data suggest that PA-LOX constitutes a fatty acid *S*-LOX and previous activity assays indicated the formation of 15*S*-HpETE and 13*S*-HpODE from arachidonic acid and linoleic acid, respectively [23]. Here we confirm the reaction specificity of wild-type PA-LOX with linoleic and arachidonic acid (Fig. 2A, C) but we also show that in side-by-side experiments the Ala420Gly mutant exhibits dual reaction specificity functioning as dominant arachidonic acid 11*R*-LOX (Fig. 2B, D). Although the specific activity of the Ala420Gly mutant was lower (20% residual activity) than that of the wild-type enzyme (Table 1) the product composition indicates that the Ala-to-Gly concept [33] is applicable to PA-LOX and that the Ala420Gly exchange significantly alters the reaction specificity of this enzyme.

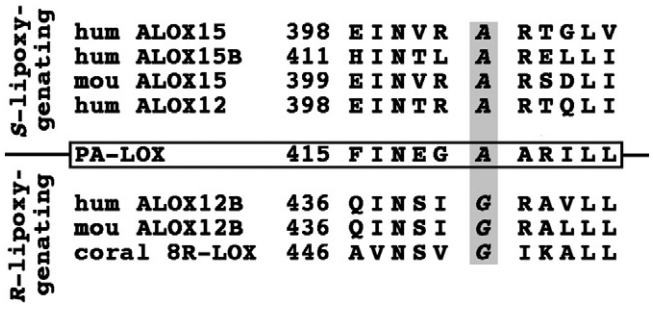

Fig. 1. Multiple amino acid sequence alignment of various eukaryotic *S*- and *R*-lipoxygenases. The relevant amino acid regions of the different mammalian LOXs were aligned and the amino acid critical for enantioselectivity of the enzymes is indicated in bold face. Amino acid numbering for the different LOX-isoforms is given.

3.2. Formation of 13S- and 9R-HpODE involves abstraction of the proS-hydrogen from C11

To explore the stereochemistry of initial hydrogen abstraction we incubated linoleic acid carrying a deuterium at the pro*S*- or the pro*R*-position at the bisallylic methylene C11 with pure wild-type and mutant PA-LOX and measured the reaction rate by following the increase in absorbance at 235 nm. Here we found that 11-pro*R*-deuterated linoleic acid was more rapidly oxygenated than the 11-pro*S*-deuterated substrate by both, wild-type PA-LOX and its Ala420Gly mutant (Table 2). This primary kinetic isotopic effect, the extent of which was comparable

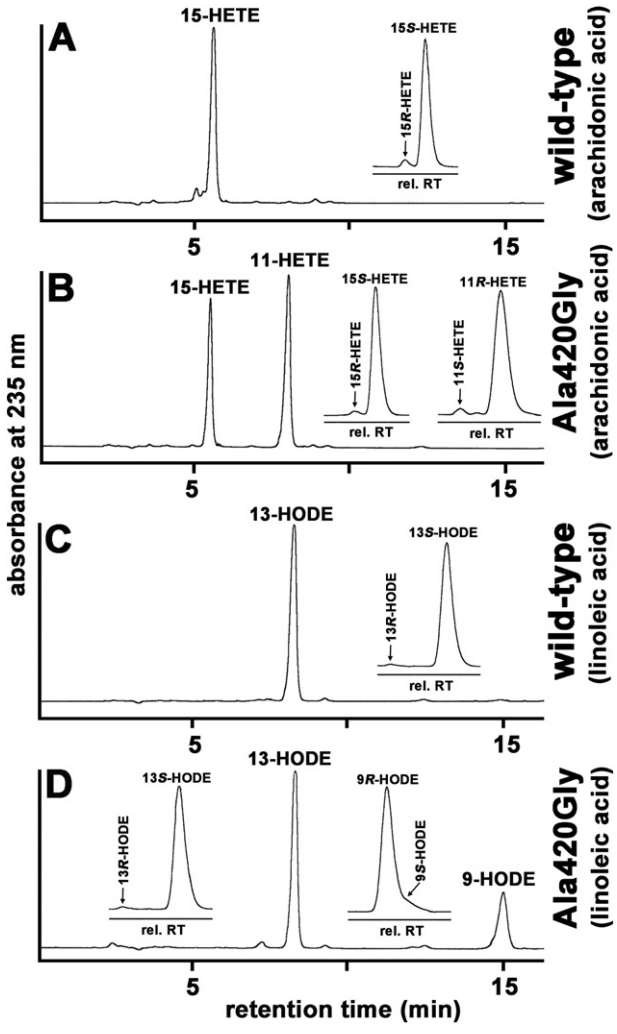

Fig. 2. Patterns of fatty acid oxygenation products formed by wild-type PA-LOX and its Ala420Gly mutant. A) Wild-type PA-LOX (3.7 μg/ml final enzyme concentration) with arachidonic acid, B) Ala420Gly mutant PA-LOX (7.6 μg/ml final enzyme concentration) with arachidonic acid, C) Wild-type PA-LOX (3.7 μg/ml final enzyme concentration) with linoleic acid, D) Ala420Gly mutant of PA-LOX (7.6 μg/ml final enzyme concentration) with linoleic acid. The insets indicate the enantiomer compositions of the oxygenation products determined by chiral phase HPLC.

Table 1
Basic kinetic parameters of wild-type PA-LOX and its Ala420Gly mutant.

Parameter	Wild-type	A420G
Turnover rate (s^{-1})[a]	20.3 ± 0.1	4.3 ± 0.4
Hyperoxia/normoxia ratio[b]	3.4	1.6
Km for O_2 (μM)[c]	406 ± 37	235 ± 44
Vmax (μM/min)	20.5 ± 1.5	12.6 ± 1.7
Catalytic efficiency (min^{-1})	0.051	0.053

[a] Standard activity assay containing 162 μM linoleic acid as substrate.
[b] The oxygenation rate of arachidonic acid under normoxic conditions was set 1.
[c] 320 μM arachidonic acid. The catalytic efficiency was calculated dividing V_{max}/Km.

for wild-type PA-LOX and its Ala420Gly mutant, suggests that the pro*S*-hydrogen is abstracted during linoleic acid oxygenation by both enzyme variants.

Next, we prepared the 13*S*-H(p)ODE and the 9*R*-H(p)ODE formed by the two enzyme variants and quantified the degree of deuterium retention. Here we found that with 11-pro*R*-deuterated substrate a deuterium retention of >85% in both, 13*S*-H(p)ODE and 9*R*-H(p)ODE (Table 2). In contrast, with 11-pro*S*-deuterated substrate >95 % of deuterium was lost. These results indicate that the formation of both 13*S*- and 9*R*-H(p)ODE involves abstraction of the pro*S*-hydrogen from C11 of linoleic acid. Thus, the reaction follows the antarafacial paradigm of the LOX reaction. A similar observation has been previously reported with wildtype- and Ala542Gly-soybean LOX-1 **(34).**

3.3. Structural models of PA-LOX-PUFA complexes are consistent with the stereo-selective hydrogen abstraction

The crystal structure of wild-type PA-LOX has previously been solved at 1.75 Å as highest resolution [7] (PDB entries 4G32 and 4G33 in two different space groups) and we recently improved the resolution to 1.48 Å [23] (PDB entries 5IR4 and 5IR5 in two different space groups). For the present study, we solved the crystal structure of the Ala420Gly mutant of PA-LOX at 1.8 Å resolution (PDB entry 5LC8) and a cartoon representation of this crystal structure is given in Fig. 3A. Table 3 summarizes the statistics for crystallographic data collection and structural refinement. Except for the lack of the Ala420 side chain and for a minor rotation of the sn1 fatty acid moiety of the endogenous ligand (Fig. 3B) the two crystal structures (wild-type vs. Ala420Gly mutant) were virtually identical. This also includes the structure of the iron cluster (inset to Fig. 3).

When we modeled arachidonic acid and linoleic acid into the substrate-binding pocket, we found that the bisallylic methylenes C11 (linoleic acid) and C13 (arachidonic acid) are located in close proximity to the iron bound water allowing hydrogen abstraction from these carbon atoms (Fig. 3C, left panel). The distance of the C_{13}-pro*S*-hydrogen of arachidonic acid to the iron-bound water was about 2.2 Å. In contrast, the distance of the pro*R*-hydrogen was 3.4 Å. Similar data were obtained for linoleic acid (Fig. 3C, right panel) and these results provide a plausible explanation for the stereo-selectivity of hydrogen abstraction (Table 2). It is important to stress that these data are not based on direct X-ray coordinates of enzyme-substrate complexes. Instead, they are the results of structural modeling. However, the conclusions are plausible and consistent with our experimental data on the stereo-selectivity of the hydrogen abstraction.

To test the quality of our modeling procedure for a third substrate we docked 5Z,8Z,11Z-eicosatrienoic acid into the active site under identical modeling condition. This substrate is not well oxygenated by PA-LOX since it lacks the bisallylic methylene at C13 [23]. When we modeled this fatty acid into the substrate-binding pocket we found that the two hydrogen atoms attached to the bisallylic methylene C10 are far away (>5 Å) from the iron bound hydroxyl. Thus, hydrogen abstraction from this pro-chiral center appears to be impossible, which is consistent with previous observation that this fatty acid is not a good substrate for this enzyme [23].

3.4. Ala420Gly mutant of PA-LOX exhibits an improved molecular oxygen affinity

Since formation of 13*S*- and 9*R*-H(p)ODE involves abstraction of the pro*S*-hydrogen from C11 of linoleic acid one may conclude that the first elementary reaction (hydrogen abstraction) of the catalytic cycle is identical for wild-type PA-LOX and its Ala420Gly substitution variant. Thus, the different reaction specificity of the Ala420Gly mutant might be related to an altered stereochemistry of the subsequent O_2 insertion. To test this hypothesis we first characterized the kinetic effects of variable dioxygen concentrations. When wild-type PA-LOX and its Ala420Gly mutant were incubated with arachidonic acid under normoxic (air saturation) and hyperoxic (O_2 saturation) conditions we found that the catalytic activity of the wild-type enzyme was more then 3-fold higher under hyperoxic conditions (Table 1). In contrast, the hyperoxic/normoxic activity ratio of the Ala420Gly mutant was only 1.3. This data suggests a higher molecular oxygen affinity of the Ala420Gly mutant when compared with the wild-type enzyme.

To put this conclusion on a broader experimental basis we determined the reaction rate of arachidonic acid oxygenation by wild-type PA-LOX and its Ala420Gly mutant at 10 different dioxygen concentrations (Fig. 4) and calculated the dioxygen Km-values. The reaction kinetic data given in Table 1 allow the following conclusions: (i) In contrast to mammalian LOX, for which dioxygen Km-values varying between 5 and 40 μM have previously been reported [56–59], wild-type PA-LOX (Km O_2 of 406 μM) exhibits a rather low molecular oxygen affinity. Such kinetic properties are characteristic for sensor proteins (see Discussion). (ii) Ala420Gly exchange almost doubled the molecular oxygen affinity (Km value of 235 μM for the Ala420Gly mutant vs. 406 μM for the wild-type enzyme). (iii) The catalytic efficiency (k_{cat}/Km) of the two enzymes is hardly altered by Ala420Gly exchange.

3.5. Ala420Gly substitution bifurcates the putative O_2 access tunnel

When we explored the crystal structures of wild-type PA-LOX and its Ala420Gly mutant with the protein tunnel prediction software *Caver 3.0* [60] we found a permanent tunnel system, which interconnects the protein surface of wild-type PA-LOX with the catalytic center. This tunnel system might constitute a molecular oxygen delivery tunnel allowing intra-protein O_2 diffusion. When we inspected this tunnel in more detail we found that approximately

Table 2
Primary kinetic isotopic effect and retention of deuterium in the reaction produced during the oxygenation of C11-pro*S*- and C11-pro*R* deuterated linoleic acid by wild-type PA-LOX and its Ala420Gly mutant.

Kinetic measurements	Enzyme	Relative reaction rate (%)		
		pro*R*-deuterated	pro*S*-deuterated	Ratio
	Wild-type	100.0 ± 16.1[a]	6.2 ± 3.3	16.1
	Ala420Gly	100.0 ± 8.0[a]	15.1 ± 3.9	6.6
Product analysis	Enzyme	Product	pro*R*-retention (%)	pro*S*-retention (%)
	Wild-type	13*S*-HODE	88.5 ± 1.5	3.3 ± 0.6
	Ala420Gly	13*S*-HODE	85.5 ± 5.5	2.5 ± 0.5
		9*R*-HODE	86.0 ± 1.0	3.5 ± 0.5

[a] The reaction rate of the pro*R*-deuterated substrate was set 100 for both enzyme variants.

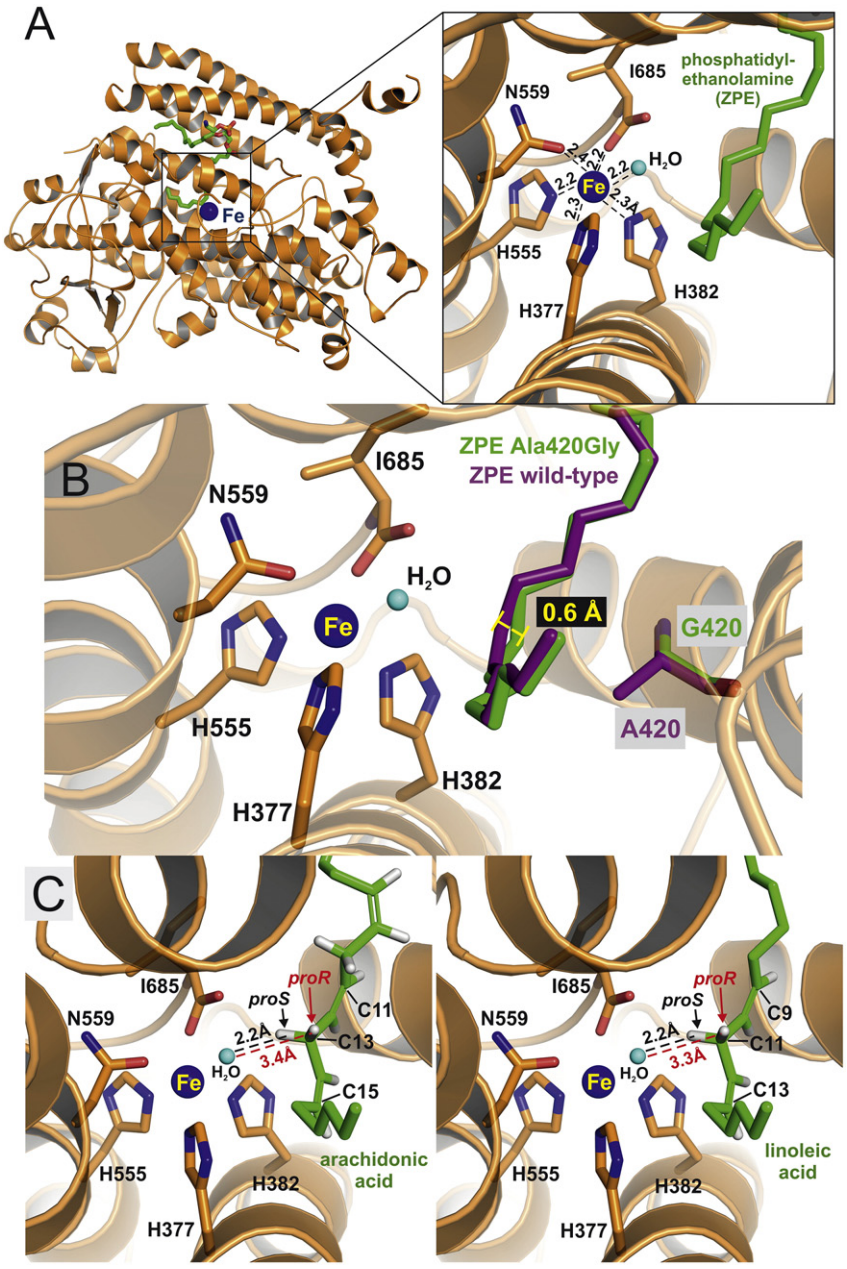

Fig. 3. Crystal structure of Ala420Gly mutant of PA-LOX and structural models of enzyme substrate complexes. A) Ribbon diagram of the overall structure of PA-LOX Ala420Gly mutant (PDB entry 5LC8). Dark blue sphere - non-heme iron. Green sticks - endogenous phospholipid ligand (ZPE). Inset: Iron ligand sphere. Light blue sphere: Iron-bound water (hydroxyl). B) Overlay of the positions of the endogenous phospholipid ligand at the active site of wild-type PA-LOX (green) and its Ala420Gly mutant (magenta). There is a subtle (around 0.6 Å) displacement of the endogenous ligand at the active site of the Ala420Gly mutant. C) Structural models for PA-LOX fatty acid complexes. Arachidonic acid and linoleic acid were manually modeled and geometrically idealized into the active site on the basis of the electron density map of the sn1 fatty acid moiety of ZPE. Left: The pro*S*-hydrogen (2.2 Å) at C13 of arachidonic acid is closer to the iron-bound hydroxyl than the corresponding pro*R*-hydrogen (3.4 Å). Right: The pro*S*-hydrogen (2.2 Å) at C11 of linoleic acid is closer to the iron-bound hydroxyl than the corresponding pro*R*-hydrogen (3.3 Å).

50% of the tunnel residues are hydrophobic (Fig. 5). In the wild-type enzyme Leu378, Ala420 and Leu425 form the bottleneck, the narrowest part of the given tunnel (Fig. 6A). In the Ala420Gly mutant deletion of the methyl group of Ala420 (Ala420Gly substitution) removes this narrowness and widens this tunnel section considerably (Fig. 6B). In the Ala420Gly variant Val86, Leu378 and Leu383 form narrowest part of the tunnel (Fig. 6B). Interestingly, in the crystal structure no water molecules were found in the putative O_2 delivery tunnels of wild-type and mutant PA-LOX. When molecular oxygen travels along these tunnels it enters the substrate-binding pocket in close proximity of the catalytic non-heme iron. In wild-type PA-LOX (Fig. 7A) the side chain of Ala420 narrows the O_2 access tunnel significantly and thus, it blocks dioxygen diffusion to the 11*R*-position of arachidonic acid or the 9*R*-position of linoleic acid. This conclusion is consistent with the arachidonate 15*S*- and the linoleate 13*S*-lipoxygenating activity of the enzyme. In the crystal structure of the Ala420Gly mutant we found that the Ala420Gly substitution opens the narrow part of the O_2 access tunnel (Fig. 7B). Doing so it bifurcated the single tunnel so that O_2 molecules traveling along this path can now also reach the *R*-position at C11 of arachidonic acid or C9 of linoleic acid. This conclusion explains the dual reaction specificity of the mutant enzyme.

In summary, our mutagenesis data suggest that atmospheric dioxygen may travel from the protein surface of PA-LOX into the catalytic center via a defined O_2 access tunnel. Ala420Gly exchange redirects intra-enzyme dioxygen diffusion, which leads to alterations in

Table 3
Data collection parameters and refinement statistics.

Crystal structure PA-LOX Ala420Gly mutant (PDB entry 5LC8)	
Beamline	ID 23–1 - ESRF (Grenoble, France)
Data collection	
Space group	$C\,2\,2\,2_1$
Cell dimensions	84.33, 97.42, 155.60;
(a, b, c [Å]; α, β, γ [°])	90.00, 90.00, 90.00[a]
Wavelength [Å]	0.972
Resolution (Å)	48.71–1.80 (1.90–1.80)[b]
R_{pim} [72]	0.04 (0.36)[b]
R_{merge} [72]	0.08 (0.67)[b]
$I/\sigma\,(I)$ [72]	10.9 (2.1)[b]
Completeness [%]	99.5 (99.6)[b]
Redundancy	4.5 (4.4)[b]
Wilson B factor (Å^2)	22.7
Refinement	
Resolution [Å]	48.71–1.80 (1.85–1.80)[b]
R_{work}/R_{free} [%]	13.9/17.1 (25.9/30.0)[b]
Average B factor (Å^2)	28.4
R.m.s[c] deviations	
Bond lengths (Å)	0.008
Bond angles (°)	1.18
Ramachandran favored [%][d]	94.3
Ramachandran allowed [%][d]	5.7
Ramachandran outlier [%][d]	0.0

[a] Number of crystals for data set: 1.
[b] Highest resolution shell is shown in parenthesis.
[c] R.m.s, root mean square.
[d] As defined in the program *RAMPAGE* [73].

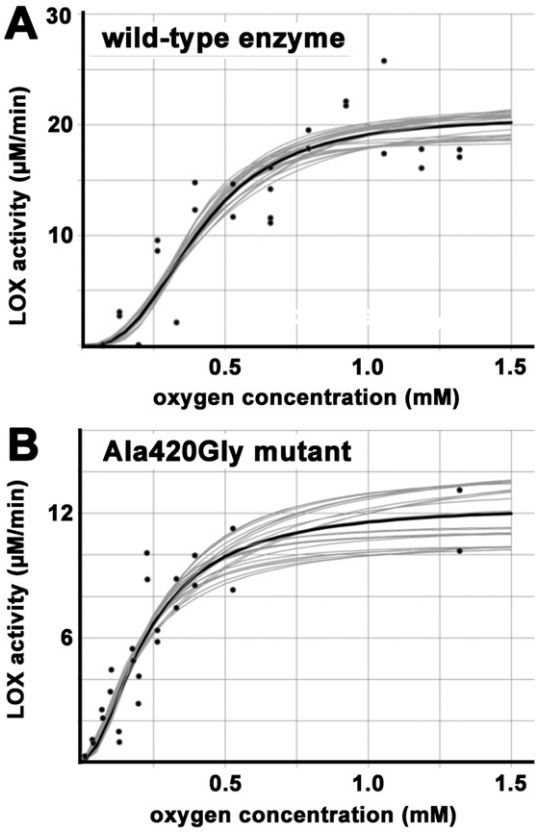

Fig. 4. Determination of molecular oxygen affinity (Km) of wild-type PA-LOX (A) and its Ala420Gly mutant. Arachidonic acid oxygenase activity was measured at 13 different dioxygen concentrations, which were adjusted by mixing argon-flushes (anaerobic) and O_2 flushed (hyperoxic) PBS in different volume ratios. The activity data were plotted against the different dioxygen concentrations and fitted against a Hill-type rate equation (see Materials and methods).

the oxygenation kinetics (improvement of molecular oxygen affinity) and to an alteration of the reaction specificity of fatty acid oxygenation.

4. Discussion

4.1. PA-LOX follows the Ala-vs-Gly concept of reaction specificity

Most LOX isoforms identified so far follow the Ala-vs-Gly concept of reaction specificity. For instance, among the six human LOX-isoforms five iso-enyzmes can be classified as *S*-LOX [ALOX15, ALOX15B, ALOX12, ALOX5, ALOXE3 [61]]. They all carry an Ala at a critical position of their primary structure. Only ALOX12B constitutes a *R*-LOX and here a Gly occupies this critical position [32]. However, not all LOX isoforms follow the rules of the Ala-vs-Gly concept. Zebrafish LOX-1, which carries a Gly at this critical position, has been identified as arachidonate 12*S*-LOX [37]. Thus, for newly discovered LOX it is important to explore whether the Ala-vs-Gly concept is applicable for this particular enzyme. Our chiral phase HPLC data show for the first time that PA-LOX can be classified as *S*-LOX since linoleic acid and arachidonic acid are oxygenated to the corresponding n-6 *S*-hydroperoxy derivatives [18]. Multiple amino acid alignments indicated that Ala420 of PA-LOX constitutes the critical amino acid and that Ala420Gly exchange altered the enantioselectivity of the enzyme in favor of linoleic acid 9*R*- and arachidonic acid 11*R*-lipoxygenation. Although these alterations were not complete our data indicate that the Ala-vs-Gly concept of enantioselectivity is applicable for PA-LOX. This has not been reported before for this particular prokaryotic LOX. To explore the structural basis for this change in reaction specificity we crystallized the Ala420Gly mutant and found that the Ala side chain in wild-type PA-LOX might prevent diffusion of molecular oxygen to the 11*R*- (arachidonic acid) and 9R-position (linoleic acid) of the substrate molecule. However, in the Ala420Gly mutant this structural barrier is removed so that dioxygen can reach these positions.

It has been suggested before [32,33] that the side chain of Ala might prevent O_2 diffusion to the 11*R*-position in arachidonic acid but until now no direct structural data (X-ray coordinates for the Ala-vs-Gly mutant) have been provided to prove this hypothesis. Our crystallographic data indicate for the first time that an Ala-to-Gly exchange opens a new putative O_2 access tunnel which was closed in the wild-type enzyme. Thus, in the mutant protein dioxygen may travel to both C15 and C11 of the arachidonic acid backbone. These direct structural data, which need to be tested for other LOX-isoforms, are consistent with the observed functional alterations and may explain the altered reaction specificity of the Ala420Gly mutant of PA-LOX.

4.2. Oxygen tunnels in LOXs

The catalytic center of LOXs, which harbors the non-heme iron, is localized deeply inside the core of the protein. Thus, in order to react with each other the two substrates (fatty acids and atmospheric dioxygen) must travel from the solvent into the catalytic center and this movement is likely to proceed along pre-formed tunnels. The substrate-binding cavity of different LOX isoforms is differently structured [62]. For rabbit ALOX15 it is boot-shaped tunnel, which intersects with the protein surface in the surrounding of Arg403 (entrance into the active site). The side chains of Ile418, Phe353 and Ile593 form the bottom of the substrate-binding pocket and the bulkiness of these residues are important for the reaction specificity [63]. For this enzyme a dynamic O_2 access tunnel has been suggested, which intersects the substrate-binding cavity, to deliver the second substrate for the oxygenase reaction [57]. Leu367 lines this putative O_2 access tunnel at a critical position and Leu367Phe exchange was hypothesized to limit the dioxygen conductivity of this tunnel. When Leu367 was replaced by a more bulky Phe (Leu6367Phe mutant) dioxygen diffusion into the active site was reduced and this functional impairment was mirrored by an increase in the Km for dioxygen [57]. For soybean LOX-1 putative O_2 access

Enzyme	Ligand	85	86	87	88	89	91	373	374	378	379	382	383	416	417	418	419
Ala420Gly	arachidonic acid	Asn	Val	Lys	Gly	Val	Met		Met	Leu	Ala	His	Leu	Ile	Asn	Glu	Gly
wild-type	arachidonic acid	Asn	Val	Lys	Gly	Val	Met	Glu	Met	Leu	Ala		Leu		Asn		Gly

Enzyme	Ligand	420	421	422	424	425	431	440	442	443	444	445	446	447	448	450	612
Ala420Gly	arachidonic acid	Gly	Ala	Arg	Leu	Leu	Ile	Gln	Thr	Gln	Ala	Thr	Ala	Gly	Gly	Arg	
wild-type	arachidonic acid	Ala	Ala		Leu	Leu	Ile	Gln	Thr	Gln	Ala	Thr	Ala	Gly	Gly	Arg	Leu

hydrophobic residues

tunnel contact residues

wild-type bottleneck residues caver analyst 1.0 with a distance ≤ 3.0 Å

mutant bottleneck residues caver analyst 1.0 with a distance ≤ 3.0 Å

Fig. 5. Amino acids lining the putative O_2 access tunnel. All amino acid residues, which contact the putative O_2 access tunnel (calculated with the *Caver* 3.0 *PyMol* plugin), are indicated. Among them amino acids with hydrophobic side chains are labeled in green. The bottleneck residues of the putative O_2 access tunnel were calculated with the program *Caver analyst* 1.0 with a distance ≤ 3.0 Å and are highlighted in blue (for the wild-type PA-LOX) and yellow (for the Ala420Gly mutant).

tunnels have also been suggested [58]. This enzyme [22,64] contains two major cavities (cavity I and II), which intersect in the proximity of the non-heme iron. The side chains of Arg707 and Val354 separate cavity II into an upstream sub-cavity IIa, which may function as substrate binding pocket and a downstream sub-cavity IIb. The putative substrate-binding pocket (sub-cavity IIa) is intersected by a side-tunnel between Ile553 and Trp500, which has been suggested as O_2 access tunnel [62]. Site-directed mutagenesis studies suggest that Ile553 may limit dioxygen availability [58] but more recent data implicate this amino acid in proper fatty acid alignment [65].

So far, all reports on putative O_2 access tunnels in LOX are based on the interpretation of the internal cavity architectures of the enzymes deduced from the crystal structures and on functional alterations (drop of enzyme activity, increase in Km O_2) observed after site-directed mutagenesis [57,58]. However, in neither of these reports the structural consequences of the mutagenesis strategy (crystal structure of the enzyme mutants) have been explored. This gap is filled in our studies. Following the conventional strategy we first explored the internal cavity structure of wild-type PA LOX for potential O_2 access tunnels. We next, identified Ala420 as bottleneck amino acid and mutated this residue to a less space-filling Gly. Interestingly, consistent with the Ala-vs-Gly concept [33] this mutation altered the reaction specificity of the enzyme but also improved the dioxygen affinity of the enzyme-substrate complex (Fig. 4). Finally, we went a step further and crystallized the Ala420Gly mutant of PA-LOX. Comparisons of the 3D structures of wild-type and mutant PA-LOX indicated that the Ala420Gly exchange bifurcates the putative O_2 access tunnel found in the wild-type enzyme, which allows dioxygen diffusion to both, C15 and C11 of arachidonic acid and C13 and C9 of linoleic acid. In other words, our strategy combined for the first time functional (altered reaction specificity, improved molecular oxygen affinity) and structural (crystal structure) characterization of a LOX mutant with altered enzymatic properties.

4.3. Kinetic properties of PA-LOX

The kinetic properties of PA-LOX, in particular the low molecular oxygen affinity of the enzyme-substrate complex, deserve more detailed discussion. When we analyzed the dependence of the reaction rate on dioxygen concentrations we obtained sigmoid curves for both, wild-type and mutant PA-LOX (Fig. 4). Although these data could be fitted to the Michaelis equation we achieved much better fitting when the Hill equation was used. These data suggest that PA-LOX exhibits

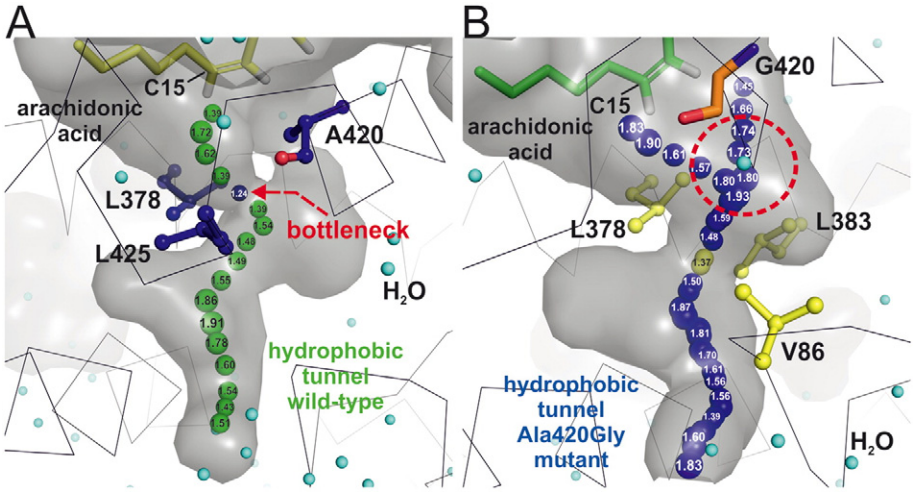

Fig. 6. Bottleneck residues of the putative molecular oxygen tunnel in wild-type PA-LOX and its Ala420Gly mutant. In both crystal structures the cavity surface representations were colored in grey and calculated with the program *PyMOL*. (A) Wild-type PA-LOX with modeled arachidonic acid is depicted as yellow sticks. The hydrophobic tunnel was calculated in *Caver 3.0* and is shown as green chain of spheres with the van der Waals radius of each sphere. The bottleneck residues (blue sticks) Leu378, Ala420 and Leu425 were identified with the program *Caver analyst* 1.0 and are in distance ≤ 3.0 Å to the narrowest point of the tunnel. (B) Ala420Gly PA-LOX with modeled arachidonic acid depicted as green sticks. The hydrophobic tunnel was calculated in *Caver* and shown as blue chain of spheres with the van der Waals radius of each sphere. The red circle indicates the enlargement of the putative dioxygen tunnel in Ala420Gly PA-LOX. The bottleneck residues for this enzyme variant (yellow sticks) were Val86, Leu378 and Leu383. They are in distance < 3.0 Å to the narrowest point of the tunnel.

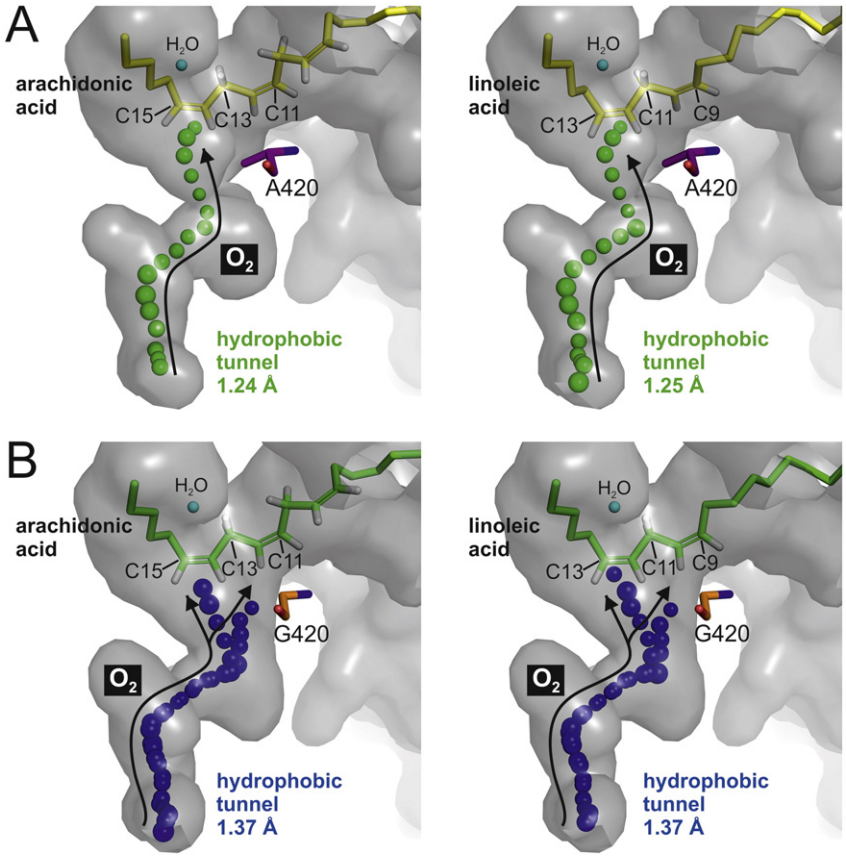

Fig. 7. Putative O_2 access tunnel in wild-type PA-LOX and its Ala420Gly mutant. (A) Wild-type PA-LOX with substrate lipids (left panel, arachidonic acid; right panel, linoleic acid) are shown as yellow sticks. Cavity surface presentations (calculated with the program *PyMOL*) are colored in grey. The putative hydrophobic O_2 access tunnel is indicated by the chain of green spheres with C15 (arachidonic acid) and C13 (linoleic acid) as starting points for the calculations. B) Similar calculations were carried out for Ala420Gly mutant. The putative hydrophobic O_2 access tunnel is indicated by the chain of blue spheres with C15 and C11 (arachidonic acid) and C9 and C13 (linoleic acid) as starting points for the calculations. Black arrows in A and B indicate the path of molecular oxygen movement.

cooperative properties, which is somewhat unusual for proteins consisting of a single polypeptide chain. However, cooperative properties have previously been reported for recombinant human ALOX15 and human ALOX15B, which also consist of a single polypeptide chains [66,67]. One way to explain the cooperative characteristics of LOX is their ability to form homodimers. Rabbit ALOX15 forms functional homodimers in aqueous solutions [68] and a similar dimerization has been suggested for human ALOX5 [69]. When we analyzed the pure recombinant PA-LOX in size exclusion chromatography we obtained two distinct peaks (data not shown). After calibrating the chromatographic scale with authentic molecular weight markers we found that early eluting peak migrated with an apparent molecular weight that was twice as high as that of the late eluting peak. When aliquots of both peaks were run in SDS-PAGE the major bands migrated at 70 kDa. These data suggest the principal capability of PA-LOX to form non-covalent dimers in aqueous solutions and this dimerization may contribute to the cooperative character of this enzyme. However, protein dimerization may not be the only way to explain the cooperative properties of PA-LOX. When traveling along the O_2 access tunnels atmospheric dioxygen may bind at different sites of the protein. Moreover, the product pattern formed by the mutant enzyme clearly indicates two different sites of O_2 insertion into the fatty acid substrate (C15 and C11 of arachidonic acid). These data indicate multiple dioxygen binding sites at the protein, which could explain the cooperative behavior.

As shown in Table 1 the Ala420Gly exchange induced two partially opposing effects on the kinetic properties of PA-LOX: i) The mutation impaired the catalytic activity by about 80%. Although the molecular basis for the impaired catalytic activity has not been explored, it may be suggested that this mutation reduces the rate-limiting step of the LOX reaction, which is the initial hydrogen abstraction. Structural modeling of enzyme-linoleic complexes suggested that in wild-type PA-LOX the fatty acid substrate is aligned at the active site in such a way that the pro*S* hydrogen at C11 of linoleic acid is localized in close proximity of the non-heme iron. In contrast, in the Ala420Gly mutant this hydrogen was shifted away by about 0.6 Å from the iron, which might explain the impaired catalytic activity. A similar drop in catalytic activity was observed when similar mutations were carried out with other LOX-isoforms [32,34,35]. ii) Despite the reduction of the catalytic activity the molecular oxygen affinity of the mutant enzyme-substrate complex was improved and this alteration counteracts the drop in catalytic activity. Since the observed alterations in the product pattern of the Ala420Gly mutant was incomplete (formation of a 1:1 mixture 15*S*-H(p)ETE and 11*R*-H(p)ETE) more drastic improvement in the molecular oxygen affinity were not expected. This might be different for enzyme species, for which a complete conversion of the reaction specificity was observed [32].

The crystallographic data suggest that this mutation bifurcates the putative O_2 access tunnel and this structural modification allows oxygenation of both C15 and C11 of arachidonic acid or C13 and C9 of linoleic acid (Fig. 7). More quantitative analysis of the arachidonic acid oxygenation products formed by the Ala420Gly mutant revealed an almost 1:1 ratio of 15-HETE/11-HETE. These data suggest that the dioxygen conductivity of the original O_2 access tunnel (leading to 15*S*-oxygenation) and the mutation-induced site-tunnel (leading to 11*R*-oxygenation) in the Ala420Gly mutant should be very similar. Since the structure of the original tunnel was not dramatically altered by the mutation it may be concluded that the overall dioxygen conductivity of the enzyme should be doubled. This situation may be mirrored by the 50% reduction of the dioxygen Km (Table 1).

Although the side chain of Ala420 narrows the putative O_2 access tunnel in wild-type PA-LOX and thus contributes to the low molecular oxygen affinity of the enzyme, it is clearly not the only reason for this property since the molecular oxygen affinity of the Ala420Gly mutant is still lower than that of other LOX-isoforms. Unfortunately, on the basis of the currently available experimental data it is impossible to define why PA-LOX exhibits such low molecular oxygen affinity. From the kinetic data one might conclude that the dioxygen conductivity of the PA-LOX O_2 access channel is lower when compared with the corresponding structures of other LOXs but the molecular basis for this conclusion remains unclear. The dioxygen conductivity of preformed intra-protein tunnels depends on the tunnel geometry (presence of bottlenecks) but also on the polarity of the amino acid side chains lining such tunnels. Since direct measurements of the dioxygen conductivity of intra-protein channels have not been carried out so far for any LOX isoform the reasons for the unusually low molecular oxygen affinity of PA-LOX remain to be explored in the future.

For most mammalian LOX- and COX isoforms dioxygen Km-values in the lower micromolar range have been reported [56–59]. Thus, under physiological conditions these enzymes work in the range of O_2 saturation and thus, alterations in the actual dioxygen concentrations hardly alter the LOX-reaction. This is clearly not the case for PA-LOX. With a Km-value of 406 μM wild-type PA-LOX has an unusually low affinity for dioxygen. These data suggest that at physiological dioxygen concentrations the enzyme does not work at substrate saturation. Thus, alterations in the dioxygen tension constitute a regulatory element of PA-LOX activity and such kinetic parameters are characteristic for sensor proteins. In other words, variations of the actual dioxygen concentrations are directly translated into changes of the catalytic activity. Thus, under hypoxic conditions less hydroperoxy lipids are formed, which impacts the extracellular and intracellular redox potential. The intracellular redox alterations will modify the activity state of various redox sensitive transcription factors, which changes the gene expression pattern of cells in the immediate surrounding. Via this mechanism alterations in the dioxygen concentrations may change the metabolism of the bacteria but also of the surrounding host cells. A similar mechanism has been suggested before for the activation of the transcription factor HIF [70]. In this context HIF-prolyl hydroxylase functions as oxygen sensor [71] and this enzyme exhibits similar kinetic properties (low molecular oxygen affinity) as PA-LOX.

Funding sources

This work was supported by Deutsche Forschungsgemeinschaft [(GRK 1673 to H.K., Ku961/11-1 to H.K.; SFB740-B6 to P.S., SFB1078-B6 to P.S.) and DFG - Cluster of Excellence UniCat “Unifying Concepts in Catalysis” (D3/E3-1) to P.S.].

Conflict of interest

The authors declare that they do not have any conflicts of interest with the content of this article.

Author contributions

S.B. carried out preparation and functional characterization of wild-type and mutant enzyme variants including kinetic measurements and product identification. J.K. and E.G.Y. performed crystal trials and collected the X-ray diffraction data. J.K., E.G.Y. and P.S. performed structural refinement and structural modeling. M.H. provided the deuterated linoleic acid isomers and carried out GC/MS analysis of the oxygenation products. H-G.H. evaluated the reaction kinetics. H.K. drafted the first manuscript and all co-authors contributed to manuscript writing. H.K. and P.S. planned the study, designed and coordinated the experiments.

Transparency Document

The Transparency document associated with this article can be found, in online version.

Acknowledgements

We thank Prof. X. Carpena from Institut de Biologia Molecular, Parc Científic de Barcelona, Barcelona (Spain) for providing the expression plasmid of PA-LOX. Moreover, we would also like to thank U. Müller, M. Weiss and the scientific staff of the BESSY MX (Helmholtz Zentrum Berlin) at beamlines BL14.1, BL14.2 and BL14.3 operated by the Joint Berlin MX-Laboratory at the BESSY II electron storage ring (Berlin, Germany) and the scientific staff of the European Synchrotron Radiation Facility (Grenoble) at beamlines ID29, ID23-2, ID30A-3, ID30B and ID23-1 for their continuous support. The authors would like to thank Dr. R. Tauber from the Institute of Laboratory Medicine, Clinical Chemistry and Pathobiochemistry, Charite - Universitätsmedizin Berlin for continuous support of our work.

References

[1] F.M. Raushel, J.B. Thoden, H.M. Holden, Enzymes with molecular tunnels, Acc. Chem. Res. 36 (2003) 539–548.
[2] A. Weeks, L. Lund, F.M. Raushel, Tunneling of intermediates in enzyme-catalyzed reactions, Curr. Opin. Chem. Biol. 10 (2006) 465–472.
[3] J. Kalms, A. Schmidt, S. Frielingsdorf, P. van der Linden, D. von Stetten, O. Lenz, P. Carpentier, P. Scheerer, Krypton derivatization of an O_2 -tolerant membrane-bound [NiFe] hydrogenase reveals a hydrophobic tunnel network for gas transport, Angew. Chem. Int. Ed. Eng. 55 (2016) 5586–5590.
[4] I. Ivanov, H. Kuhn, D. Heydeck, Structural and functional biology of arachidonic acid 15-lipoxygenase-1 (ALOX15), Gene 573 (2015) 1–32.
[5] H. Kuhn, S. Banthiya, K. van Leyen, Mammalian lipoxygenases and their biological relevance, Biochim. Biophys. Acta 1851 (2015) 308–330.
[6] J.Z. Haeggstrom, C.D. Funk, Lipoxygenase and leukotriene pathways: biochemistry, biology, and roles in disease, Chem. Rev. 111 (2011) 5866–5898.
[7] A. Garreta, S.P. Val-Moraes, Q. Garcia-Fernandez, M. Busquets, C. Juan, A. Oliver, A. Ortiz, B.J. Gaffney, I. Fita, A. Manresa, X. Carpena, Structure and interaction with phospholipids of a prokaryotic lipoxygenase from *Pseudomonas aeruginosa*, FASEB J. 27 (2013) 4811–4821.
[8] D. Bleich, S. Chen, B. Zipser, D. Sun, C.D. Funk, J.L. Nadler, Resistance to type 1 diabetes induction in 12-lipoxygenase knockout mice, J. Clin. Invest. 103 (1999) 1431–1436.
[9] O. Radmark, O. Werz, D. Steinhilber, B. Samuelsson, 5-Lipoxygenase, a key enzyme for leukotriene biosynthesis in health and disease, Biochim. Biophys. Acta 1851 (2015) 331–339.
[10] D. Zhu, Y. Ran, Role of 15-lipoxygenase/15-hydroxyeicosatetraenoic acid in hypoxia-induced pulmonary hypertension, J. Physiol. Sci. 62 (2012) 163–172.
[11] J. Wittwer, M. Hersberger, The two faces of the 15-lipoxygenase in atherosclerosis, Prostaglandins Leukot. Essent. Fat. Acids 77 (2007) 67–77.
[12] M.C. Cathcart, J. Lysaght, G.P. Pidgeon, Eicosanoid signalling pathways in the development and progression of colorectal cancer: novel approaches for prevention/intervention, Cancer Metastasis Rev. 30 (2011) 363–385.
[13] G. Rai, N. Joshi, J.E. Jung, Y. Liu, L. Schultz, A. Yasgar, S. Perry, G. Diaz, Q. Zhang, V. Kenyon, A. Jadhav, A. Simeonov, E.H. Lo, K. van Leyen, D.J. Maloney, T.R. Holman, Potent and selective inhibitors of human reticulocyte 12/15-lipoxygenase as anti-stroke therapies, J. Med. Chem. 57 (2014) 4035–4048.
[14] T. Horn, S. Adel, R. Schumann, S. Sur, K.R. Kakularam, A. Polamarasetty, P. Redanna, H. Kuhn, D. Heydeck, Evolutionary aspects of lipoxygenases and genetic diversity of human leukotriene signaling, Prog. Lipid Res. 57 (2015) 13–39.
[15] R.E. Vance, S. Hong, K. Gronert, C.N. Serhan, J.J. Mekalanos, The opportunistic pathogen carries a secretable arachidonate 15-lipoxygenase, Proc. Natl. Acad. Sci. U. S. A. 101 (2004) 2135–2139.
[16] J. Hansen, A. Garreta, M. Benincasa, M.C. Fuste, M. Busquets, A. Manresa, Bacterial lipoxygenases, a new subfamily of enzymes? A phylogenetic approach, Appl. Microbiol. Biotechnol. 97 (2013) 4737–4747.
[17] K.H.Y. Shimahara, Properties of a lipoxygenase-like enzyme produced by *Pseudomonas aeruginosa* strain A-4, J. Ferment. Technol. 51 (1973) 183–189.
[18] S. Banthiya, M. Pekarova, H. Kuhn, D. Heydeck, Secreted lipoxygenase from *Pseudomonas aeruginosa* exhibits biomembrane oxygenase activity and induces hemolysis in human red blood cells, Arch. Biochem. Biophys. 584 (2015) 116–124.
[19] N.C. Gilbert, S.G. Bartlett, M.T. Waight, D.B. Neau, W.E. Boeglin, A.R. Brash, M.E. Newcomer, The structure of human 5-lipoxygenase, Science 331 (2011) 217–219.
[20] M.J. Kobe, D.B. Neau, C.E. Mitchell, S.G. Bartlett, M.E. Newcomer, The structure of human 15-lipoxygenase-2 with a substrate mimic, J. Biol. Chem. 289 (2014) 8562–8569.
[21] J. Choi, J.K. Chon, S. Kim, W. Shin, Conformational flexibility in mammalian 15S-lipoxygenase: reinterpretation of the crystallographic data, Proteins 70 (2008) 1023–1032.

[22] W. Minor, J. Steczko, B. Stec, Z. Otwinowski, J.T. Bolin, R. Walter, B. Axelrod, Crystal structure of soybean lipoxygenase L-1 at 1.4 A resolution, Biochemistry 35 (1996) 10687–10701.
[23] S. Banthiya, J. Kalms, E. Galemou Yoga, I. Ivanov, X. Carpena, M. Hamberg, H. Kuhn, P. Scheerer, Structural and functional basis of phospholipid oxygenase activity of bacterial lipoxygenase from *Pseudomonas aeruginosa*, Biochim. Biophys. Acta 1861 (2016) 1681–1692.
[24] N. Lehnert, E.I. Solomon, Density-functional investigation on the mechanism of H-atom abstraction by lipoxygenase, J. Biol. Inorg. Chem. 8 (2003) 294–305.
[25] C.A. Carr, J.P. Klinman, Hydrogen tunneling in a prokaryotic lipoxygenase, Biochemistry 53 (2014) 2212–2214.
[26] S. Hu, S.C. Sharma, A.D. Scouras, A.V. Soudackov, C.A. Carr, S. Hammes-Schiffer, T. Alber, J.P. Klinman, Extremely elevated room-temperature kinetic isotope effects quantify the critical role of barrier width in enzymatic C-H activation, J. Am. Chem. Soc. 136 (2014) 8157–8160.
[27] W.E. Boeglin, R.B. Kim, A.R. Brash, A 12R-lipoxygenase in human skin: mechanistic evidence, molecular cloning, and expression, Proc. Natl. Acad. Sci. U. S. A. 95 (1998) 6744–6749.
[28] P. Krieg, M. Siebert, A. Kinzig, R. Bettenhausen, F. Marks, G. Fürstenberger, Murine 12(*R*)-lipoxygenase: functional expression, genomic structure and chromosomal localization, FEBS Lett. 446 (1999) 142–148.
[29] A.R. Brash, W.E. Boeglin, M.S. Chang, B.H. Shieh, Purification and molecular cloning of an 8R-lipoxygenase from the coral *Plexaura homomalla* reveal the related primary structures of R- and S-lipoxygenases, J. Biol. Chem. 271 (1996) 20949–20957.
[30] T. Hada, L.L. Swift, A.R. Brash, Discovery of 5R-lipoxygenase activity in oocytes of the surf clam, *Spisula solidissima*, Biochim. Biophys. Acta 1346 (1997) 109–119.
[31] D.J. Hawkins, A.R. Brash, Eggs of the sea urchin, *Strongylocentrotus purpuratus*, contain a prominent (11R) and (12R) lipoxygenase activity, J. Biol. Chem. 262 (1987) 7629–7634.
[32] G. Coffa, A.R. Brash, A single active site residue directs oxygenation stereospecificity in lipoxygenases: stereocontrol is linked to the position of oxygenation, Proc. Natl. Acad. Sci. U. S. A. 101 (2004) 15579–15584.
[33] G. Coffa, C. Schneider, A.R. Brash, A comprehensive model of positional and stereo control in lipoxygenases, Biochem. Biophys. Res. Commun. 338 (2005) 87–92.
[34] G. Coffa, A.N. Imber, B.C. Maguire, G. Laxmikanthan, C. Schneider, B.J. Gaffney, A.R. Brash, On the relationships of substrate orientation, hydrogen abstraction, and product stereochemistry in single and double dioxygenations by soybean lipoxygenase-1 and its Ala542Gly mutant, J. Biol. Chem. 280 (2005) 38756–38766.
[35] L. Collazo, J.P. Klinman, Control of the position of oxygen delivery in soybean lipoxygenase-1 by amino acid side chains within a gas migration channel, J. Biol. Chem. 291 (2016) 9052–9059.
[36] R. Vogel, C. Jansen, J. Roffeis, P. Reddanna, P. Forsell, H.E. Claesson, H. Kuhn, M. Walther, Applicability of the triad concept for the positional specificity of mammalian lipoxygenases, J. Biol. Chem. 285 (2010) 5369–5376.
[37] C. Jansen, K. Hofheinz, R. Vogel, J. Roffeis, M. Anton, P. Reddanna, H. Kuhn, M. Walther, Stereocontrol of arachidonic acid oxygenation by vertebrate lipoxygenases: newly cloned zebrafish lipoxygenase 1 does not follow the Ala-versus-Gly concept, J. Biol. Chem. 286 (2011) 37804–37812.
[38] M. Hamberg, Stereochemistry of oxygenation of linoleic acid catalyzed by prostaglandin-endoperoxide H synthase-2, Arch. Biochem. Biophys. 349 (1998) 376–380.
[39] M. Hamberg, Stereochemistry of hydrogen removal during oxygenation of linoleic acid by singlet oxygen and synthesis of 11(*S*)-deuterium-labeled linoleic acid, Lipids 46 (2011) 201–206.
[40] D. Nurizzo, T. Mairs, M. Guijarro, V. Rey, J. Meyer, P. Fajardo, J. Chavanne, J.C. Biasci, S. McSweeney, E. Mitchell, The ID23-1 structural biology beamline at the ESRF, J. Synchrotron Radiat. 13 (2006) 227–238.
[41] J. Gabadinho, A. Beteva, M. Guijarro, V. Rey-Bakaikoa, D. Spruce, M.W. Bowler, S. Brockhauser, D. Flot, E.J. Gordon, D.R. Hall, B. Lavault, A.A. McCarthy, J. McCarthy, E. Mitchell, S. Monaco, C. Mueller-Dieckmann, D. Nurizzo, R.B. Ravelli, X. Thibault, M.A. Walsh, G.A. Leonard, S.M. McSweeney, MxCuBE: a synchrotron beamline control environment customized for macromolecular crystallography experiments, J. Synchrotron Radiat. 17 (2010) 700–707.
[42] M.F. Incardona, G.P. Bourenkov, K. Levik, R.A. Pieritz, A.N. Popov, O. Svensson, EDNA: a framework for plugin-based applications applied to X-ray experiment online data analysis, J. Synchrotron Radiat. 16 (2009) 872–879.
[43] W. Kabsch, Xds, Acta Crystallogr. D Biol. Crystallogr. 66 (2010) 125–132.
[44] Collaborative Computational Project, N, The CCP4 suite: programs for protein crystallography, Acta Crystallogr. D Biol. Crystallogr. 50 (1994) 760–763.
[45] M.D. Winn, C.C. Ballard, K.D. Cowtan, E.J. Dodson, P. Emsley, P.R. Evans, R.M. Keegan, E.B. Krissinel, A.G. Leslie, A. McCoy, S.J. McNicholas, G.N. Murshudov, N.S. Pannu, E.A. Potterton, H.R. Powell, R.J. Read, A. Vagin, K.S. Wilson, Overview of the CCP4 suite and current developments, Acta Crystallogr. D Biol. Crystallogr. 67 (2011) 235–242.
[46] A.J. McCoy, R.W. Grosse-Kunstleve, P.D. Adams, M.D. Winn, L.C. Storoni, R.J. Read, Phaser crystallographic software, J. Appl. Crystallogr. 40 (2007) 658–674.
[47] P.D. Adams, P.V. Afonine, G. Bunkoczi, V.B. Chen, I.W. Davis, N. Echols, J.J. Headd, L.W. Hung, G.J. Kapral, R.W. Grosse-Kunstleve, A.J. McCoy, N.W. Moriarty, R. Oeffner, R.J. Read, D.C. Richardson, J.S. Richardson, T.C. Terwilliger, P.H. Zwart, PHENIX: a comprehensive python-based system for macromolecular structure solution, Acta Crystallogr. D Biol. Crystallogr. 66 (2010) 213–221.
[48] G.N. Murshudov, A.A. Vagin, E.J. Dodson, Refinement of macromolecular structures by the maximum-likelihood method, Acta Crystallogr. D Biol. Crystallogr. 53 (1997) 240–255.
[49] P. Emsley, B. Lohkamp, W.G. Scott, K. Cowtan, Features and development of Coot, Acta Crystallogr. D Biol. Crystallogr. 66 (2010) 486–501.
[50] A.T. Brunger, Free R value: a novel statistical quantity for assessing the accuracy of crystal structures, Nature 355 (1992) 472–475.
[51] H.M. Berman, J. Westbrook, Z. Feng, G. Gilliland, T.N. Bhat, H. Weissig, I.N. Shindyalov, P.E. Bourne, The protein data bank, Nucleic Acids Res. 28 (2000) 235–242.
[52] I.W. Davis, A. Leaver-Fay, V.B. Chen, J.N. Block, G.J. Kapral, X. Wang, L.W. Murray, W.B. Arendall 3rd, J. Snoeyink, J.S. Richardson, D.C. Richardson, MolProbity: all-atom contacts and structure validation for proteins and nucleic acids, Nucleic Acids Res. 35 (2007) W375–W383.
[53] R. Rodriguez, G. Chinea, N. Lopez, T. Pons, G. Vriend, Homology modeling, model and software evaluation: three related resources, Bioinformatics 14 (1998) 523–528.
[54] P. Emsley, K. Cowtan, Coot: model-building tools for molecular graphics, Acta Crystallogr. D Biol. Crystallogr. 60 (2004) 2126–2132.
[55] E. Chovancova, A. Pavelka, P. Benes, O. Strnad, J. Brezovsky, B. Kozlikova, A. Gora, V. Sustr, M. Klvana, P. Medek, L. Biedermannova, J. Sochor, J. Damborsky, CAVER 3.0: a tool for the analysis of transport pathways in dynamic protein structures, PLoS Comput. Biol. 8 (2012), e1002708. .
[56] P. Ludwig, H.G. Holzhutter, A. Colosimo, M.C. Silvestrini, T. Schewe, S.M. Rapoport, A kinetic model for lipoxygenases based on experimental data with the lipoxygenase of reticulocytes, Eur. J. Biochem. 168 (1987) 325–337.
[57] J. Saam, I. Ivanov, M. Walther, H.G. Holzhutter, H. Kuhn, Molecular dioxygen enters the active site of 12/15-lipoxygenase via dynamic oxygen access channels, Proc. Natl. Acad. Sci. U. S. A. 104 (2007) 13319–13324.
[58] M.J. Knapp, J.P. Klinman, Kinetic studies of oxygen reactivity in soybean lipoxygenase-1, Biochemistry 42 (2003) 11466–11475.
[59] I. Juranek, H. Suzuki, S. Yamamoto, Affinities of various mammalian arachidonate lipoxygenases and cyclooxygenases for molecular oxygen as substrate, Biochim. Biophys. Acta 1436 (1999) 509–518.
[60] B. Kozlikova, E. Sebestova, V. Sustr, J. Brezovsky, O. Strnad, L. Daniel, D. Bednar, A. Pavelka, M. Manak, M. Bezdeka, P. Benes, M. Kotry, A. Gora, J. Damborsky, J. Sochor, CAVER Analyst 1.0: graphic tool for interactive visualization and analysis of tunnels and channels in protein structures, Bioinformatics 30 (2014) 2684–2685.
[61] Y. Zheng, A.R. Brash, Dioxygenase activity of epidermal lipoxygenase-3 unveiled: typical and atypical features of its catalytic activity with natural and synthetic polyunsaturated fatty acids, J. Biol. Chem. 285 (2010) 39866–39875.
[62] I. Ivanov, D. Heydeck, K. Hofheinz, J. Roffeis, V.B. O'Donnell, H. Kuhn, M. Walther, Molecular enzymology of lipoxygenases, Arch. Biochem. Biophys. 503 (2010) 161–174.
[63] S. Borngraber, M. Browner, S. Gillmor, C. Gerth, M. Anton, R. Fletterick, H. Kuhn, Shape and specificity in mammalian 15-lipoxygenase active site. The functional interplay of sequence determinants for the reaction specificity, J. Biol. Chem. 274 (1999) 37345–37350.
[64] J.C. Boyington, B.J. Gaffney, L.M. Amzel, The three-dimensional structure of an arachidonic acid 15-lipoxygenase, Science 260 (1993) 1482–1486.
[65] M.P. Meyer, D.R. Tomchick, J.P. Klinman, Enzyme structure and dynamics affect hydrogen tunneling: the impact of a remote side chain (I553) in soybean lipoxygenase-1, Proc. Natl. Acad. Sci. U. S. A. 105 (2008) 1146–1151.
[66] A.T. Wecksler, V. Kenyon, J.D. Deschamps, T.R. Holman, Substrate specificity changes for human reticulocyte and epithelial 15-lipoxygenases reveal allosteric product regulation, Biochemistry 47 (2008) 7364–7375.
[67] A.T. Wecksler, V. Kenyon, N.K. Garcia, J.D. Deschamps, W.A. van der Donk, T.R. Holman, Kinetic and structural investigations of the allosteric site in human epithelial 15-lipoxygenase-2, Biochemistry 48 (2009) 8721–8730.
[68] I. Ivanov, W. Shang, L. Toledo, L. Masgrau, D.I. Svergun, S. Stehling, H. Gomez, A. Di Venere, G. Mei, J.M. Lluch, E. Skrzypczak-Jankun, A. Gonzalez-Lafont, H. Kuhn, Ligand-induced formation of transient dimers of mammalian 12/15-lipoxygenase: a key to allosteric behavior of this class of enzymes? Proteins 80 (2012) 703–712.
[69] A.K. Hafner, M. Cernescu, B. Hofmann, M. Ermisch, M. Hornig, J. Metzner, G. Schneider, B. Brutschy, D. Steinhilber, Dimerization of human 5-lipoxygenase, Biol. Chem. 392 (2011) 1097–1111.
[70] T. Hellwig-Burgel, D.P. Stiehl, A.E. Wagner, E. Metzen, W. Jelkmann, Review: hypoxia-inducible factor-1 (HIF-1): a novel transcription factor in immune reactions, J. Interf. Cytokine Res. 25 (2005) 297–310.
[71] E. Berra, E. Benizri, A. Ginouves, V. Volmat, D. Roux, J. Pouyssegur, HIF prolyl-hydroxylase 2 is the key oxygen sensor setting low steady-state levels of HIF-1alpha in normoxia, EMBO J. 22 (2003) 4082–4090.
[72] M.S. Weiss, Global indicators of X-ray data quality, J. Appl. Crystallogr. 34 (2001) 130–135.
[73] S.C. Lovell, I.W. Davis, W.B. Arendall 3rd, P.I. de Bakker, J.M. Word, M.G. Prisant, J.S. Richardson, D.C. Richardson, Structure validation by Calpha geometry: phi,psi and Cbeta deviation, Proteins 50 (2003) 437–450.

Discussion & Outlook

9 Hydrogenase *Re*MBH

In the last decade, intensive research has been carried out for understanding the structure and function of O_2-tolerant and O_2-sensitive hydrogenases. *Re*MBH belongs to the small subgroup of O_2-tolerant [NiFe] hydrogenases, which catalyse the oxidation of hydrogen into protons and electrons and *vice versa* under ambient O_2 conditions. Therefore, *Re*MBH came into focus as a biological catalyst in clean energy production. To design a high performance, long living, O_2-tolerant hydrogenase as artificial catalyst, many techniques e.g. spectroscopy, computational and structural studies were performed to investigate the characteristics of hydrogenases. As the majority of enzymes, *Re*MBH harbours the catalytic centre deeply buried within the protein matrix. For the catalytic reaction, the substrate needs to enter the protein either through free diffusion or directed transport through protein tunnels. Several aspects like regiospecificity, reduced travel time or protection of intermediates are suggesting a controlled transport of substrate between the protein exterior and the active site rather than free diffusion. Previous structural studies revealed the large contribution of the proximal [4Fe3S]-cluster in O_2 tolerance of *Re*MBH. However, the question arises, which other structural characteristics of these enzymes playing a role in O_2 tolerance. In this work, several aspects of the tunnel network in O_2-tolerant and O_2-sensitive hydrogenases were studied with structural and computational methods presenting the differences between both groups and outlining the tunnel features in *Re*MBH. A well-established structural method to study molecular tunnels is the derivatisation of protein crystals with noble gases like xenon or krypton due to their hydrophobicity and high atomic number. The first tunnel network in the O_2-sensitive hydrogenase from *Desulfovibrio fructosovorans* (*Df*) has been described by Montet and colleagues using xenon derviatisation.[28] On the basis of the existing structure of [NiFe] hydrogenase from *Desulfovibrio gigas* (*Dg*) in the same study the hydrophobic tunnels have been confirmed by MD simulations. Comparing the tunnel characteristics between O_2-sensitive and O_2-tolerant hydrogenases krypton derivatisation of *Re*MBH crystals and *Caver 3.0* tunnel calculations for both groups have been applied in this work and the results were described in the publication "*Krypton Derivatization of an O2-Tolerant Membrane-Bound [NiFe] Hydrogenase Reveals a Hydrophobic Tunnel Network for Gas Transport*" (Results, i). The krypton atom positions described two distinct routes for gas molecules between the protein

exterior and active site and a branch for potential substrate storage. In addition, these results were verified by computational tunnel calculations with the program *Caver 3.0*. Elaborate tunnel calculations of both [NiFe] hydrogenase groups from different organisms revealed a more complex pathway system in O_2-sensitive hydrogenases with an in average two times higher amount in tunnels and openings. The increased quantity of substrate tunnels with surface openings and a slightly greater diameter might have an influence in higher gas diffusion rates for substrate as well as inhibitors in O_2-sensitive hydrogenases. This leads to the hypothesis that O_2-tolerant [NiFe] hydrogenases limit gas diffusion to the active site enabling the reduction of O_2 to harmless water besides the catalytic cycle.

In the second publication, "*Tracking the route of molecular oxygen in membrane-bound [NiFe] hydrogenase of Ralstonia eutropha*" (Results, ii) the potential pathway of O_2 access has been studied for the first time with the derivatisation of *Re*MBH crystals with molecular oxygen and computational calculations with the program *Caver 3.0*. However, crystal structures as well as the *Caver3.0* calculations only provide results of static protein structures. Therefore, it was extremely helpful to compare X-ray crystallography results with *Re*MBH MD simulations kindly provided by the group of Maria Andrea Mroginski and calculated by Tillmann Utesch. The O_2-derivatised *Re*MBH crystal structure presented was pressurized at 70 bar for 15 min. As comparison data, non-derivatised and high-pressure (2000 bar) data sets were collected. The pressurization experiments have no impact on the protein core showing an overall identical [NiFe] active site, medial and distal [FeS]-cluster. Interestingly, the higher O_2 concentrations in the derivatised *Re*MBH have an impact on the proximal [4Fe3S]-cluster. The [4Fe3S]-cluster contains an additional hydroxyl ligand at one of the iron ions (Fe1) and $Glu76_S$ shifts closer (OεE76: 3.4 Å → 2.6 Å) towards another iron ion (Fe4) of the cluster. A similar shift has been detected in O_2-tolerant [NiFe] hydrogenase 1 from *Escherichia coli* (*Ec*Hyd-1), where $Glu76_S$ has two alternative positions in the enzyme as-isolated state with OεE76 distances of 3.4 Å and 2.4 Å to the iron ion (Fe4) of the proximal cluster (***Figure 30A***).[120] Volbeda and co-workers stated $Glu76_S$ was involved in proton abstraction to stabilise the approach of Fe4 to the amid-N of Cys20, which further stabilises the superoxidised state of the proximal cluster. In the ferricyanide-oxidized structure similar alternative conformations of $Glu76_S$ were found (***Figure 30B***). Both structures also show a higher flexibility for Fe4. In *Re*MBH the two structural alterations of the hydroxyl ligand and $Glu76_S$ shift might be linked to the stabilization of the cluster in its high-potential form, which needs further examination or oxidative damage through

high O_2 concentrations. In this regard it should be noticed, that no damage through O_2 was detected for the remaining metal clusters.

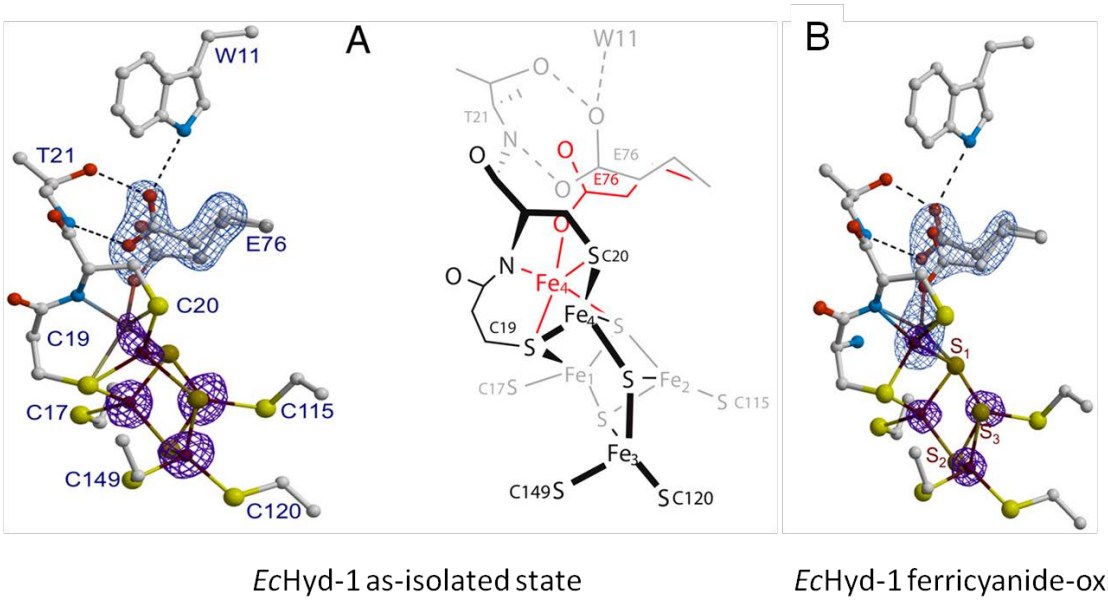

Figure 30: *Ec*Hyd-1 proximal cluster structures. Figure 30 was inherited from Volbeda *et al.*[120] **(A)** As-isolated state of *Ec*Hyd-1 with two alternative conformations of E76. The iron ions are depicted as spheres with their anomalous difference electron density peaks (purple mesh) contoured at 5 σ. The E76 omit map is shown as light blue mesh and contoured at 8 σ. The schematic representation illustrates the double conformation of Fe4 in the cluster plus the two alternative positions of E76. **(B)** The 4-OH-1,4-naphthoquinone/ferricyanide-oxidized structure shows the alternative positions of both Fe4 and E76. The iron peaks (purple mesh) and the omit map (light blue mesh) are contoured at the 6 σ and 9 σ, respectively.

X-ray crystallography results and MD simulations have demonstrated that H_2 and O_2, an inhibitor in O_2-sensitive [NiFe] hydrogenases, take the same pathways to reach the active site. H_2 and O_2 sharing the same access tunnels could indicate lower concentrations of O_2 within the tunnel as it is competing with H_2. Further, H_2 could be detected closer to the active site than O_2, suggesting that the larger O_2 is hindered by the active site gate amino acids. Therefore, the narrower tunnel towards the Ni atom might limit O_2 attack at the catalytic centre. The MD simulation results showed that the static *Re*MBH structure is mainly conform to the calculations under solvent conditions also indicating that previous tunnel calculations on the static structures of the O_2-sensitive and O_2-tolerant hydrogenases are comparatively meaningful. In the MD simulations the two substrate tunnels with tunnel A as main access route for H_2 and a storage cavity, which were proposed in the *Re*MBH crystal structures, were confirmed to make the presented gas tunnel network in *Re*MBH.

However, further mutational experiments on the hydrophobic tunnel system of O_2-tolerant and O_2-sensitive hydrogenases might shed light on the influence of the variations of these structural features between the two groups. One possible set of substitutions in O_2-sensitive hydrogenases

could be the introduction of more bulky side chains or hydrophilic amino acids to block the bottlenecks and to close the tunnel entrances (***Figure 31***). This could help to create a potential storage cavity, which might have an extremely important function for O_2 tolerance as gas storage and for catalytic activity. In turn, in O_2-tolerant [NiFe] hydrogenases hydrophobic storage cavities as found in *Re*MBH could be mutated to an extra tunnel with an opening to the protein surface. An interesting fact is the missing gas tunnel B and branch 1 in O_2-tolerant *Ec*Hyd-1 suggesting that gas tunnel A is the main tunnel as it is present in both groups. Blocking this tunnel might have a large impact in O_2 tolerance in [NiFe] hydrogenases (***Figure 32***).

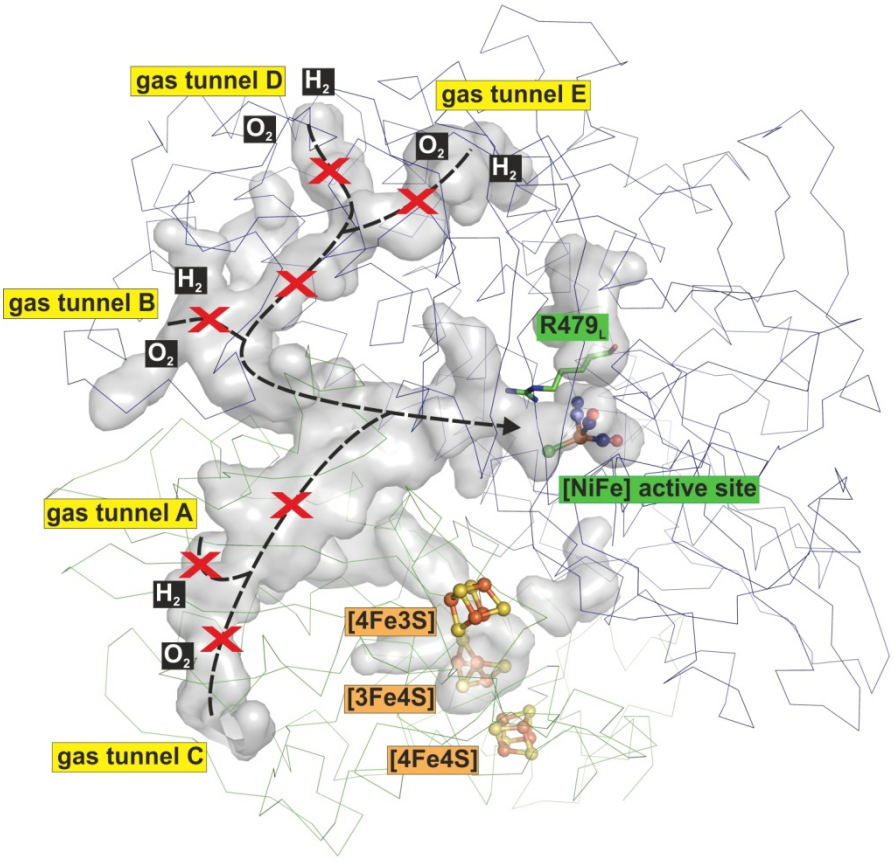

Figure 31: Possible mutational alterations at the hydrophobic tunnel network of O_2–sensitive [NiFe] hydrogenase from *Desulfovibrio vulgaris* Miyazaki F. The protein cα backbone is shown as blue C-alpha backbone representation. The [NiFe] active site is illustrated as ball/stick and the conserved arginine 479_L (initial starting point in *Caver 3.0* calculation) as stick. The grey tunnel surface was calculated in *Py*MOL. The [FeS]-clusters in the small subunit are shown as ball/stick representation in yellow and orange for the sulfur atoms and iron ions, respectively. The routes of the gas molecules in tunnel A - E, are indicated as black dashed arrows. Possible mutation sites for closing the tunnels are shown as red cross.

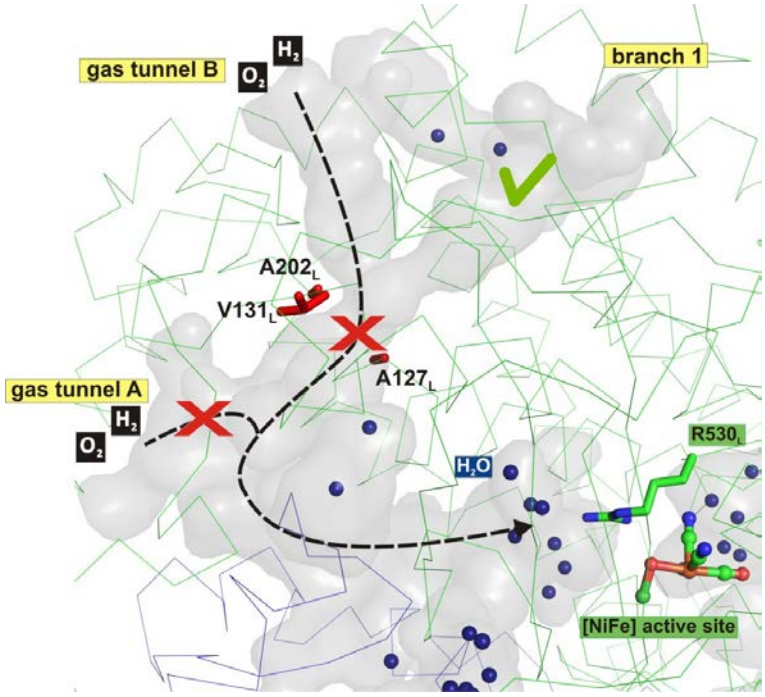

Figure 32: Possible mutational alterations at the hydrophobic tunnel network of O_2-tolerant *Re*MBH. The small and large subunits are shown in blue and green cα backbone representation, respectively. The [NiFe] active site is illustrated as ball/stick and the conserved arginine 530_L (initial starting point in *Caver 3.0* calculation) as stick. The grey tunnel surface was calculated in *Py*MOL. Water molecules are depicted as blue spheres. The bottleneck of tunnel B is composed of amino acids $A127_L$, $V131_L$ and $A202_L$ (red sticks). The routes of the gas molecules in both, tunnel A and B, are indicated as black dashed arrows. Possible mutation sites for opening or closing the tunnels are shown as green tick or red cross, respectively.

Intriguing, O_2 tolerance is not only been found in [NiFe] hydrogenases, but also in the small subgroup of [NiFeSe] hydrogenases. In this enzyme class one of the terminal Ni ligands is a seleno-cysteine compared to the cysteine present in [NiFe] hydrogenases.[7] Interestingly, besides the O_2 tolerance also a high activity for H_2 evolution with an insignificant inhibition by the product H_2 could be detected in the [NiFeSe] hydrogenase from the sulphate-reducing bacteria *Desulfomicrobium baculatum*.[121] Several advantages of the incorporated selenium compared to the cysteine sulfur have been proposed: *(i)* sterically protecting Ni from O_2 attack, *(ii)* higher nucleophilicity, thus higher enzyme activity and *(iii)* oxidized selenium is easily reducible.[121] Several studies with MD simulations on the [NiFeSe] hydrogenases from *D. baculatum* and *Desulfovibrio vulgaris* Hildenborough detected notable differences in the gas transport pathways.[122,123] Compared to the O_2-sensitive [NiFe] hydrogenase from *Desulfovibrio gigas* an alternative pathway has been found and being linked to the higher enzyme activity through higher H_2 concentrations in the protein. The tunnel network stretches closer to the active site Ni ion and the H_2 density close to the catalytic centre has been found higher compared to the O_2-sensitive [NiFe] hydrogenase from *D. gigas*. Additionally, cavities

with calculated and trapped potential H_2 molecules have been presumed to either hinder the transport of substrate to the active site or act as gas reservoirs (***Figure 33***).[122] Based on the structural and computational results of *Re*MBH as well as the MD simulation results on the [NiFeSe] hydrogenases from *D. baculatum* and *Desulfovibrio vulgaris* Hildenborough further comparative structural studies including computational calculations between O_2-tolerant and O_2-sensitive hydrogenases together with the different hydrogenase classes should be considered to gather comprehensive data about the enzyme tunnel network and their influence in enzyme activity and O_2 tolerance.

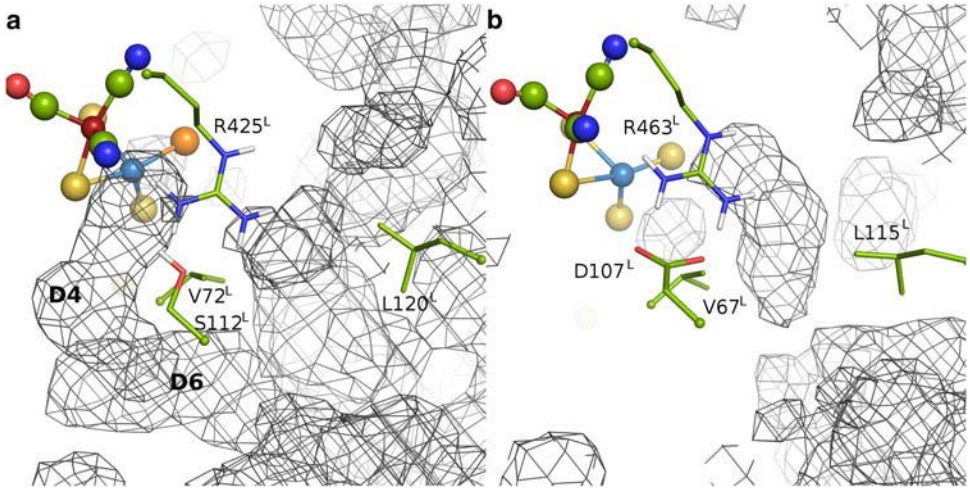

Figure 33: Calculated probability density maps of potential H_2 molecules. Figure 33 was inherited from Baltazar *et al*.[122] The binuclear active site of *D. baculatum* (a) and *D. gigas* (b) are shown in ball/stick representation with the Fe ion in red, the Ni ion in light blue, sulfur in yellow and selenium in orange. The probability H_2 density is depicted as grey mesh. The crystallographic structure is represented as a surface. The cavities surrounding amino acids and the conserved arginine are illustrated in sticks. Cavities of higher H_2 density in *D. baculatum* are named D4 and D6.

10 Lipoxygenase Pa-LOX

Lipoxygenases are widely present in eukaryotes, marginal in bacteria (< 0.5 % of bacteria contain LOX-like genes) and have not been identified in archaea. The general function of LOXs, catalysing the dioxygenation of PUFAs into hydroperoxides, is uniform in all species. However, the purpose of LOXs is commonly known in animals and plants, whereas in bacterial LOXs it remains elusive. The low appearances of LOX genes in bacteria imply that the enzymes are not essential for bacteria survival. Otherwise, in some bacteria it has been proposed that the variability in membrane composition assisted by LOX facilitates the adaption of the bacterium to a wide range of environments.[35] There are no great amounts of PUFAs found in bacteria, which indicates the possible use of LOX substrate from host cells. Knowing the contribution of eukaryotic LOX in immune response and *Pa* as human pathogen leads to the hypothesis that Pa-LOX might be involved in interfering with the host immune response system. This theory is further supported by our studies showing that Pa-LOX is able to oxygenate membrane phospholipids and takes part in biofilm formation in the host cells. Pa-LOX has been tested for leukotriene synthase activity as found in the human ALOX5, which is involved in the biosynthesis of pro-inflammatory mediators like leukotrienes. Leukotrienes are synthesised from arachidonic acid and trigger as well as sustain inflammatory reactions. In our studies, such leukotriene synthase activity has not been detected for Pa-LOX. However, the biosynthesis of anti-inflammatory mediators such as lipoxins, which reverse the inflammatory response and initiate repair activities, has been proposed for Pa-LOX. This is an additional indication for Pa-LOX playing a role in invasiveness and infectiousness of Pa. In contrast, no lipoxin synthase or phospholipid oxygenase activity has been detected in Pa-LOX as presented in the recent study from Deschamps and colleagues.[124] Several differences in both experiments like protein concentration, pH, temperature dependence and a possible difference in tag sequence length might be the reason for the varying Pa-LOX characteristics. An alignment of the experimental conditions would be needed to receive comparable data. Furthermore, studies on actual Pa infected patient material are inevitable to validate *in vitro* results of the phospholipid oxygenase activity of Pa-LOX in red blood cells.

The first structure of bacterial LOX from *Pseudomonas aeruginosa* was solved in 2013 revealing a major structural difference compared to eukaryotic LOXs. The single polypeptide monomer of Pa-LOX does not show the two-domain fold as found in eukaryotic LOXs. The eukaryotic N-terminal β-barrel domain being involved in membrane binding is missing in

bacterial Pa-LOX. However, two additional α-helices (lid-helices) seem to inherit the binding function. The structural and functional results of wild-type Pa-LOX are presented in the publication "*Structural and functional basis of phospholipid oxygenase activity of bacterial lipoxygenase from Pseudomonas aeruginosa*" (Results, 8iii). In the presented wild-type Pa-LOX structure a phosphatidylethanolamine was bound to the catalytic sn-1 cavity and the sn-2 cavity close to the lid-helices. The sn1 fatty acid and the sn2 fatty acid were incorporated in the respective cavity. The polar head group of the phospholipid sits at the substrate entrance and is surface exposed. The two amino acids Arg422 and Asp190 form hydrogen bonds with the head group ($P2_12_12$ crystal form) and orient the substrate in the cavities. However, Arg422 is flexible and shifts away in the $C222_1$ crystal form. Further data of phospholipid oxygenase activity proved the preferable binding of the sn1 fatty acid in the sn1-cavity. Interestingly, mammalian membrane phospholipids like phosphatidylcholine (PC), phosphatidyl-ethanolamine (PE) or phosphatidylinositol (PI) carry a saturated fatty acid at the sn1 position and polyunsaturated fatty acid at the sn2 position. To understand the possible function of Pa-LOX in oxygenation of the host membrane lipids the binding characteristics of these lipids need to be examined through co-crystallisation and crystal ligand soaking experiments or ligand docking studies. Substrate docking studies of linoleic acids and arachidonic acid into the positive *Fo-Fc* electron density map of the phosphatidylethanolamine present in the crystal structure gave an interesting insight into basis of the stereoselective hydrogen abstraction. Pa-LOX was described as *S*-LOX and the structural data of the substrate docking showed for the first time the orientation of linoleic acid and arachidonic acid in the sn1-cavity. The data shows a distance of the 2.2 Å between the pro*S*- hydrogen atom at C11 of the linoleic acid backbone the active site water (hydroxyl) compared to 3.7 Å for the pro*R*-hydrogen. The same has been found for arachidonic acid. The docking experiment illustrates the structural basis for the pro*S*-hydrogen abstraction during Pa-LOX catalyses. As the docking studies are based on electron density of the saturated fatty acid of the bound phosphatidylethanolamine, which has no bisallylic methylene in the vicinity of the active site, further structural studies with arachidonic acid and linoleic acid bound in the sn1-cavity are essential for detailed knowledge of Pa-LOX stereoselectivity. Another interesting approach could be the study of a crystal structure with an empty substrate tunnel to verify possible structural changes through substrate binding or selectivity of sn1 or sn2 fatty acid in either of the pockets. This could be achieved via mutations at the bottom of each cavity or at the substrate entrance. Mutation experiments in the sn-2 cavity could detect the importance of this pocket being involved in substrate binding as well as interacting with phospholipids of host membranes. An empty tunnel network is also a well-

defined starting point for crystal derivatisation experiments with krypton or better with molecular oxygen using the 'soak-and-freeze' method to further study the tunnel network in Pa-LOX. Blocking the O_2 access tunnel followed by activity experiments might offer a more detailed description of the gas tunnel function (***Figure 34***).

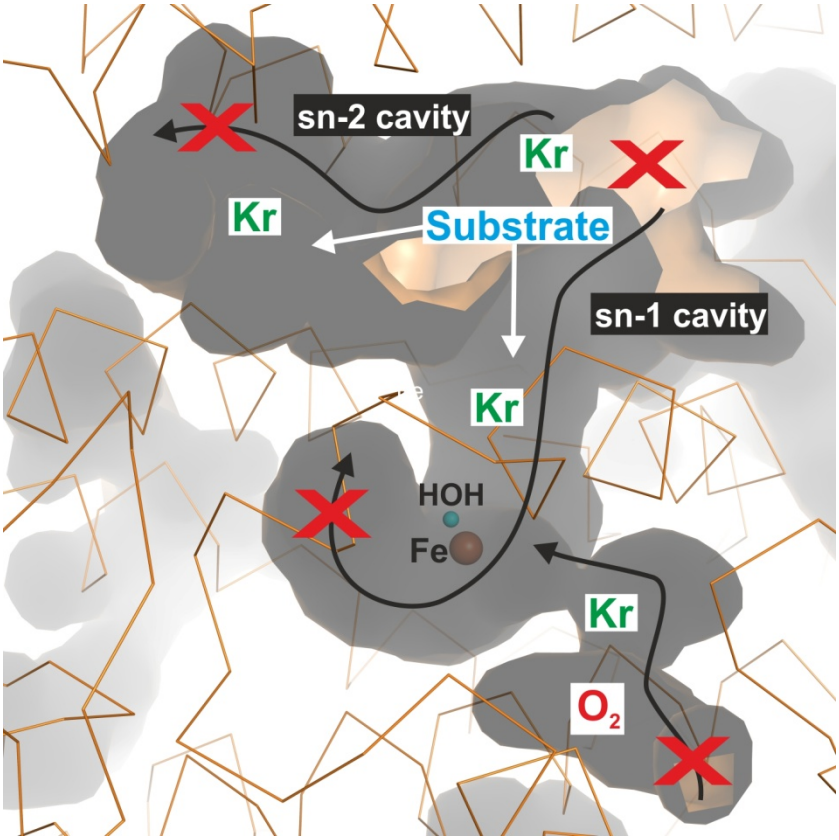

Figure 34: Pa-LOX outlook. Pa-LOX protein α-carbon backbone depicted as orange ribbon. The tunnel network is shown as grey surface calculated with the program *Py*MOL. The active site non-heme iron and the water molecule (hydroxyl) are illustrated as spheres in orange and cyan, respectively. Possible future Pa-LOX experiments: *(i)* crystal derivatisation with krypton (Kr) and molecular oxygen (O_2), *(ii)* mutations to block the substrate cavities and the O_2 access tunnel and *(iii)* various substrate binding studies.

In the publication "*The crystal structure of Pseudomonas aeruginosa lipoxygenase Ala420Gly mutant explains its altered reaction specificity*" (Results, 8iv) the research focused on the regio- and stereospecificity of the Ala-Gly concept, which was found in most LOX-isoforms, together with the substrate tunnel and O_2 access tunnel as previously illustrated in eukaryotic LOXs. Pa-LOX carries an alanine at a critical position close to the catalytic centre and is, according to Coffa classification, an *S*-LOX.[54] This is also confirmed by spectroscopic methods, showing that linoleic acid and arachidonic acid are peroxidised to *S*-hydroperoxy derivates. Compared to the wild-type Pa-LOX functioning as 15*S*-LOX, spectroscopic studies of the Ala420Gly mutant demonstrated its dual reaction specificity functioning additionally as arachidonic acid 11*R*-LOX. Further experiments with deuterated linoleic acid also proved the abstraction of the

pro*S*-hydrogen of C11. The spectroscopic results were supported by the results of the X-ray crystallography studies of wild-type Pa-LOX and the Ala420Gly mutant, which revealed the importance of the alanine in the regio- and stereospecific control of the substrate oxygenation. Computational tunnel calculations show that alanine is part of the bottleneck of the proposed O_2 access tunnel blocking the position for substrate oxygenation in *R*-configuration. Interestingly, opening this bottleneck by exchanging alanine to glycine expands the tunnel and enables the O_2 to reach the fourth position of the 1,4-pentadiene moiety of the substrate. This proves that Pa-LOX follows the Ala-Gly concept and shows for the first time the structural change within the O_2 tunnel. This tunnel enlargement might explain the improvement in O_2 affinity of the Ala420Gly mutant (${K_m}^{O_2} = 0.2\,mM$) compared to the wild-type (${K_m}^{O_2} = 0.4\,mM$). Comparing eukaryotic, bacterial and fungal substrate tunnels reveals similarities and differences. In most structures, a sn-1 cavity in a U-shape was found, were the bisallylic methylene of the substrate at the bottom of the U is arranged in close proximity to the active site. An exception is the cyanobacterial LOX from *Cyanothece sp*. PCC8801 with a shorter cavity blocked by bulkier amino acids, which are proposed to rearrange through substrate binding to open the tunnel. However, the additional sn-2 cavity found in Pa-LOX cannot be shown for the eukaryotic LOX as this cavity is formed through the contribution of the additional lid-helices. This structural difference enables Pa-LOX to bind a diglyceride in both substrate cavities. An enlargement of the substrate tunnel can also be seen in the cyanobacterial LOX presented before, probably through the additional helical structure in the catalytic domain.

In bacterial and eukaryotic LOXs an O_2 access tunnel has been described, whereas a structural gas tunnel characterisation for cyanobacterial and fungal LOX remains unknown so far. Even so no O_2 tunnel was reported in the recently published structure of fungal MnLOX from *Magnaporthe oryzae Caver 3.0* calculations revealed a gas tunnel close to the position of the other described tunnels, but with a different location of the tunnel entrance (***Figure 35***). Compared to the relatively conserved substrate tunnel, the gas tunnel seems to show greater differences in volume, length or the position of the tunnel entrance between organisms. Further on, crystal structures are static models of the studied enzyme and therefore MD simulations may reveal the existence of further transient gas tunnels.

Especially as *Pseudomonas aeruginosa* being a human pathogen, understanding the characteristics of the substrate and gas tunnels and the structure near the active site opens opportunities in searching for possible inhibitory drug targets. Inhibitors described so far in

human leukocyte 12-lipoxygenase[125], rabbit reticulocyte 15-LOX-1 and human 15-LOX-2[64] are all bound to the substrate sn1-cavity blocking the active site. Defining the structure and characteristics of the O_2 access tunnel could promote the search for different types of LOX inhibitors.

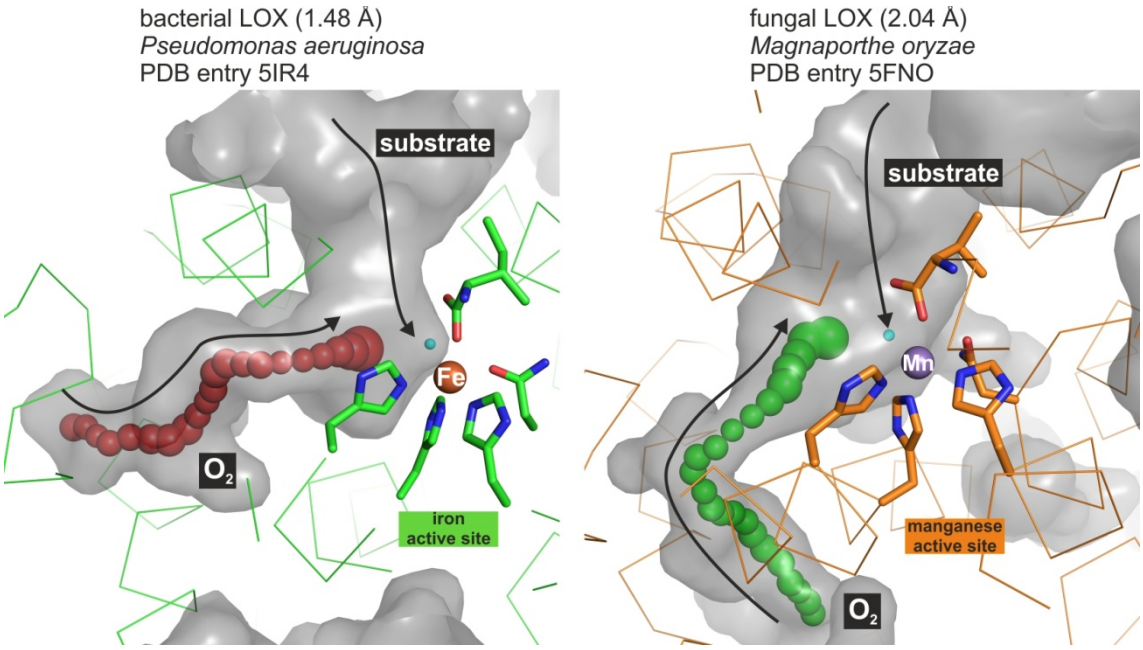

Figure 35: Comparison putative O_2 access tunnel of superposed Pa-LOX (left) and MnLOX (right). The protein matrix of Pa-LOX and MnLOX are depicted in ribbon representation in green and orange, respectively. Both active site amino acids are shown in sticks with the metal ions in orange and purple sphere for Fe and Mn, respectively. The active site water molecule (hydroxyl) is illustrated as cyan sphere. The tunnel system is calculated as grey surface in *Py*MOL and the putative O_2 access path is calculated with the program *Caver 3.0* and shown as chain of spheres in red and green for Pa-LOX and fungal MnLOX, respectively.

.

References

1. Rögner, M. in *Biohydrogen* (De Gruyter, 2015).
2. Schagger, H., Cramer, W. A. & Vonjagow, G. Classification and phylogeny of hydrogenases. *Anal. Biochem.* **217,** 220–230 (1994).
3. Zirngibl, C. *et al.* H2-forming methylenetetrahydromethanopterin dehydrogenase, a novel type of hydrogenase without iron-sulfur clusters in methanogenic archaea. *Eur. J. Biochem.* **208,** 511–20 (1992).
4. Hiromoto, T. *et al.* The crystal structure of C176A mutated [Fe]-hydrogenase suggests an acyl-iron ligation in the active site iron complex. *FEBS Lett.* **583,** 585–590 (2009).
5. Pandey, A. S., Harris, T. V., Giles, L. J., Peters, J. W. & Szilagyi, R. K. Dithiomethylether as a ligand in the hydrogenase H-cluster. *J. Am. Chem. Soc.* **130,** 4533–4540 (2008).
6. Fritsch, J. *et al.* The crystal structure of an oxygen-tolerant hydrogenase uncovers a novel iron-sulphur centre. *Nature* **479,** 249–252 (2011).
7. Garcin, E. *et al.* The crystal structure of a reduced [NiFeSe] hydrogenase provides an image of the activated catalytic center. *Structure* **7,** 557–66 (1999).
8. Hexter, S. V., Grey, F., Happe, T., Climent, V. & Armstrong, F. A. Electrocatalytic mechanism of reversible hydrogen cycling by enzymes and distinctions between the major classes of hydrogenases. *Proc. Natl. Acad. Sci.* **109,** 11516–11521 (2012).
9. Fontecilla-Camps, J. C., Volbeda, A., Cavazza, C. & Nicolet, Y. Structure/function relationships of [NiFe]- and [FeFe]-hydrogenases. *Chem. Rev.* **107,** 4273–303 (2007).
10. Friedrich, B., Fritsch, J. & Lenz, O. Oxygen-tolerant hydrogenases in hydrogen-based technologies. *Curr. Opin. Biotechnol.* **22,** 358–364 (2011).
11. Buhrke, T., Lenz, O., Krauss, N. & Friedrich, B. Oxygen tolerance of the H2-sensing [NiFe] hydrogenase from Ralstonia eutropha H16 is based on limited access of oxygen to the active site. *J. Biol. Chem.* **280,** 23791–23796 (2005).
12. Buhrke, T., Porthun, A., Friedrich, B. & Lenz, O. The H2-sensing complex of Ralstonia eutropha: interaction between a regulatory [NiFe] hydrogenase and a histidine protein kinase. *Mol. Microbiol.* **51,** 1677–1689 (2004).
13. Kleihues, L., Lenz, O., Bernhard, M., Buhrke, T. & Friedrich, B. The H2 sensor of Ralstonia eutropha is a member of the subclass of regulatory [NiFe] hydrogenases. *J. Bacteriol.* **182,** 2716–2724 (2000).
14. Burgdorf, T. *et al.* The Soluble NAD + -Reducing [NiFe] -Hydrogenase from Ralstonia eutropha H16 Consists of Six Subunits and Can Be Specifically Activated by NADPH The Soluble NAD ∂ -Reducing [NiFe] -Hydrogenase from Ralstonia eutropha H16 Consists of Six Subunits and Ca. **187,** 3122–3132 (2005).
15. Horch, M., Lauterbach, L., Mroginski, M.A., Hildebrandt, P., Lenz, O., Zebger, I. Reversible Active Site Sulfoxygenation Can Explain the Oxygen Tolerance of a NAD+-Reducing [NiFe] Hydrogenase and Its Unusual Infrared Spectroscopic

Properties. *J. Am. Chem. Soc.* **137**, 2555−2564 (2015).

16. Schäfer, C., Friedrich, B. & Lenza, O. Novel, oxygen-insensitive group 5 [NiFe]-hydrogenase in Ralstonia eutropha. *Appl. Environ. Microbiol.* **79,** 5137–5145 (2013).

17. Greening, C. *et al.* Atmospheric hydrogen scavenging: From enzymes to ecosystems. *Appl. Environ. Microbiol.* **81,** 1190–1199 (2015).

18. Constant, P., Poissant, L. & Villemur, R. Isolation of *Streptomyces* sp. PCB7, the first microorganism demonstrating high-affinity uptake of tropospheric H_2. *ISME J.* **2,** 1066–1076 (2008).

19. Greening, C., Berney, M., Hards, K., Cook, G. M. & Conrad, R. A soil actinobacterium scavenges atmospheric H 2 using two membrane-associated, oxygen-dependent [NiFe] hydrogenases. **111,** 4257–4261 (2014).

20. Conrad, R., Aragno, M. & Seiler, W. The inability of hydrogen bacteria to utilize atmospheric hydrogen is due to threshold and affinity for hydrogen. *FEMS Microbiol. Lett.* **18,** 207–210 (1983).

21. Lubitz, W., Ogata, H., Ru, O. & Reijerse, E. Hydrogenases. (2014).

22. Frielingsdorf, S. *et al.* Reversible [4Fe-3S] cluster morphing in an O2-tolerant [NiFe] hydrogenase. *Nat. Chem. Biol.* **10,** 378–85 (2014).

23. Volbeda, A. *et al.* Crystal structure of the nickel–iron hydrogenase from Desulfovibrio gigas. *Nature* **373,** 580–587 (1995).

24. Teixeira, V. H., Soares, C. M. & Baptista, A. M. Proton pathways in a [NiFe]-hydrogenase: A theoretical study. *Proteins* **70,** 1010–1022 (2008).

25. Fontecilla-Camps, J. C., Amara, P., Cavazza, C., Nicolet, Y. & Volbeda, A. Structure-function relationships of anaerobic gas-processing metalloenzymes. *Nature* **460,** 814–22 (2009).

26. Duché, O., Elsen, S., Cournac, L. & Colbeau, A. Enlarging the gas access channel to the active site renders the regulatory hydrogenase HupUV of Rhodobacter capsulatus O2 sensitive without affecting its transductory activity. *FEBS J.* **272,** 3899–3908 (2005).

27. Schäfer, C. *et al.* Structure of an Actinobacterial-Type [NiFe]-Hydrogenase Reveals Insight into O2-Tolerant H2 Oxidation. *Structure* **24,** 285–292 (2016).

28. Montet, Y. *et al.* Gas access to the active site of Ni-Fe hydrogenases probed by X-ray crystallography and molecular dynamics. *Nature Structural Biology* **4,** 523–526 (1997).

29. Teixeira, V. H., Baptista, A. M. & Soares, C. M. Pathways of H2 toward the active site of [NiFe]-hydrogenase. *Biophys. J.* **91,** 2035–2045 (2006).

30. Wang, P., Best, R. B. & Blumberger, J. Multiscale simulation reveals multiple pathways for H 2 and O 2 transport in a [NiFe] -hydrogenase. **27,** 1–5 (2011).

31. Andreou, A. & Feussner, I. Lipoxygenases - Structure and reaction mechanism. *Phytochemistry* **70,** 1504–1510 (2009).

32. Heshof, R. *et al.* A novel class of fungal lipoxygenases. *Appl. Microbiol. Biotechnol.* **98,** 1261–1270 (2014).

33. Andre, E. & Hou, K. W. The Presence of a Lipoid Oxidase in Soybean, in Glycine soya.

Acad. Sci. **194,** 645–647 (1932).

34. Feussner, I. & Wasternack, C. The Lipoxygenase pathway. *Annu. Rev. Plant Biol.* **53,** 275–297 (2002).

35. Hansen, J. *et al.* Bacterial lipoxygenases, a new subfamily of enzymes? A phylogenetic approach. *Appl. Microbiol. Biotechnol.* **97,** 4737–4747 (2013).

36. Mashima, R. & Okuyama, T. The role of lipoxygenases in pathophysiology; new insights and future perspectives. *Redox Biol.* **6,** 297–310 (2015).

37. Newcomer, M. E. & Brash, A. R. The structural basis for specificity in lipoxygenase catalysis. *Protein Sci.* **24,** 298–309 (2015).

38. Grechkin, A. Recent developments in biochemistry of the plant lipoxygenase pathway. *Prog. Lipid Res.* **37,** 317–352 (1998).

39. Gardner, H. W. Recent investigations into the lipoxygenase pathway of plants. *Biochim. Biophys. Acta (BBA)/Lipids Lipid Metab.* **1084,** 221–239 (1991).

40. Siedow, J. N. Plant Lipoxygenase: Structure and Function. *Annu. Rev. Plant Physiol. Plant Mol. Biol* **42,** 145–188 (1991).

41. Rustan, A. C. & Drevon, C. A. Fatty Acids: Structures and Properties. *Encycl. Life Sci.* 1–7 (2005). doi:10.1038/npg.els.0003894

42. Kuhn, H., Banthiya, S. & van Leyen, K. Mammalian lipoxygenases and their biological relevance. **1851,** 308–330 (2015).

43. Kuhn, H. & Thiele, B. J. The diversity of the lipoxygenase family. Many sequence data but little information on biological significance. *FEBS Lett.* **449,** 7–11 (1999).

44. Knab, L. M., Grippo, P. J. & Bentrem, D. J. Involvement of eicosanoids in the pathogenesis of pancreatic cancer: The roles of cyclooxygenase-2 and 5-lipoxygenase. *World J. Gastroenterol.* **20,** 10729–10739 (2014).

45. Noverr, M. C., Erb-Downward, J. R. & Huffnagle, G. B. Production of eicosanoids and other oxylipins by pathogenic eukaryotic microbes. *Clin. Microbiol. Rev.* **16,** 517–533 (2003).

46. Andreou, A., Brodhun, F. & Feussner, I. Biosynthesis of oxylipins in non-mammals. *Prog. Lipid Res.* **48,** 148–170 (2009).

47. Oliw, E. H. Plant and fungal lipoxygenases. *Prostaglandins Other Lipid Mediat.* **68–69,** 313–323 (2002).

48. Horn, T. *et al.* Evolutionary aspects of lipoxygenases and genetic diversity of human leukotriene signaling. *Prog. Lipid Res.* **57,** 13–39 (2015).

49. Kuhn, H. & Borchert, A. Regulation of enzymatic lipid peroxidation: the interplay of peroxidizing and peroxide reducing enzymes. *Free Radic. Biol. Med.* **33,** 154–172 (2002).

50. Hughes, R. K. *et al.* Probing a novel potato lipoxygenase with dual positional specificity reveals primary determinants of substrate binding and requirements for a surface hydrophobic loop and has implications for the role of lipoxygenases in tubers. *Biochem. J.* **353,** 345–355 (2001).

51. Hornung, E., Walther, M., Kühn, H. & Feussner, I. Conversion of cucumber linoleate 13-lipoxygenase to a 9-lipoxygenating species by site-directed mutagenesis. *Proc. Natl. Acad. Sci. U. S. A.* **96,** 4192–7 (1999).

52. Kuhn, H. *et al.* Structural biology of mammalian lipoxygenases: Enzymatic consequences of targeted alterations of the protein structure. *Biochem. Biophys. Res. Commun.* **338,** 93–101 (2005).

53. Kuhn, H. Structural basis for the positional specificity of lipoxygenases. *Prostaglandins Other Lipid Mediat.* 255–270 (2000). doi:10.1016/S0090-6980(00)00084-8

54. Coffa, G. & Brash, A. R. A single active site residue directs oxygenation stereospecificity in lipoxygenases: stereocontrol is linked to the position of oxygenation. *Proc. Natl. Acad. Sci. U. S. A.* **101,** 15579–84 (2004).

55. Jansen, C. *et al.* Stereocontrol of arachidonic acid oxygenation by vertebrate lipoxygenases: Newly cloned zebrafish lipoxygenase 1 does not follow the ala-versus-gly concept. *J. Biol. Chem.* **286,** 37804–37812 (2011).

56. Boyington, J. C., Gaffney, B. J. & Amzel, L. M. The Three-Dimensional Structure of an Arachidonic Acid 15-Lipoxygenase. *Sience* **260,** 1482–1486 (1993).

57. Hammarberg, T., Provost, P., Persson, B. & Rådmark, O. The N-terminal domain of 5-lipoxygenase binds calcium and mediates calcium stimulation of enzyme activity. *J. Biol. Chem.* **275,** 38787–38793 (2000).

58. Kulkarni, S., Das, S., Funk, C. D., Murray, D. & Cho, W. Molecular basis of the specific subcellular localization of the C2-like domain of 5-lipoxygenase. *J. Biol. Chem.* **277,** 13167–13174 (2002).

59. Brodhun, F. *et al.* An Iron 13S-Lipoxygenase with an ??-Linolenic Acid Specific Hydroperoxidase Activity from Fusarium oxysporum. *PLoS One* **8,** (2013).

60. Wennman, A., Oliw, E. H., Karkehabadi, S. & Chen, Y. Crystal structure of manganese lipoxygenase of the Rice Blast Fungus Magnaporthe oryzae. **1,** 1–20 (2016).

61. Garreta, A. *et al.* Structure and interaction with phospholipids of a prokaryotic lipoxygenase from Pseudomonas aeruginosa. *FASEB J.* **27,** 4811–4821 (2013).

62. Newie, J. *et al.* Crystal structure of a lipoxygenase from Cyanothece sp. may reveal novel features for substrate acquisition. *J. Lipid Res.* **57,** 276–87 (2016).

63. Banthiya, S. *et al.* Structural and functional basis of phospholipid oxygenase activity of bacterial lipoxygenase from Pseudomonas aeruginosa. *Biochim. Biophys. Acta - Mol. Cell Biol. Lipids* **1861,** 1681–1692 (2016).

64. Kobe, M. J., Neau, D. B., Mitchell, C. E., Bartlett, S. G. & Newcomer, M. E. The structure of human 15-lipoxygenase-2 with a substrate mimic. *J. Biol. Chem.* **289,** 8562–8569 (2014).

65. Vidal-Mas, J., Busquets, M. & Manresa, A. Cloning and expression of a lipoxygenase from Pseudomonas aeruginosa 42A2. *Antonie van Leeuwenhoek, Int. J. Gen. Mol. Microbiol.* **87,** 245–251 (2005).

66. Saam, J., Ivanov, I., Walther, M., Holzhütter, H.-G. & Kuhn, H. Molecular dioxygen enters the active site of 12/15-lipoxygenase via dynamic oxygen access channels. *Proc.*

Natl. Acad. Sci. U. S. A. **104,** 13319–24 (2007).

67. Kalms, J. *et al.* The crystal structure of Pseudomonas aeruginosa lipoxygenase Ala420Gly mutant explains the improved oxygen affinity and the altered reaction specificity. *BBA - Mol. Cell Biol. Lipids* (2017). doi:10.1016/j.bbalip.2017.01.003

68. Brezovsky, J. *et al.* Software tools for identification, visualization and analysis of protein tunnels and channels. *Biotechnol. Adv.* **31,** 38–49 (2013).

69. Raushel, F. M., Thoden, J. B. & Holden, H. M. Enzymes with molecular tunnels. *Acc. Chem. Res.* **36,** 539–548 (2003).

70. Huang, X., Holden, H. M. & Raushel, F. M. Channeling of substrates and intermediates in enzyme-catalyzed reactions. *Annu. Rev. Biochem* **70,** 149–80 (2001).

71. Kingsley, L. J. & Lill, M. A. Substrate tunnels in enzymes: Structure-function relationships and computational methodology. *Proteins Struct. Funct. Bioinforma.* **83,** 599–611 (2015).

72. Chovancova, E. *et al.* CAVER 3.0: A Tool for the Analysis of Transport Pathways in Dynamic Protein Structures. *PLoS Comput. Biol.* **8,** 23–30 (2012).

73. Thoden, J. B., Holden, H. M., Wesenberg, G., Raushel, F. M. & Rayment, I. Structure of carbamoyl phosphate synthetase: A journey of 96 Å from substrate to product. *Biochemistry* **36,** 6305–6316 (1997).

74. Krahn, J. M. *et al.* Coupled formation of an amidotransferase interdomain ammonia channel and a phosphoribosyltransferase active site. *Biochemistry* **36,** 11061–11068 (1997).

75. Oliver, J. C., Linger, R. S., Chittur, S. V & Davisson, V. J. Substrate Activation and Conformational Dynamics of GMP Synthetase. *Biochemistry* (2013). doi:10.1021/bi3017075

76. Mouilleron, S., Badet-Denisot, M. A. & Golinelli-Pimpaneau, B. Glutamine binding opens the ammonia channel and activates glucosamine-6P synthase. *J. Biol. Chem.* **281,** 4404–4412 (2006).

77. Van Den Heuvel, R. H. H. *et al.* Structural studies on the synchronization of catalytic centers in glutamate synthase. *J. Biol. Chem.* **277,** 24579–24583 (2002).

78. Coulombe, R., Yue, K. Q., Ghisla, S. & Vrielink, A. Oxygen Access to the Active Site of Cholesterol Oxidase through a Narrow Channel Is Gated by an Arg-Glu Pair. *J. Biol. Chem.* **276,** 30435–30441 (2001).

79. Klvana, M. *et al.* Pathways and Mechanisms for Product Release in the Engineered Haloalkane Dehalogenases Explored Using Classical and Random Acceleration Molecular Dynamics Simulations. *J. Mol. Biol.* **392,** 1339–1356 (2009).

80. Kalms, J. *et al.* Krypton Derivatization of an O2-Tolerant Membrane-Bound [NiFe] Hydrogenase Reveals a Hydrophobic Tunnel Network for Gas Transport. *Angew. Chemie - Int. Ed.* **55,** 5586–5590 (2016).

81. Petrek, M. *et al.* CAVER: a new tool to explore routes from protein clefts, pockets and cavities. *BMC Bioinformatics* **7,** 316 (2006).

82. Petřek, M., Košinová, P., Koča, J. & Otyepka, M. MOLE: A Voronoi Diagram-Based

Explorer of Molecular Channels, Pores, and Tunnels. *Structure* **15,** 1357–1363 (2007).

83. Yaffe, E., Fishelovitch, D., Wolfson, H. J., Halperin, D. & Nussinov, R. MolAxis: a server for identification of channels in macromolecules. *Nucleic Acids Res.* **36,** 210–215 (2008).

84. Smart, O. S., Neduvelil, J. G., Wang, X., Wallace, B. A. & Sansom, M. S. P. HOLE: A program for the analysis of the pore dimensions of ion channel structural models. *J. Mol. Graph.* **14,** 354–360 (1996).

85. Coleman, R. G. & Sharp, K. a. Finding and characterizing tunnels in macromolecules with application to ion channels and pores. *Biophys. J.* **96,** 632–45 (2009).

86. Pellegrini-Calace, M., Maiwald, T. & Thornton, J. M. PoreWalker: A novel tool for the identification and characterization of channels in transmembrane proteins from their three-dimensional structure. *PLoS Comput. Biol.* **5,** (2009).

87. Ho, B. K. & Gruswitz, F. HOLLOW: generating accurate representations of channel and interior surfaces in molecular structures. *BMC Struct. Biol.* **8,** 49 (2008).

88. Voss, N. R. & Gerstein, M. 3V: Cavity, channel and cleft volume calculator and extractor. *Nucleic Acids Res.* **38,** 555–562 (2010).

89. Aurenhammer, F. Voronoi Diagrams — A Survey of a Fundamental Data Structure. *ACM Comput. Surv.* **23,** 345–405 (1991).

90. Dijkstra, E. W. *A note on two problems in connexion with graphs. Numerische Mathematik 1* (1959).

91. Furnham, N. *et al.* The Catalytic Site Atlas 2.0: Cataloging catalytic sites and residues identified in enzymes. *Nucleic Acids Res.* **42,** 485–489 (2014).

92. Rupp, B. *Biomolecular Crystallography: Principles, Practice, and Application to Structural Biology*. (2009).

93. Bergfors, T. M. *Protein Crystallization*. (2009).

94. Drenth, J. *Principles of Protein X-Ray Crystallography*. (Springer, 2006).

95. Evans, P. & McCoy, A. An introduction to molecular replacement. *Acta Crystallogr. Sect. D Biol. Crystallogr.* **64,** 1–10 (2007).

96. Taylor, G. The phase problem. *Acta Crystallogr. - Sect. D Biol. Crystallogr.* **59,** 1881–1890 (2003).

97. Davis, I. W. *et al.* MolProbity: All-atom contacts and structure validation for proteins and nucleic acids. *Nucleic Acids Res.* **35,** 375–383 (2007).

98. Rodriguez, R., Chinea, G., Lopez, N., Pons, T. & Vriend, G. Homology modeling, model and software evaluation: three related resources. *Bioinformatics* **14,** 523–528 (1998).

99. Berman, H. M. *et al.* The Protein Data Bank. *Nucleic Acids Res.* **28,** 235–242 (2000).

100. Lovell, S. C. *et al.* Structure validation by C alpha geometry: phi,psi and C beta deviation. *Proteins-Structure Funct. Genet.* **50,** 437–450 (2003).

101. Gabadinho, J. *et al.* MxCuBE: A synchrotron beamline control environment customized for macromolecular crystallography experiments. *J. Synchrotron Radiat.* **17,** 700–707

(2010).

102. Nurizzo, D. *et al.* The ID23-1 structural biology beamline at the ESRF. *J. Synchrotron Radiat.* **13,** 227–238 (2006).

103. Incardona, M. F. *et al.* EDNA: A framework for plugin-based applications applied to X-ray experiment online data analysis. *J. Synchrotron Radiat.* **16,** 872–879 (2009).

104. Kabsch, W. Xds. *Acta Crystallogr. Sect. D Biol. Crystallogr.* **66,** 125–132 (2010).

105. Evans, P. Scaling and assessment of data quality. *Acta Crystallogr. Sect. D Biol. Crystallogr.* **62,** 72–82 (2006).

106. Collaborative Computational Project. The CCP4 suite: Programs for protein crystallography. *Acta Crystallogr. Sect. D Biol. Crystallogr.* **50,** 760–763 (1994).

107. Winn, M. D. *et al.* Overview of the CCP4 suite and current developments. *Acta Crystallogr. Sect. D Biol. Crystallogr.* **67,** 235–242 (2011).

108. McCoy, A. J. *et al.* Phaser crystallographic software. *J. Appl. Crystallogr.* **40,** 658–674 (2007).

109. Adams, P. D. *et al.* PHENIX: A comprehensive Python-based system for macromolecular structure solution. *Acta Crystallogr. Sect. D Biol. Crystallogr.* **66,** 213–221 (2010).

110. Murshudov, G. N., Vagin, A. A. & Dodson, E. J. Refinement of macromolecular structures by the maximum-likelihood method. *Acta Crystallogr. Sect. D Biol. Crystallogr.* **53,** 240–255 (1997).

111. Emsley, P., Lohkamp, B., Scott, W. G. & Cowtan, K. Features and development of Coot. *Acta Crystallogr. Sect. D Biol. Crystallogr.* **66,** 486–501 (2010).

112. Brünger, A. T. Free R value: a novel statistical quantity for assessing the accuracy of crystal structures. *Nature* **355,** 472–475 (1992).

113. The PyMOL Molecular Graphics System, Version 1.8 Schrödinger, LLC.

114. Van Der Linden, P. *et al.* Towards a high-throughput system for high-pressure cooling of cryoprotectant-free biological crystals. *J. Appl. Crystallogr.* **47,** 584–592 (2014).

115. Lafumat, B. *et al.* Gas-sensitive biological crystals processed in pressurized oxygen and krypton atmospheres: deciphering gas channels in proteins using a novel `soak-and-freeze' methodology. *J. Appl. Crystallogr.* **49,** (2016).

116. De Sanctis, D. *et al.* ID29: A high-intensity highly automated ESRF beamline for macromolecular crystallography experiments exploiting anomalous scattering. *J. Synchrotron Radiat.* **19,** 455–461 (2012).

117. Winn, M. D., Isupov, M. N. & Murshudov, G. N. Use of TLS parameters to model anisotropic displacements in macromolecular refinement. *Acta Crystallogr. Sect. D Biol. Crystallogr.* **57,** 122–133 (2001).

118. Vaguine, A. A., Richelle, J. & Wodak, S. J. SFCHECK: a unified set of procedures for evaluating the quality of macromolecular structure-factor data and their agreement with the atomic model. *Acta Crystallogr. D. Biol. Crystallogr.* **55,** 191–205 (1999).

119. Laskowski, R. A., MacArthur, M. W., Moss, D. S. & Thornton, J. M. PROCHECK: a

program to check the stereochemical quality of protein structures. *J. Appl. Crystallogr.* **26,** 283–291 (1993).

120. Volbeda, A. *et al.* X-ray crystallographic and computational studies of the O2-tolerant [NiFe]-hydrogenase 1 from Escherichia coli. *Proc. Natl. Acad. Sci.* **109,** 5305–5310 (2012).

121. Wombwell, C., Caputo, C. A. & Reisner, E. [NiFeSe]-Hydrogenase Chemistry. *Acc. Chem. Res.* **48,** 2858–2865 (2015).

122. Baltazar, C. S. A., Teixeira, V. H. & Soares, C. M. Structural features of [NiFeSe] and [NiFe] hydrogenases determining their different properties: A computational approach. *J. Biol. Inorg. Chem.* **17,** 543–555 (2012).

123. Gutiérrez-Sanz, O. *et al.* Influence of the protein structure surrounding the active site on the catalytic activity of [NiFeSe] hydrogenases. *J. Biol. Inorg. Chem.* **18,** 419–427 (2013).

124. Deschamps, J. D. *et al.* Biochemical and Cellular Characterization and Inhibitor Discovery of Pseudomonas aeruginosa 15-Lipoxygenase. *Biochemistry* **55,** 3329–3340 (2016).

125. Xu, S., Mueser, T. C., Marnett, L. J. & Funk, M. O. Crystal structure of 12-Lipoxygenase catalytic-domain-inhibitor complex identifies a substrate-binding channel for catalysis. *Structure* **20,** 1490–1497 (2012).

Table of Figures

Acknowledgement

Ich möchte mich bei allen bedanken, die diese Arbeit ermöglicht haben und mich während der Promotion immer unterstützt haben.

Ganz besonders möchte ich mich bedanken bei Dr. Patrick Scheerer für die Bereitstellung des sehr interessanten Themas, die Möglichkeit die Dissertation in seiner Arbeitsgruppe durchzuführen und die immer sehr inspirierenden sowie motivierenden Mettings.

Weiterhin möchte ich mich bei Dr. Oliver Lenz und Dr. Stefan Frielingsdorf für die Bereitstellung von unglaublichen Mengen an MBH, der Nutzung des Labors und die zahlreichen anregenden Diskussionen bedanken.

Bei Prof. Peter Hildebrandt möchte ich mich für die Übernahme der Zweitkorrektur und für die anregenden Meetings bedanken.

Prof. Hartmut Kühn und Dr. Swathi Banthiya möchte ich herzlich danken für die Bereitstellung von Pa-LOX und die biochemische Charakterisierung.

Allen Freunden und Kollegen des IMPB und der Arbeitsgruppe Prof. Christian Spahn danke ich sehr für das entspannte Klima am Arbeitsplatz.

Besonderer Dank gilt auch meiner lieben Kollegin und Freundin Andrea Schmidt. Vielen Dank für die großartige Zeit im Labor, am Synchrotron, im Roten und Grünen und manchmal auch im Dunkeln und nicht zu vergessen, im Kalten. Für die ständige Erreichbarkeit, die unzähligen Diskussionen, das kritische Korrekturlesen meiner Arbeit und das wir immer was zu schmunzeln hatten.

Dr. Michal Szczepek, Brian Bauer, Anja Koch, Gabriele Chusainow, Aschat Chusainow und Dr. Ciara Lally danke ich für das angenehme Arbeitsklima, die Unterstützung im Labor und für die organisatorischen Feinheiten.

Dr. Maria Andrea Mroginski und Dr. Tillmann Utesch für die MBH MD simulationen und die unzähligen Emails zum Austausch von Ergebnissen, klären von Fragen und noch mehr Fragen.

Ich danke allen, die zur Entstehung der Publikationen und somit meiner kumulativen Dissertation beigetragen haben.

Vielen Dank der MX-group von Dr. Manfred Weiss und Dr. Uwe Müller am BESSY in Berlin und dem Team am ESRF für die fantastische Unterstützung am Synchrotron. Vor allem Dr. Philippe Carpentier und Peter van der Linden für die Möglichkeit der Nutzung ihres Pumping Systems für die Derivatisierung unserer Kristalle.

Ich danke meiner Familie: David, Jack, Heinz, Simone, Steffen, Marion und Germanus für die unglaubliche Unterstützung in jeder Lebenslage.